The Hygrothermal Performance of Cold Climate Basement Walls Retrofitted with Insulation and a Water Separation Plane

A THESIS
SUBMITTED TO THE FACULTY OF THE
UNIVERSITY OF MINNESOTA
BY

Anna C. Harmon

IN PARTIAL FULFILLMENT OF THE REQUIREMENTS
FOR THE DEGREE OF
MASTER OF SCIENCE

Advisors:
Louise Goldberg, Ph.D
Patrick Huelman, M.S.

June 2015

Acknowledgements

Thank you to Louise Goldberg and Patrick Huelman for sharing with me their expertise and passion for building science. Your guidance and support were invaluable. An additional thank you to Thomas Kuehn for serving on my committee and providing feedback. I was fortunate to have a committee with such knowledgeable and kind people.

Table of Contents

List of Figures

List of Tables

List of Acronyms

BCF	Buoyant Cavity Flow
BUFETS	BUilding Foundation and Energy Transport Simulation
CMU	Concrete Masonry Unit
CRRF	Cloquet Residential Research Facility
ESL	Equivalent Soil Layer
FAF	Final Archival Format
FS	Face Shell
HDPE	High-density Polyethylene
IAF	Intermediate Archival Format
IECC	International Energy Code Council
IRC	International Residential Code
MC	Moisture Content
NCDC	National Climatic Data Center
o.c.	on center
OSB	Oriented Strand Board
PAF	Processed Archival Format
PVC	Polyvinyl Chloride
SBP	Spun-bonded Polyolefin
TMY	Typical Meteorological Year
USDA	United States Department of Agriculture
WS	Weather Station
WSP	Water Separation Plane
XPS	Extruded Polystyrene

List of Symbols

A	Area
c	Heat Capacity
C	Celsius
F	Fahrenheit
G	Electrical conductance
h	Half the height of the soil domain below the footing
i	Current
k	Thermal conductivity
K	Kelvin
L	Height of segment
m	Meter
M	Mass
Q	Heat
R	Thermal resistance
S	Degree of saturation
T	Temperature
t	Time
V	Voltage or Volume
W	Watts or Arbitrarily defined variable
X	Arbitrarily defined variable
Z	Arbitrarily defined variable
θ	Moisture content
ξ	Porosity
ρ	Density

List of Subscripts

A	Domain between bottom of footing and boundary m
a	Outdoor ambient
avg	Weighted average temperature at top of domain A
B	Domain in concrete slab
$base$	Basement slab
C	Domain between boundary m and deep ground
$crib$	Crib
D	Domain between soil surface and bottom of footing
dg	Deep ground
$horz$	Between basement and soil adjacent to wall/footing
i	Element under consideration
j	Time step
m	Mid-point of soil domain below footing
M	Mass
mat	Soil matrix (water + soil particles)
od	Oven-dry
P	Domain between bottom of slab and bottom of footing
s	Soil
t	During drying process
tot	Total (voids + skeleton)
v	Volumetric
w	soil
x	Pins, leads, and epoxy

Chapter 1: Introduction

This research addresses the hygrothermal performance of below-grade foundation walls in cold climates (International Energy Conservation Code (IECC) climate zones 6 and 7). Specifically, the evaluation of hollow core concrete masonry unit (CMU) below-grade foundation walls retrofitted with insulation and a water separation plane (WSP). For this research, existing, below-grade, full basement walls were retrofitted and instrumented to better understand their hygrothermal performance. Fourteen months of experimental data were collected and analyzed. The data were used to evaluate the hygrothermal performance, hollow core buoyant cavity flow, soil moisture transport, and basement heat loss. Further, the experimental data were compared to a three-dimensional thermal model of the wall system and used to evaluate the accuracy of the model. Basic heat transfer calculations were then used to validate the explanation proposed for the differences between the experimental data and the model.

1.1 Wall System Selection

Four wall systems were constructed for this research. The walls differed by the type of WSP, the location and extent of the insulation, and the type of soil used for the backfill. Table 1-1 provides a listing of the wall systems' components.

Wall/Bay	WSP	Insulation	Interior Finish	Soil
1	Adhered	Interior, full-height 3 in. XPS	2x3 open cavity stud wall, ½ in. gypsum board	Imported loam
2	Adhered	Interior, full-height 3 in. XPS	2x3 open cavity stud wall, ½ in. gypsum board	Imported sand
3	Non-adhered	Interior, full-height 3 in. XPS	2x3 open cavity stud wall, ½ in. gypsum board	Native sand with silt
4	Adhered	Exterior, half-height 3 in. XPS	2x3 open cavity stud wall, ½ in. gypsum board	Native sand with silt

Table 1-1: Wall System Details

The selection of the wall systems was based on previous research by Goldberg and Steigauf (2013). The walls were designed to meet the hygrothermal performance criteria of the 2009 Minnesota Building Code stipulated in Chapter 1322, Section N1102.2.6.12 (Chapter 2.5). Accordingly, R-10 foundation wall insulation was required. However, the 2012 IECC Energy Code and the proposed 2015 Minnesota Energy Code required R-15 insulation. To meet the 2012 IECC standards, R-15 rigid board insulation was used on all the wall systems tested.

All the wall systems used 3 in. extruded polystyrene (XPS) insulation that provided R-15 thermal resistance. Three wall systems used full-height insulation on the interior face of the wall and the fourth wall system used half-height insulation on the upper half of the exterior face of the wall. Interior insulation was used on three of the systems because full height insulation is usually easier and more economical to install on existing below-grade walls since no excavation is required. The fourth wall system used exterior insulation for comparison because warm interior walls are far less susceptible to moisture-related failures. However, half-height insulation, instead of full-height insulation, was used because it is more economical to install as it does not require excavation down to the footing. Further, insulation on the upper half of the wall nominally is thermally more effective[1] since heat loss is greater through the upper half of the wall (where the temperature difference is larger) than the lower half.

The walls used either an adhered or non-adhered WSP. The adhered WSP was a peel-and-stick rubberized asphalt material adhered to the wall that was pre-coated with a solvent-based liquid primer. The non-adhered WSP was a $^1/_4$ in. thick dimpled high-density polyethylene (HDPE) sheet. The non-adhered WSP provided a drainage cavity between the wall and the WSP. The non-adhered WSP edges and fasteners had to be carefully sealed to maintain the integrity of the water separation plane. Further, at the base of the wall, it required the installation of a drainage channel to drain any bulk water from the drainage cavity. The additional complexity made it more time-consuming to install than the adhered WSP. This system is considered necessary for wet walls with evidence of bulk water which has the potential to cause delamination of an adhered

[1] Thermal effectiveness is the ratio of one-dimensional heat flux to three-dimensional heat flux for the same thermal resistance.

WSP. The fourth wall used an adhered WSP with the exterior insulation which allowed for the comparison of the wall with the Bay 1 and 2 walls that also used an adhered WSP.

Two of the walls (Bays 1 and 2) used imported backfill to test the comparative hygrothermal performance of the wall when exposed to a well-drained soil (sand) and a poorly-drained soil (loam). The walls were of identical construction except for the backfill. The other two walls (Bays 3 and 4) were backfilled with the native soil, a reasonably well-drained sand with silt.

1.2 Instrumentation Philosophy

The long-term durability of a wall system is highly dependent on its moisture performance. The soil and CMU moisture contents, the surface dew points, and the vapor pressures and absolute humidities of the air spaces provide the necessary understanding of the moisture performance of a wall system.

The soil on the exterior face of a below-grade wall creates a complex boundary condition for understanding the wall performance. The ability of the soil to retain moisture significantly impacts the moisture content of the wall itself. The soil domain was instrumented with moisture content sensors that provided bulk water boundary conditions for the wall. Further, the sensors provided a means of analyzing how water moves through the soil domain. It also allowed for the comparison of the moisture content and water flow paths in different soil types.

The CMU moisture content sensors provided a means of assessing condensation, bulk water flow, and freeze/thaw potential. Interior and exterior CMU face shell moisture content sensors allowed the determination of the variation in moisture content across the CMU. The exterior CMU face shell moisture content enabled understanding of the relationship between the wall and the exterior ambient and soil conditions. In the case of the adhered WSP, the interior moisture content sensors provided insight into the likelihood of delamination of the WSP from the wall. In the case of the non-adhered WSP, the interior moisture content sensors provided a means of determining if condensation occurred. The CMU face shell moisture contents also allowed the

relationship between the hollow core psychrometric conditions and the enclosing masonry to be established.

The vapor pressures in the air spaces of the wall system provided knowledge of the direction of the vapor drive. The direction of the vapor drive was important for understanding the walls' ability to dry. Since it is generally inevitable that a basement wall will get wet, it is important to understand if it dries to the interior or the exterior and the extent to which it can dry. Absolute humidity sensors[2] located on the layers and down the height of the wall system allowed for the vapor pressure to be calculated.

Monitoring of the condensation plane was necessary for understanding the potential for generating liquid within the wall systems. A condensation plane occurs at the nearest impermeable material surface with a temperature less than or equal to the dew point of the cavity air. This causes moisture to condense out of the air and liquid moisture to accumulate on the material. Liquid in the wall system has the potential to cause durability problems such as mold and rot. Condensation on the interior side of the WSP and on rot-susceptible materials was of particular concern. To assess the condensation potential of the condensing surfaces, a temperature sensor was paired with an absolute humidity sensor. The absolute humidity sensor was used to calculate the dew point of the air and the temperature sensor measured the surface temperature of the material.

Absolute humidity sensors not only allowed for the vapor pressure and dew point of the air to be calculated, but they also measured the effectiveness of the insulation and WSP in reducing moisture transport. This provided a means of checking the wall for compliance with the moisture requirements of the Minnesota Building Code (Chapter 2.5).

The thermal performance of a wall system impacts the building energy use and occupant comfort, and for this reason, is an important element for evaluating below-grade walls. To evaluate the thermal performance, the heat flux through the walls and the temperatures throughout the wall systems were measured. The exterior thermal boundary condition for below-grade walls is not uniform because of the soil's insulating

[2] Thin film capacitance relative humidity sensor paired with a temperature sensor for measurement of absolute humidity (Chapter 3.5).

effect. Hence, the temperature sensors and heat flux plates were spaced over the height of the wall.

Heat flux plates measured the horizontal heat loss through the wall systems. The variation in heat loss was measured down the height of the walls and between walls with differing insulation configurations. The heat flux plates measured the heat loss through the insulated wall, but did not capture the heat loss through the slab to the ground and through the slab to the hollow CMU wall cavity.

Temperature sensors were located on all planes of the wall system and additional temperature sensors were located in the soil, interior of the basement, and rim joist cavity to measure the boundary conditions. The grid of temperature sensors across the width and down the height of the wall system allowed the direction of heat transfer to be evaluated. The sensors also allowed the heat flux through wall materials of known thermal conductance to be calculated and compared to the measured heat fluxes. In the hollow core, they provided insight to the pattern of air movement and the existence of buoyant cavity flow.

1.3 Research Objectives

To expand understanding of the hygrothermal performance of below-grade walls, this research aimed to:

- Generate an experimental set of hygrothermal data for below-grade, ground-coupled walls;
- Obtain reliable CMU moisture content data;
- Expand understanding of buoyant cavity flow in below grade walls;
- Study the relationship between soil and wall moisture;
- Evaluate the accuracy of a computer simulation of the experimental wall in predicting the thermal performance of the wall; and,
- Evaluate hypotheses for explaining any observed differences between the experimental and simulation results with simplified heat transfer models and calculations.

Chapter 2: Literature Review

2.1 Thermal Performance of Below-Grade Walls

A large body of work exists that addresses the thermal performance of below-grade walls (Latta and Boileau 1969; Krarti, Claridge, and Kreider 1988b; Krarti, Claridge, and Kreider 1988a; Wang 1979; Mitalas 1983; Claesson and Hagentoft 1991). The below-grade heat flow and temperature field are calculated by analytical, semi-analytical, numerical, and manual methods. The more complex methods accommodate a variety of insulation configurations, two or three dimensions, more than one soil type, and/or the location of the water table. However, many of the models account for limited wall configurations and soil types, thus limiting their range of applicability.

Thermal models do not account for moisture transport as it relates to heat transport or durability. Instead they use a set of soil properties based on a fixed moisture content. The accuracy of this approximation significantly influences the results (Zoras 2009). If a reasonable approximation of the soil properties is made, the models are capable of estimating annual heat loss, but are unable to accurately estimate seasonal heat loss (Deru and Kirkpatrick 2002b; Deru and Kirkpatrick 2002a). Further, the thermal models do not include the effects of buoyant cavity flow in hollow cores (Zoras 2009). Lastly, and of critical importance, there is limited experimental data for validating the thermal models for below-grade walls (Deru 2003).

2.2 Thermal Performance of Below-Grade Walls based on Ground-Coupled Heat and Moisture Transport

A much smaller body of work exists that looks at the thermal performance of below-grade walls by considering ground-coupled heat and moisture transport. Soil moisture affects the thermal performance of ground-coupled below-grade walls in three primary ways (Deru and Kirkpatrick 2002a):

- The moisture (vapor and liquid) transports heat;
- The thermal properties of the soil are dependent on the moisture content; and,
- The latent heat effects from phase change.

Considering moisture transfer along with heat transfer is a more accurate representation of the actual soil physics. Analyzing soil heat and moisture transport requires that the two models be coupled together because each model is dependent on the conditions of the other.

2.2.1 Shen and Ramsey

Shen and Ramsey (1988) used a mechanistic approach to model coupled heat and moisture transfer. The governing equations were expressed in terms of soil matric potential instead of volumetric moisture content because they allowed the model to include heterogeneous soils and saturated conditions. The moisture transport equations included transport due to matric potential gradients, thermal gradients, and gravity. The heat transfer equations accounted for conduction, latent heat transfer in the vapor phase, the heat of vaporization, and sensible heat advected by moisture flow.

The model was developed to simulate the moisture and temperature profiles in the vicinity of an uninsulated below-grade wall. The model did not include the below-grade wall. Instead the boundary was based on the heat flux through an uninsulated wall driven by conduction through the wall and convection on the interior surface.

The equations were integrated into a two-dimensional numerical model that utilized a fully implicit, integrated finite difference technique. The numerical model was verified against one-dimensional analytical solutions and validated against experimental soil test cylinders. The numerical model results were within 2% of the analytical solutions and 15% of the experimental test cylinders. The model was not validated against experimental data from a below-grade wall.

The numerical model test cases considered a winter and a summer day with a rain event and two soil types, sand and clay loam. It was found that the heat transfer between the below-grade wall and the soil could be underestimated if the coupled effect of the moisture was not considered, but this effect was dependent on soil type. For the sand, the wall in the coupled model lost a maximum of 9% more heat on a winter day and gained a maximum of 42% more heat on a summer day than the non-coupled model. The increased heat flow was primarily attributed to the increased energy flow at the surface of the soil due to the surface moisture flow. For the clay soil there was no reportable difference in the heat flow between the coupled and non-coupled models.

The effects were more pronounced in course grained soils such as sand because the moisture can move quickly through the soil.

2.2.2 Deru and Kirkpatrick

Deru and Kirkpatrick (2002a) developed a two-dimensional model for heat and mass transfer in soils adjacent to below-grade walls. The moisture transport equations were formulated in terms of matric potential because they allowed saturated conditions to be considered (like Shen and Ramsey, Chapter 2.2.1). The moisture transfer equations included both liquid and vapor transport and the heat transfer equations included conduction in the soil system due to temperature gradients, heat transfer by diffusion of moisture due to a moisture gradient, and sensible heat transport by bulk water flow of the liquid moisture. The equations for ground-coupled heat and mass transfer were incorporated into a two-dimensional finite element model. The model included detailed heat and mass transfer at the soil-atmosphere boundary that included heat conduction, liquid convection, and vapor drive.

The numerical solutions from the model were verified against a two-dimensional analytical solution for a heat conduction problem and against an analytical isothermal infiltration problem. The model was found to be in good agreement with both. Lastly, a one-dimensional version of the model was used to compare atmospheric boundary conditions and heat and moisture transfer results to field data that was collected in an open, undisturbed field. It was found that the boundary conditions were difficult to accurately simulate due to the numerous influencing factors. However, the temperature gradients compared well. The heat transfer by conduction was dominant except after precipitation when heat transfer by convection was dominant briefly. The model was not validated against experimental data from a below-grade wall.

The two-dimensional model for ground-coupled heat and moisture transfer was applied to two building types, a slab on grade and a below-grade wall (2002b). Precipitation, season, ground-water depth, soil type, and insulation were evaluated for their effects on the building thermal performance. The two soil types considered were Bighorn sandy loam and Yolo light clay. The water table depth was modeled at 3 m, 5 m, and 10 m below the grade (bottom of the wall was 2 m below grade). For the insulated case,

insulation (thermal conductivity of 0.029 W/m-K) was located on the exterior face of the below-grade wall and below the slab.

It was found that the ground water depth has a significant impact on heat transfer from buildings. The most dramatic impact was on uninsulated slabs. In general, the wall thermal performance was affected to a greater extent by surface conditions such as precipitation and the slab was affected to a greater extent by deep-ground conditions. The heat loss through the floors and slabs was greater for sandy loam than it was for light clay. Insulation obviously reduced heat loss, but it also reduced the heat loss effects that were caused by precipitation and ground-water depth.

The coupled heat and moisture transfer model was compared to a heat transfer model that used a constant soil thermal conductivity. The model that used a constant thermal conductivity underpredicted the heat loss in the summer and fall. If the right thermal conductivity was selected, the thermal only model did a reasonable job of predicting the annual heat loss. Caution must be used if thermal-only models are used to look at seasonal variation.

2.2.3 Janssen, Carmeliet, and Hens

Research conducted by Janssen, Carmeliet, and Hens (2004) examined the heat loss to the ground through an insulated below-grade wall and slab and compared a fully coupled heat and moisture transfer model to a linear thermal conduction only model. The linear model used space-varying yearly-averaged soil thermal conductivities and heat capacities that were derived from the coupled model. The linear model assumed heat transfer at the soil surface was controlled solely by air temperature. For the fully coupled model, the heat balance at the soil surface considered sensible heat exchange, solar long-wave radiation, and the transfer of sensible and latent heat by evaporation and precipitation. The moisture balance at the soil surface included precipitation and evaporation.

The heat and moisture transfer equations were solved with a finite element spatial discretization scheme. The numerical model was validated against a series of analytical solutions for a soil column with varying thermal and moisture boundaries (Janssen 2002). The numerical model was found to have good to excellent agreement with the

analytical solutions. The model was not validated against experimental data from a below-grade wall.

The research found that the linear model underestimated the heating season heat loss by 8.2% through the slab and 13.2% through the wall when compared to the fully coupled model. The difference was attributed to the soil surface heat balance (the surface temperatures amplitudes differed by 1.7 deg. C) and the inclusion of moisture transport and storage in the soil heat transfer equations.

The climate, soil type, amount of precipitation, thermal resistance of the wall and slab, width of the foundation, and shape of the foundation were evaluated to determine which parameters caused the most significant differences between the fully coupled and the linear model. It was found that climate, precipitation, and thermal resistance resulted in the largest differences between the models.

The fully coupled model was compared to the European Standard ENISO 13370 for the calculation of building heat loss via the ground. It was found that the ENISO 13370 returned heat loss values that were less than those calculated by the fully coupled method and of the same order as those calculated by the linear method. For the fully coupled simulations, the relationship between the moisture content and thermal conductivity was assumed known and accurate. However, when using design guide methods this is not usually the case. The ENISO 13370 method has two representative values for thermal conductivity, one for clays and silts and one for sands. The thermal conductivity of the sand used in the fully coupled model had a maximum value 13% greater, and an average value 18% less than the ENISO thermal conductivity for sand. It was concluded that the error in predicting building heat loss to the ground using design guides is greater due to inaccuracies in thermal conductivity values than due to excluding moisture transport for the heat transport equations.

It was found that the fully-coupled heat and moisture transfer model is more accurate than the linear model and the linear model underestimates heat losses. However, incorporation of the coupled model into standard calculation methods and design guides could not be justified when the thermal conductivity introduces a greater error in heat loss calculations.

2.2.4 Additional Work

Santos and Mendes (2006) developed a three-dimensional model for heat and mass transfer in soils that was coupled with a one-dimensional conduction only model of the building envelope. The model was used to predict heat flux and indoor temperature and relative humidity. The authors did not state how the model was validated.

Shipp (1979) studied the thermal performance of below-grade walls by collecting experimental data from an existing earth-sheltered building on the University of Minnesota's campus. The experiment collected soil temperature, heat flux, and moisture content data adjacent to the building wall and ranging from 0.25 to 7.5 m below grade. A thermal-only numerical model was developed and validated using the experimental data. Despite collecting soil moisture content data, an average moisture content was used for establishing soil properties for use in the model.

Thomas and Rees (1998) developed an experiment to measure the temperature, heat flux, and moisture content below a normal-weight and a light-weight slab of a concrete slab-on-grade building. The authors found that variation in moisture content was negligible at the center of the slab but significant adjacent to the building, thus suggesting the need for a model that couples heat and moisture transport.

2.3 Buoyant Cavity Flow in Hollow Core Concrete Masonry Unit Below-Grade Walls

2.3.1 Shipp

Shipp (1983) studied heat transfer in hollow concrete masonry unit (CMU) below-grade walls using a hot-box. Four full-size wall systems were tested with the following insulation systems:

- Full-height fiberglass batt insulation in $3^1/_2$ in. stud cavities with gypsum board for an R-11 system;
- On the upper-half of the wall, fiberglass batt insulation in $3^1/_2$ in. stud cavities with gypsum board for an R-11 system;
- Continuous, full-height fibrous glass board insulation for an R-5 system; and,
- No insulation.

The four systems were tested with hollow cores and with sand-filled cores. All of the wall systems were constructed with tapered insulation on the ‘exterior’ face of the wall to mimic the effect of the soil backfill. The concentric circular arc method was used to calculate the ‘soil’ insulation thickness. Heat flux sensors were placed across the height of the wall on the interior and exterior faces of the CMU. Temperature sensors were placed on each side of the gypsum board, on each side of the interior insulation, and on each side of the ‘soil’ insulation. The tests were run with -3.4 deg. C (25 deg. F) outdoor ambient air and 24 deg. C (75 deg. F) indoor ambient air.

If heat flow was purely one-dimensional at a given height, the interior heat flux would equal the exterior heat flux. For all eight configurations, the interior and exterior heat fluxes were not equal and at the top of the wall the exterior heat flux was larger than the interior heat flux. These effects were the most pronounced in the hollow core configurations and were caused by buoyant cavity flow. The sand-filled cores eliminated the effects of buoyant cavity flow, but two-dimensional heat transfer due to conduction still existed.

The experimental heat flux data was compared to a steady-state one-dimensional heat transfer model. The concentric circular arc method was used to calculate the thermal resistance of the wall and soil system and estimate the heat transfer. The model used the isothermal-planes method to calculate the apparent thermal resistance of the concrete block. The model was compared to the test data and it was found that for all configurations the model overestimated the thermal resistance. For the case with half-height insulation and hollow cores, the model overestimated the thermal resistance by R-4.3. For all other cases, the thermal resistance was not overestimated by more than R-1.0. The discrepancy in thermal resistance between the model and experiment was due to vertical heat transfer.

The research confirms the presence of two-dimensional heat flow in hollow CMU below-grade walls. Shipp concluded that although the steady-state one-dimensional model did not capture the effects of vertical heat transfer and specifically buoyant cavity flow in the hollow cores, the results were adequate to not warrant a more complex analysis except for the case of half-height insulation.

2.3.2 McBride

In this research McBride (2013) studied buoyant cavity flow in hollow CMU below-grade walls using a hot-box. The same four wall systems were used as Shipp (1983) (Chapter 2.3.1) with hollow cores and sand-filled cores. The soil backfill was also mimicked, in the same manner as Shipp, using tapered insulation. Six levels of interior and exterior temperature and heat flux sensors were installed on the faces of the block wall.

The difference between the interior and exterior heat flux at a given node quantified the heat flux in the vertical direction. Vertical heat flux in the hollow core wall systems was primarily attributed to buoyant cavity flow, radiation, and conduction in the CMU webs and face shells. In the sand-filled core wall systems, vertical heat flux was primarily attributed to conduction through the sand and CMU webs and face shells. For the insulated wall systems, the vertical heat flow in the hollow core wall systems was at least three times greater than in the wall systems with sand-filled cores.

The author investigated buoyant cavity flow using the Grashof Number and the heat transfer coefficient. It was found that the below-grade hollow core experimental data did not match empirical formulas that modeled buoyant cavity flow in above-grade hollow core walls. It was concluded that the soil boundary condition increased buoyant cavity flow when compared to a uniform exterior boundary condition of air. Further, it was concluded that interior insulation increased buoyant cavity flow. Buoyant cavity flow was the greatest with half-height interior insulation.

Overall, it was concluded “that the heat transfer in hollow cores [was] extremely complex” in below-grade walls and that “natural convection was identified as the major driving force.” No revisions were made to the traditional arc-length method of modeling below-grade heat flow. It was determined that revisions to this method would require a thermal network model that connected all the nodes and included all the modes of heat transfer.

2.3.3 Huelman, Goldberg, and Jacobson

Huelman, Goldberg, and Jacobson (2013) studied a retrofit foundation system for hollow core CMU walls that aimed to improve the thermal and moisture performance of below-grade walls while improving occupant comfort. The retrofit entailed filling the hollow cores with an insulating material and installing a water separation plane (WSP)

and R-10 insulation on the exterior face of the wall that extended from above the rim joist to one foot below grade. Simulation models using BUFETS/Energy Plus and WUFI-2D were used to evaluate the wall system heat loss and hygrothermal performance, respectively.

Values for the thermal conductivity of the retrofit wall and the reference uninsulated hollow core wall were calculated using a steady-state model based on the work of Shipp (Chapter 2.3.1) for use in the simulation. The heat loss for the reference wall was estimated using the calculated thermal conductivity and compared to experimental data for a similar wall at the Foundation Test Facility. The calculated heat loss for the reference wall was found to underestimate the heating season heat loss by 28%. It was concluded that a steady-state model exposed to actual environmental conditions did not accurately model a hollow core wall with buoyant cavity flow. For the simulation, the thermal conductivity was calculated for the reference wall using the experimental data. It was found that the retrofit system decreased the below-grade zone heat loss by up to 27%.

2.4 Hygrothermal Computer Simulations for Below-Grade Walls

Computer software provides an economical means for understanding the hygrothermal performance of wall systems based on differing boundary conditions and building materials. It is important to include moisture transport in software models because moisture impacts thermal performance and has a significant impact on durability. AnTherm, Delphin, MOIST, UMIDUS, and WUFI have the capability to model the hygrothermal performance of above-grade wall systems (U.S. Department of Energy 2011). However, none of these software packages have the capability to explicitly model below-grade wall systems. No software was identified that models the hygrothermal performance of below-grade walls in the U.S. Department of Energy's Building Energy Software Tools Directory (2011).

2.4.1 WUFI 2D

WUFI 2D software developed by the Fraunhofer-Insitut fur Bauphysik, Germany, allows for the two-dimensional, transient analysis of the hygrothermal performance of multi-layer building components exposed to weather (Fraunhofer IBP 2014). A database of building material properties and climate files is included with the software. The software

accounts for construction moisture, interstitial condensation, wind-driven rain, and interior and exterior climate conditions. As configured, WUFI 2D does not directly model wall systems with soil as a boundary layer, nor does it model buoyant cavity flow in hollow cavities.

Huelman et al. (2013) manipulated WUFI 2D in an attempt to model the hygrothermal performance of below-grade walls. An “equivalent soil layer” (ESL) was modeled adjacent to the below-grade wall that used manually defined material properties that represented the fluid mechanics of the porous media. The modeled results were considered questionable without validation against experimental data. It was concluded that more research and experimental validation was required before WUFI 2D could be used in this capacity.

2.5 2009 Minnesota Building Code: Foundation Walls

The 2009 Minnesota Building Code which adopts the 2006 International Residential Code (IRC) with amendments was in place when this work was developed (State of Minnesota 2009). Chapter 1322 of the Minnesota Building Code addresses residential energy and deletes chapter 11 of the IRC and any references to energy. Section 1102.2.6 of Chapter 1322 governs the thermal and moisture design of foundation walls. The Code requirements apply to new construction and not to retrofits. Insulation, water separation planes (WSP), and air barriers for retrofits are not addressed in the Code.

Foundation wall requirements can be met through a prescriptive or performance method. The prescriptive method provides a variety of predetermined options to meet the intent of the Code. The key characteristics of the options are:

- Full height interior or exterior insulation; and,
- Minimum R-10 insulation on walls and in rim joist, except in the Southern Zone where it can be reduced to R-5 if certain criteria are met.

If interior insulation is used for the prescriptive method, the following must be met:

- Masonry block walls shall be drained through the block cores to a drainage system;

- Interior frame walls cannot be in direct contact with the foundation wall unless a water proofing membrane is present;
- Meet requirements of an interior air barrier; and,
- If using rigid insulation, damp proofing or water proofing must be installed on the entire interior wall surface or to the exterior above-grade wall surface.

The performance method of the Code is open to any system that is designed to meet a set of hygrothermal requirements. The performance requirements are:

- A continuous WSP between the interior and exterior that prevents liquid or capillary flow across it and establishes the following interior side conditions:
    - No net accumulation of water or ice over a calendar year and is free of adsorbed water for a minimum of four months a year;
    - Prevents moisture and temperature conditions favorable to mold growth; and,
    - Prevents liquid water from the wall system reaching the floor system at any time.
- Air barrier system separating the interior and exterior that has an air permeability less than or equal to 0.004 $ft^3/min.ft^2$ under a pressure differential of 0.3 inches of water.

2.6 Summary

The glaring issue with the research on below-grade walls discussed is the lack of long-term, reliable experimental data from full-scale wall systems. Cost, resources, and time limit the generation of building ground-coupled, below-grade experimental data. However, experimental data are necessary to understand how below-grade walls perform and to validate computer models. The majority of thermal and hygrothermal computer models for below-grade walls were validated using existing analytical methods and/or open field soil columns. Without validation by experimental data from below-grade walls, it is difficult to truly understand the accuracy of the models. If design decisions and code requirements are to be made using these models, it is imperative that they are linked back to experimental data.

Experimental data from full-scale, in-situ below-grade walls are needed to understand the impacts of buoyant cavity flow on the hygrothermal performance. Existing computer models do not account for buoyant cavity flow in open core below-grade walls and without experimental data, the accuracy of models with this omission is unclear. To further refine computer models, experimental data are necessary for validation.

More research is needed on the hygrothermal performance of below-grade walls. Much of the research focuses on the thermal performance of the walls and does not consider moisture. Moisture needs to be included in the analysis because it influences the thermal performance of the wall system. The inclusion of wall moisture in computer models will allow for more accurate thermal performance estimates. Further, and arguably more importantly, moisture needs to be accounted for in research because it has a significant impact on durability. Excessive moisture can lead to mold growth, rotting building materials, and structural damage. For this reason, experimental research and computer models should account for moisture parameters in addition to thermal parameters. This reinforces the need for hygrothermal experimental data to develop and improve below-grade ground-coupled hygrothermal computer models.

A prescriptive method for below-grade wall retrofits is needed in the Building Code. Retrofit construction has a distinctly different set of constraints than new construction and therefore requires a separate set of prescriptive Code requirements. Hygrothermal experimental research on retrofit wall systems is necessary for providing robust recommendations. Further, the improvement of hygrothermal computer models through validation with experimental data will allow the models to be used for the design and development of retrofit below-grade wall systems to meet the performance criteria of the Code.

The research objectives (Chapter 1.3) for this work were developed based on the gaps found in the literature and stated above. The intent of this research was to enhance the body of knowledge available on the hygrothermal performance of below-grade hollow core CMU walls in cold climates.

Chapter 3: Experimental Setup

3.1 Site

The experiment was located at the Cloquet Residential Research Facility (CRRF) at the University of Minnesota's Cloquet Forestry Center in Cloquet, Minnesota. Cloquet is approximately 20 miles southwest of Duluth, Minnesota and Lake Superior and approximately 125 miles north of Minneapolis-Saint Paul, Minnesota. Cloquet is located in International Energy Conservation Code (IECC) climate zone 7. The average number of heating degree days (base 65°F) for Cloquet is 9,506 (Western Regional Climate Center 2012). The average monthly minimum temperature is 1.4°F and the average monthly maximum temperature is 80.0°F (Western Regional Climate Center 2013).

The CRRF is a single-story, 5,000 ft.^{2} (including basement) building that was built in 1997. The building is 124 ft. long by 20 ft. wide and is oriented with its long axis along the east-west axis. The building basement is divided into 10 bays that are 10 ft. wide with a service bay with stairs at each end (Figure 3-1). Each bay has a north and a south wall. Bay 1 is located on the west side of the building, numbering consecutively to bay 10 on the east side of the building. The foundation walls of Bays 1-5 are constructed of 12 in. concrete masonry units (CMU) and the foundation walls of Bays 6-10 are constructed of 8 in. cast-in-place concrete. At the midpoint of the long axis, on the south side of the building, there is a 20 ft. wide bump-out that extends 11 ft. south (building is 31 ft. wide at this location); Bays 5 and 6 are located in the bump-out. Due to the building's orientation, the west side of the bump-out is partially shaded in the morning and the east side of the bump-out is partially shaded in the afternoon. The experiment was constructed in Bays 1-4.

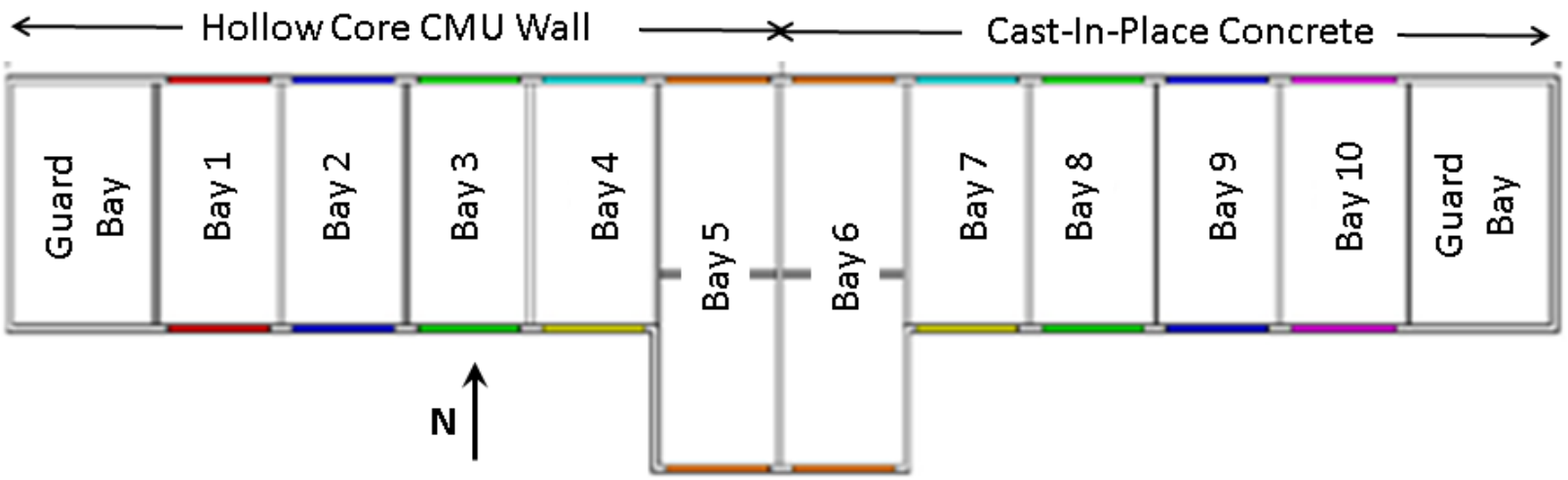

Figure 3-1: Cloquet Residential Research Facility Basement Plan Layout

This research was conducted in the west CMU wall section. Specifically, this section is constructed of nominal 12 in. wide, 2-core, CMU with vertical reinforcing at 48 in. o.c. and a continuous reinforced bond beam in the top course. The CMU was confirmed to have a 'stretcher' configuration (Figure 3-3 and Figure 3-4). A reinforced concrete strip footing supports the wall. The basement floor is a 4 in. thick concrete slab reinforced with welded-wire fabric and placed on a 6 in. sand base with a 6 mil polyethylene vapor retarder between the slab and the sand. At the perimeter of the slab, the vapor retarder wraps around the slab and extends approximately 8 in. up the wall.

During construction of the experiment, the walls were excavated down to the top of the footing. The exterior face of the wall is coated with a masonry parging and painted with a bituminous damp-proofing from the bottom of the footing to the top of the grade. It was observed that granular fill sits on top of the footing and is covered with filter fabric. It was evident that during the installation of the damp-proofing, the gravel was coated with bitumen; further, the filter fabric was poorly installed allowing soil to penetrate the gravel layer. Eight inch Form-A-Drain™[3] was used as the foundation drainage system and the form for the cast-in-place concrete footing. The product is a drainage channel that is located on each side of the footing. The two channels are connected together by a pipe and drain to a sump with a pump at either end of the building (Figure 3-1).

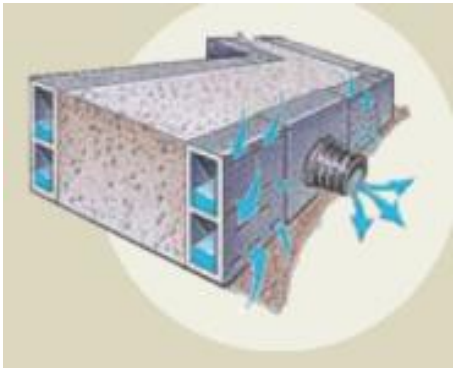

(CertainTeed 2014)

Figure 3-2: Foundation Drainage System

[3] At the time of construction, a product of the CertainTeed Corporation.

In the west test basement, the floor system comprises 14 in. deep wood I-joists spaced at 24 in. o.c and supported on a 2x6 continuous treated wood sill plate that is anchored to the top of the CMU wall. Moving from the interior to the exterior of the rim joist cavity, the wall is constructed of a $1^{3}/_{16}$ in. oriented strand board (OSB) rim, $^{1}/_{2}$ in. OSB exterior sheathing, spun-bonded polyolefin (SBP) building weather barrier, and vinyl siding. In the rim cavity, 2 in. thick polyisocyanurate insulation is fitted tightly to the floor sheathing between the I-joists.

The roof has a 6:12 pitch with a 1 ft. 6 in. overhang. There is no gutter system and rain and snow melt sheet drain to the ground below. The building is located in a clearing in the forest. Trees have been completely cleared for approximately 150 ft. to the south and north and 30 ft. to the east and west. The experiment required excavation of Bays 1-4 which disturbed the existing grass. Grass was not replanted and exposed soil is present from Bay 1 to mid-way through Bay 5.

3.2 Wall System Layouts

For Bays 1-4, there was one vertical line of interior and exterior sensors that was installed approximately at the mid-point of each bay. The line of sensors was installed on a plane that aligned with the center of a CMU hollow core, except for Bay 3N where it was installed on a grouted core (Figure 3-3 and Figure 3-4). All sensors were located using the top of the wall as a reference point. For sensors at the same height, there were no vertical offsets between the sensors, unless noted below. On the inside face of the basement wall, an existing 2x4 baseplate was left in place that served as the ‘bottom plate’ for the new wall systems. A new 2x3 baseplate was added adjacent to the 2x4 to accommodate the width of the new wall systems.

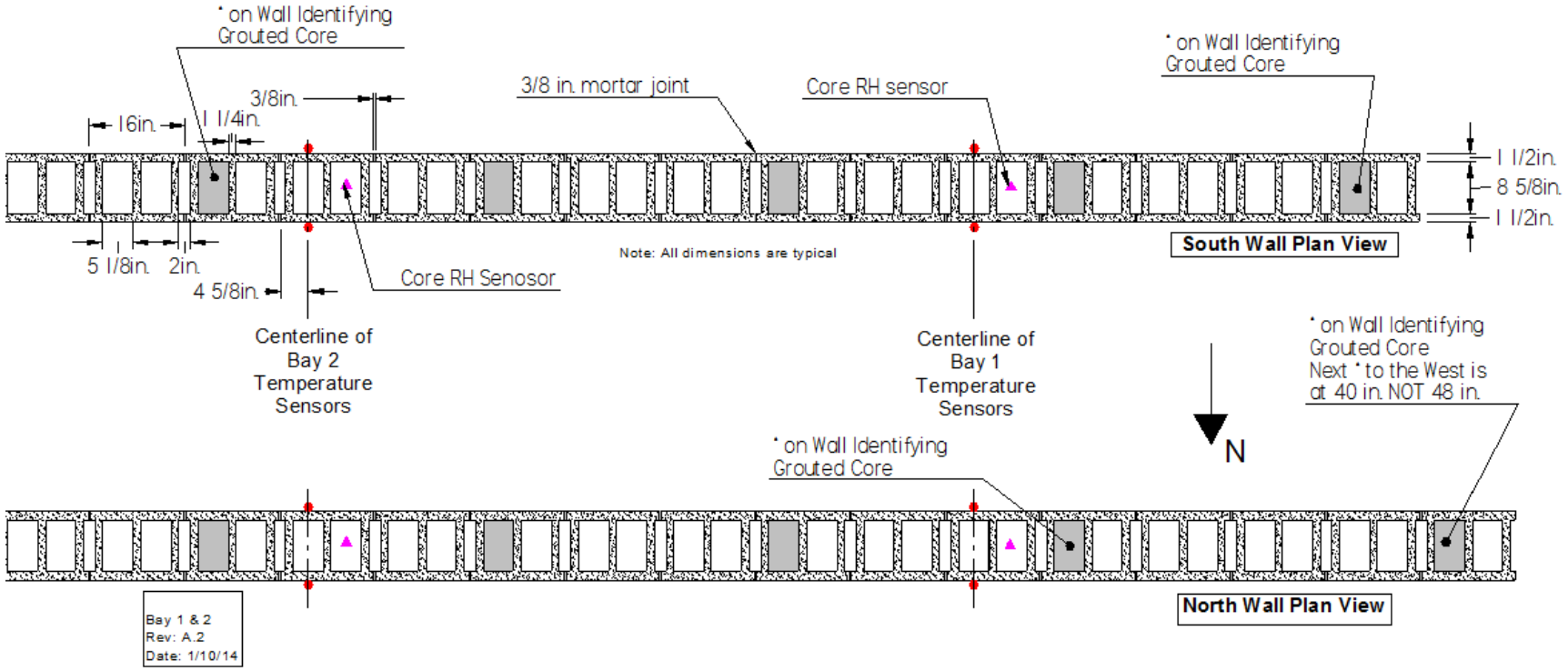

Figure 3-3: Wall Sensor Layout for Bays 1 and 2 North and South

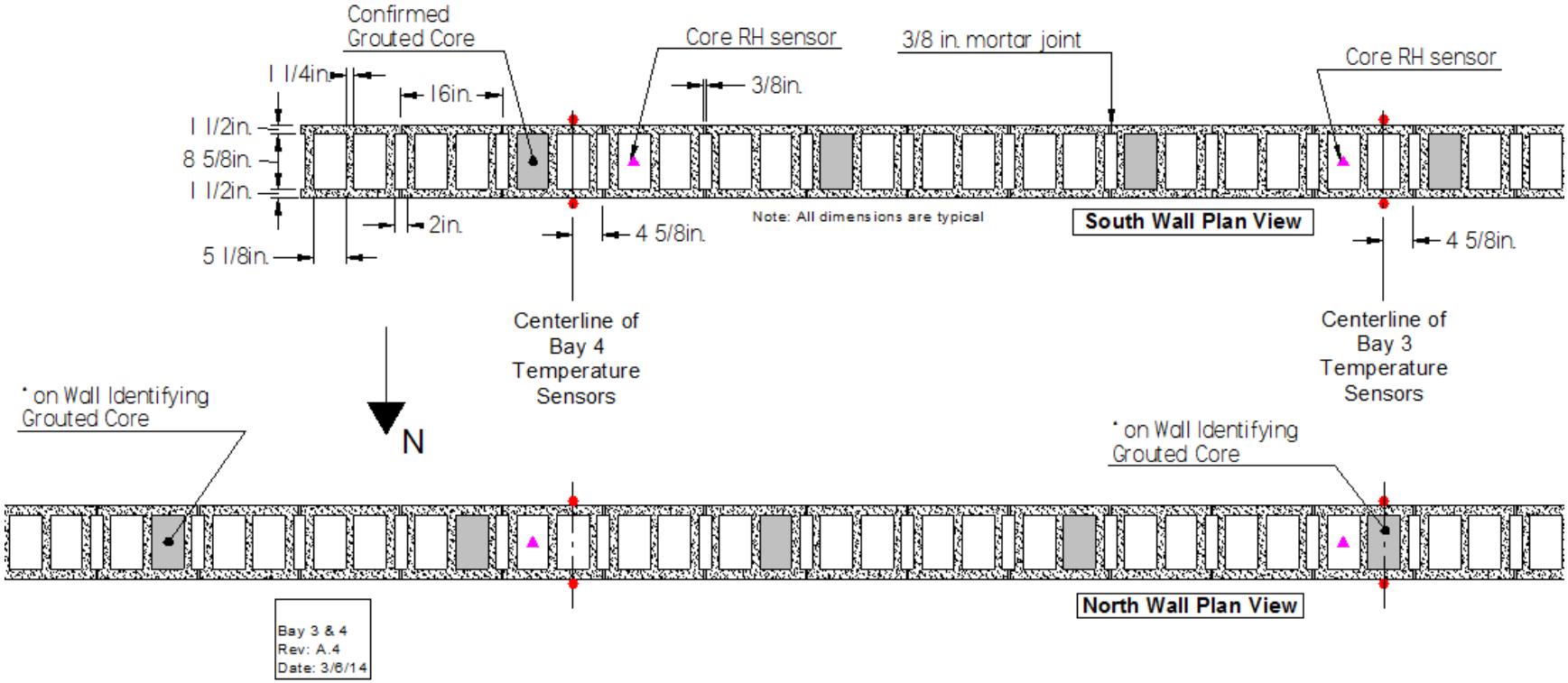

Figure 3-4: Wall Sensor Layout for Bays 3 and 4 North and South

When installing sensors, the wires typically ran horizontally approximately 12 in. from the sensor and then turned vertical and ran out the top of the wall system. The wires were routed through small holes drilled in the top plate of the wood stud wall and these holes were caulked afterwards. On the exterior, wires were fed into a conduit box that was installed on the rim joist cavity exterior face and routed through the wall in a conduit to the data acquisition system in the basement. The hole in the rim for the conduit was caulked on the interior and exterior and the interior of the conduit box was filled with spray foam insulation.

Interior and exterior work (wall system and sensor installation and excavation/backfill) was completed in the fall of 2012 for Bays 1 and 2. Interior work (wall system and interior sensor installation) was completed during the 2012-13 winter, but due to freezing conditions, exterior work for Bays 3 and 4 was not completed until the spring of 2013. Bays 1 and 2 began full data collection (interior and exterior) in November 2012 and Bays 3 and 4 began partial data collection (interior only) in January 2013 and full data collection (interior and exterior) in June 2013. As described below, Bay 4 utilizes an exterior insulation system, which was not installed until the spring of 2013. Data collected from Bay 4 between January 2013 and May 2013 represented an uninsulated basement wall and served as a control for Bays 1, 2, and 3.

3.2.1 Bays 1 and 2

Bays 1 and 2 were identical in construction, except for the soil backfill. Bay 1 was backfilled with a sandy-silt (Unified Soil Classification System ML) that fell within the ‘loam’ section of the U.S. Department of Agriculture (USDA) Soil Classification Triangle. Bay 2 was backfilled with a sand (Unified Soil Classification System SP) that fell within the ‘sand’ section of the USDA Soil Classification Triangle (Figure 3-5). The imported fill was contained in a three sided crib that was fitted tightly to the basement wall and was open on the top and bottom (Figure 3-6). The native soil outside the crib was classified as a sand with silt (Unified Soil Classification System SP-SM) that fell within the ‘sand’ section of the USDA Soil Classification Triangle (Figure 3-5).

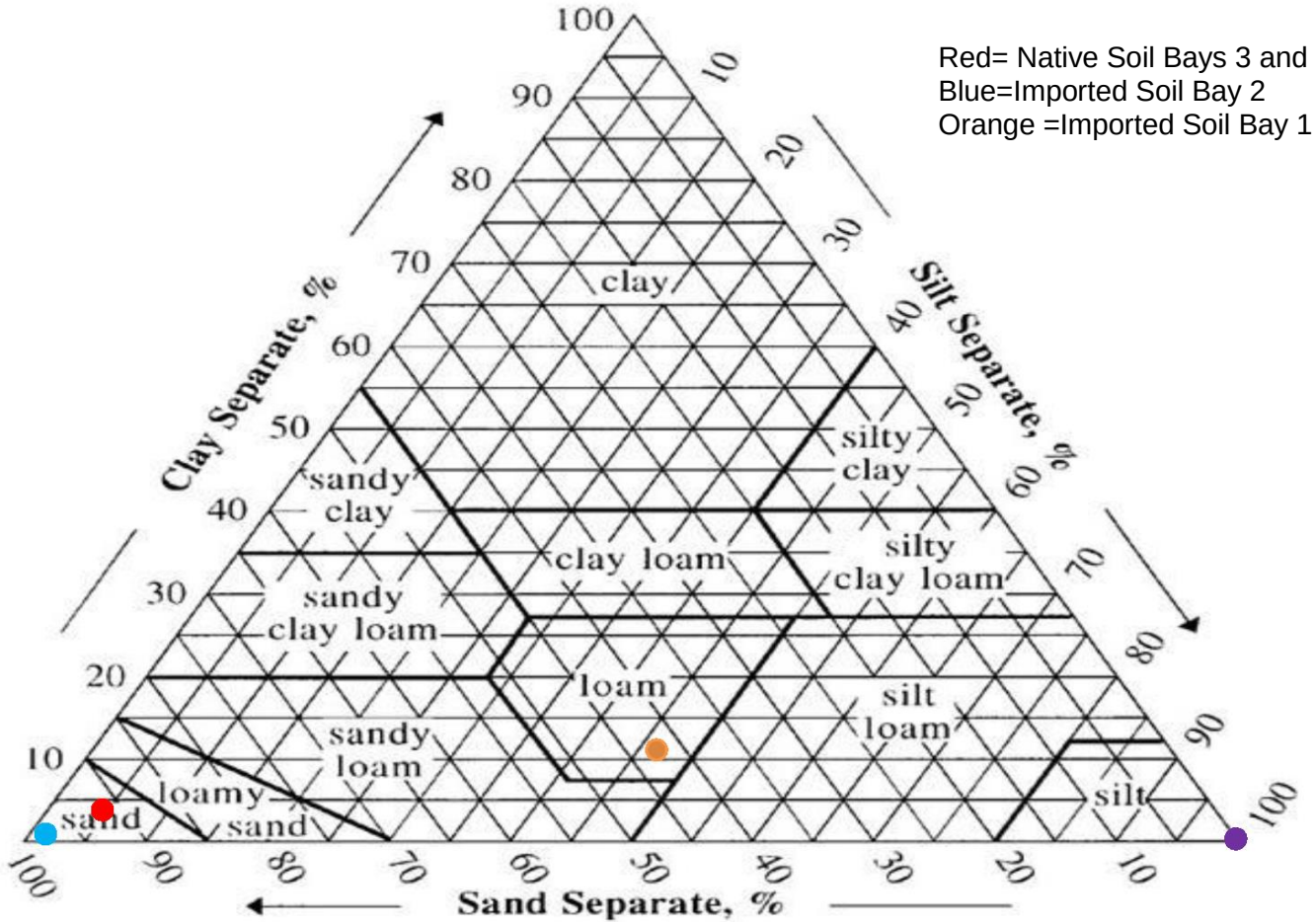

(U.S. Department of Agriculture)

Figure 3-5: Soil Classification of Site Soils

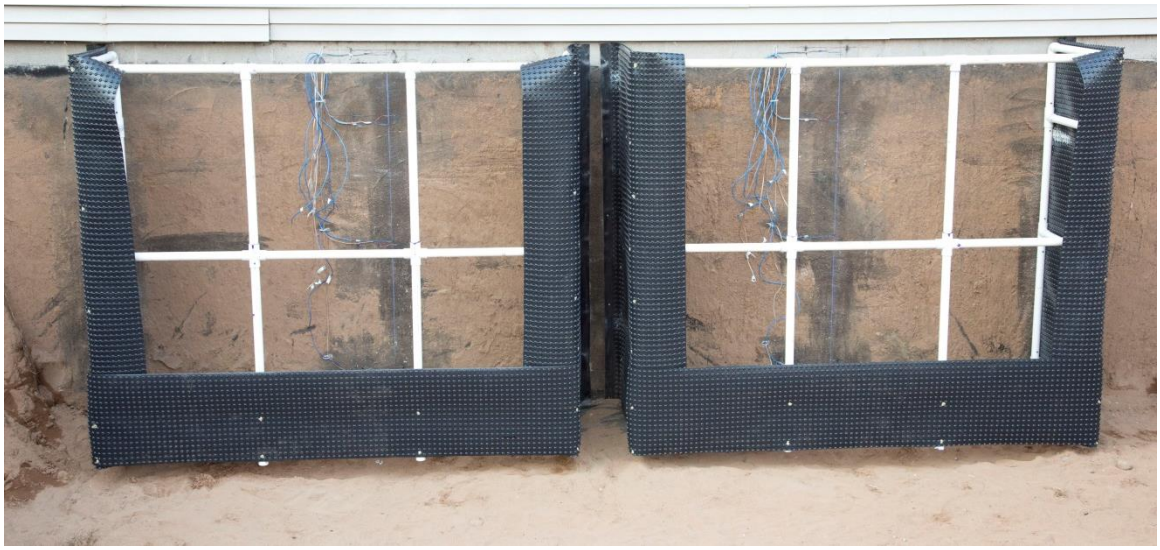

Figure 3-6: Soil Cribs for Soil Containment on Bays 1 and 2

Figure 3-7 shows the wall system and instrumentation layout for Bays 1 and 2. A peel-and-stick rubberized asphalt water separation plane (WSP), was adhered to the interior CMU wall that was first coated with a solvent-based, liquid primer. Three inches of extruded polystyrene insulation was fitted tightly to the WSP membrane, and the top, bottom, and vertical joints were sealed with foam board construction adhesive. A 2x3 wood frame with studs at 24 in. o.c. was constructed against the insulation with the frame spaces left open. Half inch gypsum board was attached to the stud frame and vertical joints were sealed with foam board construction adhesive. The frame and insulation extended to the underside of the floor joists. An existing piece of $1^1/_2$ in. rigid insulation covered the top of the portion of the CMU wall that was not covered by the 2x6 sill plate.

Figure 3-8 illustrates the interior sensor layout for Bays 1 and 2. On the interior face of the CMU wall, the temperature sensors were shifted from the horizontal midpoint of the bay to the nearest un-grouted CMU core and located at the horizontal midpoint of the core. The CMU's were not perfectly aligned vertically; therefore, the temperature sensors do not have true vertical alignment. After installing the four interior CMU wall temperature sensors, a mean vertical line was located between the temperature sensors by visual inspection so that the horizontal differences between the locations of the temperature sensors were approximately averaged. This mean line was used as the centerline for the temperature sensors located on the face of insulation, on the back of

the gypsum board, in the room, and on the exterior CMU wall; that is on all planes where the CMU face shells were not visible.

The CMU moisture content sensors for a given height were placed in the same block as the temperature sensor for that height. A CMU moisture content sensor consisted of two electrodes spaced horizontally approximately $10^{1}/_{8}$ in. apart (refer to Table 3-1 and Table 3-2 for the actual installed spacing of the electrodes). The midpoint between the probes corresponded with the midpoint of the CMU block and the probes were located at mid-height of the CMU block. Since the CMU moisture content sensors were always placed at mid-height of the block, there was a vertical offset between the block moisture content sensor and the corresponding temperature sensor (Figure 3-8). The electrodes were installed first by drilling two $^{1}/_{4}$ in. diameter by approximately 1 in. deep holes (as-installed dimensions are given in Table 3-1 and Table 3-2) in the face shell of the block. Then a $^{1}/_{4}$ in. diameter graphite rod (with the perimeter of the rod coated in an electrically conducting epoxy paste) was inserted into the holes. A #2 stainless steel screw (0.089 in. diameter) was installed into a pre-drilled hole on the front face of the graphite rod, and wire leads were connected to the screw. The top of the screw and graphite rod were covered with a non-conducting marine epoxy.

As each CMU block had two cores, where possible, the core humidity sensor was located in the same block as the temperature sensor, but in the adjacent core. This was done so the core behind the temperature sensor was left undisturbed, but the two sensors were at the same height without interference. However, the top core humidity sensor was moved down one course from the location of the corresponding temperature sensor because the top course was a solid grouted bond beam. The bottom core humidity sensor was moved up one course from the location of the corresponding temperature sensor because the second course up from the footing was filled with grout and/or mortar that likely fell during the wall construction process (Figure 3-8). The filled cores at the bottom of the wall were discovered when installing the first core humidity sensor. As a result, for consistency, the bottom core humidity sensors were moved up one course from the temperature sensor on all the walls. The remaining walls were not checked to see if the lower courses were filled with grout and/or mortar. To install the sensors, a hole was drilled in the interior face of the CMU wall at the horizontal midpoint of the core and $1^{1}/_{2}$ in. above the vertical midpoint of the block. The

humidity sensor[4] was installed at a 15 deg. downward angle from horizontal that positioned the sensor port at the centroid of the block core. The sensors were installed at an angle to prevent water accumulation on the sensor relative humidity element.

The humidity sensors on the interior face of the WSP were installed by cutting a pocket into the back of the insulation and fitting the sensor into the pocket. The edge of the sensor was flush with the back face of the insulation and had an open port in the sensor casing facing the water separation plane (WSP). This allowed the insulation to fit tightly to the wall and avoided air gaps around the humidity sensors. The sensors were offset 1 in. horizontally from the centerline of the temperature sensors (Figure 3-8). This was done so the temperature sensors and heat flux plates would be exposed to a full 3 in. of insulation and not a reduced thickness due to the humidity sensor pocket. The humidity sensors on the interior face of the insulation were aligned with the humidity sensors on the face of the WSP and were mounted on the face of the insulation.

The heat flux plates were located on the interior face of the WSP. The plates were not embedded in the insulation, which produced a small air gap around the approximately $^1/_8$ in. thick plate because the insulation was not flush with the WSP. The plates were 2 in. square and were offset $1^1/_2$ in. horizontally from the centerline of the temperature sensors on the side opposite to the humidity sensor (Figure 3-8). This was done because the temperature sensor behind the WSP created a small bump that would have prevented the plate from fitting tightly to the membrane, and as noted above, it permitted the heat flux plates to be covered by a full 3 in. of insulation. However, at one location in Bay 1S at approximately 40 in. above the floor, the bump in the WSP produced by the temperature sensor behind the WSP was small enough to permit the heat flux plate to be mounted flush against the WSP. Thus at this location, the heat flux plate was not offset from the centerline of the temperature sensor, but the humidity sensor was still only offset 1 in. as noted above. At this location, the humidity sensor was located on top of the plate and there was a reduced insulation thickness (approximately $2^1/_2$ in.).

[4] Thin film capacitance relative humidity sensor paired with a temperature sensor for measurement of absolute humidity (Chapter 3.5).

A spring-loaded string that extended from the slab to the bottom of joists was installed 10 in. away from the face of the interior gypsum board. The string was aligned with the temperature sensor averaged centerline. Two temperature sensors at approximately 5.5 in. and 86 in. above the slab and one humidity sensor at approximately 40 in. above the slab were installed on the string.

A humidity and temperature sensor were located in the rim joist cavity. Both sensors were aligned with the temperature sensor averaged centerline. The temperature sensor was mounted directly on the existing insulation located on the top of the CMU wall and the humidity sensor was mounted directly on the rim board.

The exterior walls were excavated down to the footing for the installation of sensors and the containment soil crib. There were four levels of exterior sensors, three of which were below grade. The wall moisture content and the wall temperature sensors were all installed with the wall fully exposed.

The top exterior CMU wall temperature sensor was aligned with the top interior CMU wall temperature sensor. An existing parging/damp-proofing covered the CMU wall from 8 in. below the top of the wall down to the top of the footing and rendered the exterior surface of the CMU invisible. This prevented use of the same alignment method that was used for the interior CMU wall temperature sensors. Instead, the remainder of the exterior block wall temperature sensors were aligned with the top exterior block wall temperature sensor. This means that the bottom three temperature sensors were not precisely aligned with the midpoint of the CMU block core.

The top CMU moisture content sensor was installed using the same method as was used on the interior. Again, the parging/damp-proofing prevented the remaining three CMU moisture content sensors from being installed using the same method as was used on the interior. The CMU moisture content sensors were aligned horizontally with the top CMU moisture content sensor and located vertically the same distance from the top of the wall as the respective CMU moisture content sensor on the interior. Again, this means the bottom three CMU moisture content sensors are not precisely centered on the CMU block.

The soil crib separated the imported fill from the existing fill. Additionally, in the absence of precipitation, if water was intentionally introduced (as was originally planned), the crib waterproofing membrane allowed a controlled soil moisture profile to be achieved. The soil crib was 3 ft. wide by 9 ft. long (parallel to building) by 7.6 ft. deep (Figure 3-6). A three-sided frame was constructed that fitted-tight to the basement wall. Both the top and bottom of the frame were open to allow water drainage. The frame was constructed of $1^1/_2$ nominal schedule 40 polyvinyl chloride (PVC) pipe with horizontals and verticals at approximately 36 in. o.c. and wrapped in a high-density polyethylene (HDPE) dimpled waterproofing membrane. The membrane was fastened to the exterior of the frame with screws and lapped with the basement wall where it was fastened with concrete anchors. All fasteners and joints were caulked to prevent water infiltration. The WSP was pre-installed on the 3 ft. sides of the frame and installed in three lifts on the 9 ft. side. During each lift, 6 in. of backfill was placed inside the crib then 6 in. of backfill was place outside the crib, this was repeated until the top of the lift was reached. This method was used to limit the soil pressure induced on the waterproofing membrane. At the top of the soil lift at the appropriate height, soil sensors and the next sheet of WSP were installed. The membrane was ship-lapped with the layer below and the joint was caulked. The backfilling process was then repeated.

The soil sensors were installed as the wall was backfilled (reference Chapter 3.2.4 for details on soil compaction). The soil sensors have three long prongs that were positioned vertically in the soil. The midpoint of the prongs was aligned with the elevation of the exterior CMU wall temperature sensors at the specified distance from the wall. To install the sensor, a mound of soil was built-up and hand-packed to the desired elevation. The sensor was then installed and additional soil was hand-packed around the sensor to prevent movement during backfilling. As the prongs are about 3 in. long, this provides for $1^1/_2$ in. of settlement before the sensor becomes vertically misaligned.

In October of 2013, exterior above-grade humidity sensors were installed to measure the ambient temperature and relative humidity above the soil cribs. Each sensor was installed in a closed electrical street elbow that was located approximately 10 in. from the face of the building and approximately 21 in. above the top of the grade. The elbow bottom port was covered with an insect screen.

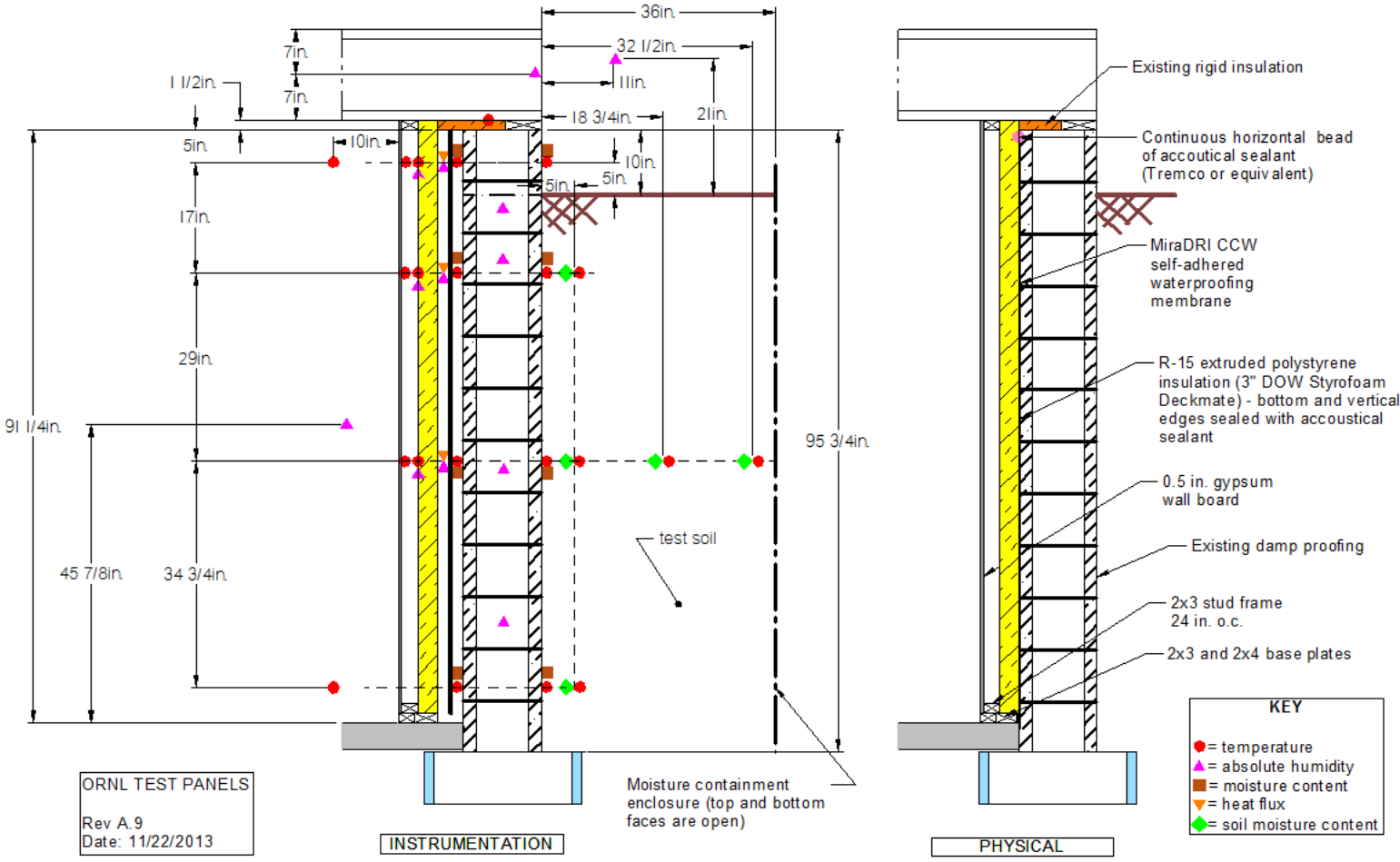

Figure 3-7: Bay 1 and 2 Wall System and Instrumentation Layout

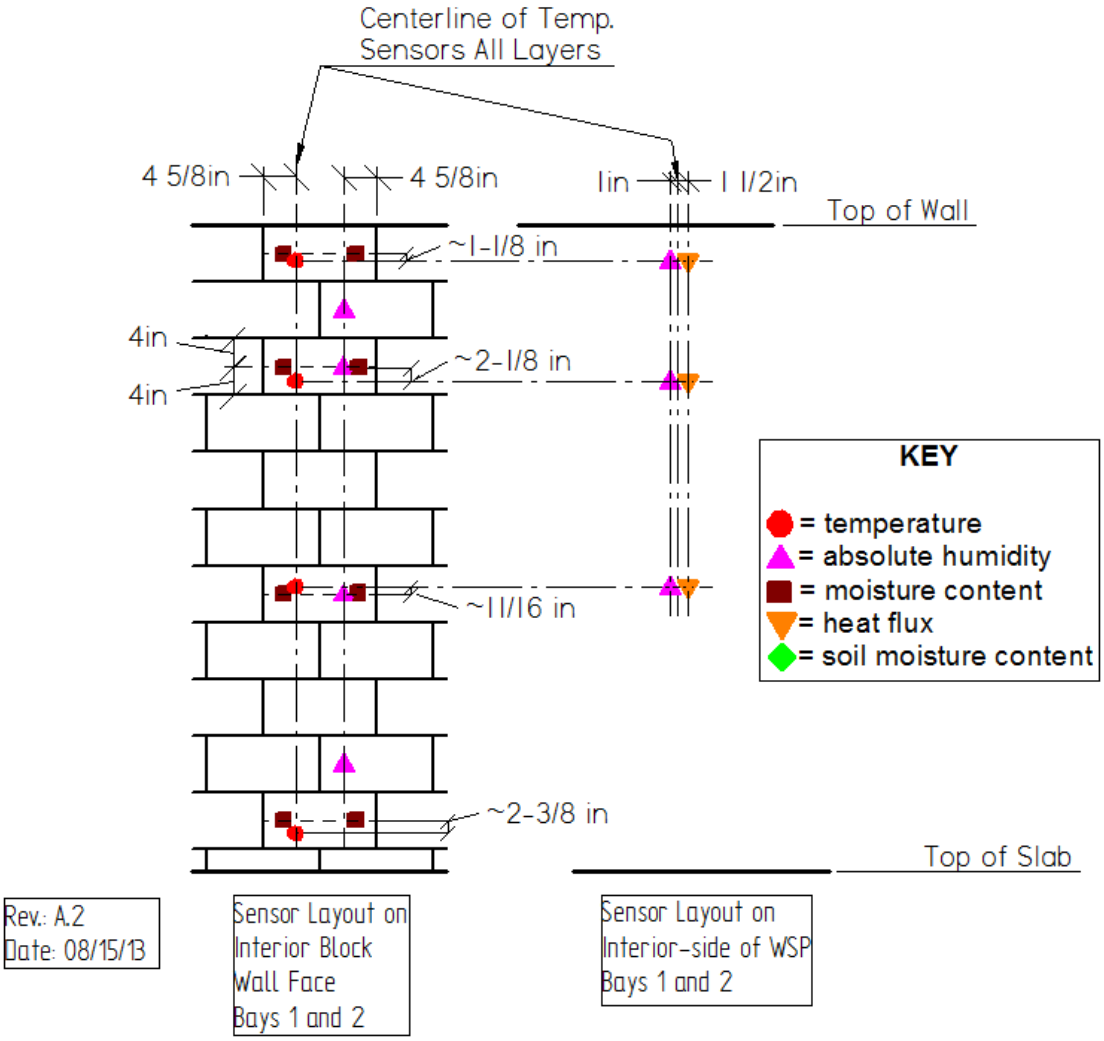

Figure 3-8: Bay 1 and 2 Interior Wall Sensor Layout

Location on Wall (Inches above Slab)	Measurement	Installation Measurements (Inches)							
		1S	1N	2S	2N	3S	3N	4S	4N
86	Spacing	10 1/8	10 1/8	10 1/8	10 1/16	10 1/8	10 5/16	10 3/16	10 3/16
	Depth (East)	1	1	1 1/8	1	1	1	15/16	15/16
	Depth (West)	1	1	1	1 1/16	15/16	15/16	1	15/16
69	Spacing	10 1/16	10 1/16	10 1/16	10 1/8	10 3/16	10 3/16	10 1/8	10 3/16
	Depth (East)	1	1	1	1	7/8	15/16	15/16	7/8
	Depth (West)	1 3/16	1	1	1 1/16	15/16	15/16	15/16	15/16
40	Spacing	10 1/16	10 1/16	10 1/16	10 1/8	10 1/8	10 1/4	10 1/16	10 1/8
	Depth (East)	1	1	1	1 1/16	15/16	15/16	7/8	1
	Depth (West)	1	1	1	1	15/16	15/16	15/16	1
5.5	Spacing	10 1/16	10 1/16	10 1/16	10 1/8	---[5]	10 3/16	---[5]	10 1/4
	Depth (East)	1	1	1	1	15/16	15/16	15/16	15/16
	Depth (West)	15/16	1	1	1	1	1	15/16	1

Table 3-1: Exterior CMU Wall Moisture Content Installation Measurements

[5] Soil was backfilled without obtaining dimension.

Location on Wall (Inches above Slab)	Measurement	Installation Measurements (Inches)							
		1S	**1N**	**2S**	**2N**	**3S**	**3N**	**4S**	**4N**
86	Spacing	$10^{3}/_{16}$	$10^{1}/_{8}$	$10^{1}/_{16}$	$10^{3}/_{16}$	$10^{1}/_{16}$	$10^{3}/_{16}$	$10^{3}/_{16}$	$10^{1}/_{8}$
	Depth (East)	$^{15}/_{16}$	1	1	1	$^{7}/_{8}$	$^{15}/_{16}$	$^{15}/_{16}$	1
	Depth (West)	$^{7}/_{8}$	$^{15}/_{16}$	$1^{1}/_{16}$	$^{15}/_{16}$	$^{15}/_{16}$	$^{15}/_{16}$	$^{15}/_{16}$	$^{15}/_{16}$
69	Spacing	$10^{3}/_{16}$	$10^{1}/_{16}$	$10^{1}/_{16}$	$10^{3}/_{16}$	$10^{1}/_{4}$	$10^{1}/_{4}$	$10^{1}/_{4}$	$10^{3}/_{16}$
	Depth (East)	1	$^{15}/_{16}$	$1^{1}/_{16}$	$^{15}/_{16}$	$^{7}/_{8}$	1	$^{15}/_{16}$	$^{15}/_{16}$
	Depth (West)	1	1	1	$^{15}/_{16}$	$^{7}/_{8}$	1	$^{15}/_{16}$	1
40	Spacing	$10^{1}/_{8}$	10	$10^{1}/_{8}$	$10^{3}/_{16}$	$10^{1}/_{4}$	$10^{3}/_{16}$	$10^{3}/_{16}$	$10^{3}/_{16}$
	Depth (East)	$^{15}/_{16}$	$^{15}/_{16}$	1	$^{15}/_{16}$	$^{15}/_{16}$	$^{15}/_{16}$	1	$^{15}/_{16}$
	Depth (West)	$^{15}/_{16}$	$^{15}/_{16}$	1	$^{15}/_{16}$	$^{15}/_{16}$	1	$1^{1}/_{16}$	$^{15}/_{16}$
5.5	Spacing	$10^{1}/_{8}$	$10^{1}/_{16}$	$10^{1}/_{16}$	$10^{1}/_{8}$	$10^{1}/_{4}$	$10^{1}/_{16}$	$10^{1}/_{4}$	$10^{3}/_{16}$
	Depth (East)	1	$^{15}/_{16}$	1	$^{15}/_{16}$	$^{15}/_{16}$	$^{15}/_{16}$	1	$^{7}/_{8}$
	Depth (West)	$1^{1}/_{16}$	$^{15}/_{16}$	$^{15}/_{16}$	$^{15}/_{16}$	$^{7}/_{8}$	$^{15}/_{16}$	$^{15}/_{16}$	$^{15}/_{16}$

Table 3-2: Interior CMU Wall Moisture Content Installation Measurements

3.2.2 Bay 3

Figure 3-9 shows the wall system and instrumentation layout for Bay 3. On the interior face of the CMU wall, a $^1/_4$ in. thick dimpled high-density polyethylene membrane was used as the WSP. The dimples created an air space, with the dimples oriented towards the CMU wall, a drainage plane was formed between the wall and the WSP. The dimples also created a small void on the interior face of the WSP at the dimple. The WSP was mechanically fastened to the CMU wall and all fasteners were caulked. The bottom of the WSP was slotted into a drainage channel and the gaps at the top and vertical edges of the wall between the WSP and the CMU wall were sealed with foam board construction adhesive and taped with biaxially-oriented polypropylene film tape.

The drainage channel was constructed by placing a PVC channel with the flanges pointing up at the base of the wall (on top of the existing 2x4) and then placing a second PVC channel with its flanges oriented down over the first as a 'cover'. The WSP was slotted between the two flanges nearest the wall. Each end of the channel had a PVC end plate and one end plate was fitted with a plastic drainage tube. The drainage tube was connected to a condensate pump that removed any accumulated bulk water. The channel was not sloped for drainage. A moisture sensing device consisting of two bare parallel nickel plated copper wires about 1 in. apart was installed on the base of the drainage channel over the center 49 in.

Two courses down from the top of the wall, a horizontal spray bar was installed along the mortar joint of the wall. The spray bar was $36^1/_2$ in. wide and its midpoint was aligned with the midpoint of the CMU moisture content sensors. Working from one side of the spray bar to the other, the spray holes were as follows: (3) $^1/_{16}$ in. diameter holes, (2) $^5/_{16}$ in. diameter holes, and (3) $^1/_{16}$ diameter holes, all spaced 4 in. apart. The spray bar allowed water to be introduced between the WSP and the CMU wall to test the drainage performance of the non-adhered WSP system.

From the WSP to the interior of the basement, the remainder of the wall system was identical to Bays 1 and 2 both in terms of components and installation methods (Chapter 3.2.1). This included 3 in. of extruded polystyrene insulation, a 2x3 stud frame with studs at 24 in. o.c., and $^1/_2$ in. gypsum board. The existing piece of $1^1/_2$ in. rigid insulation that covered the portion of the top of the wall that was not covered by the 2x6

sill plate, was left in place. The identical construction of Bays 1, 2, and 3 from the WSP to the interior of the basement reduced the number of experimental variables and allowed the performance of the non-adhered and adhered WSPs to be compared.

Figure 3-10 illustrates the layout of the interior CMU wall and WSP sensors for Bay 3. Interior CMU wall temperature and moisture content sensors, core humidity sensors, humidity sensors on the interior face of the WSP, temperature and humidity sensors in the frame cavity, interior basement temperature and humidity sensors, and temperature and humidity sensors in the rim joist cavity were installed using the same methods as for Bays 1 and 2 (described above). The three humidity sensors that were located in the void between the CMU wall and the WSP were mounted on the back of the WSP prior to installation. The temperature sensors located on the interior face of the WSP on the south wall were aligned with the averaged centerline of temperature sensors located on the interior CMU wall. On the north wall, the temperature sensors located on the interior face of the WSP, were offset $^{1}/_{4}$ in. horizontally from the averaged centerline of temperature sensors located on the interior CMU wall towards the humidity sensor, so they were installed between dimples. Heat flux plates were located on the face of the WSP and offset from the averaged centerline of temperature sensors on the interior CMU wall to the side opposite the humidity sensors located on the WSP. They were mounted so a dimple indentation was centered behind the middle of the heat flux plate. This location yielded the smallest area of dimple voids behind the plate based on the dimple spacing of approximately $1^{3}/_{16}$ in. On the north wall, the plates had a horizontal offset of $1^{9}/_{16}$ in. and a vertical offset between $-^{1}/_{4}$ in. and $-^{7}/_{8}$ in. On the south wall, the horizontal offset was $2^{13}/_{16}$ and the vertical offset ranged from $-^{9}/_{16}$ in. to $-1^{5}/_{16}$ in. (Figure 3-10).

On the north exposure the CMU temperature sensors were located on a grouted core, and on the south exposure they were located on an un-grouted core (Figure 3-4). Bay 3N is the only wall in the entire experiment that had the CMU temperature sensors located on a grouted core (Figure 3-3 and Figure 3-4). It provides a control for the study of hollow cavity buoyant cavity flow.

Bay 3 had no soil crib for soil containment and was backfilled with the existing soil (reference Chapter 3.2.4 for details on soil compaction). The soil was classified as a

sand with silt (Unified Soil Classification System SP-SM) that fell within the ‘sand’ section of the USDA Soil Classification Triangle (Figure 3-5). The exterior CMU wall temperature and moisture content sensors and soil sensors were installed using the same methods as for Bays 1 and 2 (Chapter 3.2.1).

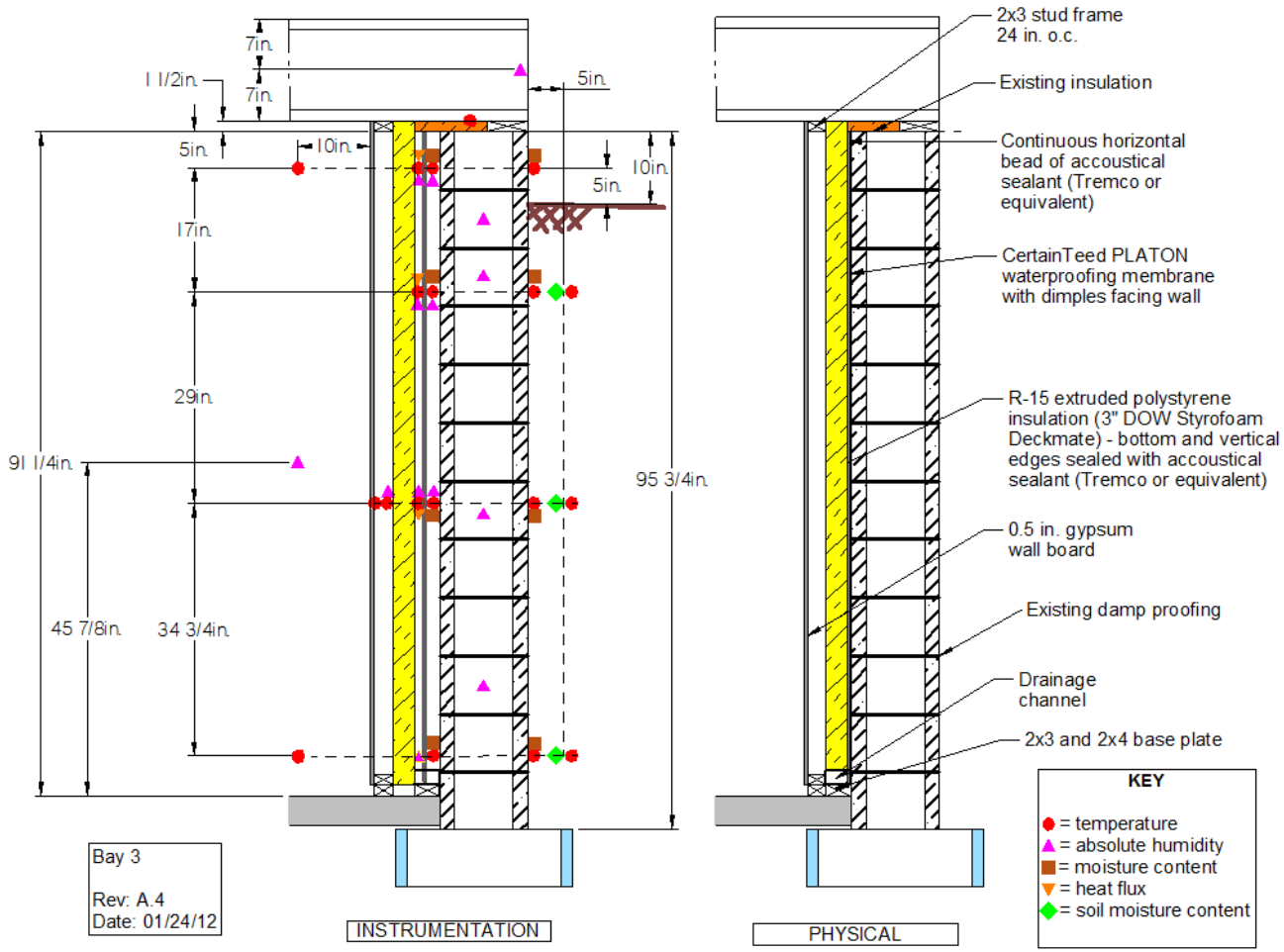

Figure 3-9: Bay 3 Wall System and Instrumentation Layout

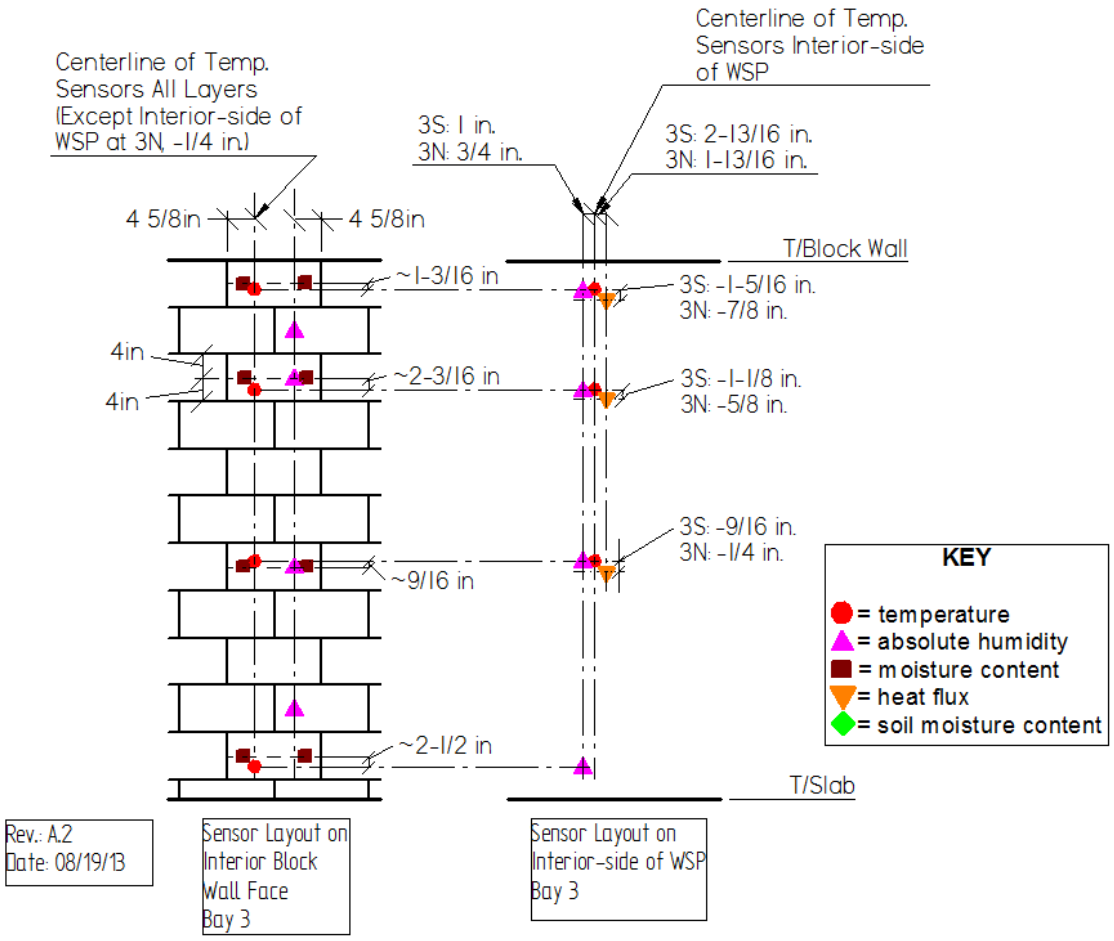

Figure 3-10: Bay 3 Interior Wall Sensor Layout

3.2.3 Bay 4

Figure 3-11 shows the wall system and sensor layout for Bay 4. For this wall system, exterior half-height 3 in. thick extruded polystyrene insulation was used. The insulation was aligned with the top of the CMU wall and extended 48 in. down the wall. It was attached to the wall using 4 in. concrete anchors with large washers that were offset from the instrument plane. The washers allowed the anchors to lock the insulation tight to the wall without the anchors penetrating the insulation and prevented the insulation from pulling out over time. The portion of insulation that extended above grade was covered with z-shaped metal flashing to prevent UV damage and provide drainage. One leg of the flashing was fitted under the siding and the other leg extended down the face of the insulation to a few inches below grade.

Starting from the interior side of the CMU wall and moving inward, a peel-and-stick rubberized asphalt WSP was adhered to the CMU wall that was first coated with a water -based, liquid primer. A 2×3 frame with studs at 24 in. o.c. was constructed against the WSP and extended to the underside of the floor joists. The frame cavities were left open. A $^{1}/_{2}$ in. gypsum board with the vertical joints sealed with foam board construction adhesive was attached to the stud frame. An existing piece of $1^{1}/_{2}$ in. rigid insulation that covered a portion of the top of the CMU wall that was not covered by the 2x6 sill plate, was left in place.

Figure 3-12 depicts the CMU wall and WSP sensor layout for Bay 4. The CMU wall temperature and moisture content sensors, temperature sensor in the frame cavity (located on the back of the gypsum board), interior room temperature and humidity sensors, and rim joist cavity temperature and humidity sensors were installed using the same approach as was used for Bays 1 and 2 (see above). The core humidity sensors also were installed using the same method as used for Bays 1 and 2, with the exception of the location of the sensors on the south wall. On the south wall, the core adjacent to and in the same CMU block as the core with the temperature sensor (core 8 in. east of the temperature sensor) was grouted solid. For this reason, the core humidity sensor was located in the core adjacent to the temperature senor, but in the next CMU block core (8 in. west of the temperature sensor).

The heat flux plates located on the face of the WSP were offset to avoid the wires and probes of the sensors located on the face of the CMU wall that created small bumps in the WSP. All heat flux plates were located horizontally with reference to the averaged centerline of the temperature sensors and vertically with reference to the centerline of the temperature sensor at each level. The upper two heat flux plates on the north and south walls were offset horizontally $1^{1}/_{2}$ in. and vertically between 0 and $-^{1}/_{8}$ in. The bottom heat flux plates on the walls were offset horizontally $2^{1}/_{8}$ to $2^{1}/_{2}$ in. and vertically between $-^{3}/_{16}$ and $+^{1}/_{2}$ in. The humidity sensor on the face of the WSP was offset 1 in. from the averaged centerline of the temperature sensors on the face of the CMU wall and this sensor was offset to the opposite side of the averaged centerline from the heat flux plate.

The exterior block wall temperature and moisture content sensors and soil sensors were installed using the same method as was used for Bays 1 and 2 (Chapter 3.2.1). The wires for the upper two sensor levels were routed horizontally then outwards through a small hole in the insulation before entering the street elbow. The hole in the insulation was caulked. Wires for the sensors at the lower two levels were routed over the insulation. A soil crib for soil containment was not installed and the existing soil was used for backfill (reference Chapter 3.2.4 for details on soil compaction). Per the Unified Soil Classification System, the existing soil was a sand with silt (Unified Soil Classification System SP-SM) that fell within the ‘sand’ section of the USDA Soil Classification Triangle (Figure 3-5).

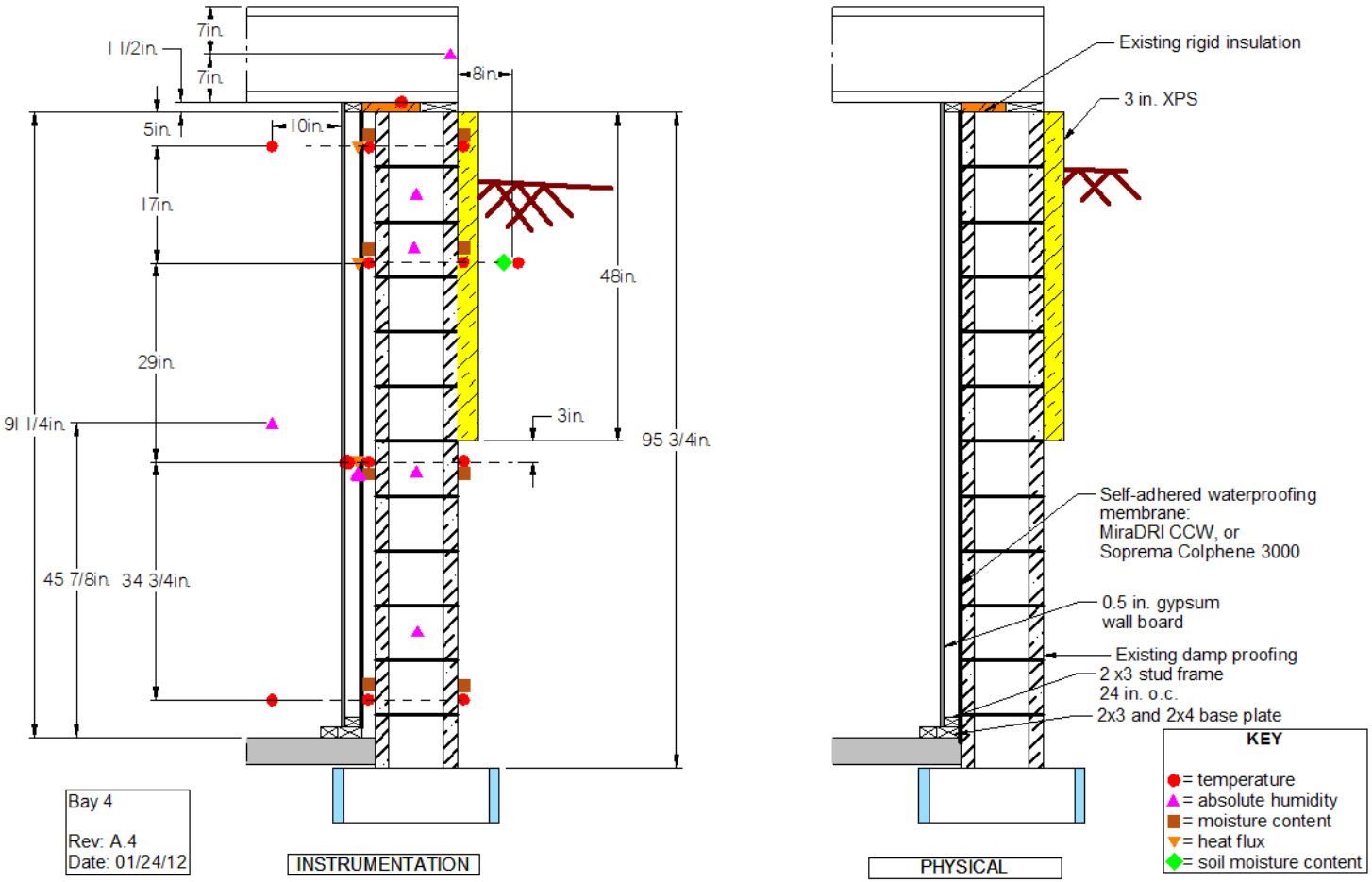

Figure 3-11: Bay 4 Wall System and Instrumentation Layout

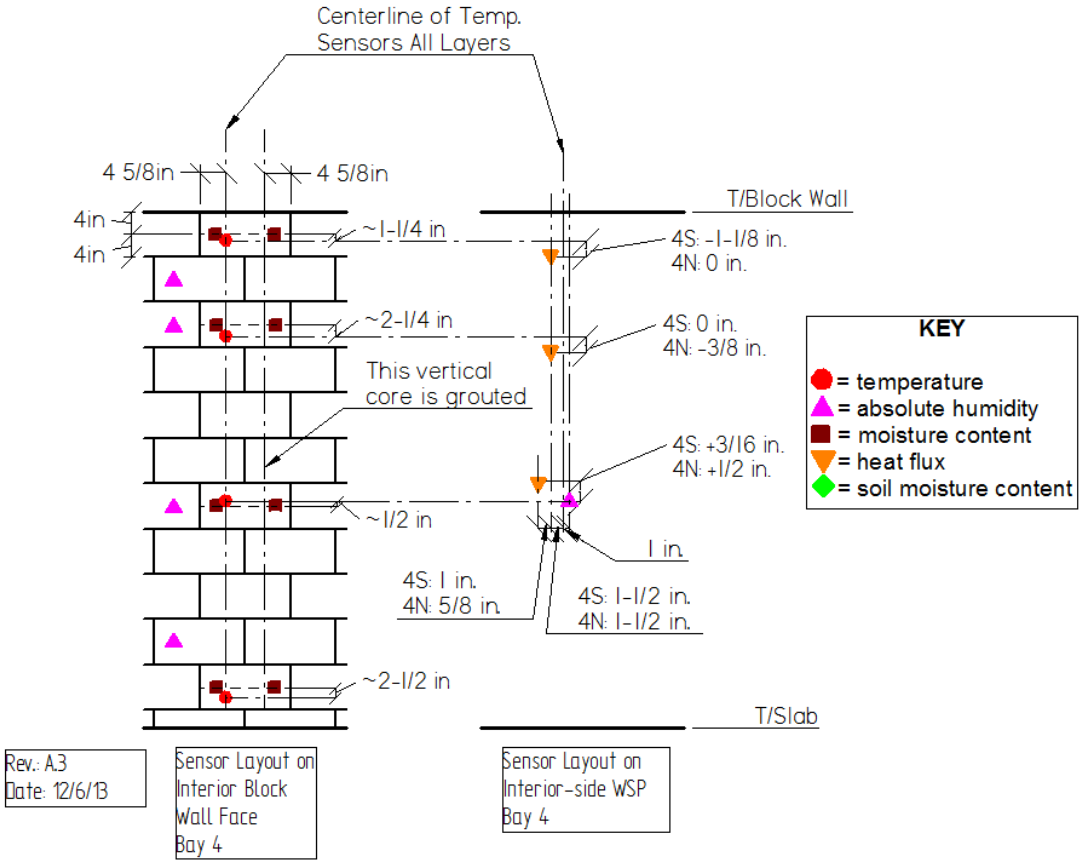

Figure 3-12: Bay 4 Interior Wall Sensor Layout

3.2.4 Soil Compaction and Settlement

On Bays 1 and 2 the imported fill was backfilled inside the soil crib adjacent to the building. To compact the soil a hand compactor would have been required and it would have been a time-consuming (and, therefore cost-prohibitive) task to achieve consistent compaction densities for each bay which is of prime importance from an experimental perspective. Thus consistency was achieved by not compacting the soil anywhere, allowing natural compaction over time to achieve consistency. All soil sensors were installed a couple of inches above their desired height (5.5 in., 40 in., and 69 in. above the slab) to account for soil settlement.[6] Throughout the experiment the soil was observed for settlement and soil was added as required. This approach did not allow the height of the soil sensors after natural compaction to be known with precision for analysis and modeling purposes.

On June 5, 2014 the soil above the top soil sensor was excavated on Bays 1, 2, and 3 to determine the amount of settlement that occurred from the time of sensor installation. By this time, the soil in Bays 1 and 2 had over 1 year and 9 months to consolidate and in Bays 3 and 4 had over 1 year to consolidate. Bay 4 was not excavated and assumed to have the same settlement as Bay 3, since the two bays had the same soil type. The settlement was referenced to the distance of the sensor from its desired height (5.5 in., 40 in., and 69 in. above the slab). The settlement for the two lower soil sensors was calculated using linear interpolation between no settlement at the top of footing (bottom of the excavation) and the measured settlement at the top sensor. All values were rounded to the nearest $^1/_8$ in. Table 3-3 shows that Bay 1 (loam soil) had the greatest settlement and Bays 3 and 4 (sandy soil) had minimal settlement. Settlement on the north side was greater than that on the south side.

[6] The exact number of inches the sensors were offset was not documented. The offset was the same for the sensors at all heights, in all bays.

Intended Location (Inches above Slab)	Settlement (Inches)							
	South Exposure				North Exposure			
	1	2	3	4	1	2	3	4
69.25	8	$2\frac{3}{8}$	$\frac{5}{8}$	$\frac{5}{8}$	$9\frac{7}{8}$	$2\frac{5}{8}$	1	1
40.25	$4\frac{7}{8}$	$1\frac{1}{2}$	$\frac{3}{8}$	$\frac{3}{8}$	6	$1\frac{5}{8}$	$\frac{5}{8}$	$\frac{5}{8}$
5.5	$1\frac{1}{8}$	$\frac{3}{8}$	$\frac{1}{8}$	$\frac{1}{8}$	$1\frac{3}{8}$	$\frac{3}{8}$	$\frac{1}{8}$	$\frac{1}{8}$

Notes: 1. Settlement for Bays 1, 2, and 3 for level 69.25, are measured values.

2. Settlement in Bay 4 was not measured, but assumed identical to Bay 3 since the two bays are the same soil.

Table 3-3: Inches of Settlement of Soil Sensor below Intended Location

3.3 Ambient Boundary Conditions

Exterior ambient conditions were collect at the Cloquet Forestry Center weather station, approximately $\frac{1}{4}$ mile from the CRRF. The weather station collected the following data:

- Air temperature;
- Soil temperature (at 4 in. and 8 in. below surface);
- Wind speed and direction;
- Relative humidity;
- Barometric pressure;
- Precipitation;
- Solar radiation (pyranometer); and,
- Net and downward infrared radiation (pyrgeometer).

The following exterior ambient conditions were collected at the CRRF:

- Solar radiation (pyranometer); and,
- Precipitation.

In July 2013, it was discovered that solar radiation data from the Cloquet Forestry Center pyranometer were incorrect. The values appeared to be incorrect by approximately a factor of two compared with published solar radiation data for Cloquet. The pyranometer had been in service for 20+ years and was mounted on top of a 65 ft. mast. The inaccessibility of the pyranometer prevented it from being serviced over the years or from being inspected when the inaccuracy arose. To address the problem, a

new pyranometer was purchased and installed above the peak of the CRRF roof. Data collection for the new pyranometer commenced on July 31, 2013. Thereafter, the two pyranometers measured the solar irradiance concurrently, allowing the old pyranometer to be calibrated against the new one (Chapter 5.1.4). In turn, this allowed the solar radiation data measured prior to July 31 to be corrected.

3.4 Interior Boundary Conditions

The basement interior temperature was controlled by an electric furnace. During the heating season the thermostat was set to 68°F and reset to 60°F from the late spring to the early fall. The furnace initially was controlled by a mechanical analog thermostat that resulted in an interior boundary temperature condition at Bay 1S (furthest from the thermostat) of 70.0 +5.4/-2.9 °F for a typical day. On January 28, 2013, the furnace control was switched to a computerized real-time digital control system and the Bay 1S interior temperatures (at the location most remote from the control system sensors) yielded a much smaller temperature range of 68.7 +1.4/-1.1 °F. During the 2012-2013 heating season there was no humidification. A humidification system was installed and became operational on January 10, 2014. No air-conditioning system was installed in the building, so temperature was not controlled during the cooling season. Dehumidification was not performed during the 2013 cooling season.

3.5 Instrumentation

The details of the CRRF instrumentation are provided in Table 3-4 and the details of the weather station instrumentation are provided in Table 3-5. The absolute humidity sensors referred to in Figure 3-7 through Figure 3-12 consist of a vented plastic tube enclosure with a relative humidity and temperature sensor in close proximity (Goldberg and Harmon 2014).

Snow depth was measured on the north and south sides of Bay 5. The ultrasonic sensor projected roughly 3 ft. from the building and was located below an 18 in. soffit. This sensor emitted ultrasonic pulses and read the return echoes. The sensor had a cone projection of 30 deg. (Figure 3-13). The snow depth measured was an average at the base of the projection cone.

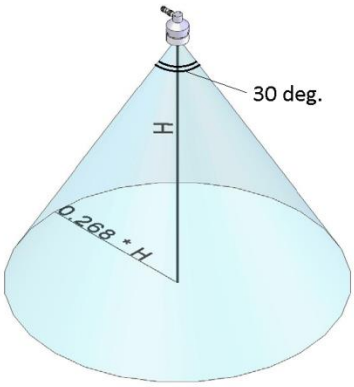

(Campbell Scientific Inc. 2011)

Figure 3-13: Snow Depth Sensor Projection Cone

The raw data was recorded as a height from the instrument to the surface below (ground or snow) along with a quality reading. The quality reflected the accuracy of the reading. According to the instrument manual, quality readings between 152 and 210 were considered good measurements, readings between 210 and 300 had reduced echo signal strength, readings between 300 and 600 had high measurement uncertainty, and zero meant no reading was obtained. For this work, height readings with a quality reading between 152 and 210 were used for the north side and between 152 and 230 for the south side, all other readings were ignored. The height reading for snow depth calculations was corrected for temperature to compensate for the dependence of the speed of sound on temperature based on the following equation:

$$corrected\ height = instrument\ reading \sqrt{\frac{T\ (in\ Kelvin)}{273.15}}$$

The temperature was based on the average temperature over the soil cribs in Bays 1 and 2 for the north or south exposure. As the crib temperature sensors were installed on October 11, 2013, prior to this date, height readings were not corrected for temperature. The height of the instrument was measured from the instrument sensor to the surface of the ground. Snow depth was calculated by subtracting the corrected height reading from the instrument height.

Instrument	Measurement	Manufacturer	Model No.	Manufacturer's Listed Performance
Heated precipitation gauge	precipitation (solid & liquid)	RM Young	52202	Resolution: ±0.1mm Temp > 20 deg. C
Thin film capacitance relative humidity sensor	relative humidity	Honeywell	HIH-4000-003	Calibrated accuracy: ± 3.5 %
Thermocouple	temperature	Omega Engineering	PR-T-24-SLE	Accuracy: max (±0.5 °C, ±0.4% of reading)
Heat flux plate	heat flux	Concept Engineering	F-002-4 HFP	Accuracy: ±5 %
Soil dielectric sensor	soil moisture content and temperature (Bays 1 and 2)	Stevens Water Monitoring Systems, Inc	Hydraprobe	Moisture content accuracy: ±0.03 water fraction by volume Temp. accuracy: ±0.6 °C
Soil dielectric sensor	soil moisture content and temperature (Bays 3 and 4)	Stevens Water Monitoring Systems, Inc	HydraProbe II RS485	Mositure Content accuracy: ± 0.01 water fraction by volume for most soils ± 0.03 max for fine textured soils Temp. accuracy: ± 0.1° C
Barometer	atmospheric pressure	Setra Sensing Solutions	276	Accuracy: 0.25 % of full scale
Pyranometer	solar irradiance flux	Kipp and Zonen	CMP 3	Non-linearity: <±2.5 %, Temp. dependence: ±5 %
Pelton wheel flow sensor	water flow	Kobold	DPM1157N 2F500	Accuracy: ±1.5% of full scale
Ultrasonic snow depth gauge	snow depth	Campbell Scientific	SR50A	Accuracy: max (±0.4 in., 0.4 % of target distance)

Table 3-4: CRRF Instrumentation Schedule

Instrument	Measurement	Manufacturer	Model No.	Manufacturer's Listed Performance
Pyrgeometer FIR (4500-42000 nm)	long wave sky radiation	Kipp and Zonen	CGR3	Non-linearity: <1%
Humidity and temperature probe	relative humidity and temperature (combined sensor)	Vaisala	HMP155A	--
Unheated precipitation gauge	precipitation (liquid only)	Texas Electronics	TE525	--
Pyranometer	solar irradiance flux	Hukseflux	LP02-L	--
107-L thermistor	soil temperature			--
Barometer	atmospheric pressure	Setra	CS100	--
Anemometer	wind speed and direction	R.M. Young	03002-L	--

Table 3-5: Weather Station Instrumentation Schedule[7]

For reference, the equipment used in the data acquisition system is listed in Table 3-6 (Goldberg and Harmon 2014). The sensors were connected to data acquisition systems that, in turn, were controlled by one of five individual computer hosts that collected the raw data (Goldberg and Harmon 2014). The hosts were connected to a local data server within the CRRF via an intranet. The server processed the data, archived the data locally and transmitted the data to a secure cloud server on the Twin Cities campus.[8] The entire system could be controlled remotely.

[7] Except for the pyrgeometer which was purchased new, the specifications of the now obsolete weather station instruments are not known. The listed sensors are the current models of the original sensors installed prior to 1997.

[8] The design, development, and deployment of the data acquisition system hardware and software was not part of my MS thesis research program.

To minimize data loss from failure of the data acquisition system, these procedures were followed:

- The hosts and server were checked twice daily to verify the system was operational;
- The server issued notification e-mails for all fault conditions;
- All the hosts and the server were connected to large capacity uninterruptable power supplies to minimize system failures caused by power outages; and,
- Two of the hosts (primary and weather station) had additional local raw data storage (about 24 hours of data for the weather station and a full backup for the primary host) in the event of a prolonged failure of the server.

The stored raw data availability was greater than 97% for the duration of the experiment.

The data management system was developed in four layers. Each layer required separate processing and separate, daily data files were archived for each layer. The first layer of the system was the raw data (e.g. the voltage reading from a thermocouple). The raw data had different time stamps and time intervals depending on which host the sensor was connected to.

The second layer of the data management system was the intermediate archival format (IAF) in which the raw data was calibrated to yield physically meaningful measurements in SI units. The IAF data maintained the same time stamps and time intervals as the raw data. In the IAF, all snow depth gauge readings with unacceptable quality readings were removed.

The third layer was the final archival format (FAF) that converted the IAF data from the five hosts with different time stamps and intervals to a single data set with coincident time stamps. The host to which the vast majority of the sensors were connected, principally, the temperature, relative humidity, and heat flux measurements, was defined as the primary host that established the governing time stamp. The data on the remaining hosts were linearly interpolated to the time stamp of the primary host. If the primary host data were not available (owing to a host failure), there was a priority hierarchy for the remaining hosts for determining which host became primary.

The fourth layer of the system was the processed archival format (PAF) where the FAF data was processed. In the PAF, the snow depth gauge reading (height from the instrument to the surface below) was corrected for temperature and converted to a snow depth. A single precipitation reading was output based on both rain gauges instead of two readings (one from each gauge) as was the case in the earlier formats. The single precipitation reading used the most accurate reading available from either the precipitation gauge at the CRRF or the weather station (see Chapter 5.1 for more details).

Component	Manufacturer	Qty.	Model No.	Listed Performance
A/D converter (16 bit)	National Instruments	1	PCI-MIO-16XE50	Accuracy: ±54 µV at 0 to ±100mV range; ±1.443 mV at 0 to ± 10V range
A/D converter (16 bit)	National Instruments	1	PCI-6220	Accuracy: ±112 µV at 0 to ±200 mV range; ±3.1 mV at 0 to ± 10 V range
A/D converter (24 bit)	National Instruments	1	NI 9219	Accuracy: ±0.3 % at 0 to ±60 V range; ±0.1 % at 0 to ± 1 V range
RS485 Serial interface	National Instruments	1	PCI-485/2	Max baud: 115.2 kbits/s
Digital signal input	National Instruments	1	NI 9421	Channels: 8 Mode: 5V sinking
Digital signal output	National Instruments	1	NI 9475	Channels: 8 Mode: 60V max sourcing
Digital signal output	National Instruments	2	SCXI-1163R / SCXI-1326	Channels: 8 Mode: optically isolated solid-state relay

Table 3-6: Data Acquisition Equipment (continued on next page)

Component	Manufacturer	Qty.	Model No.	Listed Performance
Thermocouple/ voltage signal conditioning:	National Instruments	11	SCXI-1100 / SCXI-1303	Channels: 32 Max. gain: 2000 Accuracy: 0.006% at 30 µs settling time
Thermocouple/ voltage signal conditioning	National Instruments	2	SCXI-1102 / SCXI-1303	Channels: 32 Accuracy: 0.0061% at 10 µs settling time
Voltage signal conditioning	National Instruments	4	SCXI-1100 / SCXI-1300	Channels: 32 Max. gain: 2000 Accuracy: 0.006% at 30 µs settling time
Relay multiplexer	Campbell Scientific	6	AM16/32B	Channels: 32 differential
Signal conditioning chassis	National Instruments	2	SCXI-1001	No. of slots: 12
Signal conditioning chassis	National Instruments	1	SCXI-1000	No. of slots: 4
Signal conditioning chassis	National Instruments	1	cDAQ-9188	No. of slots: 8
Weather station controller	Campbell Scientific	1	CR10X	Analog channels: 12 single-ended or 6 differential

Table 3-6: Data Acquisition Equipment (continued from previous page)

Chapter 4: Moisture Content Sensor Development

4.1 Concrete Masonry Unit Moisture Content Sensors

4.1.1 Introduction

Concrete masonry unit (CMU) moisture content was an important measurement for understanding the moisture performance of the wall systems. The relative humidity sensors alone would not provide sufficient information. In this experiment, Honeywell HIH-4000-003 relative humidity sensors were used and had an accuracy of $\pm$3.5%. Masonry sorption isotherms exhibit a steep increase in moisture content at relative humidities greater than approximately 90% (Straube and Burnett 2005). Above this threshold, a small change in relative humidity results in a large change in surface moisture content and the relative humidity is not accurate for estimating the CMU moisture content. For this reason a sensor that measured the CMU moisture content directly was desired.

A low-cost, conductance based method for measuring CMU moisture content was developed by the Principal Investigator, Louise Goldberg (Goldberg and Stender 2013). The transducer was comprised of two sheet metal screws (electrodes), spaced 14 in. apart, installed directly in the face shell of the CMU and connected to a standard wood moisture content transmitter via a relay multiplexer that took an intermittent moisture content reading. The potential difference across the electrodes was inversely proportional to the moisture content. The transducers provided qualitative data for approximately 80% of the experiment and then failed. The failure was attributed to corrosion of the electrodes that produced a galvanic corrosion cell. The galvanic corrosion cell produced a large enough voltage to burn out the input stage of the moisture transmitter. In this project, the transducer was further refined and developed.

4.1.2 Design

The revised CMU moisture content sensors consisted of two electrodes spaced horizontally approximately $10^{3}/_{16}$ in. apart and centered across the height and width of the CMU. The electrodes were installed by drilling two $^{1}/_{4}$ in. diameter by approximately 1 in. deep holes in the face shell of the CMU and installing a $^{1}/_{4}$ in. diameter graphite rod, with the perimeter (not the end) of the rod coated in an electrically conducting epoxy paste. A #2 stainless steel screw (0.089 in. diameter) was installed into a pre-

drilled hole at the exposed end of the graphite rod, and wire leads were connected to the screw. The top of the screw and graphite rod were coated with epoxy (Figure 4-1). Refer to the “Experimental Setup” chapter for details of the field installation.

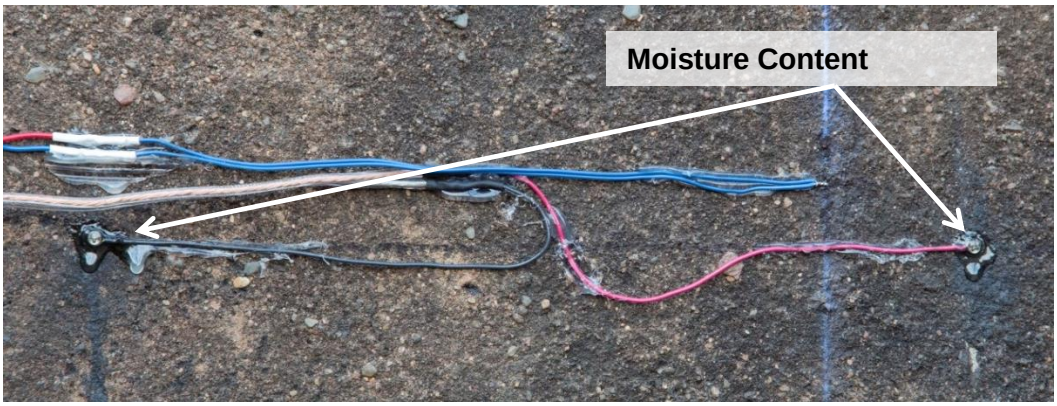

Figure 4-1: Exterior CMU Moisture Content Sensor and Temperature Sensor

The wire leads that were connected to each electrode created a closed circuit with the CMU, a 249 ohm 1% tolerance resistor, and a DC power supply all in series (Figure 4-2). The power supply supplied a constant 24 V voltage to the circuit, which resulted in a current that varied between approximately 1 µA and 3 mA through the CMU face shell between the electrodes. The voltage across the resistor (V_{AB}) and the voltage across the power supply (V_{AC}) were measured and the current in the circuit (i), the voltage drop across the electrodes (V_{BC}), and the conductance across the electrodes (G) were calculated with the following equations:

$$i = \frac{V_{AB}}{249\ \Omega}$$ **Equation 4-1**

$$V_{BC} = V_{AC} - V_{AB}$$ **Equation 4-2**

$$G = \frac{i}{V_{BC}}$$ **Equation 4-3**

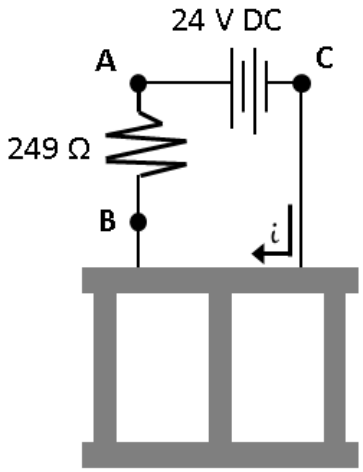

Figure 4-2: CMU Moisture Content Sensor Circuit Diagram

CMU's are comprised of a concrete skeleton that is filled with voids. The ratio of void volume to total volume (voids and skeleton) is the porosity of the CMU. The voids are filled with air, water, or a combination of the two. The volumetric moisture content is the ratio of the volume of water to the total volume. At 100% saturation the volumetric moisture content equals the CMU porosity. The moisture content sensors measured the electrical conductance that depends on the varying amounts of air and water in the voids of the CMU. Air has a very low electrical conductivity compared to water. Therefore the conductance across the electrodes (Equation 4-3) increases with the moisture content of the CMU.

The CRRF was constructed of 12 in. wide x 8 in. high x 16 in. long nominal stretcher CMU's (Figure 4-3). A moisture content sensor was installed on the interior and the exterior face shells of a single CMU. Interference did not occur between the interior and exterior moisture content sensors because each sensor was connected into a closed loop circuit with a separate and electrically isolated power supply.

The electrodes of the sensors were located in a single CMU and did not cross any mortar joints to avoid material property differences between the mortar and the CMU. They were spaced approximately $10^{3}/_{16}$ in. apart which was considered wide enough apart to limit the impact of local CMU irregularities (e.g. porosity, imperfections in the concrete mixture, damage to the CMU from the graphite rod installation) on the electrical conductance between the electrodes. Yet, they were spaced close enough

together to avoid localized effects at the edge of the CMU (approximately $2^3/_4$ in. to the edge of the CMU).

Short circuiting through the far face shell if it was wet (higher conductance) and the one under measurement was dry (lower conductance) was not likely. If the current followed a path through the outer webs and far face shell instead of directly across the face shell being measured, the distance traveled would be approximately 32 in. instead of approximately $10^3/_{16}$ in. With the longer travel path, more than half the distance would be through the webs which would have a gradient in moisture content from dry to wet. Since the webs would not have the same high conductance as the far face shell, it is unlikely that this longer path would have a higher conductance than the shorter, direct path.

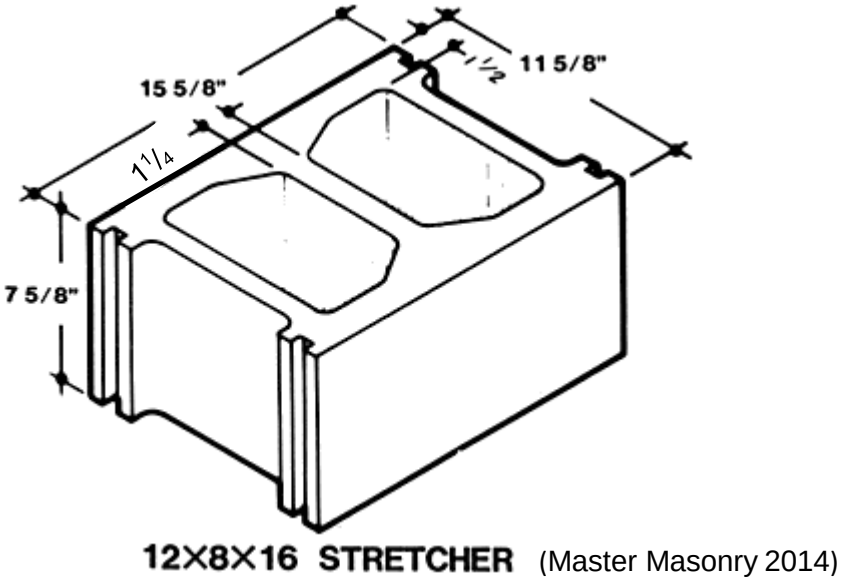

(Master Masonry 2014)

Figure 4-3: Dimensions of 12 in. x 8 in. x 16 in. CMU Stretcher Block

The screws were installed in a graphite rod to protect them from the moisture in the CMU and minimize the 21c potential between the screw and the water in the CMU. Graphite was selected because it is a low-cost, highly conductive material that would have a negligible effect on the conductance readings and does not corrode in a moist environment. The perimeter of the graphite rods were coated in an electrically conducting epoxy paste (graphite particles provide the electrical conductance). The electrically conducting paste filled any voids around the rod that would have otherwise

filled with water or air and caused irregular readings. The top of the screw and graphite rod were covered with epoxy to isolate the probe from surface moisture, thus reducing the potential for corrosion of the screw and minimizing the intrusion of water around the perimeter of the rod and screw.

Initially during sensor development, a manual resistance reading was taken directly across the electrodes approximately every twenty minutes. The resistance readings were not steady at the time of reading. Further, over time, the readings fluctuated up and down without consistency. To address the inconsistency of the manual readings, the transducer leads were touched together to drain any charge prior to the reading. The volt meter leads were then attached to the transducer leads and a reading was taken 10 seconds after connection. This approach did not improve the consistency of readings.

It was concluded that the CMU acts like a parallel resistor-capacitor circuit. When an intermittent resistance reading was taken, the reading was irregular due to the charging and discharging of the ‘capacitor’. To address this issue, a constant voltage was applied across the CMU that prevented charging and discharging of the ‘capacitor’ and resulted in steady readings.

An indirect voltage reading across the electrodes (Equation 4-1, Equation 4-2, and Figure 4-2) was used instead of a direct reading for improved accuracy. When a voltmeter is connected to a circuit, it creates a parallel path with the portion of the circuit under measurement and draws a portion of the current from the circuit, thus reducing the accuracy of the voltage reading. The impedance of the CMU was high and on the same order of magnitude as the impedance of the volt meter. A direct reading would therefore result in a false voltage reading. By including a resistor in the circuit with a small impedance compared to the volt meter, an accurate voltage could be obtained across the resistor (Figure 4-2). This voltage along with the voltage across the power supply was used to calculate the voltage across the electrodes (Equation 4-1 and Equation 4-2).

The conductance of the system was calculated because as the current in the system approaches zero, the conductance approaches zero, which is a finite value. If the

resistance of the system was calculated, as the current approaches zero, the resistance approaches infinity, which is computationally inconvenient.

4.1.3 Testing

The moisture content sensors installed at the CRRF were calibrated to provide the CMU moisture content associated with a given conductance reading. The calibration was completed on a set of CMU face shells by installing the same moisture content electrodes, saturating the face shell, and using a data acquisition system to record the mass of the face shell and the conductance across the electrodes as the face shell dried. For each CMU, two data sets were collected, one for each face shell. The two data sets provided a comparative check for a given CMU that the electrodes worked properly and that the data collected were valid. The data were then used to graph the volumetric moisture content versus the conductance of each face shell. Testing multiple CMU's yielded a set of moisture content / conductance curves parametric in CMU porosity. These data were used to calibrate the experimental data collected at the CRRF based on the measured porosity of the CRRF CMU's.

Five full-size CMU's were used for the calibration. This number of CMU's was considered acceptable for calibration because it provided a sufficient number of data sets to determine a relationship between varying CMU porosities and to bracket the experimental wall porosity. First, the porosity, skeleton density, and total volume (skeleton and voids) of the complete CMU (that is, including face shells and webs) was calculated using *ASTM C140: Standard Test Methods for Sampling and Testing Concrete Masonry Units and Related Units* (ASTM International 2012). Table 4-1 shows the properties of the complete calibration CMU's. For the procedure, a scale with an accuracy of $\pm$ 0.02 kg was used. The accuracy of the CMU porosity resulting from the accuracy of the scale is reflected in the table.

Since the CRRF was constructed in 1997, there were no CMU's available to measure the in-situ properties. Instead, three coupons approximately 8 in. by 5 in. were removed from the face shell of three different CMU's in the basement wall in locations that had no impact on the experiment. The properties of the three coupons were calculated in aggregate to reduce the error introduced by the scale precision and are provided in Table 4-1.

	CMU	1A	1B	2A	2B	3A	3B	4A	4B	5A	5B	Experimental Wall
Full CMU	Porosity (%)	13.18 ± 0.18		10.80 ± 0.18		11.27 ± 0.22		13.24 ± 0.34		9.30 ± 0.17		11.73 ± 0.78
	Skeleton Density (kg/m^3)	2477		2446		2441		2469		2481		2537
	Total Volume (m^3)	0.0110		0.0110		0.0093		0.0059		0.0121		0.0026
Separate Face Shells	Porosity (%)	12.45 ± 0.08	12.41 ± 0.08	9.62 ± 0.09	9.51 ± 0.07	10.81 ± 0.07	10.85 ± 0.08	11.15 ± 0.11	12.00 ± 0.13	8.88 ± 0.08	9.06 ± 0.08	11.73 ± 0.12
	Skeleton Density (kg/m^3)	2472	2488	2415	2429	2416	2425	2418	2421	2475	2446	2530
	Total Volume (m^3)	0.0037	0.0038	0.0031	0.0039	0.0040	0.0039	0.0027	0.0024	0.0034	0.0035	0.0026

Table 4-1: Properties of CMU Calibration Blocks

The face shells of the five calibration CMU's were then separated from the webs of the CMU's and as much of the webs was broken off as possible without damaging the face shells (see Figure 4-4). This provided two calibration face shells for a given CMU porosity. Two face shells from the same CMU provided a means of checking the uniformity of porosity within a single CMU and it also provided a means of verifying the performance of the electrodes by comparing two face shells of like porosity.

Figure 4-4: Calibration Face Shell Drying Configuration

The graphite rods for the moisture content probes were then installed in the face shells. Next, the saturated weight of the face shell was determined per ASTM 140. The CMU's were then allowed to dry to ambient conditions and the sensor installation was completed by installing the screws, leads, and epoxy for the sensors (total mass approximately 3 g).

The porosity, skeleton density, and total volume of the face shells and CRRF coupons were determined after the electrodes were fully installed in the face shells. The previous method that was used for the full CMU's was used for the faceshells, except with a scale having a precision of $\pm$ 1 g. Hence, the precision of this scale was 20 times greater than the scale used for the full CMU's ($\pm$ 20 g). The porosity of all the face

shells was less than the porosity of the corresponding full CMU for all samples. In the most extreme case, the porosity of the face shell was 2.09% less than that of the full CMU (Table 4-1). The full CMU/face shell porosity difference was larger than the margin of error for the full CMU, even when accounting for the mass of the installed electrodes. This indicated that it was not just the accuracy of the scale that caused the variation. Although the porosity of all the face shells changed, there was no change to the porosity of the CRRF sample. Unlike the face shells, no electrodes were installed in the CRRF samples between the two porosity tests, confirming the consistency of the two scales used within their respective measurement precision. It was theorized that the webs of the CMU's had a higher porosity than the face shells of the CMU's. The full CMU porosity was a volume average of the face shells and the web elements. When the webs were removed the porosity was of the face shell only and decreased compared to the full CMU. For this reason, the face shell porosities were used for calibration as they more closely reflected the porosity of the CMU where the sensors were installed.

A face shell with fully installed electrodes was saturated per ASTM C140 and then connected to the data acquisition system to measure the drying process variables (mass and electrical conductance). The face shell was dried in a controlled climate chamber that was set at 54 deg. F. Inside the chamber, the scale and face shell were placed at the end of a tunnel with a 1500 W space heater (with the fan set on low) at the front of the tunnel. The front of the space heater/fan was $21^{1}/_{2}$ in**.** from the leading edge of the scale (see Figure 4-5). Ambient conditions in the vicinity of the face shell were approximately 90 deg. F and 20% relative humidity. The face shell was dried in a horizontal position with the broken off webs facing upwards. Horizontal drying reduced the effects of gravity drying by reducing the hydraulic head from $7^{5}/_{8}$ in. (height of face shell) to approximately $1^{1}/_{2}$ in. (thickness of face shell). Having the webs on top also decreased the number of potential drip edges. To allow air circulation on all sides of the face shell, the face shell was elevated above the scale approximately $1^{1}/_{8}$ in. with three metal supports covered with polyethylene to prevent corrosion.

The first mass reading was taken approximately 3 minutes after the face shell was removed from the bath and successive readings were taken at 2 minute intervals. After 10 minutes the scale was checked for any bulk water accumulation; none was ever

present. Readings continued until the mass readings reached a steady-state, which took approximately 7 days.

Figure 4-5: Drying Enclosure for Calibration CMU

4.1.4 Calibration

The mass reading that was taken simultaneously with the conductance reading while the face shell was drying allowed for the volumetric moisture content, θ_v, to be calculated at each interval with the following equation:

$$\theta_v = \frac{M_t - \rho_{sk}(1-\xi)V_{tot}}{\rho_w V_{tot}} \qquad \textbf{Equation 4-4}$$

where M_t was the mass at the time interval t, V_{tot} was the total volume of the CMU (voids and skeleton), ξ, was the porosity of the CMU, ρ_w was the density of water, and ρ_{sk} was the density of the concrete skeleton.

Figure 4-6 shows a graph of the volumetric moisture content versus the electrical conductance where the volumetric moisture content steps due to the 0.02 kg precision of the scale can be seen. In reality the volumetric moisture content did not plateau at any level, but the scale was not sensitive enough to detect the change until it reached a

magnitude of 0.02 kg. To create a more realistic drying curve, the first data point on a step that consistently stayed at that step (no oscillation with the previous step) was selected and the conductance and volumetric moisture content for these points were graphed. These data are shown in Figure 4-7.

The measured porosity of the CRRF CMU face shells was 11.73%. The field data were calibrated using the two face shells that bracketed this porosity – face shells 4A and 4B with porosities of 11.15% and 12.00%, respectively. The first conductance reading for face shell 4A was 42.2 μS at 100% saturation and the first conductance reading for face shell 4B was 50.5 μS at 93% saturation. Since the first reading for face shell 4B was not at saturation, this curve had to be extrapolated to 100% saturation. The upper four data points were used for a linear extrapolation to 100% saturation. The extrapolated saturated conductance of the 12.00% porosity face shell was 54.5 μS.

For each curve, at a given conductance, the calibration curve was represented by a third order Lagrangian interpolation. Then linear interpolation between the volumetric moisture contents of the two bounding porosity curves at the given conductance was used to determine the volumetric moisture content of the field data. Any field conductance reading that exceeded the saturated conductance was considered to be 100% saturated (maximum volumetric moisture content). The increased conductance was attributed to free water on the surface of the face shell.

4.1.5 Discussion of the Data

High electrical conductance correlated with high moisture content and low conductance with low moisture content. As the face shells approached 0% saturation, the conductance approached zero, demonstrating that the air filling the voids was primarily responsible for the decrease in conductance. In general, the data show that for a given volumetric moisture content (V_w / V_{tot}) high porosity face shells have lower conductance readings than low porosity face shells (Figure 4-7). This occurred because the volume of water in the high porosity and low porosity face shells was the same, but in the low porosity face shells the pores were filled to a greater extent (higher saturation) than the high porosity face shells. The critical factor affecting the conductance reading and the relationship between different porosity face shells was the ratio of air to water in the pores. The greater the ratio, the lower the conductance measured. The volumetric

moisture content was plotted instead of the degree of saturation, because at a given volumetric content it reflects the same volume of water in all of the face shells, regardless of porosity.

The location of the CMU 2 face shell curves (9.62% and 9.51% porosity), when compared to the other curves, is inconsistent for its porosity (Figure 4-7). It is expected that these curves should fall between the curves from CMU's 3 and 5 (10.81%/10.85% and 8.88%/9.06% porosity, respectively). The curves developed from the two face shells from CMU 2 are consistent with one another, indicating that there likely was not an error with the data collection procedure or the electrode installation. It is speculated that the CMU material mix affected the conductance readings. It is possible that admixtures such as silica fume and blast furnace slag affect the conductance (Kovler and Roussel 2011). This particular CMU was acquired from a construction waste yard and there was no way to learn the details of its composition.

The location of curve 5A (8.88% porosity) does not closely match 5B (9.06% porosity) and based on its porosity, it does not align with the other curves (Figure 4-7). It is presumed that curve 5B is accurate as it follows the general pattern of the graph (decreasing porosity for increasing conductance). The saturated conductance reading for face shell 5A was taken a second time and it confirmed that there was not an error in the data collection procedure. It is therefore speculated that there was a problem with the installation of the electrodes, such as a crack in a graphite rod.

4.1.6 Method Refinement

To further refine the moisture content sensor, a larger calibration data set needs to be developed. CMU's with a larger range of porosities should be used to test if the pattern identified in the above data set holds true. Multiple CMU's with a given porosity should be used to evaluate the consistency of the calibration curves for that porosity. CMU's with varying mix designs should be included to provide insight into the impact of mix design materials on the calibration curves.

The bottom of the graphite rod was not coated with electrical conducting paste when it was installed. By coating the bottom of the rod with paste, it would fill any voids at the bottom of the hole that might otherwise fill with water and cause irregular readings.

The graphite rods are delicate and can crack when installed in the CMU or when the hole for the screw is drilled in them. It was found that the installer could feel when the rod cracked and replace the rod, but it is unknown if the rod can crack without the installer noticing. The effect of cracked rods on the conductance readings is not understood. Further, the installation should be refined to ensure that the graphite rod penetrates to the bottom of the drilled hole and no gap remains. If this installation cannot be improved, other materials besides graphite should be researched.

Consistently wet conditions caused the CMU moisture content sensors to fail (see Chapter 5.5.2 for details). It was speculated that the graphite paste (Anders Products) was water-based and broke down when exposed to water for long periods of time. Alternative electrically conducting pastes need to be experimented with to determine if they give improved results in wet conditions. Also, it should be determined if the epoxy coating the electrode is still effective at the temperature extremes encountered in this work.

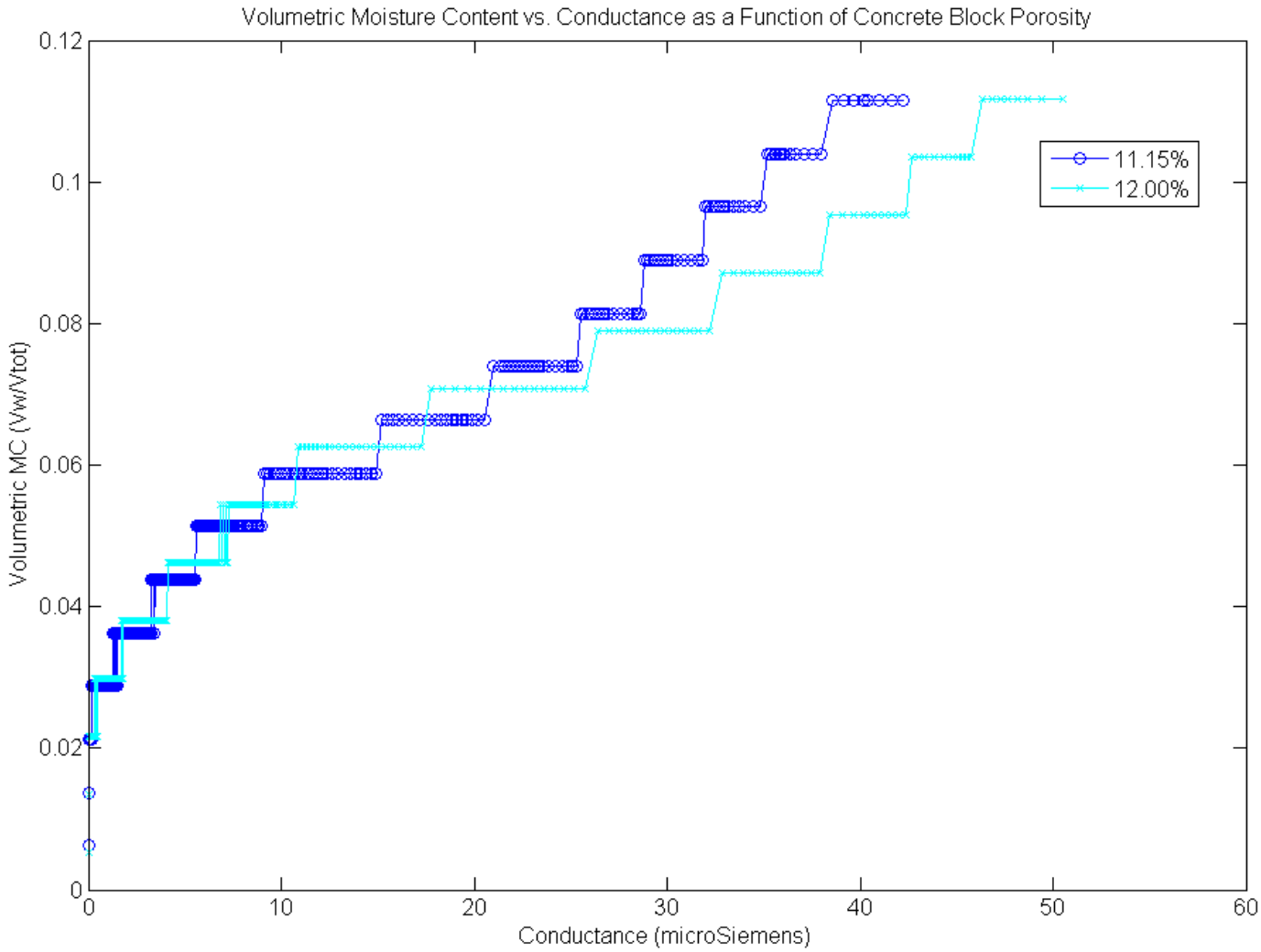

Figure 4-6: Drying Data for a set of CMU Face Shells

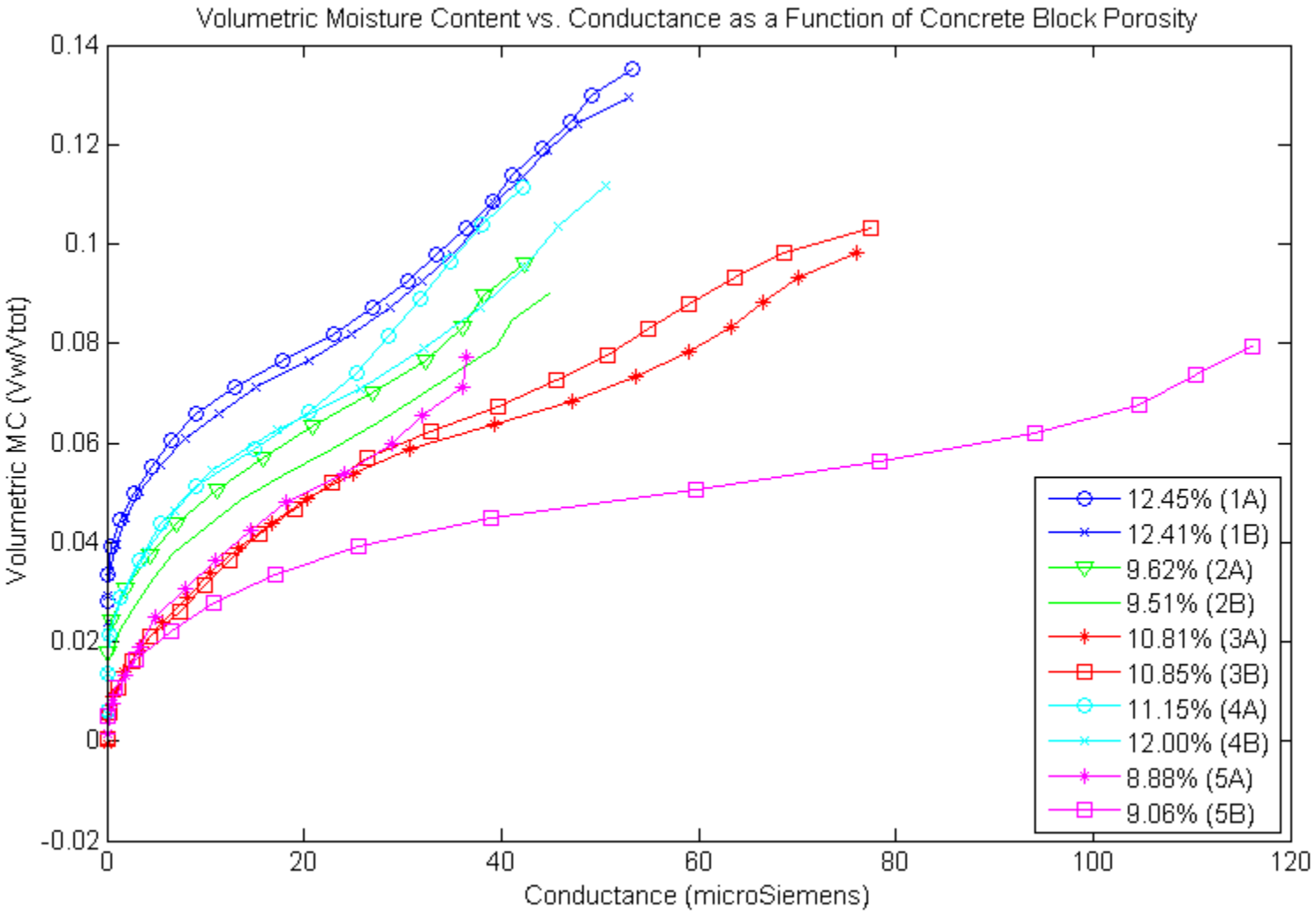

Figure 4-7: CMU Face Shell Moisture Content Calibration Curves

4.2 Wood Moisture Content Sensors

4.2.1 Introduction

Traditional wood moisture measurement devices operate by measuring the electrical resistance between two electrodes (Delmhorst Instrument Co. 2013). The presence of moisture decreases the electrical resistance between the electrodes. The meters are calibrated to correlate an electric resistance reading to a wood moisture content. The meters take a direct, instantaneous resistance reading. Similar to the direct, instantaneous readings across the CMU face shell, the readings tend to be unstable because the wood acts as a parallel resistor-capacitor circuit. The charging and discharging of the 'capacitor' causes the unsteady readings. The dielectric constant of wood is smaller than that of concrete, so the unsteady readings are less dramatic, however still present. To eliminate this problem, the wood moisture content was measured using a similar moisture content sensor design as that used for the CMU's.

4.2.2 Design

Two stainless steel pins with an exposed tip and an insulated shank, approximately one inch apart, were installed to half the depth of the wood. The exposed exterior portion of the pin was coated in marine epoxy to protect it from moisture. Wire leads soldered to each pin created a closed circuit that included the wood, a 249 ohm 1 % tolerance resistor, and a 24 V DC power supply all in series. The configuration was similar to Figure 4-2, except the CMU was replaced with wood and the pins were spaced 1 in. apart not $10^{3}/_{16}$ in. apart. The irregularities in wood and the voids introduced from the installation of the pins are less than those in the CMU, so the sensors did not need to be spaced as far apart to minimize the effects of the material and installation irregularities. Further, the electrical conductivity of moist wood is much less than that of moist masonry. Measurements of the voltage across the resistor and the voltage across the power supply were used to determine the current in the circuit and the voltage drop across the pins (Equation 4-1 and Equation 4-2). The conductance across the wood was then determined using these two values (Equation 4-3).

4.2.3 Testing

The CRRF sensors were installed in the web of the I-Joists (OSB), the exterior sheathing (OSB), the interior rim board (OSB), and 2x6 treated rim plate. Calibration of

the wood moisture content sensors was conducted in the laboratory to create a correlation for the field data. The calibration was conducted using a 6 in. × 6 in. × $^1/_2$ in. OSB sample and a 6 in. × $5^1/_2$ in. × $1^1/_2$ in. sample of 2x6 treated lumber. The OSB sample was scrap sheathing from the CRRF and the 2x6 sample was purchased new. The wood species and treatment method were not labeled on the purchased 2x6 sample. The treated 2x6 was the only available product at a national building supply store and considered a 'standard' product. Note that the 2x6 sill plate at the CRRF would likely be treated with Chromated Copper Arsenate (CCA) as this was typical in 1997 when the building was constructed. However, CCA is no longer used for such applications. The CRRF rim board was an uncoated OSB and there were no scraps at the site large enough to use for the calibration. Instead, the $^1/_2$ in. OSB calibration was used for the $1^1/_8$ in. OSB rim board. The thickness of the material may affect the OSB wetting and drying process. For this reason the sensors in the rim board provide a qualitative sense of the moisture content versus a rigorous quantitative value.

After the samples were cut to size, the oven-dry weight was determined using method B from *ASTM D4442: Standard Test Methods for Direct Moisture Content Measurement of Wood and Wood- Base Materials* (ASTM International 2007). The samples were dried in a 103 deg. C oven until there was no change in the mass over a four hour period. The $^1/_2$ in. OSB took 3 days to reach a steady-state oven-dried condition and the 2x6 took 8 days. All mass measurements were taken using a scale with a $\pm$ 1 g accuracy (Table 4-2 shows the oven-dry mass of the samples).

Immediately after the oven-dry mass was attained, the pins with leads were installed and coated in epoxy. The mass was then taken to determine the mass of the pins, leads, and epoxy (see Table 4-2). After allowing a minimum of 24 hours for the epoxy to cure, the sample was placed in a water bath to saturate. The sample was removed from the bath when there was no appreciable change in mass over an approximate 24 hour period (2.4% for the $^1/_2$ in. OSB and 1% for the 2x6).

When the saturated condition was reached, the sample was placed on the scale and connected into the circuit to dry while a data acquisition system collected conductance and mass readings. The sample was elevated above the scale approximately $1^1/_8$ in. by two steel spacers covered in polyethylene. The drying process occurred inside a

climate chamber that was set to 54 deg. F. The scale was placed in a tunnel with a 1500 W space heater/fan, set on low, at one end of the tunnel and was located 25 in. from the edge of the scale. The scale was set to take readings at the first reading as opposed to the stable reading. This was required because the movement of air over the scale from the fan caused the mass to oscillate (≤ 1 g). In the future this can be prevented by conducting the calibration in a climate chamber that provides direct control of the temperature and humidity so that a space heater/fan is not required.

The data were collected at an interval of 30 seconds or less for at least the first 12 minutes, after which the collection interval was increased to 2 minutes. After 10 minutes the scale was checked for accumulated water and none was ever present. The readings continued until the conductance reached a steady-state. The $^1/_2$ in. OSB sample achieved a conductance measurement of 0 µS and the 2x6 plateaued at 0.000333 µS.

4.2.4 Calibration

The drying process generated a data set with a conductance and mass at every time interval. The data set was filtered by taking the first reading at a given mass and eliminating all data points that followed that had a mass of equal or greater value. Since the space/heater fan caused the mass reading to oscillate (see above), this was required so that moisture content decreased with time. This reduced data set was further filtered by removing all data points where the conductance increased over a time interval. The overall trend was that the conductance decreased with time and moisture content; however the frequency of the readings caused this to not always be true in the data set. For the overall trend to be represented in the calibration curve, it was necessary to remove any conductance readings that increased over time. These two filters together generated a smoothed data set (see Figure 4-8).

To determine the moisture content, the mass of the pins, epoxy, and leads, M_x, was subtracted from the mass reading taken during the drying process, M_t,. The moisture content by mass, θ_M, for each data point was calculated based on the oven-dry mass, M_{od}, M_t, and M_x using the following equation:

$$\theta_M = \frac{M_t - M_x - M_{od}}{M_{od}} \qquad \textbf{Equation 4-5}$$

The initial and final moisture content of the samples are provided in Table 4-2.

Conductance versus the mass moisture content was plotted to create a calibration curve for the field data (Figure 4-8). Laboratory data were related to the field data using a second order Lagrangian interpolation at each measured electrical conductance.

	½ in. OSB	2x6
Oven-Dry Mass (g)	161.3	449.9
Mass of Pins, Leads and Epoxy (g)	4.0	5.6
Saturated Mass with Pins, Leads and Epoxy (g)	301.8	642.5
Saturated Moisture Content (% mass)	85%	42%
Moisture Content at End of Drying Period (% mass)	2%	6%

Table 4-2: Wood Calibration Data

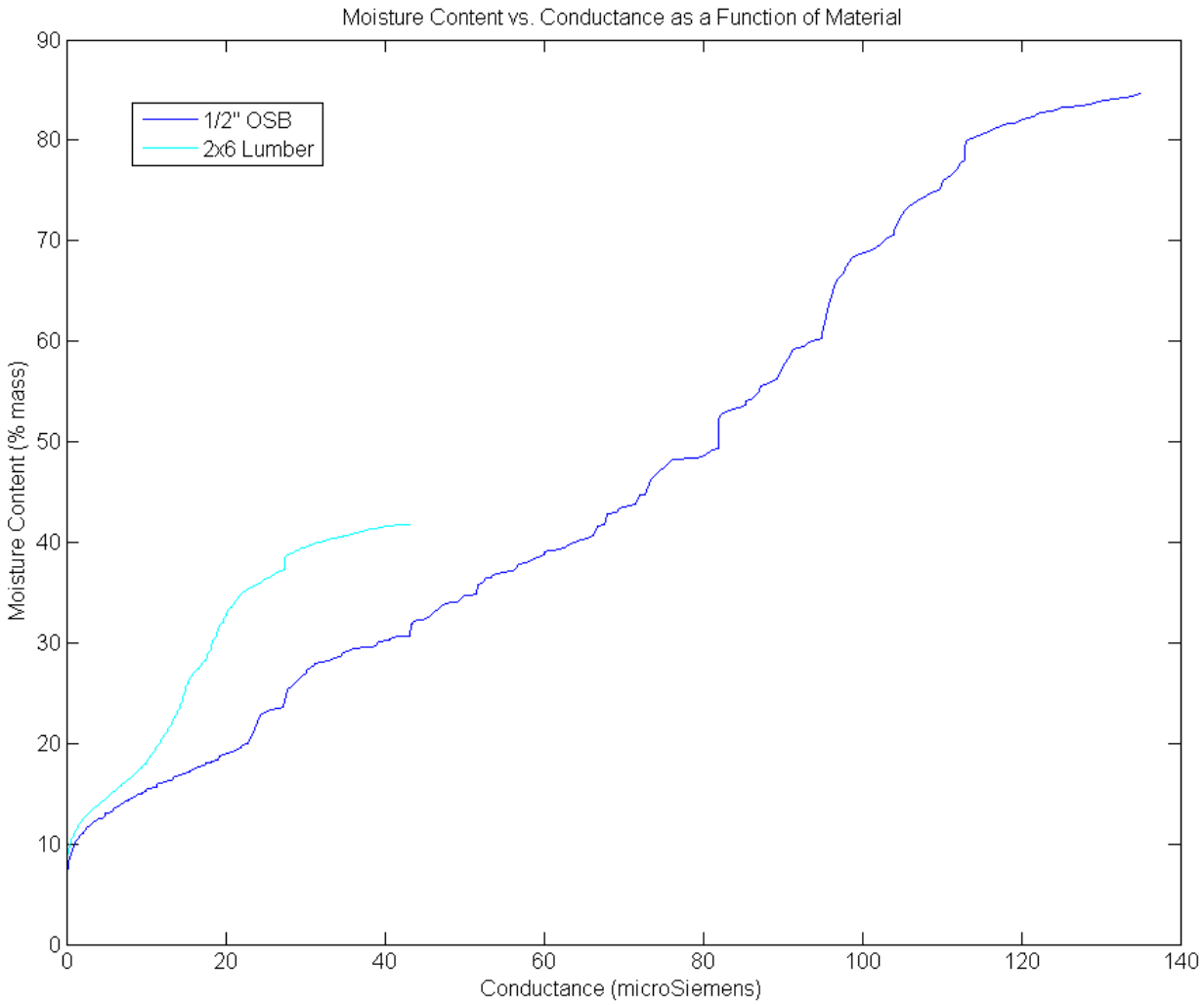

Figure 4-8: Wood Moisture Content Calibration Curves

4.2.5 Discussion of the Data

As noted above, the final conductance readings for the OSB and 2x6 were 0 μS and 0.000333 μS, respectively. In reality, the OSB did not reach a conductance of 0 μS or infinite resistance, but the reading was caused by the quantization error in the data acquisition system analog-to-digital converter. In this experiment the quantization error was 0.000166 μS. At one quantization error, the OSB was at 2% moisture content. Anything below this value was not accurate. The final reading for the 2x6 was within two quantization errors of 0 μS at a moisture content of 6%. This method was therefore accurate down to 6% moisture content for the 2x6. For the field data, any conductance below the lower limit (0.000166 μS for OSB and 0.000333 μS for 2x6) was reported as -9999.

After the samples finished drying they were left in ambient conditions. The moisture content of the samples was checked using a Lignomat pin moisture content meter with a lower measurement moisture content limit of 5%. The OSB and 2x6 were checked 16 days and 7 days, respectively, after the calibration drying was completed. For both samples, the moisture content was less than 5%. The ambient conditions at the time of testing were approximately 70 deg. F and 22% relative humidity.

4.2.6 Method Refinement

The wood moisture content calibrations were based on two types of materials ($^1/_2$ in. OSB and 2x6 treated lumber) and one sample for each material. A calibration curve for $1^1/_8$ in. OSB should be developed to see if it was valid to use the $^1/_2$ in. OSB as a substitute calibration. To further refine the calibration, a larger sample size should be used to ensure the repeatability of the results. Also, additional wood materials should be investigated, such as differing species and sizes.

As mentioned earlier, the 2x6 was treated by an unspecified treatment process and the 2x6 sill plate at the CRRF was likely treated with Chromated Copper Arsenate (CCA). The effects of the different treatment processes were not investigated in this work nor were the effects of treated versus untreated wood. Further investigation in this area would be valuable.

The sensors produced moisture content data that were steady with small oscillations. For an insulated rim joist with a south exposure, the moisture content of the sill plate

was approximately 7% $\pm$ 0.5% and the interior rim board and east joist were both approximately 4% $\pm$ 1.25% (Figure 4-9). The data shown in Figure 4-9 are representative of the quality of all the data produced by the wood moisture content sensors installed. Based on the consistency of the data and the steady readings, it appears that the sensors were effective at producing reasonable moisture content readings. The small oscillations indicate that the sensor was effective at eliminating the effects of a parallel resistor-capacitor circuit that result from periodic direct moisture content readings.

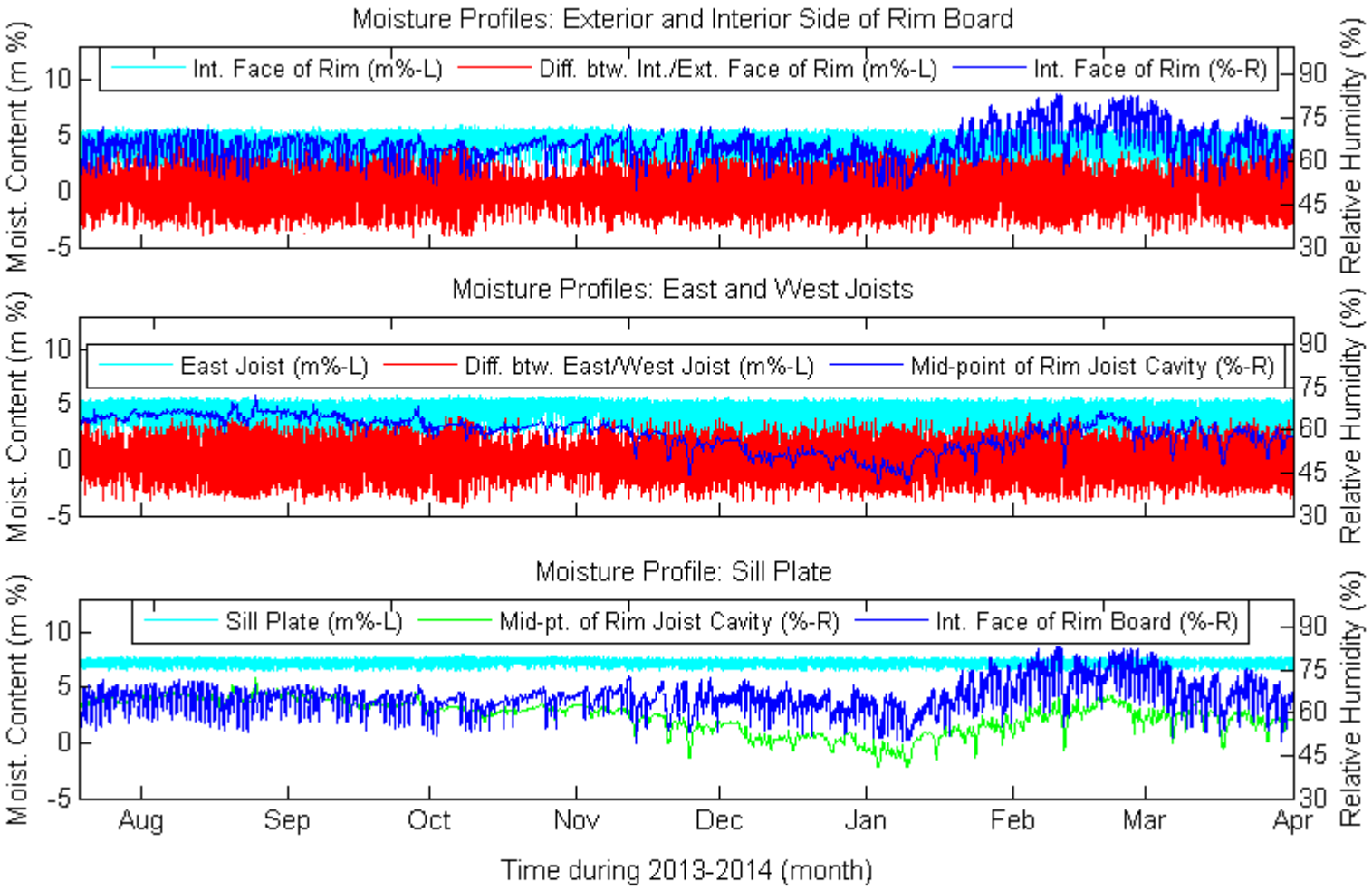

Figure 4-9: Moisture Profiles for an Uninsulated Rim Joist Cavity with a South Exposure

Chapter 5: Results and Analysis

5.1 Boundary Conditions

Measurement of the boundary conditions is necessary to understand the wall performance. Interior and exterior temperatures and relative humidities, precipitation, snow depth, solar irradiance, and long-wave irradiation were all measured. These parameters all impact the thermal and moisture performance of the wall systems tested.

5.1.1 Interior Process Temperature and Relative Humidity

The basement interior temperature control system performance is shown in Figure 5-1. The basement interior temperature was set to 20 deg. C (68 deg. F) during the first heating season. On May 1, 2013 the setpoint was reduced to 15.6 deg. C (60 deg. F) for the cooling season. On November 5, 2013 the setpoint was increased to 18.3 deg. C (65 deg. F) and again on November 14, 2013 it was increased to 20 deg. C (68 deg. F) for the second heating season. The furnace was controlled by a mechanical analog thermostat until January 28, 2013 when it was switched to a computerized real-time digital control system. The digital system reduced the process temperature variability (Figure 5-1).

On October 10, 2013, recording of the process temperature commenced. Prior to this date the process temperature recorded was approximated by averaging the Bay 3N and Bay 3S interior basement temperatures at 46 in. above the slab. The furnace did not run from approximately mid-June to mid-October, since the interior basement process temperature was elevated above the process setpoint temperature (Figure 5-1).

Figure 5-2 shows the temperature of Bay 1N at 10 in. from the face of the interior wall system at 5.5 in., 46 in. (mid-height), and 86 in. above the floor and in the rim joist cavity. The digital system also reduced the temperature variability in Bay 1N, but it can be seen that the variation was larger than the measured process temperature variation (Figure 5-1). Bay 1N interior temperature sensors were the furthest from the process temperature measurement location (approximately 22 ft). The process temperature was based on an average of the temperature sensors that were located 10 in. from the face of the Bay 3N and 3S walls at mid-wall height. Figure 5-2 shows that prior to May 2013 the temperatures are stratified vertically (temperatures increase with height) with the smallest amplitude at 46 in. above the slab. However, after November, 2013 during the

second heating season, the stratification disappears with the mean temperature being about the same at all levels with the variation in amplitude being the smallest at 46 in. above the slab. The basement was unheated from 2007 to the beginning of this experiment. When the experiment began, the operation of the furnace raised the temperature of the basement air, the concrete slab, and the soil below the slab. The total heat capacity of the basement air is less than that of the concrete slab and soil. Therefore, during the first heating season it took longer to warm the concrete and soil than it did to warm the air. Since the basement air was warmer than the slab and soil, it caused the basement air temperatures to be stratified with the temperatures closer to the slab colder. During both heating seasons the amplitude was the smallest at 46 in. above the slab because this was the sensor closest to the height of the process temperature sensor.

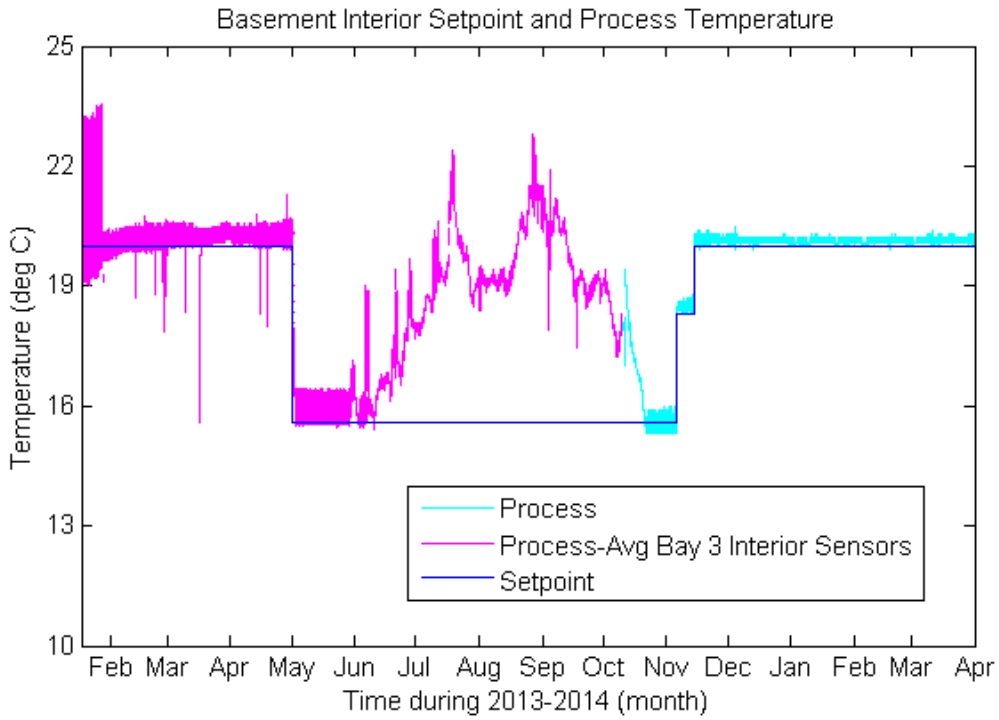

Figure 5-1: Basement Interior Setpoint and Process Temperature

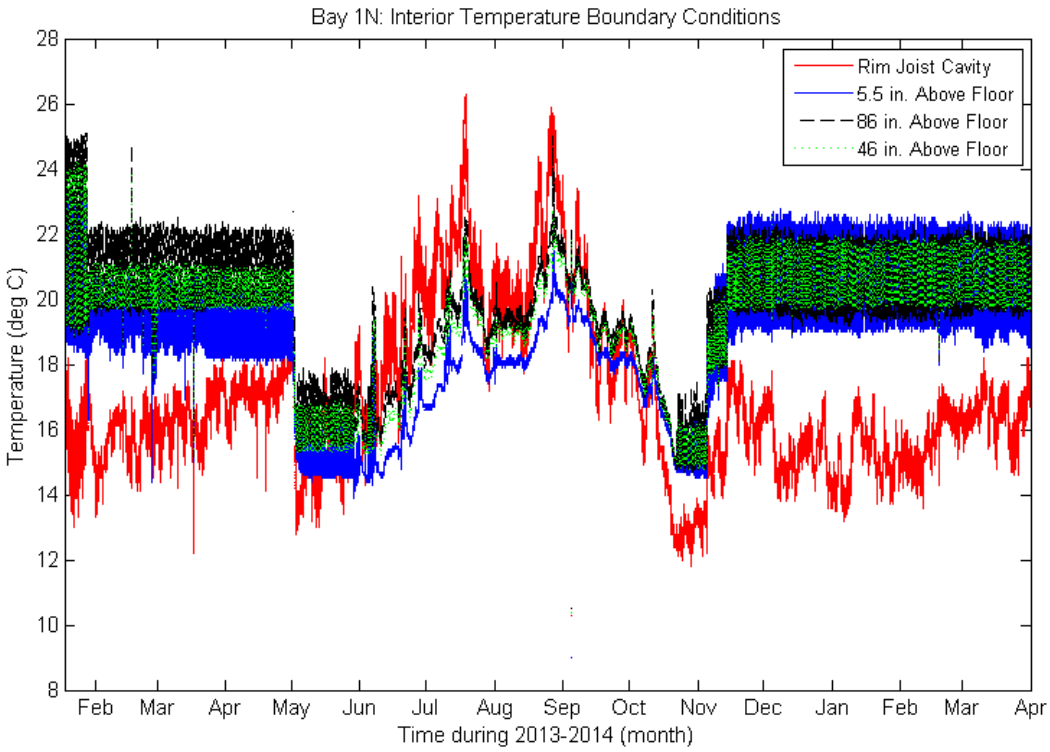

Figure 5-2: Interior Temperature Boundary Conditions at Bay 1N

A humidification system was installed to test the walls at extreme moisture conditions during the heating season. The process humidity sensor was located approximately seven feet above the floor in the return air stream above the furnace air handler at the mid-point of the basement. This location provided a reasonable approximation of the mixed basement air relative humidity. On January 10, 2014 the relative humidity was set to 35%. The setpoint was increased to 40% on January 17, 2014, to 45% on January 24, 2014, and to 50% on February 3, 2014. The setpoint was then stepped down to 45% on January 18, 2014, to 40% on March 4, 2014, and to 35% on March 12, 2014 (Figure 5-3). On April 21, 2014, the humidifier was shut down. The relative humidity bandwidth during humidification was approximately +2.5/-0%. Prior to humidification, the process relative humidity reached a low of approximately 25%. The air in a heated basement can hold more moisture than an unheated basement because of the higher temperature. At 50% relative humidity, moisture was condensing on the floor joists and dripping onto the basement slab. Because of this visible condensation, 50% relative humidity was selected as the maximum setpoint. This was considered a realistic maximum because of the onset of condensation on the floor joists.

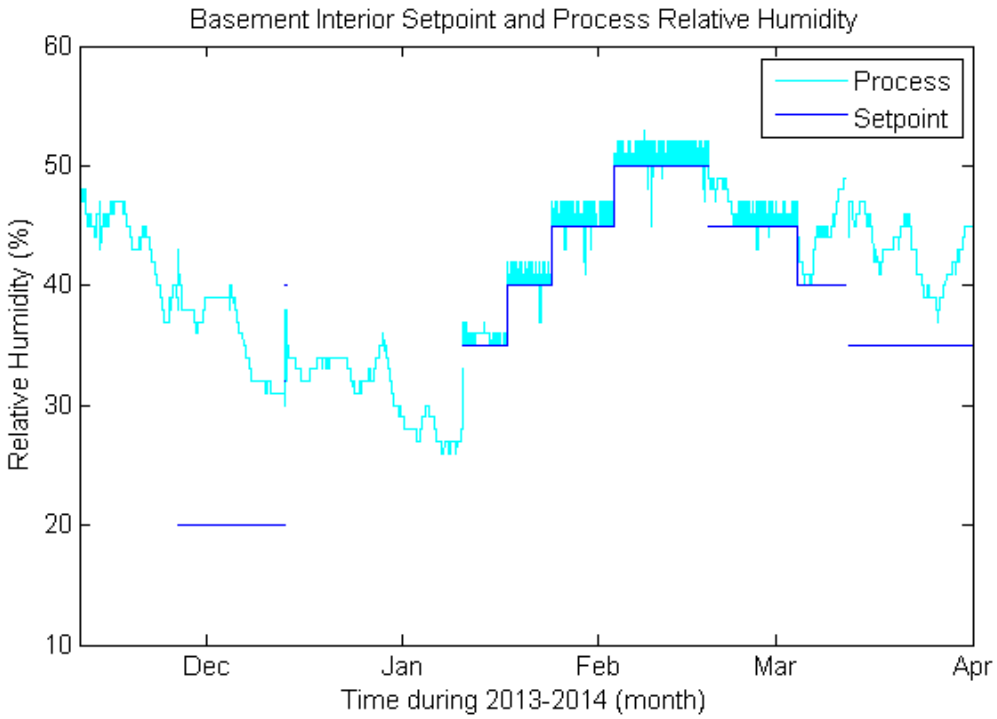

Figure 5-3: Basement Interior Setpoint and Process Relative Humidity

5.1.2 Precipitation

There was a heated precipitation gauge located at the CRRF and an unheated precipitation gauge (only able to record precipitation when temperatures are above freezing) at the Cloquet Forestry Center weather station approximately 1/4 mile from the building (Table 3-4). In addition, a manual reading was taken daily at the weather station and reported to the National Climatic Data Center (NCDC)[9]. The orifice in the heated precipitation gauge collection trough through which water drained was susceptible to clogging with coagulated silt or clay due to its small diameter. The orifice likely became clogged at the end of May 2013 when the excavation for Bay 3 and Bay 4 occurred in close proximity to the instrument. The blockage was not discovered and cleaned until the end of October 2013. The heated precipitation gauge is specified to operate in temperatures down to -20 deg. C (Table 3-4). From December 2013 to March 2014, the outdoor ambient temperatures regularly reached below -20 deg. C. The precipitation gauges at the CRRF and weather station provided readings every 10 to 12 minutes, whereas the manual readings were taken once a day at approximately

[9] The data can be downloaded from http://cfc.cfans.umn.edu/weather/

4:00 p.m. A composite precipitation time series was constructed using the three available data sets that selected the best available data based on the functionality of the two instruments. The CRRF heated precipitation gauge was preferred due to its proximity to the experiment, but when it was not operational because it was clogged or the outdoor temperatures were regularly below -20 deg. C, the non-heated precipitation gauge at the weather station was used. The weather station precipitation gage was preferred over the manual data because it had data readings every ten minutes versus once a day. When the ambient temperature was below freezing and neither the weather station nor CRRF precipitation gages were functional, the manual data was used for the composite time series. The following schedule describes the manner in which the composite precipitation series was assembled (Figure 5-4):

- CRRF heated precipitation gauge: beginning of experiment – May 28, 2013
- Weather station non-heated precipitation gauge: May 29, 2013 – October 31, 2013
- CRRF heated precipitation gauge: November 1, 2013 – December 5, 2013
- Manual precipitation readings: December 6, 2013 – March 16, 2014
- CRRF heated precipitation gauge: March 17, 2014 – March 31, 2014

Figure 5-4 shows the composite data set for the precipitation which includes the liquid equivalent of snow fall. From December 6, 2013 to March 16, 2014 the precipitation was recorded as a daily total and not at 10 to 12 minute intervals. This is why the precipitation events are large compared to the rest of the time period. For the experimental time period the total recorded precipitation was 1098 mm (43.2 in.). The historical average (1981-2010) was 878 mm (34.6 in.) based on the monthly averages (National Climatic Data Center 2011). From May 1, 2013 to October 2013 the total precipitation was 472 mm (18.6 in.) and the historic average was 588 mm (23.1 in.). During the experimental period, the winter, early spring, and late fall were wetter than normal and the late spring, summer, and early fall were drier than normal. Overall, the experimental period was 25% wetter than the historical average.

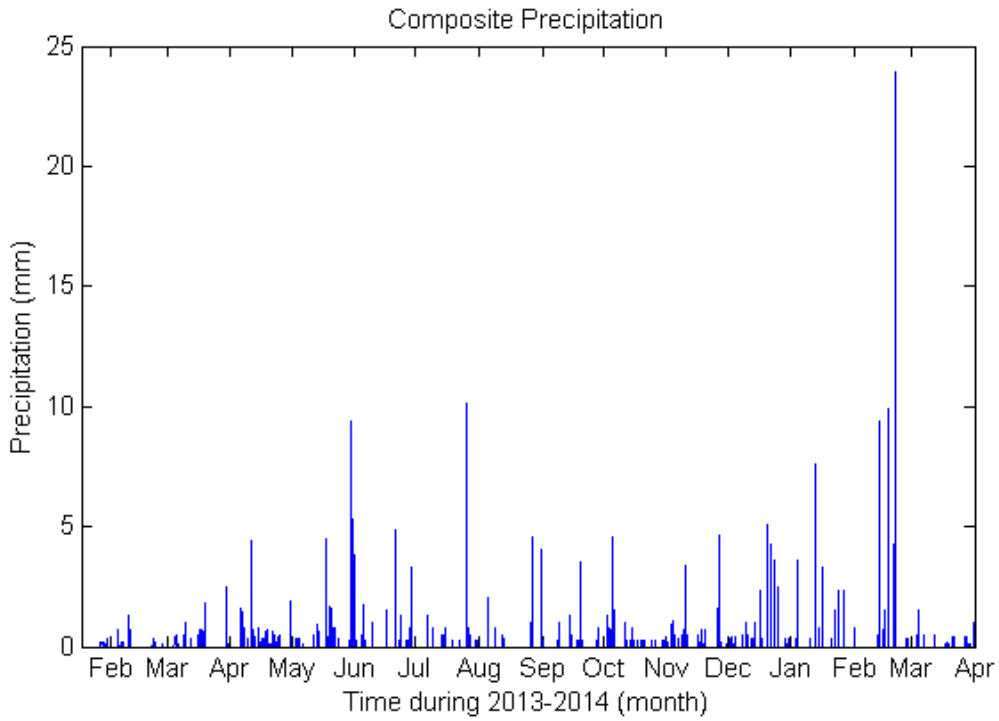

Figure 5-4: Precipitation Boundary Condition

5.1.3 Snow Depth

All the snow depth readings had an associated quality reading (see Chapter 3.5 for details of quality readings). Poor quality readings when snow was on the ground were caused by an increased snow slope. The sensor works by emitting ultrasonic pulses and reading the return echoes. A slope in the snow causes the reflected pulses to scatter and reduces those returning to the sensor and, in turn, the quality reading. For this work, height readings with a quality reading between 152 and 210 were used for the north side and between 152 and 230 for the south side, all other readings were ignored. If an upper limit of 210 was used for the quality readings on the south side, there were a limited number of available data points from approximately mid-February 2014 to April 2014. Increasing the acceptable range to 230 provided a trend for the snow depth during this time period and was still an acceptable level of quality. During this time period, the south side required a higher quality range because there was a steeper snow slope than on the north side. The south side had increased infrared solar radiation reflected off the building that melted the snow adjacent to the building. The solar

exposure also caused greater snow melt on the roof that then dripped onto the snow below and melted some of the snow on the ground and increased its slope.

Figure 5-5 shows the snow depth approximately three feet from the north and south sides of the building. The snow depth was greater on the north side of the building because there was less melting due to solar exposure. Based on the historic monthly averages (Table 5-1), the average snowfall over the duration of the experiment should be 2.39 m (94.3 in.) (National Climatic Data Center 2011). According to the National Climatic Data Center (NCDC), the snowfall for Cloquet, Minnesota was 4.24 m (167.1 in.)[10] (Table 5-1) during the experimental time period (January 18, 2013 to March 31, 2014) (2014). The snowfall during the experimental time period was approximately 77% greater than the historic average during this period. The historic annual snowfall (1981-2010)[10] is 1.68 m (66.2 in.) (NCDC 2011). According to the NCDC, the historic annual snowfall in Duluth, Minnesota (approximately 21 miles northeast of Cloquet on Lake Superior) is 2.19 m (86.1 in.) and in Pine River Dam, Minnesota (approximately 100 miles west of Cloquet) is 0.83 m (32.8 in.)[10] (2011). Based on this data it appears that Cloquet receives lake effect snow.

	Jan.	Feb.	March	April	May	June -Sept	Oct.	Nov.	Dec
Historic Average	13.9	11.2	10.6	3.6 [10]	.1	0	1.4	11.2 [10]	14.2
2013	7.1	12.3	20.0	41.1	0	0	0.4	4.2	37
2014	6.4	26.5	19.1	--	--	--	--	--	--

Table 5-1: Snow Fall Data for Cloquet, MN

[10] Per the National Climatic Data Center (2011) the data is "provisional (at least 10 years used, but not sufficiently complete to be labeled as standard or representative)."

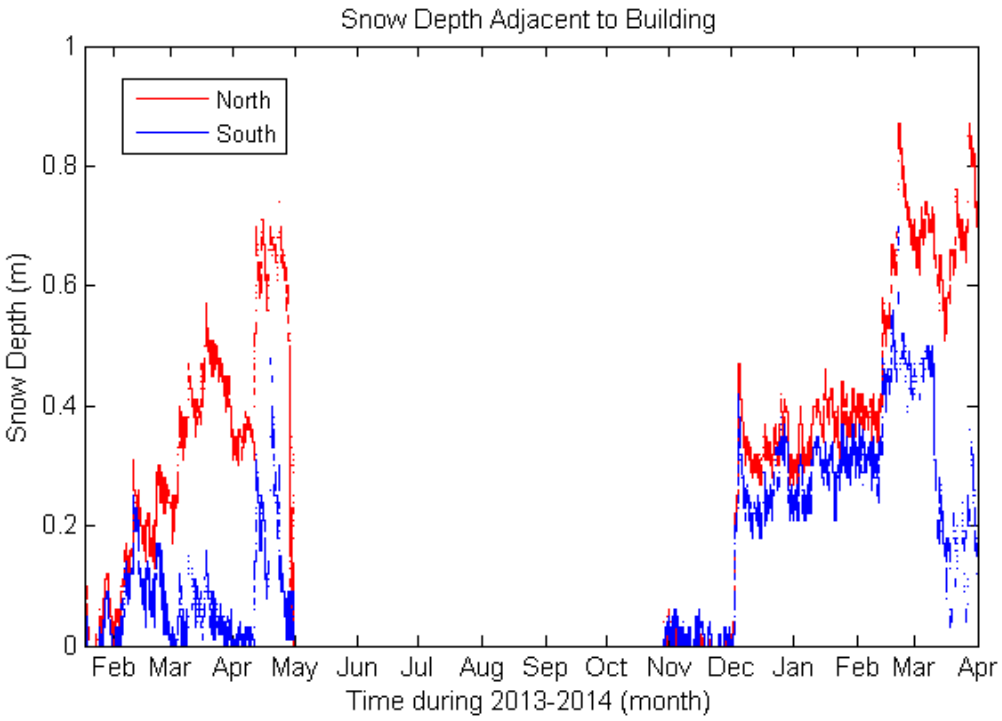

Figure 5-5: Snow Depth on North and South Sides of Building

5.1.4 Horizontal Plane Solar Irradiance and Net Long Wave Irradiation

Horizontal plane solar irradiance was initially measured with a pyranometer located on a tower at the Cloquet Forestry Center Weather Station approximately 80 ft. above the ground. In July of 2013, it was discovered that this pyranometer was out of calibration and the readings were approximately half of the values recorded historically. The pyranometer had been in service for over 20 years and, as it was located on the top of a tower, it was not inspected or maintained owing to the poor accessibility. To address the problem, a new pyranometer was installed on the roof of the CRRF on July 31, 2013. The pyranometer on the CRRF roof read the instantaneous irradiance and the pyranometer at the weather station read the time averaged value over a 10-12 minute period. The two pyranometers ran concurrently and the readings from the new pyranometer were used to create a calibration for the old pyranometer so its previous erroneous data could be corrected.

The weather station pyranometer data was calibrated as follows:

- The weather station pyranometer readings were linearly interpolated to the time stamp of the CRRF pyranometer readings;
- The ratio of the CRRF pyranometer reading to the weather station pyranometer reading was calculated;
- The weather station pyranometer data was separated into bins with intervals of 10 W/m^2 from 0 to 500 W/m^2;
    - Within each bin, the average weather station pyranometer reading was calculated along with the average ratio;
- This data was plotted and a third order polynomial was fitted to the data to determine the weather station pyranometer correction factor (CRRF pyranometer irradiance/weather station pyranometer irradiance) (Figure 5-6);
    - For weather station readings greater than 500 W/m^2 the multiplier for 500 W/m^2 was used (approximately 2.15), since there were no readings greater than 500 W/m^2 in the calibration period.

Figure 5-7 shows the horizontal plane irradiance as a composite of the corrected weather station and directly measured irradiance.

The horizontal plane solar irradiance is directly correlated to the sun's angle above the horizon. It is a maximum in the summer when the sun's angle above the horizon is the greatest. A maximum clear sky solar irradiance of approximately 1100 W/m^2 occurred between June and August. A minimum clear sky solar irradiance of approximately 400 W/m^2 occurred between December and February.

Horizontal plane net long-wave irradiation was measured at the Cloquet Forestry Center Weather Station. Figure 5-7 shows the values over the experimental period. The values of net long-wave irradiation are negative because they are a measure of energy lost from the earth's surface to the outer atmosphere. They are independent of season and instead dependent on sky conditions. The near zero values from late November 2013 to mid-January 2014 were caused by snow covering the instrument and preventing accurate measurement. The spike in mid-December 2013 occurred after snow was

removed from the sensor. Shortly after cleaning, new snowfall again prevented accurate readings.[11]

[11] Instrument maintenance evidently lapsed during the holiday season.

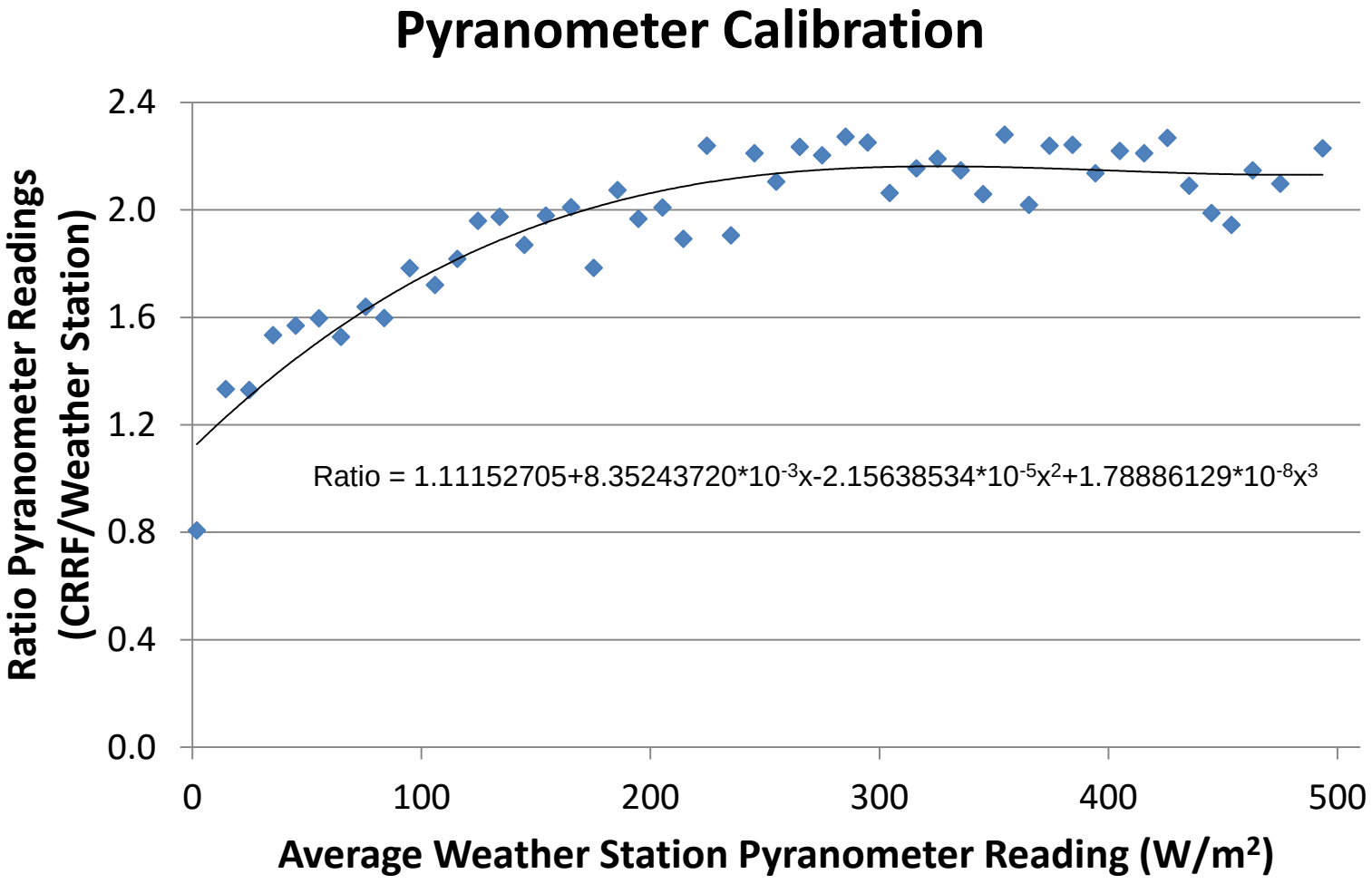

Figure 5-6: Calibration Curve for Weather Station Pyranometer

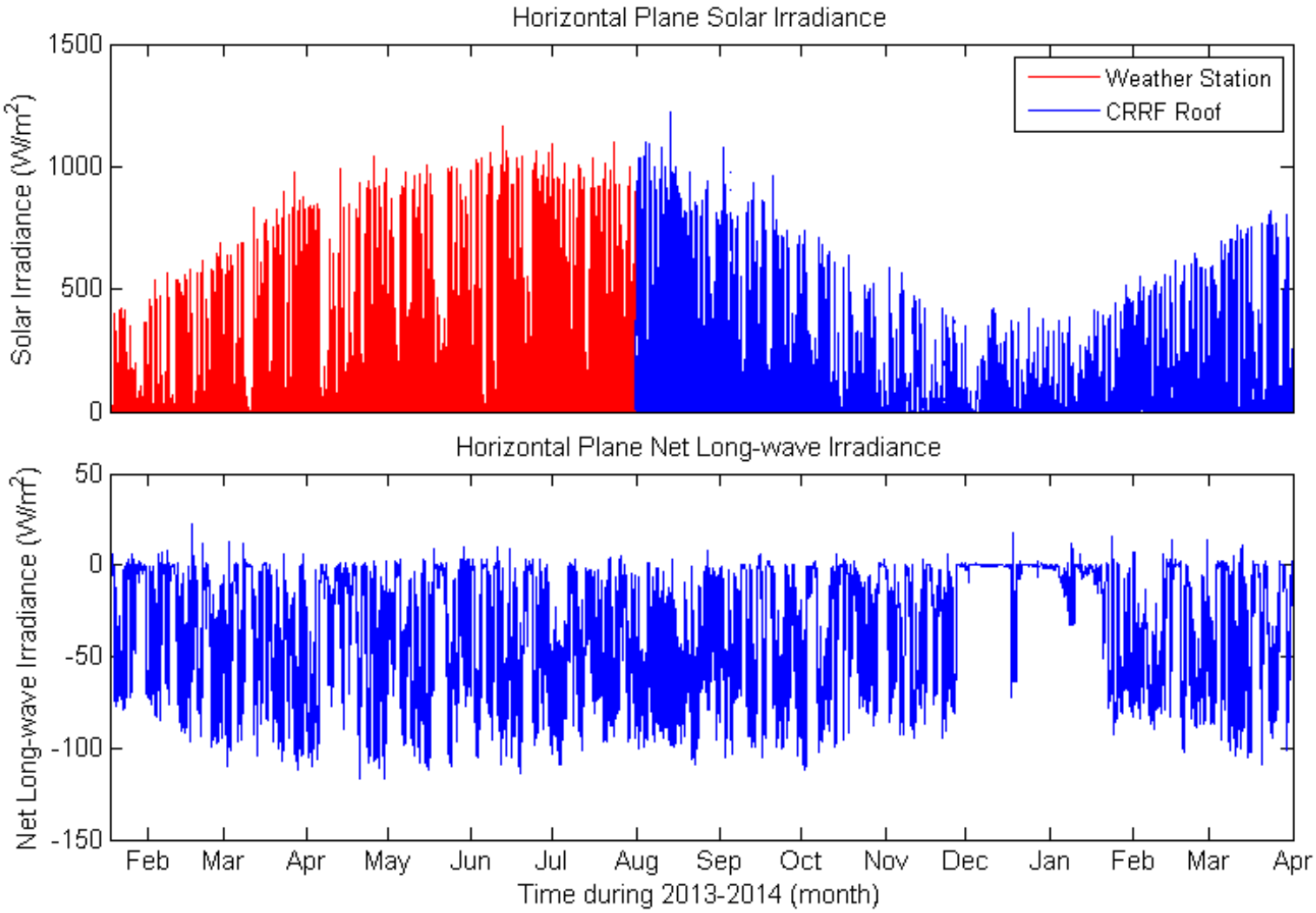

Figure 5-7: Horizontal Plane Solar Irradiance and Horizontal Plane Net Long-wave Irradiance

5.1.5 Outdoor Ambient Temperature and Relative Humidity

The Bay 1 and Bay 2 north and south exterior face shell temperatures on the above grade portion of the walls is shown in Figure 5-8. Figure 5-9 shows the corresponding temperature readings for Bays 3 and 4, north and south. The temperature sensor was approximately 5 in. above the top of the grade. The larger diurnal variation on the south was due to the solar irradiance. Year round, the Bay 4 diurnal variations were significantly damped because the sensor was located behind 3 in. of XPS insulation. From December 2013 to mid-March 2014, the diurnal variation on the north and south sides of Bays 1, 2, and 3 was damped. This was caused by snow covering the face shell temperature sensors and reducing the impact of the solar irradiance. From July 17, 2013 to July 31, 2013 the Bay 3S exterior above-grade face shell temperature sensor failed and this is reflected in Figure 5-9 by the lack of diurnal variation during this period.

The maximum and minimum face shell temperatures for Bays 1, 2, and 3 were very similar. The maximum temperature on the south side was approximately 47 deg. C and occurred in late August 2013. The maximum temperature on the north side was approximately 28 deg. C and occurred in mid-July and late August 2013. The maximum face shell temperatures for the north and south exposures of Bay 4 were approximately 24 deg. C and occurred in late August. The minimum temperature for Bays 1 and 2 occurred in late January 2013 and was approximately -15 deg. C on the north side and -10 deg. C on the south side. The Bay 4 minimum temperature was approximately 10 deg. C for the north and south sides and occurred in early January 2013. In general, on a wall without exterior insulation the temperatures are greater on the south side than the north side. For a wall with exterior insulation the temperatures for the north and south exposures are approximately the same and the temperature extremes are less than for a wall without exterior insulation.

Outdoor ambient temperature and relative humidity were recorded at the Cloquet Forestry Center Weather Station and the CRRF (Figure 5-10 and Figure 5-11). At the CRRF, the sensors were located within a radiation shield provided by an opaque enclosure that was open at the bottom. The enclosure was approximately 21 in. above grade and 11 in. from the face of the building over Bays 1 and 2 on both the north and

south sides. The crib sensors were not installed until October 2014 so there is not a full data set. The south side temperatures were warmer than the north side due to the solar exposure and the relative humidities were lower due to the higher temperatures. The solar exposure on the south also increased the diurnal variation of the temperature and the relative humidity. The damping of the temperature and the relative humidity from mid-February 2014 to mid-March 2014 was due to snow covering the sensor enclosure.

The weather station temperature and the crib temperatures on the north side of the building were very similar. The crib temperatures on the south side of the building were warmer than those on the north side of the building and at the weather station. The maximum weather station temperature was approximately 33 deg. C and occurred in mid-July and late August 2013. The minimum weather station temperature was approximately -33 deg. C and occurred at various times between January 2014 and March 2014. The relative humidity at the weather station did not closely match the relative humidity above the cribs on either the north or south sides of the building from mid-October onwards. The crib relative humidity on the south side of the building had a range of 20%-100% and on the north side of the building the range was 70%-100%. The relative humidity at the weather station had a range of 40%-100%. When available the crib temperature and relative humidity data were preferred over the weather station data because of the proximity to the experiment and the differentiation between the north and south exposures.

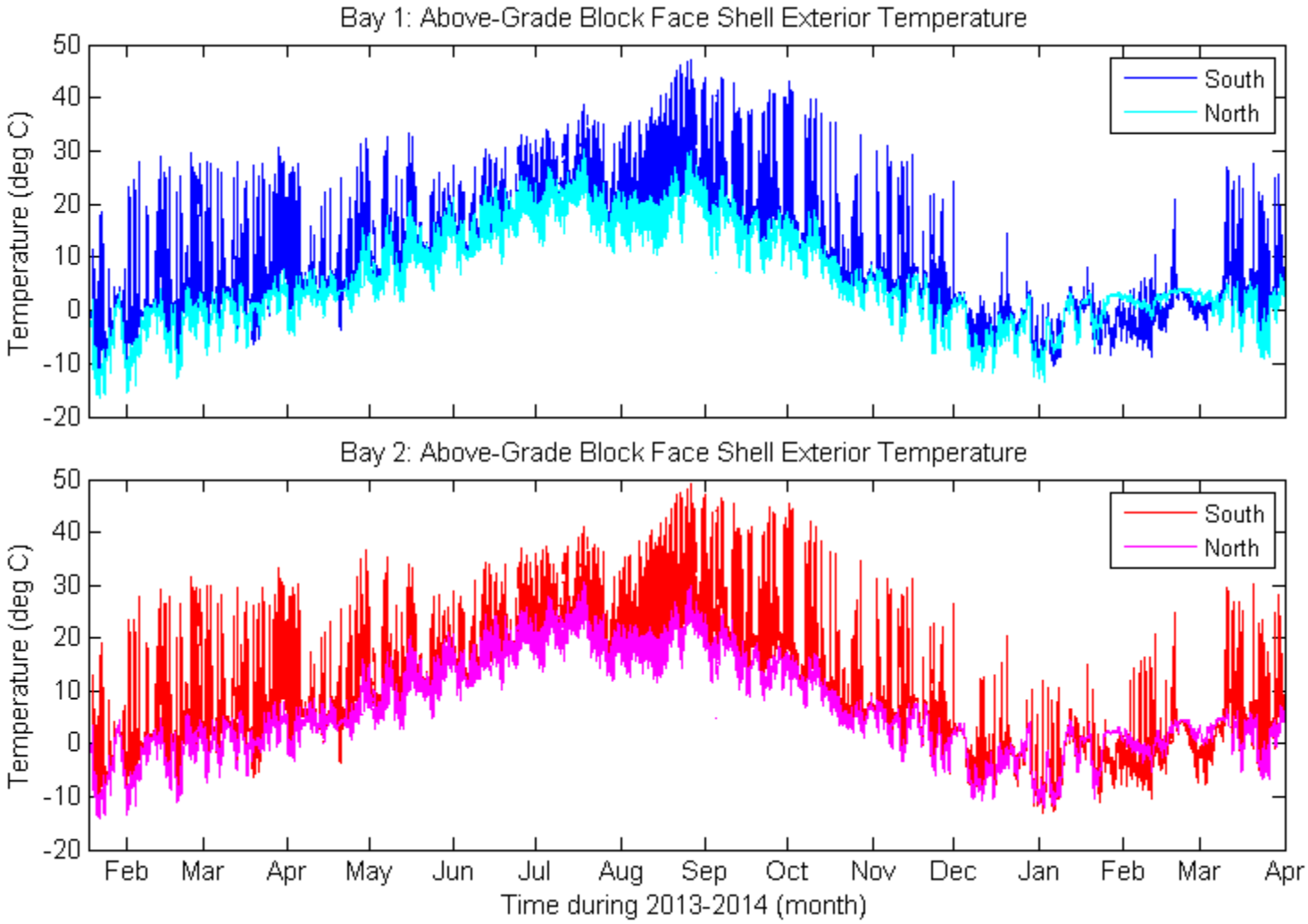

Figure 5-8: Bay 1 and 2 Above Grade Masonry Block Temperature

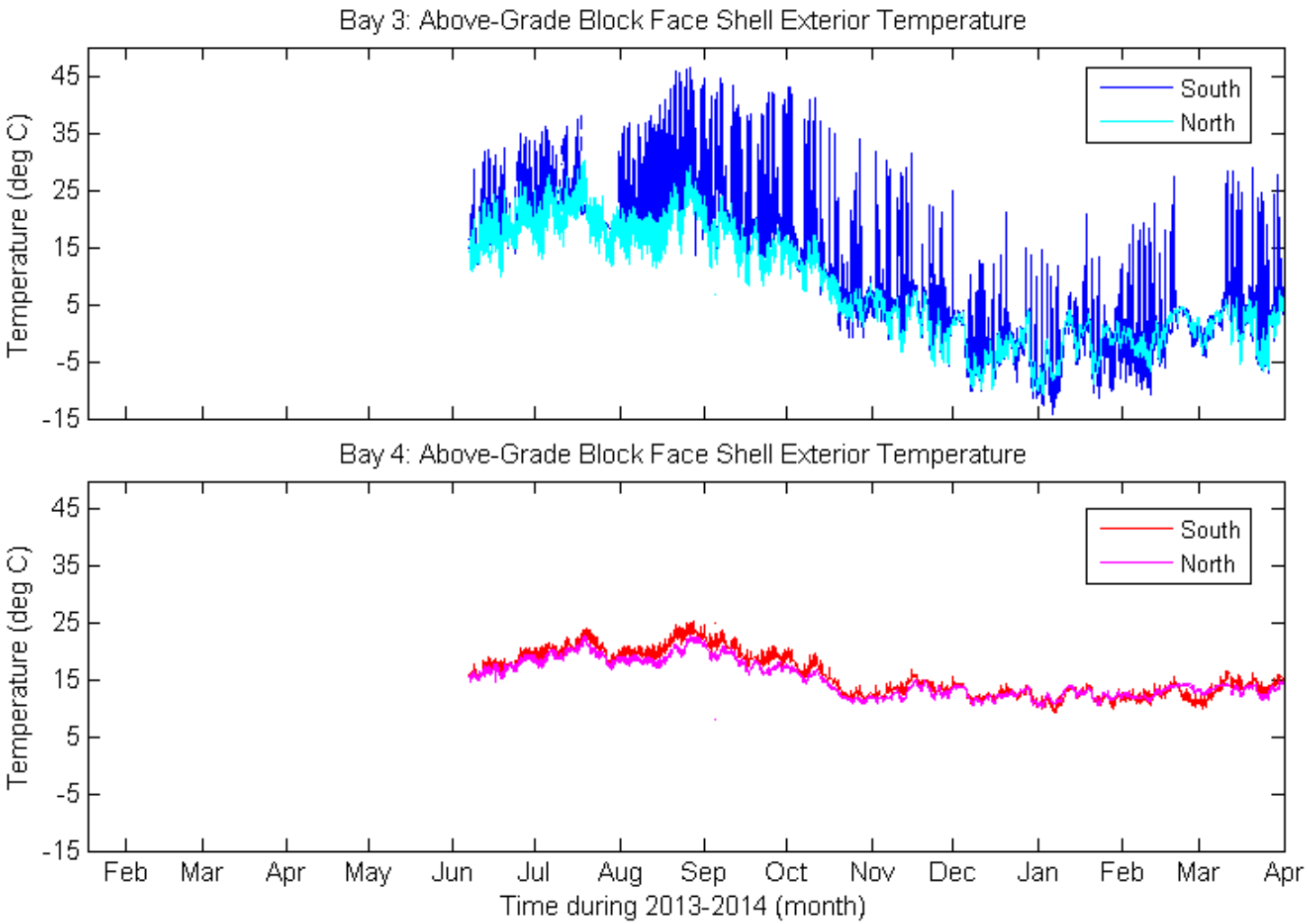

Figure 5-9: Bay 3 and 4 Above Grade Masonry Block Temperature

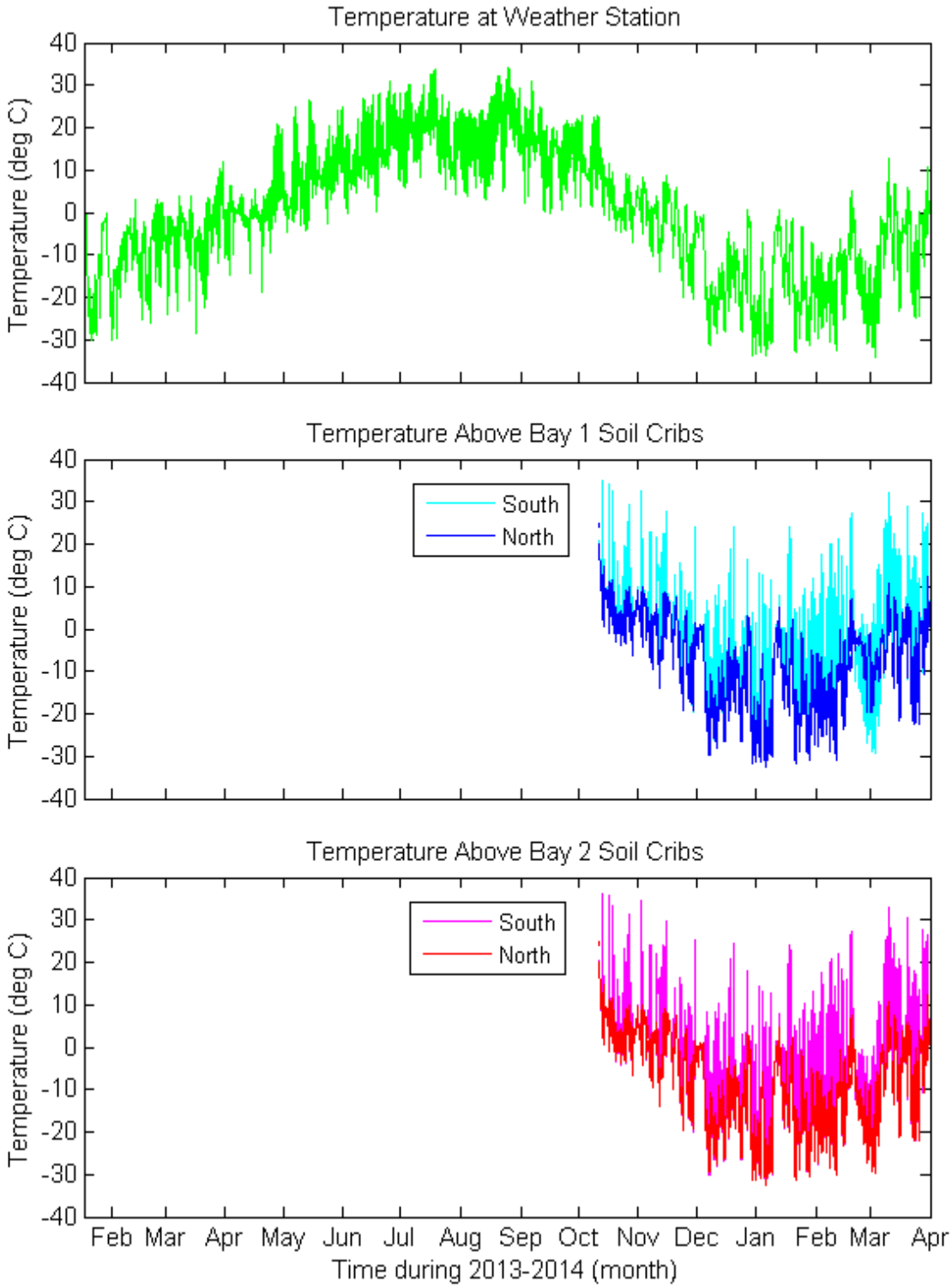

Figure 5-10: Exterior Temperature Boundary Condition

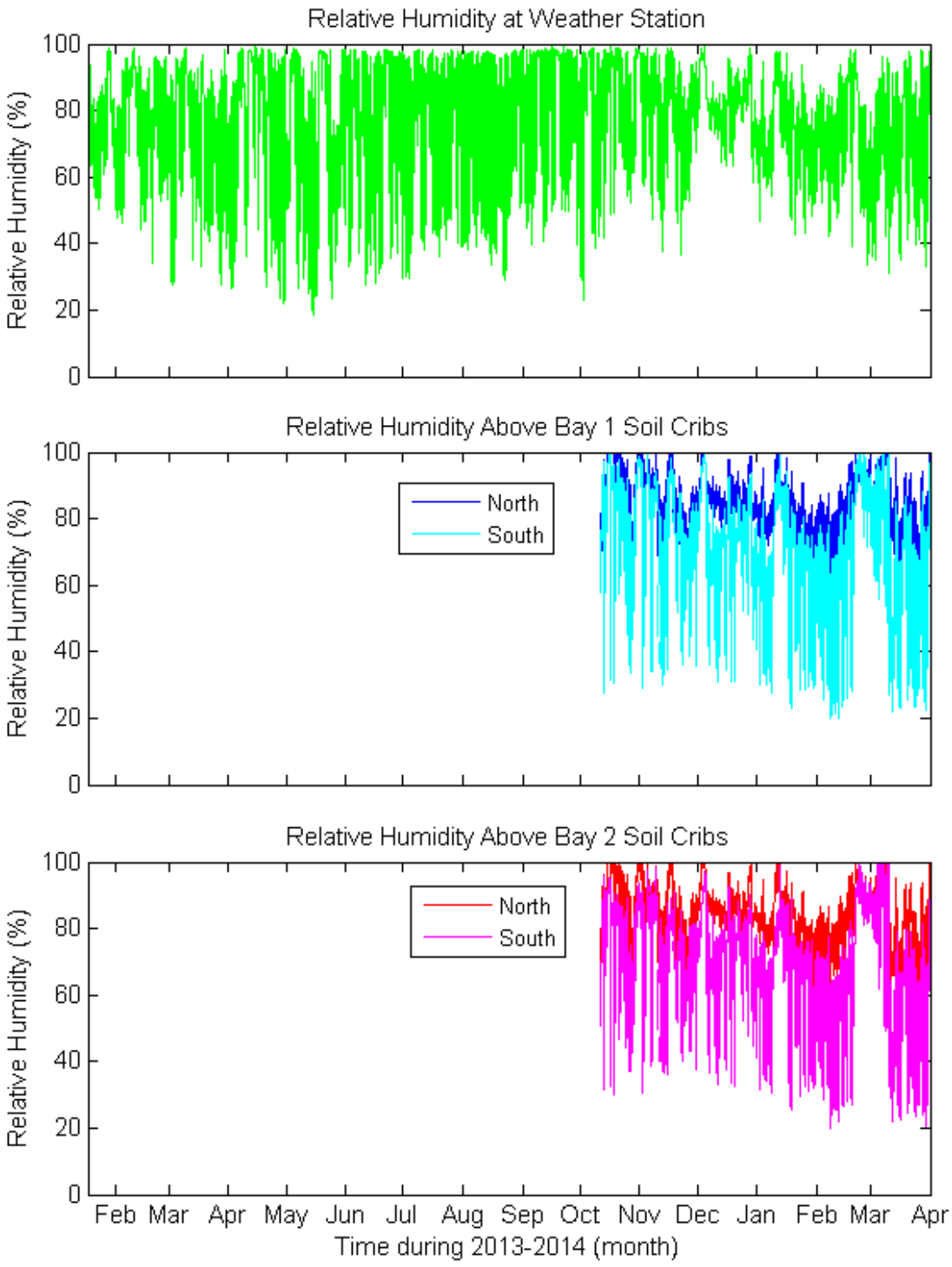

Figure 5-11: Exterior Relative Humidity Boundary Condition

5.2 The Hygrothermal Performance of a Wall with an Interior Water Separation Plane and Partial Exterior Insulation

Bays 2 and 4 both had a full-height adhered WSP on the interior face of the CMU wall. Bay 2 had full-height interior rigid insulation fitted tightly to the interior face of the WSP, whereas Bay 4 had four feet of rigid insulation installed on the upper half of the exterior face of the wall. When data collection began for Bay 2, the entire wall system was in place (WSP and insulation). Data collection began for Bay 4 on January 18, 2013 after the WSP was installed, but prior to the installation of the exterior insulation. The Bay 4 insulation was installed on May 31, 2013. For both bays there was a solid grouted bond beam block at the top of the wall and solid grouting in at least the first course above the slab. Sensors at 5.5 in. and 86 in. above the slab were at a grouted portion of the wall and sensors at 16 in., 40 in., 69 in., and 79 in. were at a hollow core portion of the wall.

Figure 5-12 shows that from January 2013 to May 2013, Bay 4S had core relative humidities lower than and core temperatures higher than Bay 2S across all heights of the wall. However, from mid-November 2013 to March 2014, the relationship between the Bay 4S and Bay 2S relative humidities reversed, such that Bay 4S core relative humidities were higher than those of Bay 2S. The relationship between the Bay 4S and Bay 2S core temperatures remained unchanged (Bay 4S was higher than Bay 2S) between the two time periods. From mid-June 2013 to mid-October 2013, at wall heights 40 in. above the slab or greater, the core relative humidities in Bay 4S were higher than in Bay 2S and the core temperatures in Bay 4S were lower than in Bay 2S. For the same time period at 16 in. above the slab, the Bay 4S and Bay 2S relative humidities and temperatures were approximately the same.

Since relative humidity is dependent on temperature and warmer air can hold more moisture, it was expected that the warmer hollow core CMU wall would have a lower relative humidity. This relationship held true from January 2013 to mid-October 2013, but from mid-November 2013 to March 2014, after the installation of the exterior insulation on Bay 4, this relationship was not true (Figure 5-12). The exterior insulation present during the second heating season yielded warmer and more constant core temperatures at 69 and 79 in. above the slab compared with the first heating season

temperatures without exterior insulation. Therefore, adding the exterior insulation produced an additional and unexpected effect.

To further investigate this anomaly, the core vapor pressures and humidity ratios were reviewed (Figure 5-13). Figure 5-13 shows that the Bay 4S core vapor pressures and humidity ratios were both greater than Bay 2S from January 2013 to May 2013 and mid-October 2013 to April 2014 and both were less than Bay 2S at heights 40 in. and greater above the slab from mid-June 2013 to October 2013. At 16 in. above the slab for this latter period, the core vapor pressures and humidity ratios in Bay 4S and Bay 2S were approximately equal.

Comparing the first and second heating seasons, the vapor pressures and humidity ratios for Bay 2S were approximately equal, but the Bay 4S values were not. Across all heights, the Bay 4S core vapor pressures increased by approximately 450 Pa and the humidity ratios increased approximately 0.003 kg/kg from the first heating season to the second heating season. From June 2013 to March 2014 (when Bay 4S was insulated) the maximum variation in hollow core moisture was approximately 0.014 kg/kg for Bay 4S and larger (approximately 0.023 kg/kg) for Bay 2S.

To understand the Bay 2S and Bay 4S hollow core moisture profiles, they must be discussed in the context of their construction. Both bays had an interior adhered WSP with a maximum permeance of 0.05 perms (Carlisle Coatings & Waterproofing 2013), which severely limited moisture transport between the cores and the basement. The rigid insulation used on both bays had a permeance of 0.5 perms (Dow 2014). The insulation on Bay 2S was located on the interior face of the WSP; therefore it had no additional effect on the core moisture beyond that provided by the WSP. On Bay 4S, the insulation was located on the upper four feet of the exterior face of the CMU wall, thus reducing the moisture transport between the core and the exterior. The exterior insulation on Bay 4S reduced the moisture gain in the cores during the spring and summer months, but it also reduced the drying potential of the cores during the fall and winter months. Thus, the Bay 4S hollow cores had more moisture during the winter months. The approximately uniform vapor pressure across the height of the hollow core caused the moisture in the core to be relatively uniformly mixed. For this reason, the

elevated moisture in Bay 4S over Bay 2S was evident at all heights, not just those with exterior insulation (69 in. and 79 in. above the slab).

To further verify that the exterior insulation was preventing the CMU wall from drying during the fall and winter months, the CMU moisture contents were studied. Figure 5-14 graphs the interior and exterior face shell moisture contents of Bays 2S and 4S at 5.5 in., 40 in., 69 in., and 86 in. above the slab. Limited data is available for the exterior moisture content sensors at 5.5 in., 40 in., and 69 in. above the slab on Bay 2S and the exterior moisture content sensors on Bay 4S at 5.5 in. and 40 in. above the slab because they failed (the sensor failures are discussed in greater detail in Chapter 5.5.2).

Across all heights for both Bays 2S and 4S, the interior face shell moisture content was relatively low (< 17% saturation) and maintained a fairly constant moisture content over the graphing period. At 86 in. above the slab, the exterior face shells for Bays 2S and 4S were dry (< 17% saturation) and had little variability ($\pm$ approximately 1.5% vol. MC) over the time frame.

The interior face shell moisture content remained relatively low for both Bays 2S and 4S. This occurred because the interior WSP prevented condensation from forming on the interior side of the face shell and the higher temperature of the face shell reduced the condensation potential on the core side of the face shell. At 86 in. above the slab, the exterior face shells on both bays maintained a relatively constant moisture content throughout the year. These sensors were located on solid grouted cores that were not significantly impacted by the moisture in the hollow cores. Further, they were above grade where they were not in direct and continuous contact with soil moisture.

There were insufficient CMU exterior face shell moisture content data at 5.5 in., 40 in., and 69 in. above the slab for Bays 2S and 4S for a full analysis. For walls with an interior WSP and well-drained soil, it is hypothesized that the exterior face shell moisture contents behind exterior insulation (Bay 4S) would be higher than the exterior face shell moisture content on walls with interior insulation (Bay 2S) because the exterior insulation reduces the drying potential of the wall. This is the case from mid-June 2013 to mid-September 2013 when the sensors at 69 in. above the slab for Bays 2S and 4S were both available (Figure 5-14). In the case of half-height exterior

insulation, at locations below the exterior insulation, it is expected that the exterior face shell moisture contents would be similar to that of an interior insulated wall. Additional research is required to test this hypothesis.

The previous discussion compared the south exposures of Bays 2 and 4. Similar behavior occurred on the north bays and these figures can be found in Chapter 6. During the heating seasons, the Bay 4N core temperatures were greater than the Bay 2N core temperatures across all heights of the wall (Figure A-1). Bay 4N core temperatures were warmer than Bay 2N because Bay 4N was not insulated on the interior face of the wall, so the core temperatures were closer to that of the basement. Also, the hollow core relative humidities on the north were greater for Bay 2 than for Bay 4 at all heights from January 2013 to May 2013 (Figure A-1). From December 2013 to mid-February 2014 at 5.5 in., 40 in., and 69 in. above the slab, Bay 4N core relative humidities were greater than Bay 2N. Between the first and second heating seasons, the Bay 4N hollow core humidity ratios and vapor pressures increased across all heights, whereas Bay 2N's did not (Figure A-2). Similar to the south exposure, the core relative humidities, humidity ratios, and vapor pressures for the north exposure increased between heating seasons when exterior insulation was added. The CMU wall moisture content sensors exposed to wet conditions on the north also failed and provided limited data for analysis (Figure A-3).

From January 2013 to October 2013 the hollow core temperatures at 79 in. above the slab in Bays 2 and 4 had greater diurnal temperature variation on the south exposure than on the north exposure (Figure 5-12 and Figure A-1). The hollow core temperatures and humidity ratios were greater for Bay 2S than for 2N from June 2013 to November 2013 at 40 in., 69 in., and 86 in. above the slab (Figure 5-13 and Figure A-2). For the same time period they were approximately equal for Bays 4N and 4S. From December 2013 to mid-March 2013 the hollow core temperatures and humidity ratios were approximately equal for north and south exposures in Bays 2 and 4.

During the cooling season for Bay 2, the solar exposure at the top of the CMU wall on the south increased the core temperatures and humidity ratios over those on the north. This resulted in a decreased core relative humidity (Figure 5-12). In Bay 4, the core temperatures, humidity ratios, and relative humidities were approximately the same

between the north and south exposures because the exterior insulation damped the solar effects on the south side (Figure A-1 and Figure A-2). During the second heating season, the hollow core temperatures and humidity ratios were approximately the same between north and south exposures. This was because the snow pack shielded the above-grade portion of the basement wall from solar effects. In general, when the above-grade portion of the basement wall was exposed, the solar effects on the south increased the core temperatures and humidity ratios over those on the north, but when the above-grade potion of the wall was shielded by insulation or snow, there was little difference between north and south exposures.

In conclusion, placing vapor retarding materials on the interior and exterior faces of a below grade wall reduces the wetting and drying potential of the wall. This reduction occurs even when the exterior vapor retarder (in this case, 3 in. thick XPS insulation) only covers the upper half of the wall. An interior full-height WSP significantly reduces the moisture transport from the soil and wall into the basement, but it also prevents the wall from drying to the interior. This means the only way the wall can dry is to the exterior. The greatest drying potential to the exterior is the portion of the wall above the grade because the vapor drive between the hollow core and outdoor air is greater than between the hollow core and the moist soil. For this reason, a vapor barrier on the exterior face of the wall that covers at a minimum the upper half of the wall significantly reduces the drying potential of the wall. Although the exterior vapor barrier reduces the wetting potential of the wall from soil and ambient moisture, the benefits do not outweigh the negative effects of significantly reducing the potential of the wall to dry. When the wall is unable to dry, it can lead to elevated wall moisture contents that have the potential to cause freeze/thaw damage to the wall, rotting of the sill plate, and/or delamination of the interior WSP. It is therefore essential that the wall be able to dry to the interior or the exterior at a minimum and that a low permeance vapor retarder should not be placed on both faces of a CMU below-grade wall. Preferably, an exterior WSP would be coupled with exterior insulation and an interior WSP would be coupled with interior insulation. One wetting and one drying cycle are shown in the data, however multi-cycle data would be valuable to see if there is a long-term net accumulation of moisture in a wall with interior and exterior vapor retarders.

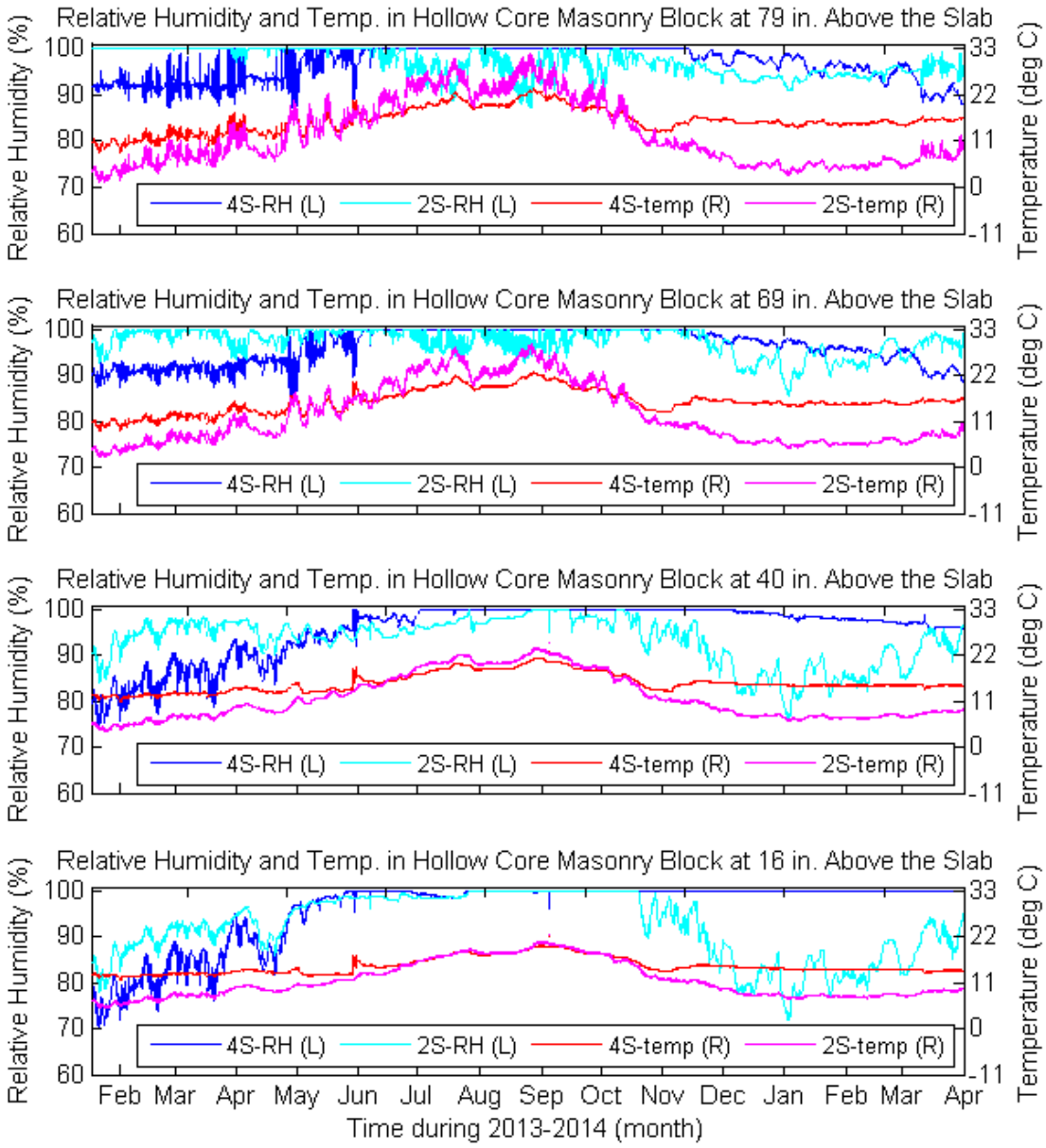

Figure 5-12: Comparison of Hollow Core CMU Wall Relative Humidities and Temperatures in Bay 2 (Full-Height Interior Insulation) and Bay 4 (Half-Height Exterior Insulation) with South Exposure

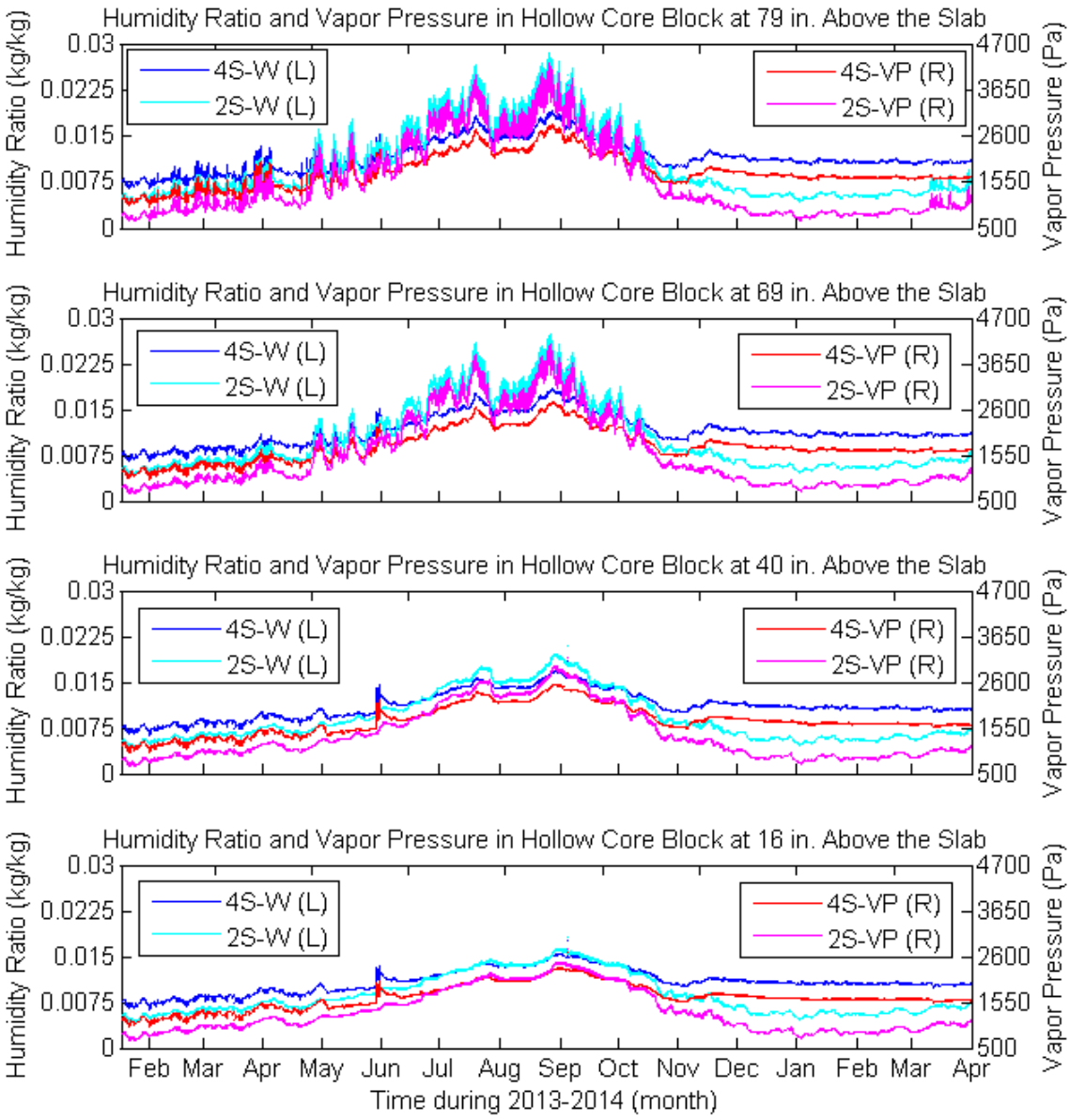

Figure 5-13: Comparison of Hollow Core CMU Wall Humidity Ratios and Vapor Pressures in Bay 2 (Full-Height Interior Insulation) and Bay 4 (Half-Height Exterior Insulation) with South Exposure

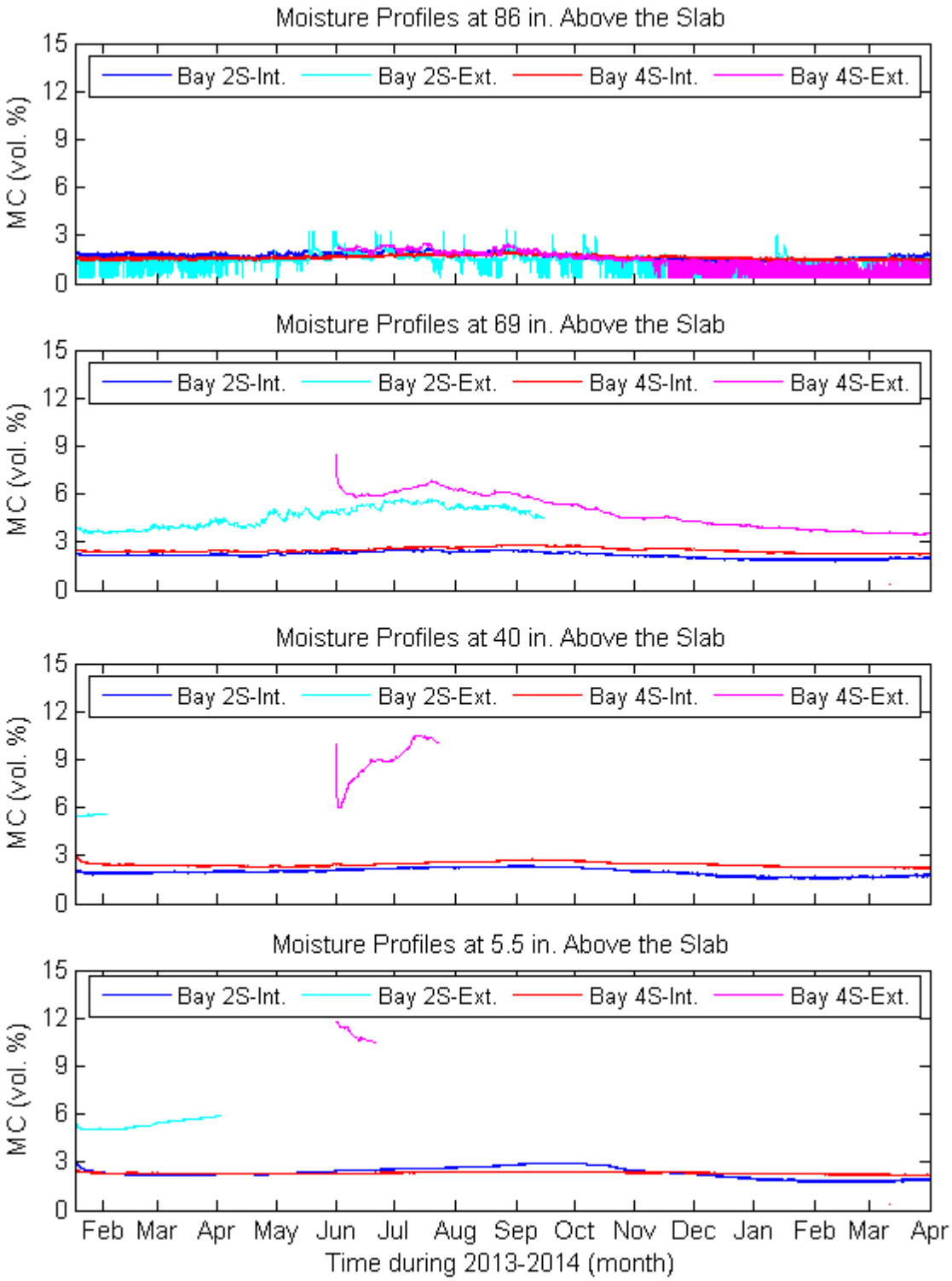

Figure 5-14: Comparison of Interior and Exterior CMU Face Shell Moisture Contents in Bay 2 (Full-Height Interior Insulation) and Bay 4 (Half-Height Exterior Insulation) with South Exposure

5.3 The Impact of the Ground Water Table on Foundation Wall Heat Transfer

Figure 5-16 and Figure 5-17 show the temperatures at 5.5 in. above the slab on the interior and exterior face shells of the CMU wall and in the soil 5 in. from the face of the CMU wall for Bays 1, 2, and 3 on the north and south sides, respectively. Data collection for the exterior face shell and soil temperature sensors began on June 6, 2013 for Bay 3. The exterior face shell temperature sensor in Bay 3S at 5.5 in. above the slab failed on September 8, 2013. In Bays 1 and 2 at 5.5 in. above the slab, for the north and south exposure, the soil temperature was warmer than the exterior face of the wall throughout the year (Figure 5-16 and Figure 5-17). This phenomenon also was true for the soil sensors 40 in. and 69 in. above the slab and 5 in. from the face of the wall in Bay 1S (Figure B-1 and Figure B-2), Bay 2S (Figure B-3 and Figure B-4) and 2N (Figure 5-22 and Figure 5-31). In Bay 3N the soil temperature approximately 5.5 in. above the top of the slab and 5 in. from the face of the wall was approximately the same temperature as the exterior face of the wall during the heating season and during the cooling season the soil was warmer than the exterior face of the wall (Figure 5-16 and Figure 5-17). The phenomenon held true for Bay 3N at 40 in. above the slab, but at 69 in. above the slab during the heating season the exterior face shell was warmer than the soil and during the cooling season the exterior face shell and soil were approximately at the same temperature (Figure B-5 and Figure B-6). The same graphs also show that for all heights, the interior masonry face shell was warmer than the exterior face shell during the heating season and at approximately the same temperature during the cooling season. Bay 3S was not reviewed because the exterior face shell sensors at 5.5 in. and 40 in. above the slab failed. Bay 4 was not included because only one soil sensor was installed at 69 in. above the slab and there was exterior insulation instead of interior insulation, so a comparison of the exterior face shell and soil temperatures was not relevant for this analysis.

The bottom two courses of the CMU wall were presumed to be filled with mortar and/or grout that fell during construction (Chapter 3.2.1). However, this was only confirmed on one wall. The filled cores likely had air pockets as the grouting was not intentional and therefore were not thermally equivalent to a core that was intentionally grouted solid.

The temperature sensors at approximately 5.5 in. above the top of the slab were located on this upper 'grout-filled' course, 6 in. down from its top. Throughout the year, the interior basement temperature (Figure 5-1) was greater than the masonry wall and soil temperatures at 5.5 in. above the slab (Figure 5-16 and Figure 5-17) such that heat transfer was always out of the basement at this height. Due to the likely grouting, thermal conduction was probably the primary heat transfer mechanism through the wall at this location. With conductive heat transfer, it would be expected that the interior face shell, exterior face shell, and soil temperature would decrease in temperature from interior to exterior. However, the soil temperature does not fit this pattern. Following the assumption that the bottom cores were partially filled with grout, it was concluded that there must be another heat transfer mechanism or another heat source.

The other potential heat transfer mechanism was buoyant cavity flow. The walls were hollow masonry block with solid vertical grouted cores at 48 in. o.c. For all bays, except Bay 3N, the sensors were located at a hollow core (Figure 3-3 and Figure 3-4). Figure 5-28 provides a diagram of buoyant cavity flow in a hollow CMU wall during the heating season in a cold climate. During the heating season, a cavity flow loop in the hollow core had the potential to reduce the hollow core temperature below the temperature of the grouted core located just below the open core. If this occurred, there would be conductive heat transfer from the grouted core into the open core, reducing the exterior face shell temperatures at 5.5 in. above the slab (located on the grouted core) with a reduced effect on the adjacent soil temperature. This potentially explained the phenomenon of the relatively warmer soil temperature during the winter months (i.e. the exterior wall surface temperature was depressed).

During the cooling season, the soil temperatures may have been elevated above the wall temperatures due to heat transfer from the ground surface. Figure 5-18 shows the soil temperature profiles at 5.5 in., 40 in., and 69 in. above the slab for Bays 1N and 2N along with the ambient temperature. From June 2013 to September 2013 the soil temperature at 69 in. above the slab was the warmest with the temperature decreasing through the depth of the soil. This temperature gradient resulted in heat transfer from the surface to the deep ground, thus potentially elevating the soil temperature above the temperature of the wall during the cooling season.

In Bays 3S and 3N, the wall was fitted with 3 in. of XPS insulation on the interior face that extended from 1½ in. above the slab to the top of the 1½ in. thick rigid sill insulation that, in turn, extended all the way across the top of the wall (Chapter 3.2.2). Therefore, the principal heat loss path through the wall from the interior was at the bottom of the wall through the concrete slab where there was no insulation (Figure 3-9). To further investigate the elevated soil temperatures, 3 in. of extruded polystyrene (XPS) insulation was placed on top of the slab from December 13, 2013 until January 22, 2014. The insulation was centered on the bay and extended approximately 4 ft. to either side of the measurement plane along the length of the wall and 5 ft. into the basement (Figure 5-15). It was expected that adding the floor insulation would decrease the heat loss through the slab and bottom of wall and thus cause a decrease in the CMU wall and soil temperatures, most notably at 5.5 in. above the slab.

Figure 5-15: Bay 3 Temporary Floor Insulation

However, there was no change in the temperature temporal gradients of the wall face shells or soil when the insulation was installed or removed. Figure 5-19 shows the face shell and soil temperatures at 5.5 in. and 40 in. above the slab for Bay 3N when insulation was on the floor with an additional 12 days prior to and 24 days after insulation placement. A comparison of Bay 3N, with floor insulation, to Bay 2N, without floor insulation, shows that the temperature trends for the two bays were the same

(Figure 5-20). Bay 3S also showed no change in temperature due to the floor insulation (Figure B-7 and Figure B-8).

The basement was 18 ft. wide between the north and south interior wall faces. The 5 ft. of floor insulation on each side of the basement left 8 ft. of uninsulated slab at the center of the basement. The uninsulated slab heat loss at the center of the basement was less than the uninsulated slab heat loss at the perimeter of the basement because the temperature gradient was smaller at the center. The center temperature gradient was smaller because the sub-slab soil had been conditioned by the basement during the building's life and because the center of the slab was further from the effects of the outdoor ambient conditions. Despite this center uninsulated slab heat loss, the 5 ft. of perimeter insulation should have been sufficient to at least see a change in wall and soil temperatures if slab heat loss was the dominant heat source. Since the floor insulation had no impact on the measured wall and soil temperatures as would be expected if the slab heat loss was the primary heat source, it was concluded that heat loss through the slab at the bottom of the wall was not the primary heat source influencing the wall and soil temperatures. Instead, there had to be another heat source.

It was hypothesized that a high ground water table could act as a heat sink during the cooling season and a heat source in the winter. The U.S. Environmental Protection Agency reports the average shallow ground water temperature in this part of the country at 39 deg. F (3.9 deg. C) (2013). During the cooling season, heat was potentially transferred to and stored in the ground water table by:

- Ambient flow from the swamp to the east (Figure 5-21);
- The septic field located on the north side of the building for treatment and dispersal of septic tank effluent (Appendix D);
- The basement (interior temperature approximately 15 to 21 deg. C); and,
- The ground surface (average ambient temperature approximately 10 to 25 deg. C).

The soil temperatures at 5.5 in. above the slab between the north and south exposures of like bays were approximately the same (Figure 5-16 and Figure 5-17). Further, the soil temperatures at 5.5 in. above the slab between bays with like exposure did not consistently increase or decrease from east to west (Figure 5-16 and Figure 5-17).

The similar soil temperatures between the north and south exposures on like bays indicates that there was negligible ground water flow perpendicular to the building (north-south axis) and the inconsistent soil temperatures across the bays for a given exposure demonstrates that there was negligible flow parallel to the building (east-west). If there was significant flow in the water table, heat transferred from the basement to the water table below or from an adjacent source (e.g. septic field, swamp) would have then flowed horizontal and disproportionally affected the soil temperatures surrounding the building. Soil temperatures would have been greater on one exposure or bay compared with another exposure or bay. As shown by the experimental data, this was not the case. Since the north and south soil temperatures were the same, it follows that any heat from the septic tank effluent did not affect the experimental wall and soil temperatures. Also, since the temperatures across bays with like exposures did not consistently increase or decrease, it proves that any heat from the swamp did not affect the experimental wall and soil temperatures.

To further investigate the water table heat source hypothesis, a topographic map of the area was obtained (Figure 5-21). The map shows that the grade at the building is at an elevation a little higher than a nearby marsh and creek (roughly 10 ft.). This means that the base of the footing which is approximately 7.8 ft. below grade is roughly 2.2 ft. above the surface of the creek. In addition, a soils report was found from August 2000 that was conducted in the immediate vicinity of the building for the onsite wastewater treatment system (Appendix C) located just north of the building. The soils investigation found ground water at 109 in. below the top of grade approximately 160 ft. north of the building. If the ground water table was at a constant height, based on the boring location having a soil surface approximately 2 in. below that of the building, the ground water was approximately 13 in. below the bottom of the building footing (approximately 29.5 in. below the top of the building slab). At another boring location, approximately 60 ft. to the east of the building, the soils indicated that saturated conditions existed in the recent past as high as 72 in. below grade. If the boring was indicative of conditions at the building, this would translate to saturated soils at approximately 22 in. above the bottom of the footing (approximately 5.5 in. above the top of the building slab). Further, in June 2012, after a period of prolonged rain, the basement of the CRRF was flooded to a height approximately 9 in. above the slab. Together, these factors reinforce the likelihood of a high water table at the building site.

Although buoyant cavity flow during the heating season and heat transfer from the ground surface during the cooling season may contribute to the elevated soil temperatures in relation to the wall, the most significant factor is likely a high ground water table. The floor insulation experiment demonstrated an unmeasurable effect on the soil and wall temperatures, so adding credibility to this hypothesis. Archived soils reports, topographic maps, and previous flooding provide additional support.

The experimental results reinforce the conclusion drawn by Deru and Kirkpatrick (2002b) using a numerical model that the ground water depth has a significant impact on heat transfer from buildings (Chapter 2.2.2). Calculations (reported in Chapter 6) and simulations (Goldberg and Harmon 2014) were performed to evaluate this hypothesis. In summary, these computations confirmed the validity of the hypothesis.

For elevated ground water tables, the height and temperature typically varies throughout the year. This has a significant impact on the temperature profile of the wall and soil which influences the rate of heat loss from the building. The location and temperature of the ground water table is a significant factor for understanding below grade thermal performance and therefore should be measured in any future experiments.

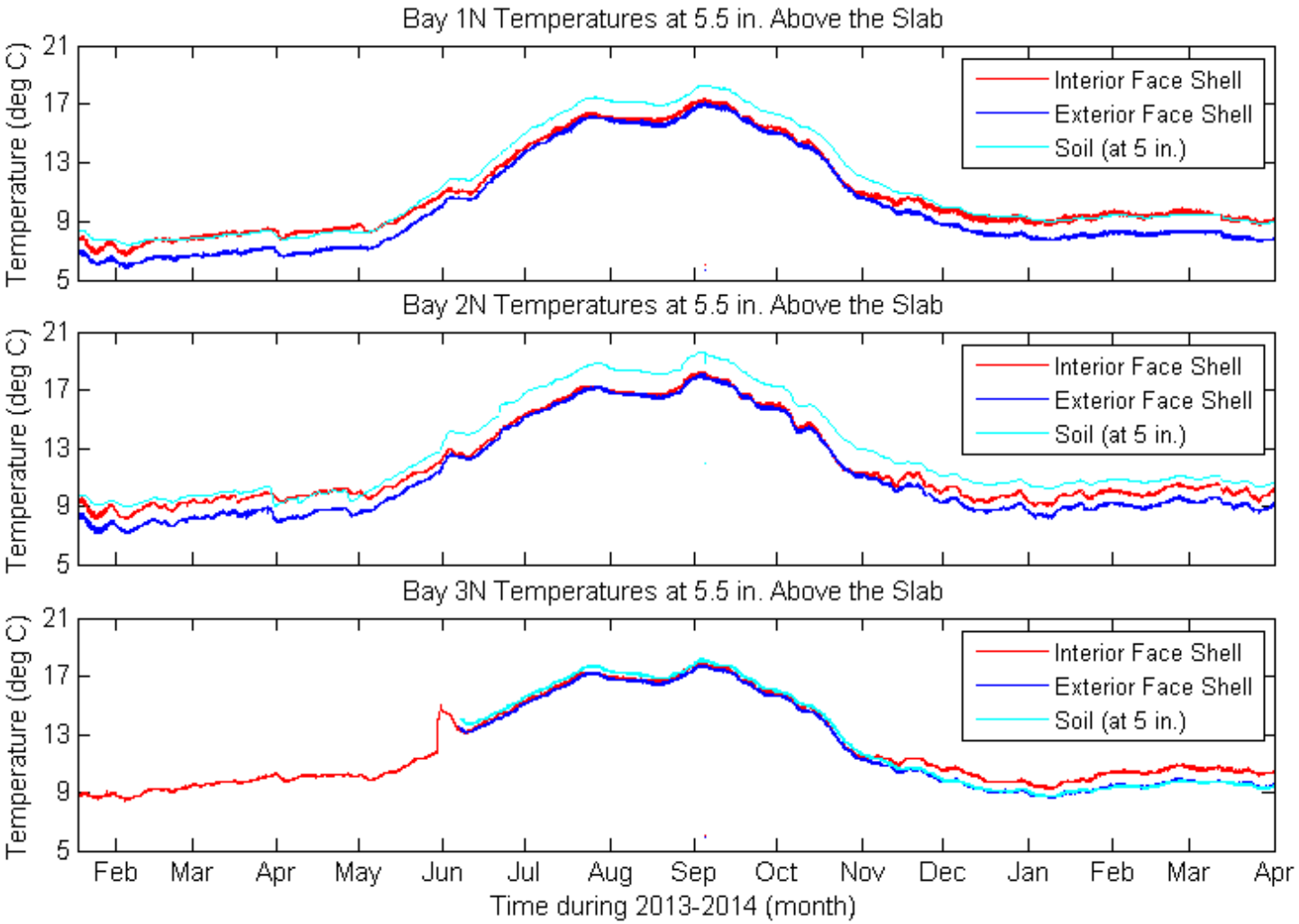

Figure 5-16: Temperature Profile at Base of Wall with North Exposure

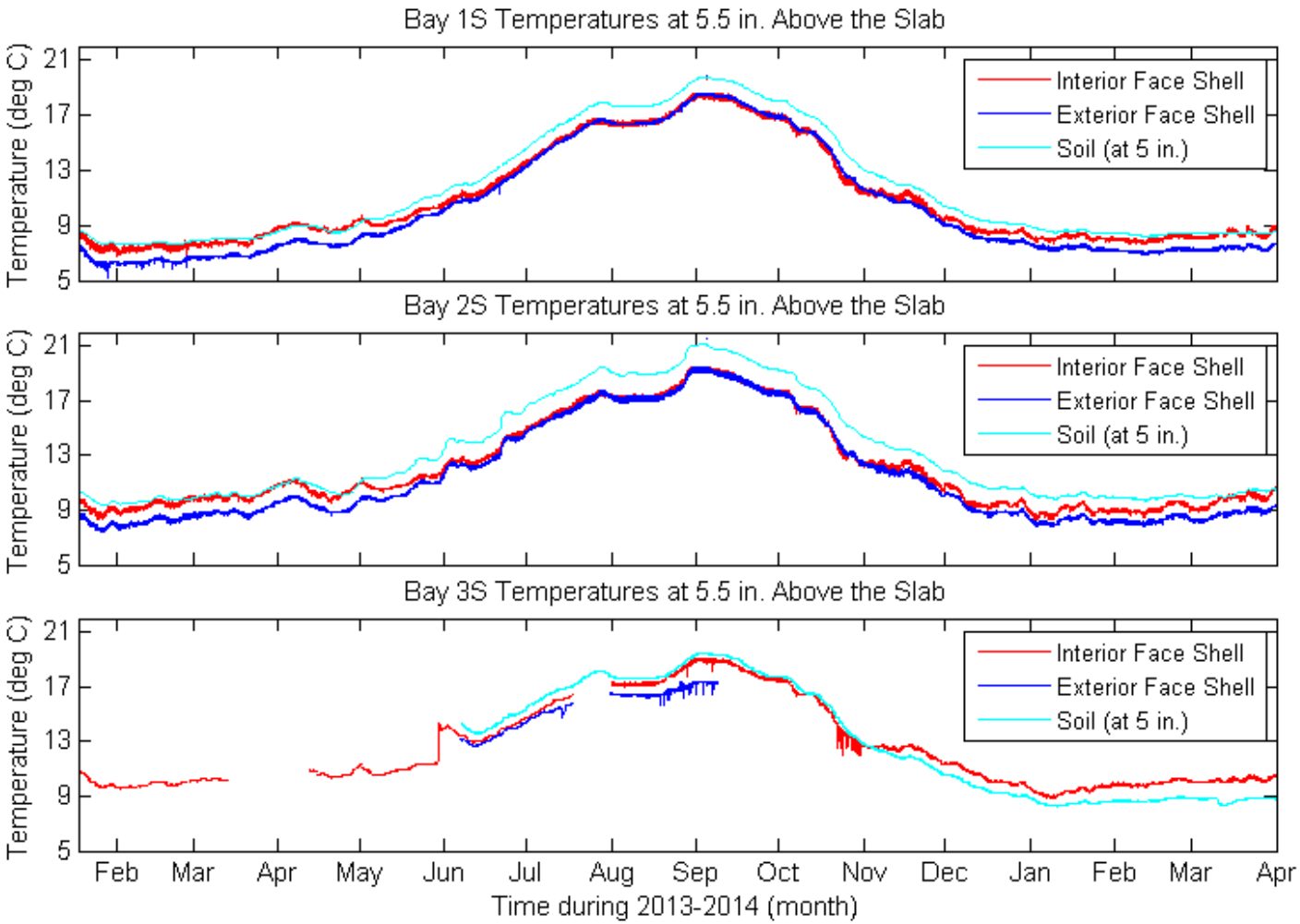

Figure 5-17: Temperature Profile at Base of Wall with South Exposure

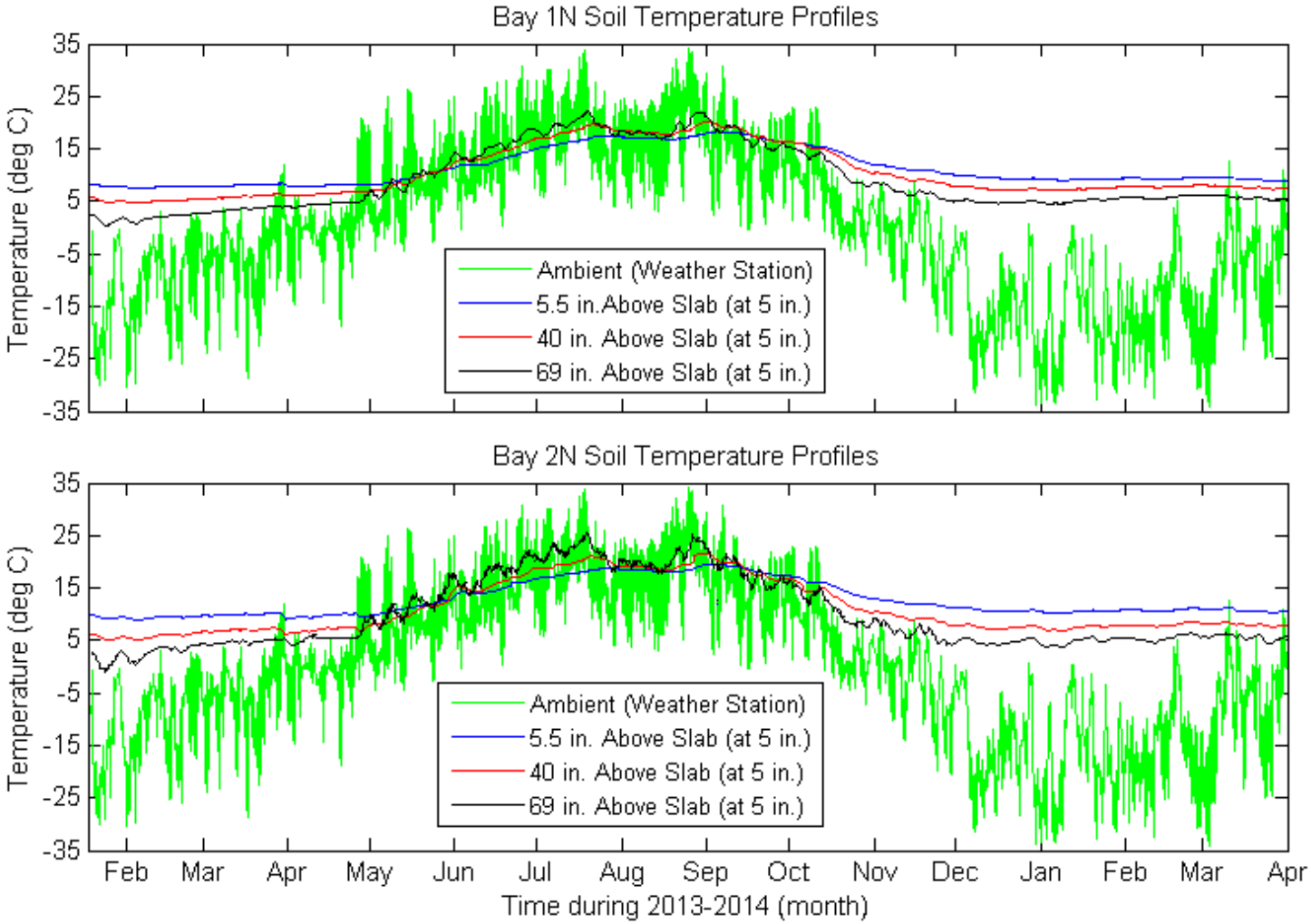

Figure 5-18: Bay 1N and 2N Soil and Ambient Temperature Profiles

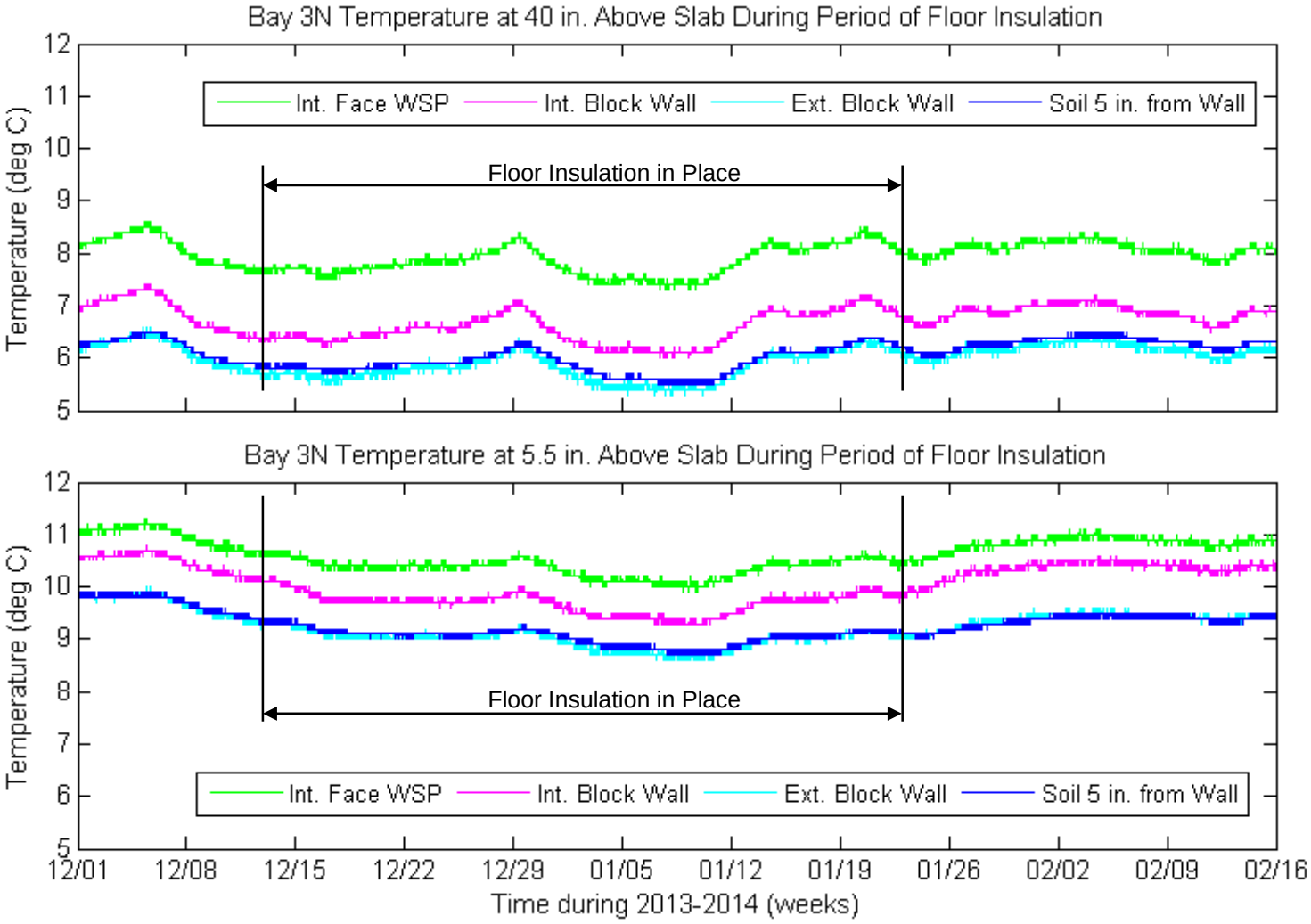

Figure 5-19: Bay 3N with Floor Insulation December 13, 2013 through January 22, 2014

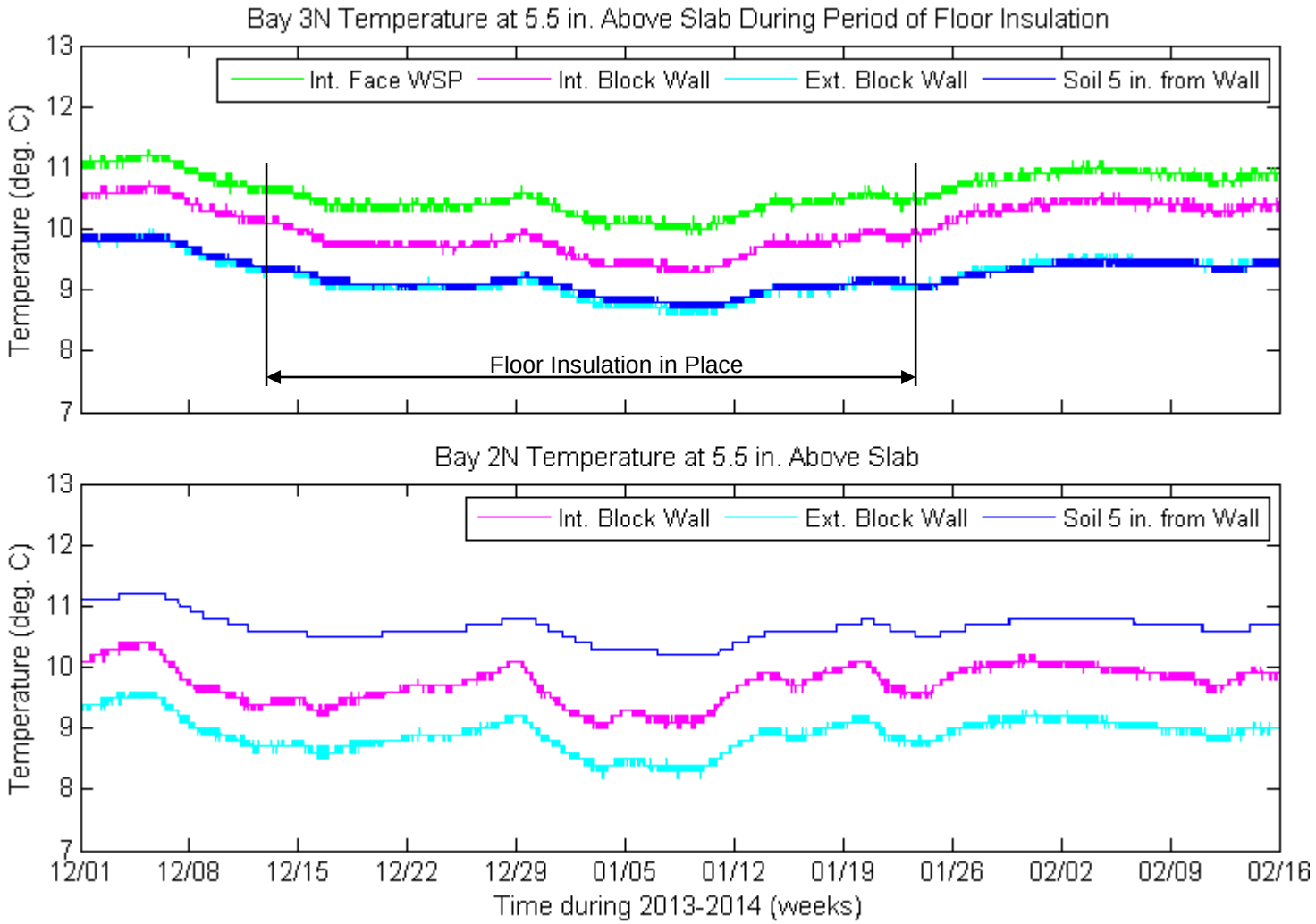

Figure 5-20: Comparison of Bay 3N with Floor Insulation and Bay 2N without Floor Insulation

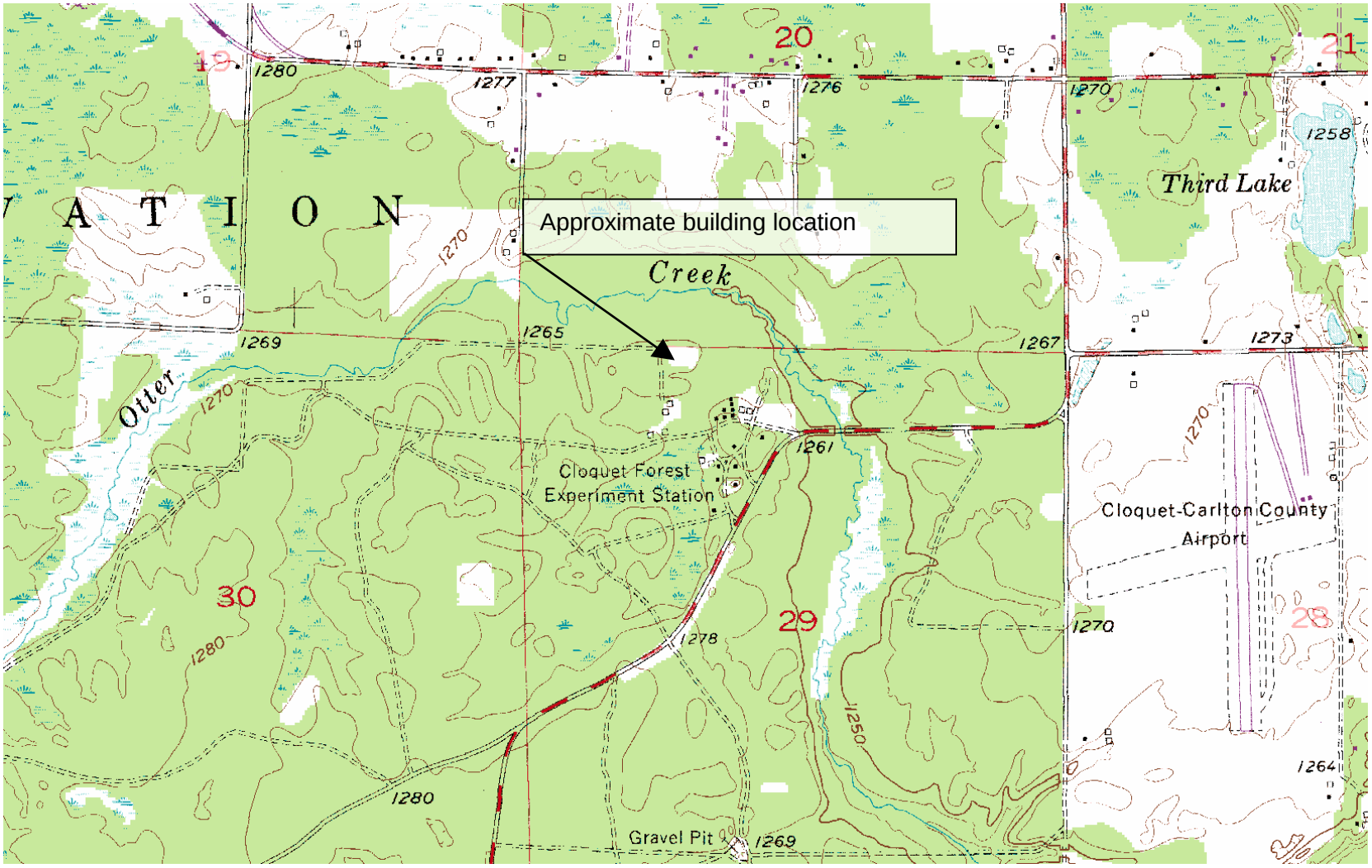

Figure 5-21: Topographic Map of Cloquet Residential Research Facility Building Site (U.S. Geological Survey 1954)

5.4 Buoyant Cavity Flow in Hollow Concrete Masonry Unit Walls

An examination of the temperatures on the interior face shell, hollow masonry core, exterior face shell, and soil 5 in. from the wall provides insight into the dominant thermal transport mechanisms in the wall. The phenomenology of the walls in Bays 1 and 2 was similar and hence only Bay 2N will be discussed in detail. Bay 3N was not included in the analysis because the interior and exterior masonry block face shell temperature sensors were installed on a grouted core and core temperature sensors were installed in the adjacent core (Figure 3-4). Bay 3S was not included in the analysis because the exterior masonry block face shell temperature sensors 5.5 in. and 40 in. above the slab failed on September 8, 2013 and August 11, 2013, respectively. The exterior face shell temperature sensor on Bay 1S, 69 in. above the slab, failed on December 24, 2012 and was replaced on June 6, 2013. Evaluation of horizontal temperature differences across the hollow block wall was limited to sensors 40 in. and 69 in. above the slab, because the wall was grouted solid at the location 86 in. above the slab and likely was mostly filled with grout at 5.5 in. above the slab.

5.4.1 Bay 2N

Figure 5-22 depicts the Bay 2N masonry wall and soil temperatures during the heating seasons for 40 in., 69 in., and 79 in. above the slab. At 69 in. above the slab, from January 2013 to the end of April 2013, the sensors in order of decreasing temperature were the interior face shell, the hollow core, the soil, and then the exterior face shell. During this period at 40 in. above the slab, the interior face shell and soil temperatures were approximately the same, followed by the hollow core, and then exterior face shell. From mid-October 2013 to April 2014, at 69 in. above the slab, the sensors in order of decreasing temperature were the hollow core, the interior face shell, the soil, and then the exterior face shell. At 40 in. above the slab for the same time period, the soil was the warmest, with the hollow core and interior face shell approximately the same, and the exterior face shell the coldest. Figure 5-23 and the lower panel of Figure 5-24 show the masonry block wall and soil temperatures in Bay 2N at 5.5 in, 16 in. and 86 in. above the slab during the heating season.

To better illustrate the temperature relationships, Figure 5-25 shows the differences in temperature between the interior and exterior face shells, the hollow core, and the soil.

A negative temperature difference indicates a decrease in temperature from the interior to the exterior. From January 2013 to June 2013 and mid-October 2013 to April 2014, at 40 in. and 69 in. above the slab, the interior face shell/hollow core and the hollow core/exterior face shell temperature differences were not equal. From December 2013 to April 2014, at 69 in. above the slab, the differences were the most dramatic with an interior face shell/hollow core temperature difference of approximately 0.5 deg. C, a hollow core/exterior face shell temperature difference of approximately -2.5 deg. C, and an exterior face shell/soil temperature difference of approximately 1 deg. C.

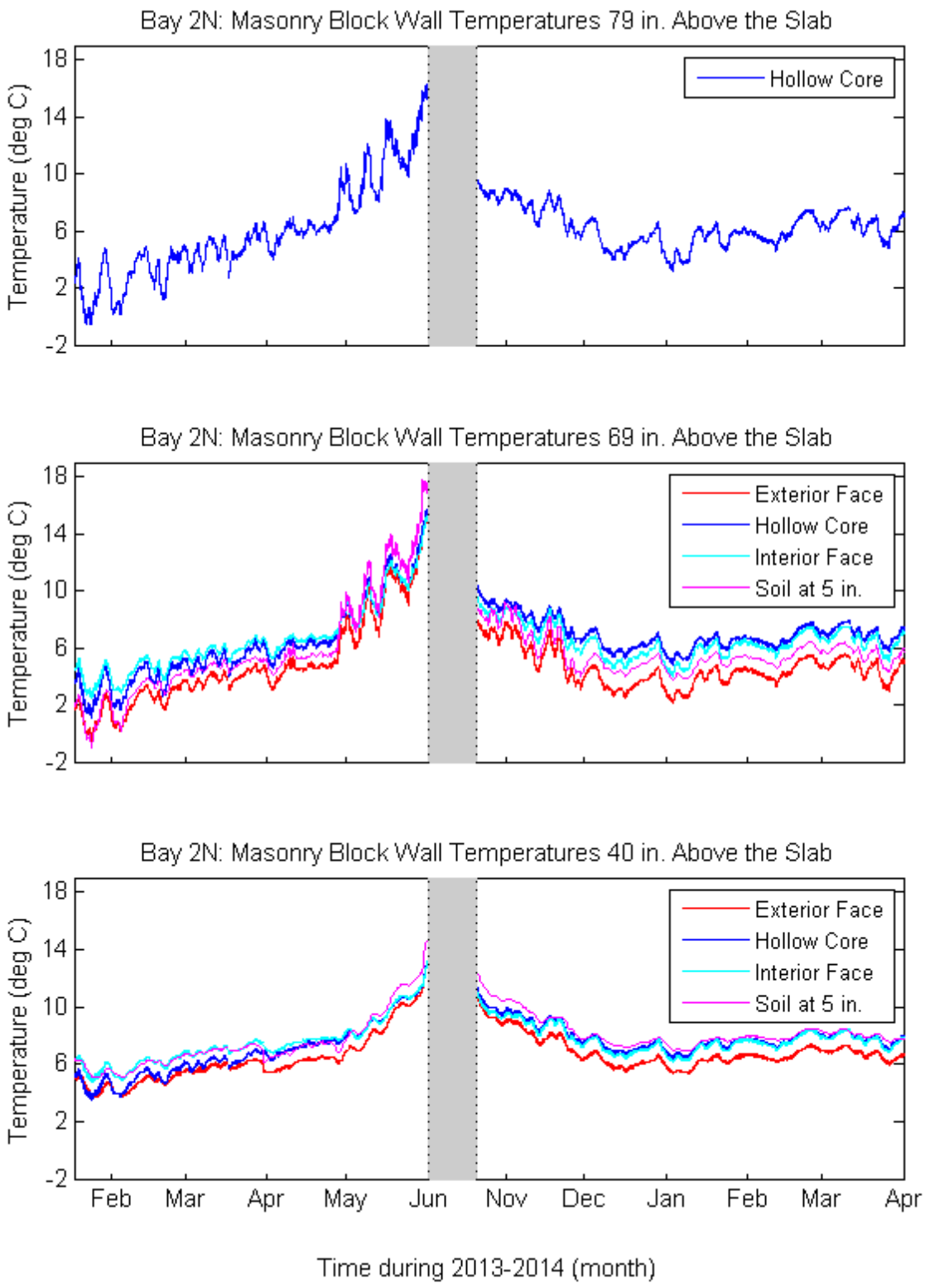

Figure 5-22: Bay 2N Masonry Block Wall and Soil Temperatures during Heating Season at Upper Heights of Wall

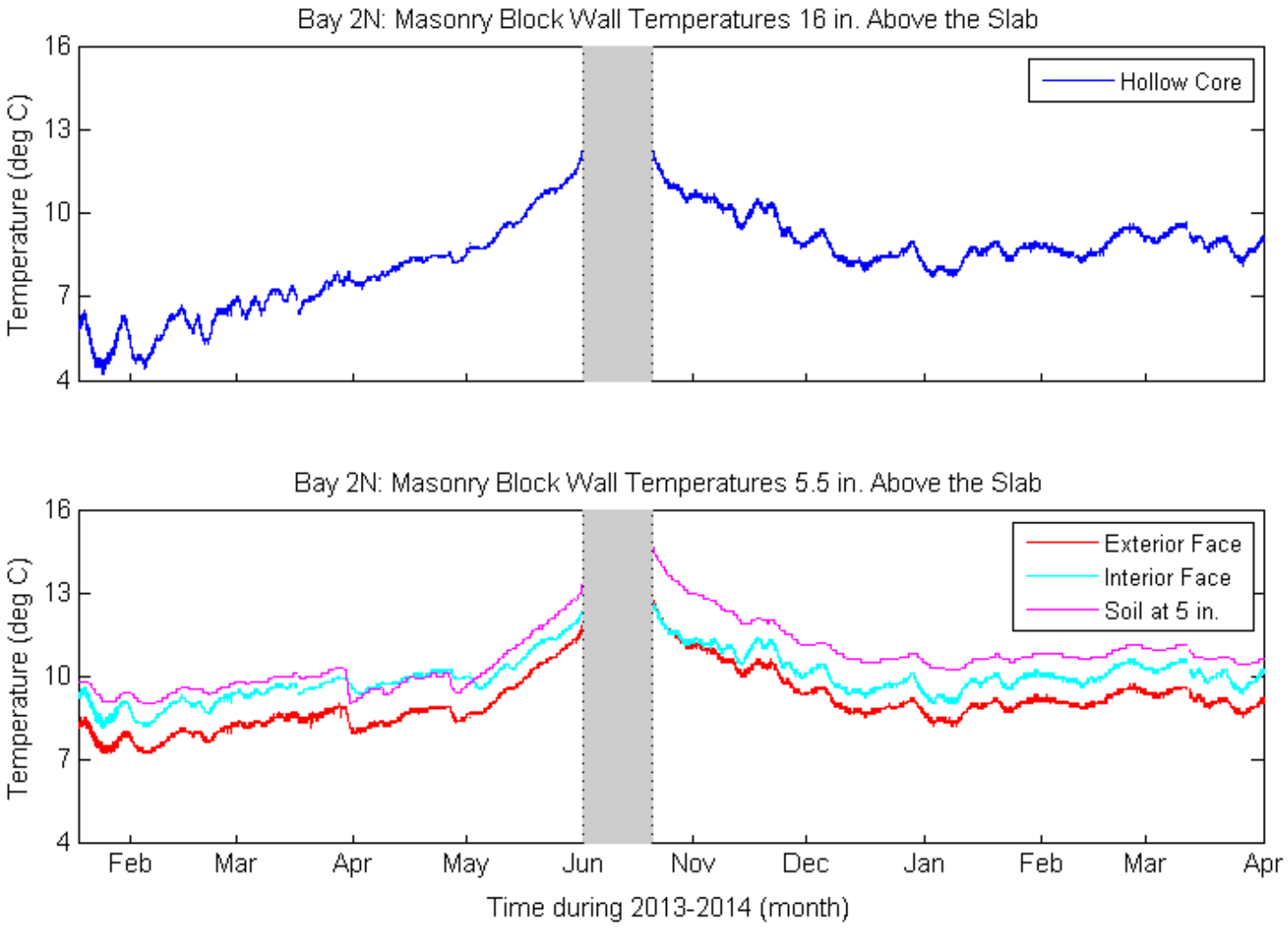

Figure 5-23: Bay 2N Masonry Block Wall and Soil Temperatures during Heating Season at Lower Heights of Wall

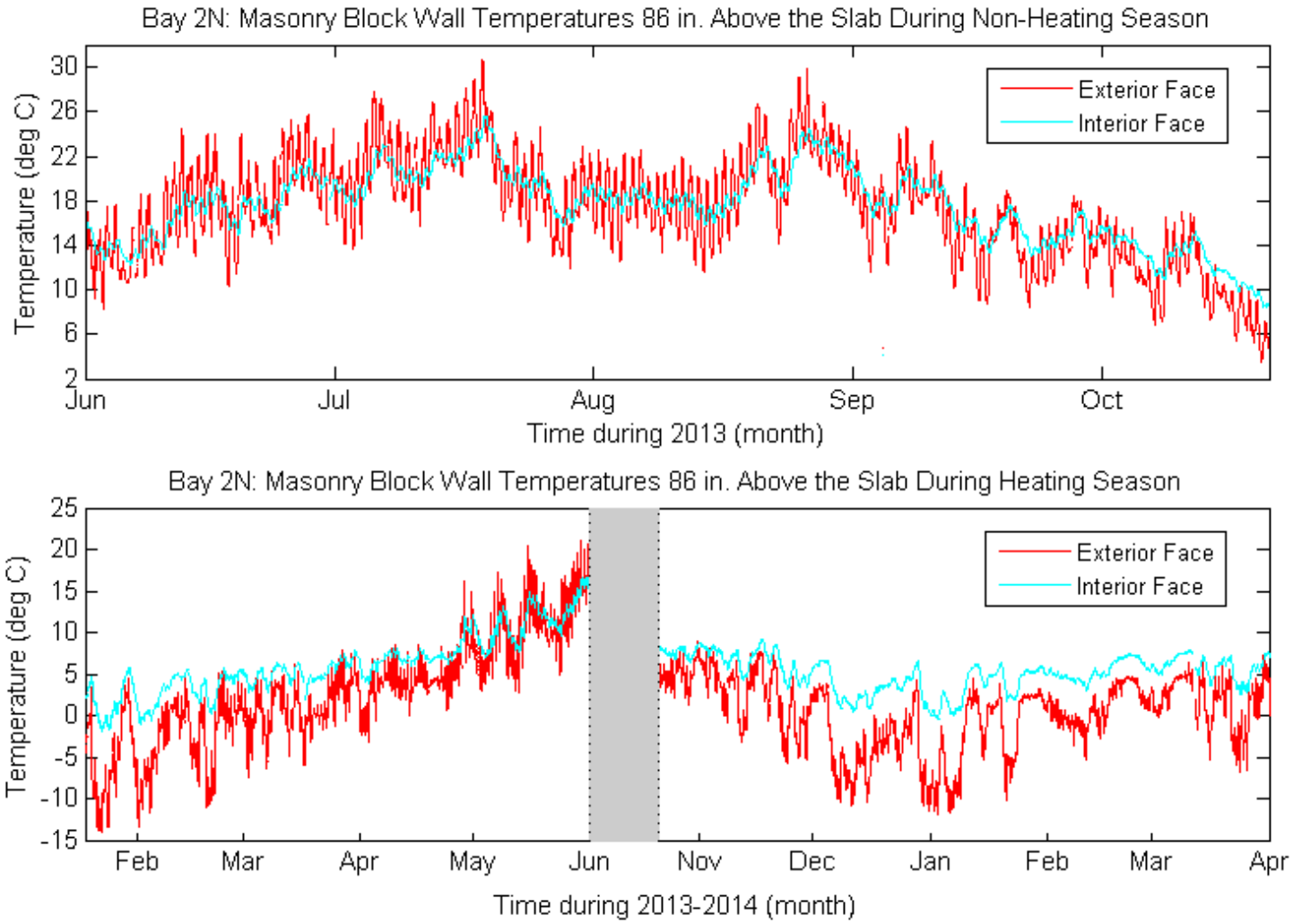

Figure 5-24: Bay 2N Masonry Block Wall Temperatures during Heating and Cooling Season at Top of Wall

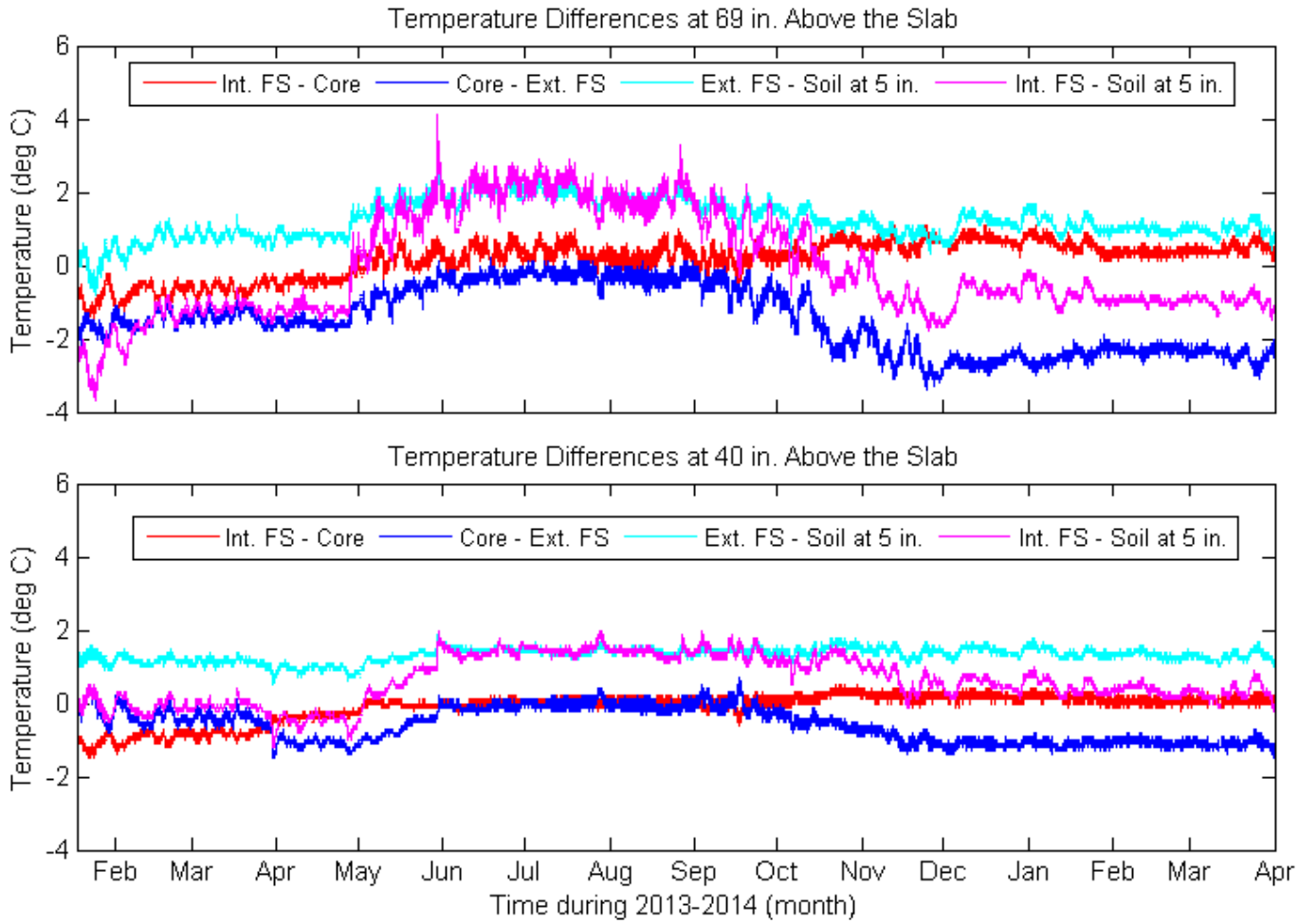

Figure 5-25: Bay 2N Hollow Masonry Block Wall Temperature Differences

If the hollow masonry block cavity was filled with still air such that the primary heat transfer mechanism was conduction, during the heating season the measured temperatures would decrease from the interior masonry face shell to the soil 5 in. from the face of the masonry wall. For pure conduction, all temperature differences in Figure 5-25 would be negative during the heating season. It should be noted that the ground water table effects discussed in the section above (Chapter 5.3) would not affect this behavior. It would only affect the magnitude of the temperature differences because a high ground water table would increase the soil temperatures, thus decreasing the interior to exterior temperature difference. This was not the case for Bay 2N described above. At 40 in. and 69 in. above the slab, during the heating season, the exterior face shell was consistently the coldest part of the system, not the soil. Also, from mid-October 2013 to April 2014 at 69 in. above the slab, the hollow core was the warmest part of the wall system, not the interior face shell.

For pure conduction, the temperature difference between the interior face shell/hollow core and the hollow core/exterior face shell would be approximately equal for the given interior and exterior face shell temperatures. This arises because the thermal resistance between the interior face shell/hollow core and the hollow core/exterior face shell would be almost equal with still air in the hollow cavity. The thermal conductivities would not be exactly equal because the thermal conductivity of air is dependent on temperature and the temperature gradient across the cavity would cause the interior face shell/hollow core and the hollow core/exterior face shell thermal conductivities to differ slightly. Figure 5-25, shows that the temperature differences between the interior face shell/hollow core and the hollow core/exterior face shell were not approximately equal during the heating season.

Figure 5-26 shows the core temperatures across the height of the hollow cavity. From January 2013 to April 2013 and October 2013 to April 2014, the bottom of the hollow wall cavity (16 in. above the slab) was the warmest and the temperature decreased with the height of the cavity, with the coldest temperature at the top (79 in. above the slab). During the same time periods, the interior face shell temperatures for Bay 2N were the warmest at the bottom of the wall (5.5 in. above the slab) and decreased up the wall (Figure 5-27).

Thus these temperature profiles in Bay 2N during the heating season were indicative of buoyant cavity flow. Buoyant cavity flow is the result of density differences in a fluid that exist due to a temperature difference between bounding surfaces. The bounding surfaces warm or cool the adjacent air initially by conduction (where the air is still in the boundary layer) and then by advection, thus causing the warm, less dense air to rise adjacent to the interior face shell, and the cold, denser air to drop adjacent to the exterior face shell, resulting in a cavity air flow loop. In this experiment, buoyant cavity flow was driven by two sets of surface temperatures. The interior face shell / exterior face shell temperature pair was the first set and is referred to as 'side-to-side' flow (Figure 5-29 and Figure 5-30). The second set, referred to as 'top-to-bottom' flow (Figure 5-28), was the top bond beam / bottom CMU with a filled core temperature pair.

During the heating season, the Bay 2N hollow core temperatures were the warmest at the bottom of the cavity and the coldest at the top of the cavity (Figure 5-26). The cold dense air at the top and the warm less dense air at the bottom were a driver for top-to-bottom buoyant cavity flow (Figure 5-28). Also, during the heating season, the interior face shell was warmer than the exterior face shell causing side-to-side buoyant cavity flow (Figure 5-29). Both flows resulted in a cold air plume dropping down the exterior face of the cavity and a warm air plume rising up the interior face of the cavity. As the cold air dropped down the cavity, heat was transferred by convection from the exterior face shell into the dropping air stream. This depressed the exterior face shell temperature as shown in Figure 5-22 and produced an exterior face shell temperature colder than that of the soil measured 5 in. away from the wall.

During the heating season, the temperatures of the interior face shell decreased as the height above the slab increases (Figure 5-27) because the core air temperatures decrease with height (Figure 5-26). Further, the buoyant cavity air plume on the interior face of the hollow core has a velocity that increases with height, so increasing the convective heat transfer between the core and the interior face shell. This further equalized the core and interior face shell temperatures.

In Bay 2N at 69 in. above the slab from mid-October 2013 to April 2014, the hollow core temperature was warmer than the interior face shell. This also is evidence of buoyant cavity flow. The warm air temperatures were advected from the bottom of the hollow

cavity upwards and caused the increase in the hollow core temperature compared to the interior face shell temperature.

The hollow core temperature sensors were located at the mid-width of the hollow cavity. In this experiment, intermediate hollow core temperatures were not obtained, so the cold and warm air plume widths cannot be determined with any precision. Since the face shell temperatures were closely linked to the temperatures of the adjacent air plumes, the interior face shell approximated the warm air plume temperature and the exterior face shell approximated the cold air plume temperature. If the warm and cold air plumes were approximately the same width, the hollow core temperature sensor would read the average temperature of the interior and exterior face shell temperatures. However, if the warm air plume was wider than the cold air plume, the core temperature sensor would read closer to the interior face shell temperature; if the cold air plume was wider than the warm air plume, the core temperature sensor would read closer to the exterior face shell temperature. In Bay 2N from October 2013 to April 2014 at 40 in. and 69 in. above the slab, the warm air plume was wider than the cold air plume as evident by the small temperature difference (0 and 0.5 deg. C, respectively) between the interior face shell/hollow core as compared to the temperature difference between the hollow core/exterior face shell (-2.5 and -1 deg. C, respectively) (Figure 5-25).

For Bay 2N during the cooling season from approximately June 2013 to mid-September 2013, the hollow cavity and interior face shell temperatures were the coldest at the bottom of the cavity and increased up the height of the wall (Figure 5-26 and Figure 5-27). From June 2013 to October 2013, at 40 in. and 69 in. above the slab, the interior face shell, the hollow core, and the exterior face shell temperatures were approximately the same, and the soil was warmer than the wall temperatures (Figure 5-31). The upper panels of Figure 5-24 and Figure 5-32 show the cooling season temperature profiles at 86 in. and 16 in. above the slab, respectively.

For Bay 2N, during the cooling season, the warmest air in the hollow masonry block cavity was at the top of the cavity eliminating the potential for top-to-bottom buoyant cavity flow. The negligible temperature difference between the interior and exterior face shells indicates there was negligible potential for side-to-side buoyant cavity flow and the primary heat transfer mechanism was conduction. Since the soil temperature was

warmer than the wall temperatures, heat was transferred from the soil to the wall. It should be noted that this was not the case for all bays and there was the potential for buoyant cavity flow during the cooling season (discussed in Chapter 5.4.3).

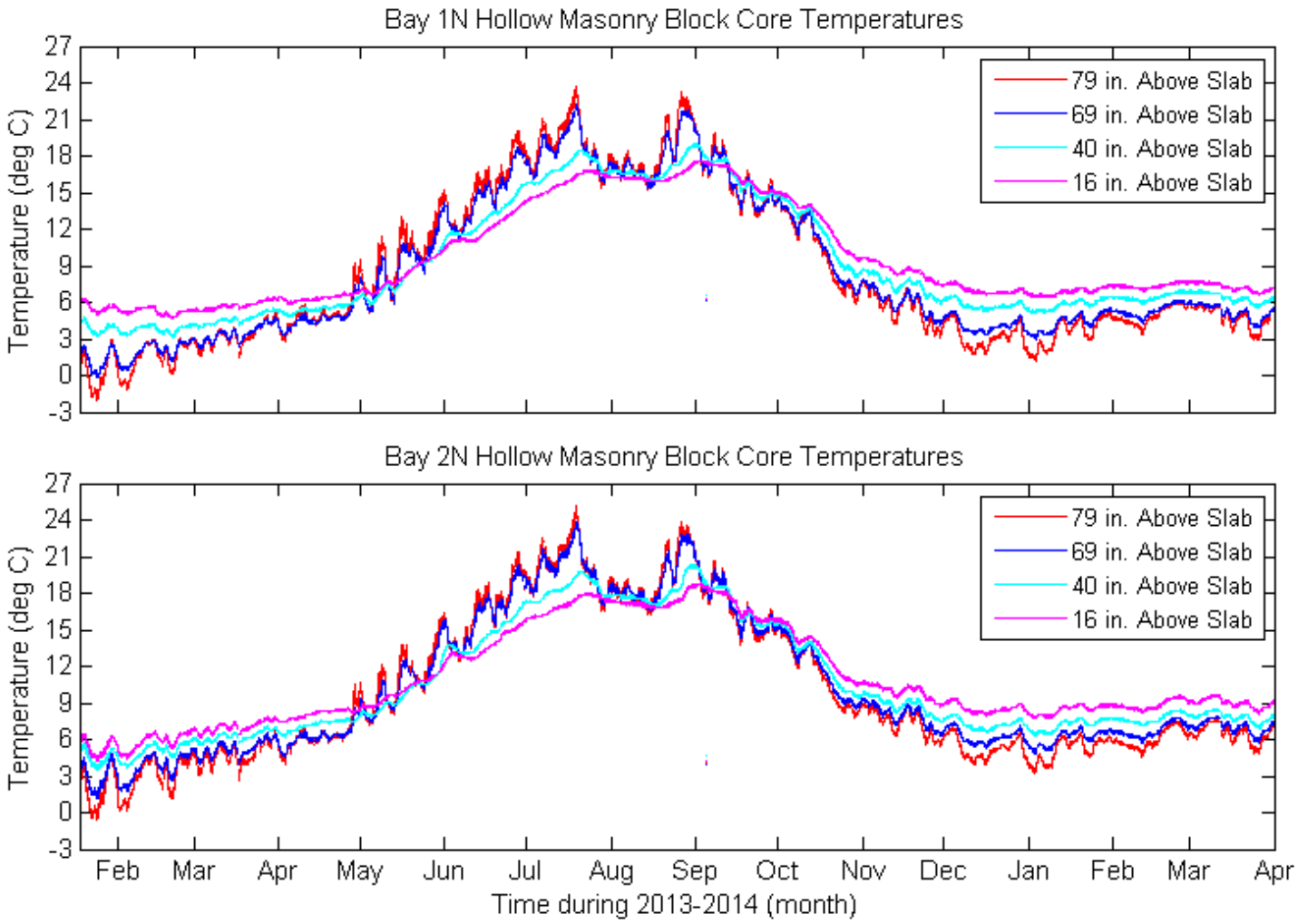

Figure 5-26: Bay 1N and 2N Hollow Masonry Block Core Temperatures

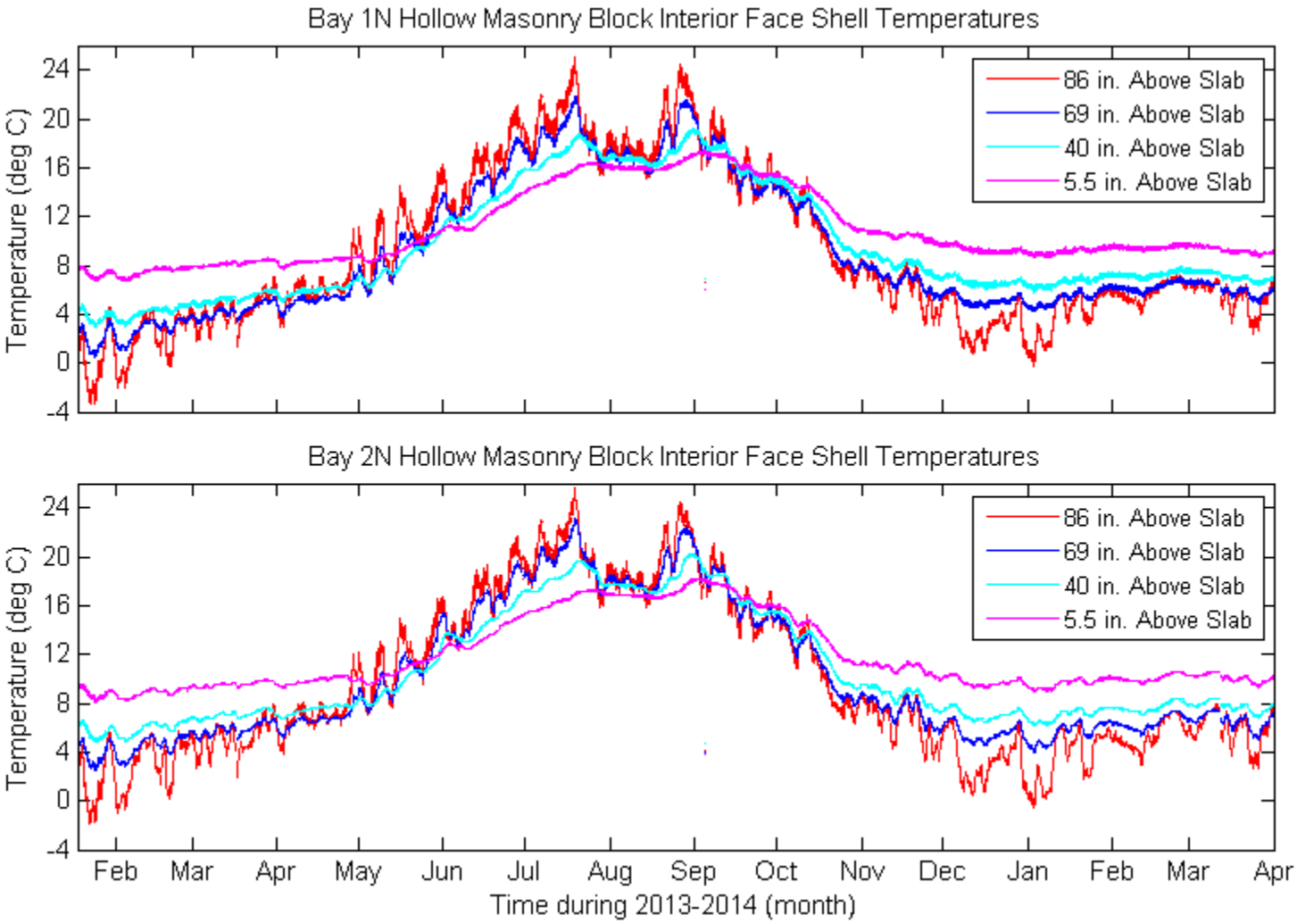

Figure 5-27: Bay 1N and 2N Hollow Masonry Block Interior Face Shell Temperatures

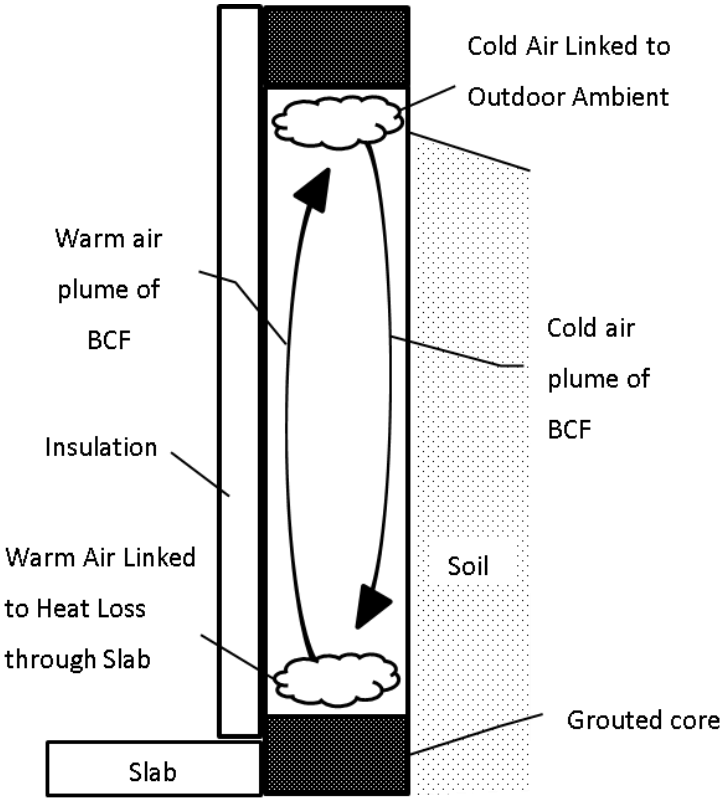

Figure 5-28: Top-to-Bottom Buoyant Cavity Flow

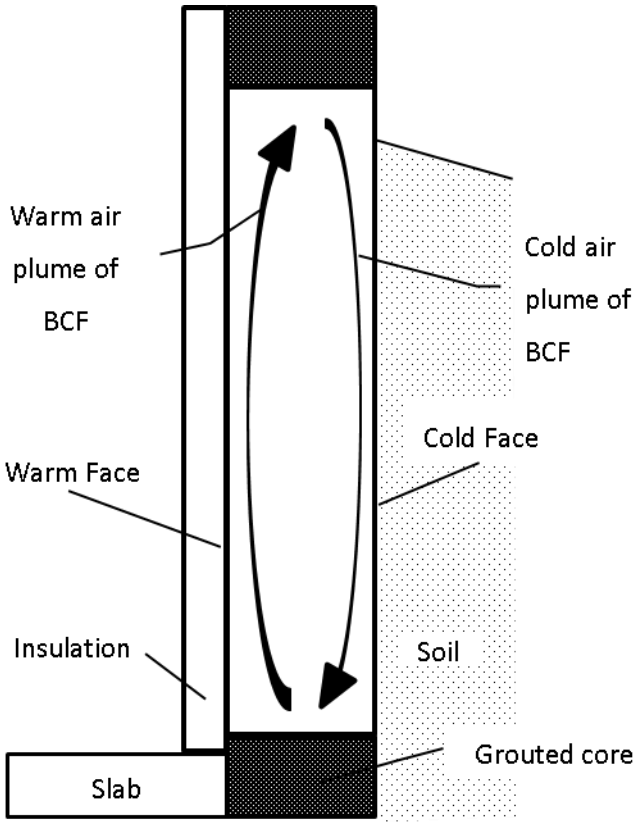

Figure 5-29: Side-to-Side Buoyant Cavity Flow (Warm Face Interior and Cold Face Exterior)

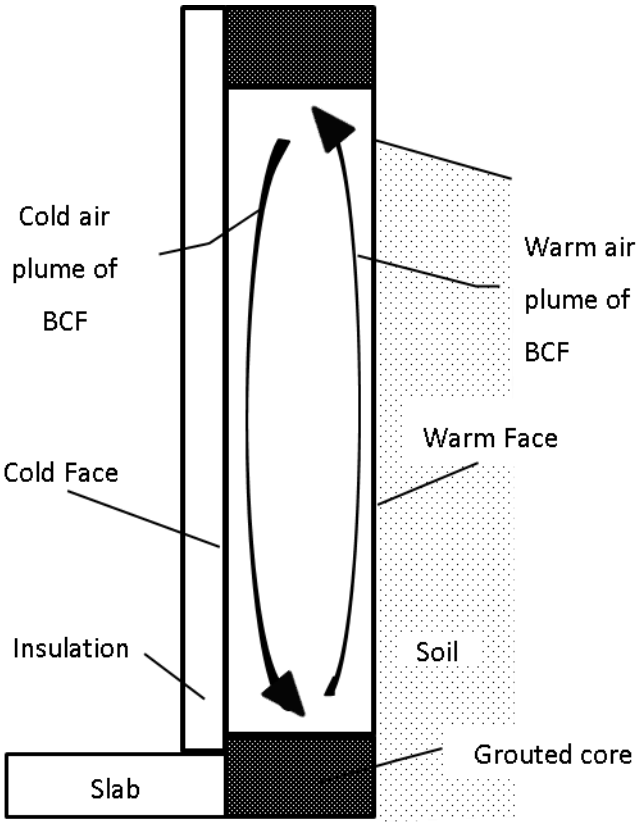

Figure 5-30: Side-to-Side Buoyant Cavity Flow (Cold Face Interior and Warm Face Exterior)

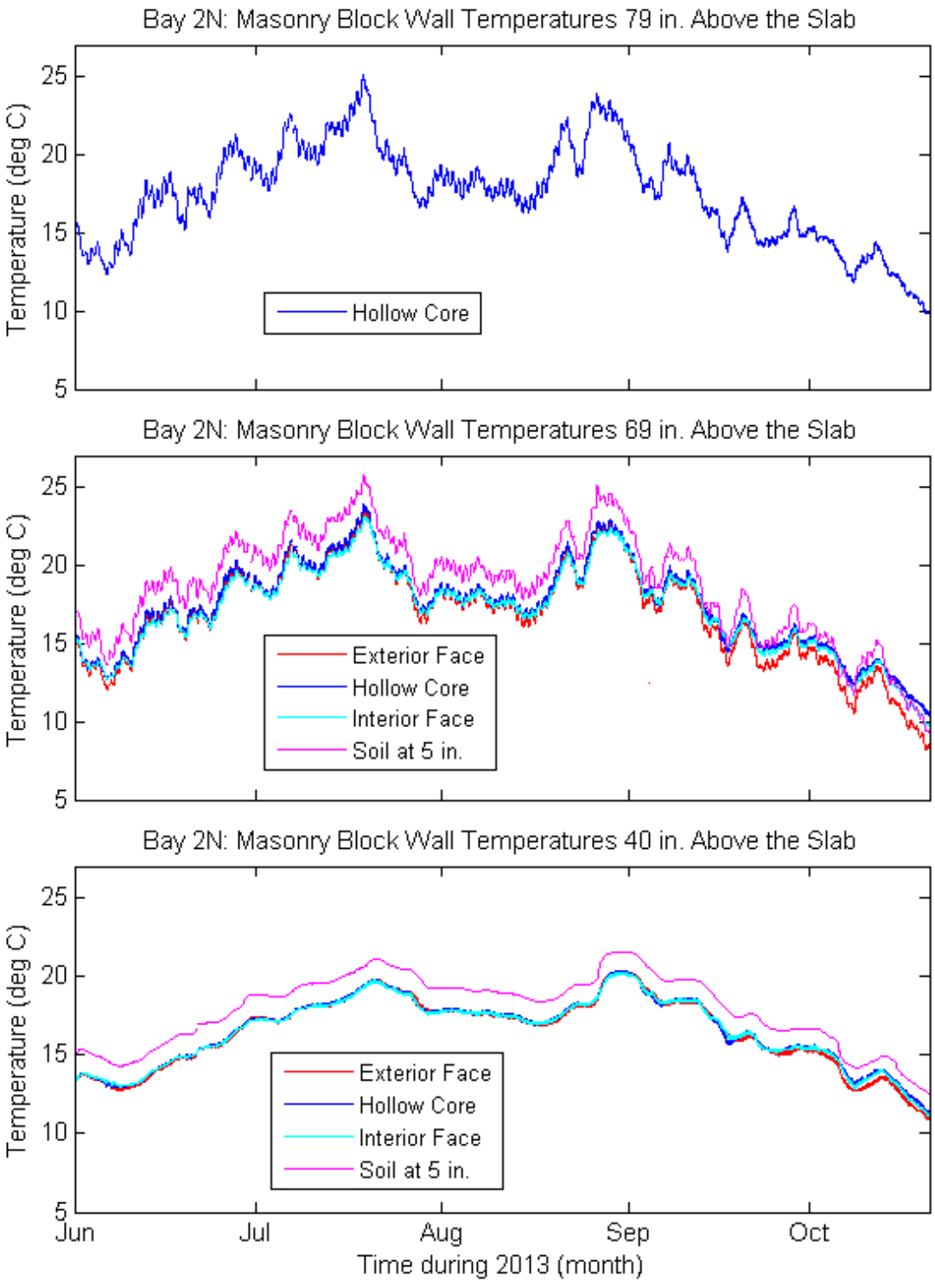

Figure 5-31: Bay 2N Masonry Block Wall and Soil Temperatures during Cooling Season at Upper Heights of Wall

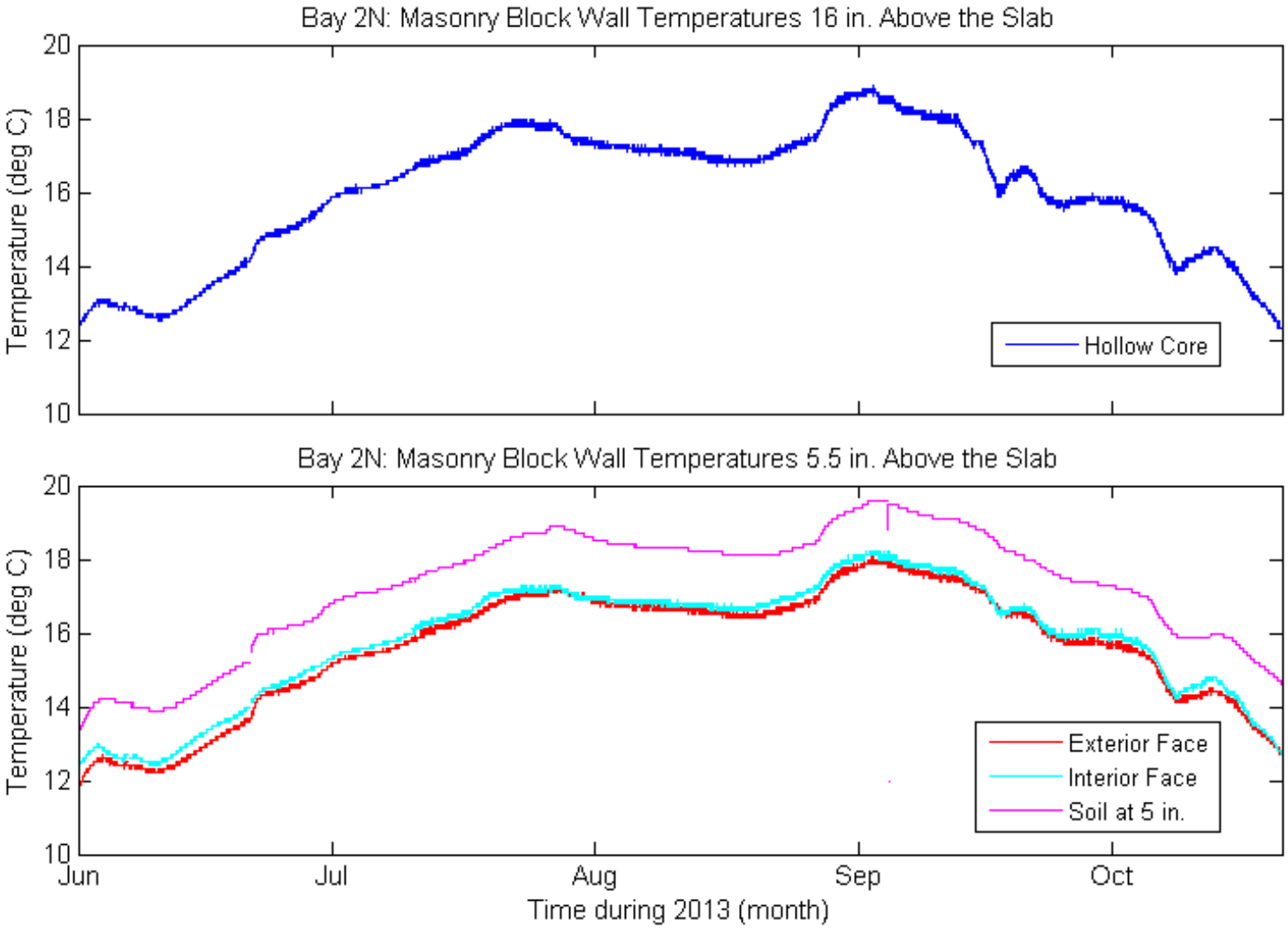

Figure 5-32: Bay 2N Masonry Block Wall and Soil Temperatures during Cooling Season at Lower Heights of Wall

5.4.2 Comparison of Bay 2N with Other Bays

The magnitude of the temperature differences for Bays 2N (Figure 5-25) and 2S (Figure 5-33) were similar throughout the time period evaluated, with the exception that Bay 2S had a larger diurnal variation. Both bays had steady temperature differences form December 2013 to April 2014 and unsteady temperature differences from January 2013 to June 2013.

For Bays 2N and 1S, from December 2013 to April 2014, at 40 in. above the slab, the temperature differences were approximately the same and held steady. The hollow core/exterior face shell temperature difference was approximately -1 deg. C and the interior face shell/hollow core temperature difference was approximately 0 deg. C (Figure 5-25 and Figure 5-34). At 69 in. above the slab, the approximate hollow core/exterior face shell temperature difference was -2.5 deg. C for Bay 2N and -1.75 deg. C for Bay 1S; the approximate interior face shell/hollow core temperature difference was 0.5 deg. C for Bay 2N and 0 deg. C for Bay 1S (Figure 5-25 and Figure 5-34). From January 2013 to May 2013 at 40 in. above the slab for Bay 2N, there was a larger decrease in temperature between the interior face shell and hollow core than the hollow core and exterior face shell (Figure 5-25), whereas Bay 1S (Figure 5-34) had the opposite relationship. The comparison at 69 in. above the slab cannot be made because the exterior face shell sensor on Bay 1S failed during this period.

For Bay 1N from November 2013 to April 2014, the interior face shell/hollow core and the hollow core/exterior face shell temperature differences were approximately the same at 40 in. (approximately -0.75 deg. C) and 69 in. (approximately -1 deg. C) above the slab (Figure 5-35). This was unlike Bay 2N where the hollow core/exterior face shell temperature difference was approximately -2 deg. C and the interior face shell/hollow core temperature difference was approximately 0.2 deg. C (Figure 5-25). Both bays had steady temperature differences from December 2013 to April 2014 and unsteady temperature differences form January 2013 to May 2013.

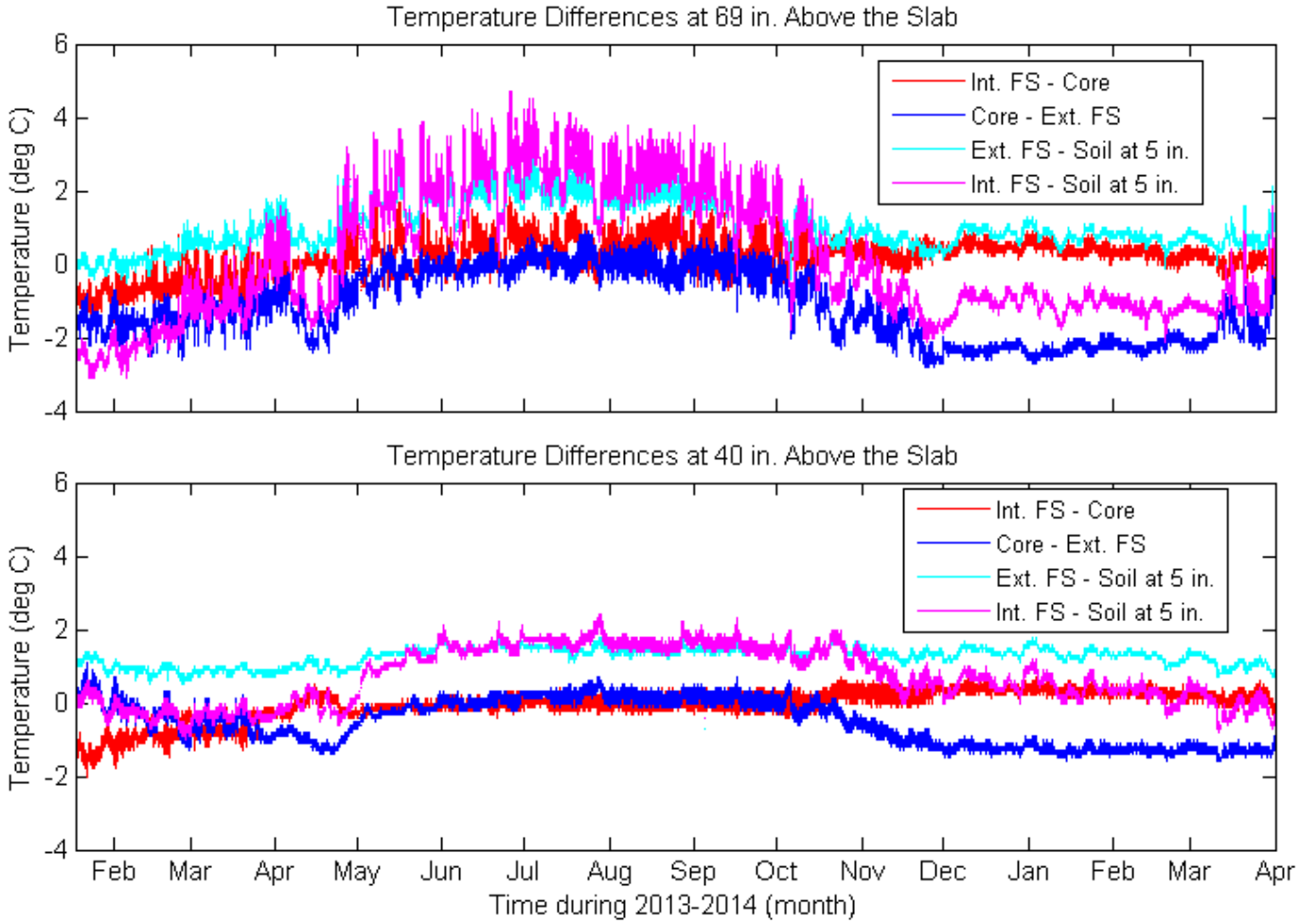

Figure 5-33: Bay 2S Hollow Masonry Block Wall Temperature Differences

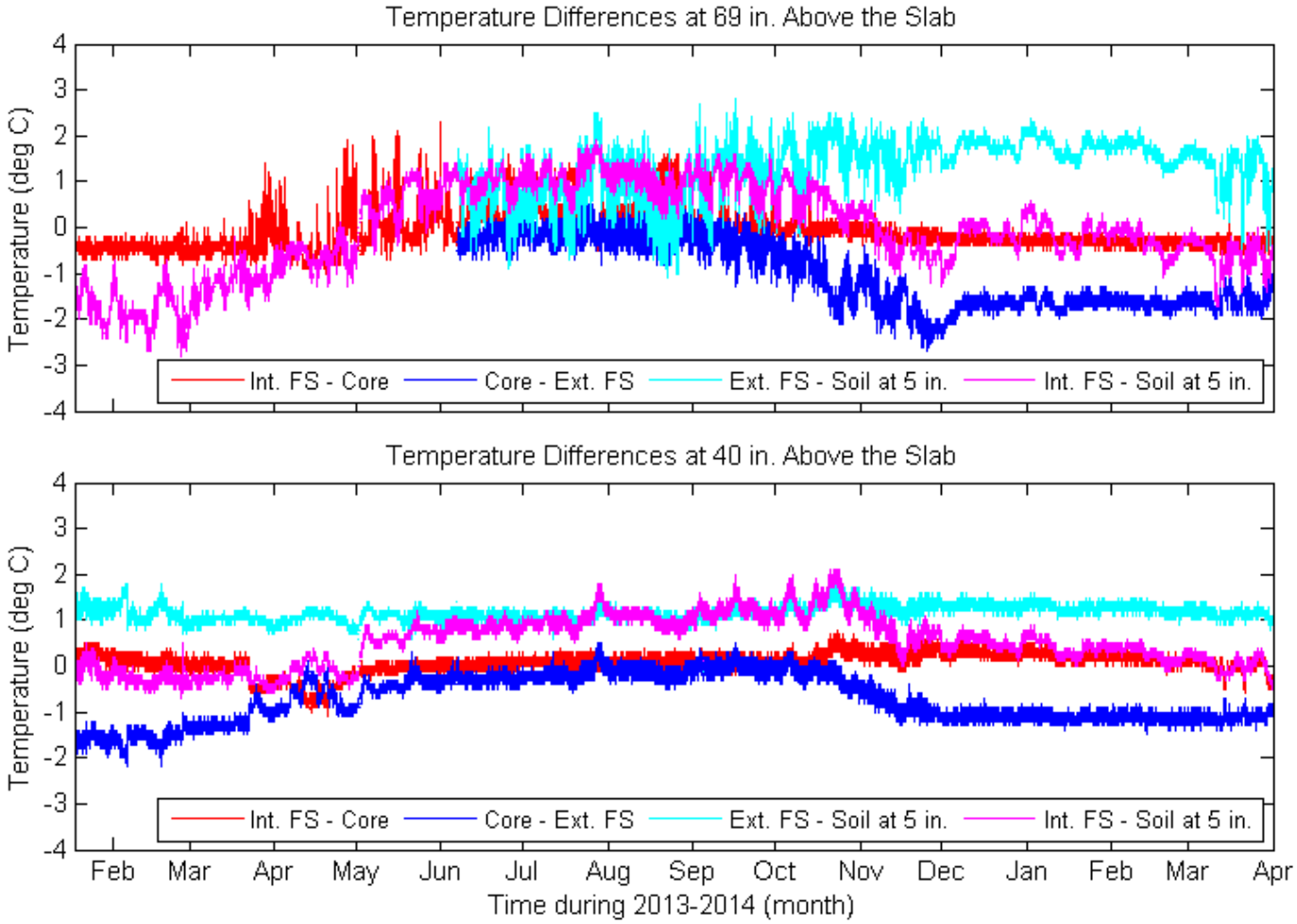

Figure 5-34: Bay 1S Hollow Masonry Block Wall Temperature Differences

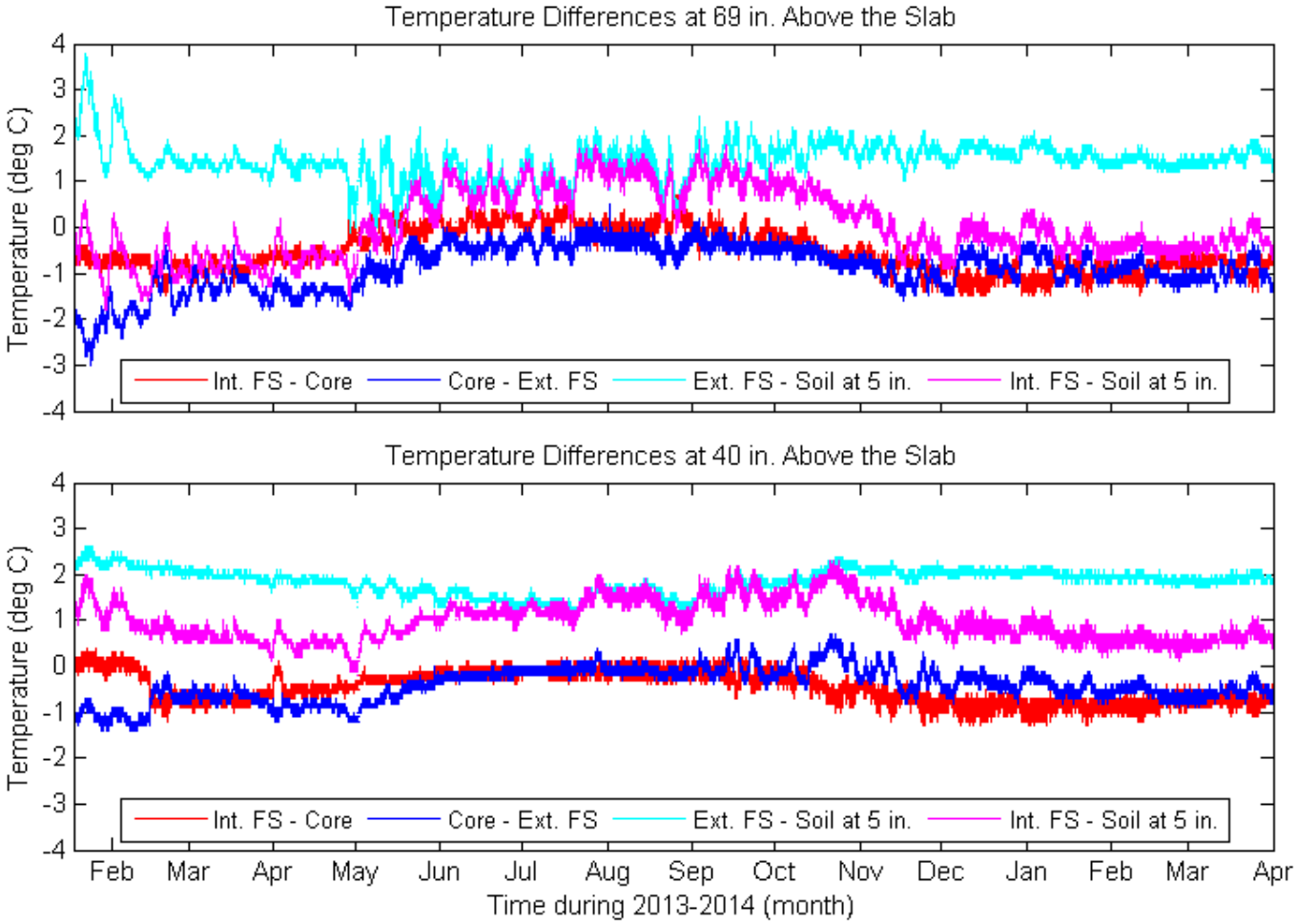

Figure 5-35: Bay 1N Hollow Masonry Block Wall Temperature Differences

These data show that there was a distinct difference in the buoyant cavity flow between the first heating season (approximately January 2013 through May 2013) and the second heating season (approximately mid-October 2013 through March 2014). The second heating season appears to have experienced relatively stable buoyant cavity air flow patterns for Bays 2N, 2S, 1N, and 1S, as is evident by the constant temperature differences between the wall elements (Figure 5-25, Figure 5-33, Figure 5-35, and Figure 5-34, respectively). The variation in temperature differences between the wall elements during the first heating season indicates unstable buoyant cavity air flow patterns (Figure 5-25, Figure 5-33, Figure 5-35, and Figure 5-34, respectively).

The second heating season had a minimum of 0.3 m (11.8 in.) of snow depth on the north and south sides from December 2013 through mid-March 2014. The maximum snow depth on the north side was approximately 0.85 m (33.5 in.) and the maximum on the south side was approximately 0.5 m (19.7 in.) (Figure 5-5). The first heating season had no appreciable snow pack prior to February 2013. Beginning in February of 2013, the north side accumulated snow through the end of April 2013, with a maximum accumulation of approximately 0.7 m (27.6 in.). The south side accumulated snow through mid-February and then the snow depth decreased through mid-April, with a spike and maximum snow pack in late April of approximately 0.4 m (15.7 in.).

The snow depth is a critical element for explaining the wall temperatures. Approximately the top 10 in. of the masonry wall was above grade and of this, the upper 8 in. was a solid grouted bond beam. The snow depth data demonstrate that snow insulated the wall from the exterior ambient conditions. The earlier and higher snow pack of the second heating season had a greater insulating effect and created a more constant exterior boundary condition. This resulted in the more stable buoyant cavity air flow patterns.

At the beginning of May 2013, on the north side of the building, the hollow core temperature gradient reversed from cold at the top and warm at the bottom, to warm at the top and cold at the bottom (Figure 5-26). On the south side of the building, the reversal consistently held from May 2013 onward, however, as early as March 2013 Bay 2S had oscillations back and forth (Figure 5-36). On the north side of the building, the gradient transitioned from warm at the top and cold at the bottom back to cold on

the top and warm on the bottom in mid-September 2013. On the south side, this reversal occurred in mid-October 2013.

The reversal of the hollow core temperature gradient provides insight into the hollow core buoyant cavity flow. When the temperature gradient was warm on the top and cold on the bottom, top-to-bottom buoyant cavity flow could not exist and the only driver for buoyant cavity flow was a side-to-side temperature gradient. This would reduce the strength of the buoyant cavity flow because the distance and temperature differences between bounding surfaces were smaller (Figure 5-44 and Figure 5-45). The earlier summer-to-fall transition in temperature gradient on the north side of the building meant the stronger buoyant cavity flow existed earlier on the north side. The timing of this reversal in temperature gradient coincides with the time when the interior face shell/ hollow core and exterior face shell/hollow core temperature differences began to diverge from one another in Bays 2N, 2S, and 1S (Figure 5-25, Figure 5-33, and Figure 5-34, respectively).

The variability in wall element temperature differences between Bays 2N, 2S, 1N, and 1S could not be fully explained. A number of parameters influenced the thermal performance of the wall that could not be extracted from the data or were not collected. The temperature, width, and velocity of the buoyant cavity air plumes would provide insight into the strength of the buoyant cavity flow across the height and width of the cavity. The temperatures of the surfaces bounding the hollow cavity also would indicate the strength of the flow in addition to when conditions existed for buoyant cavity flow. The heat flux through the slab into the wall would provide additional data for understanding the temperatures at the bottom of the cavity that drive buoyant cavity flow. The temperature and height of the ground water table would also provide insight into the wall temperatures that affect buoyant cavity flow.

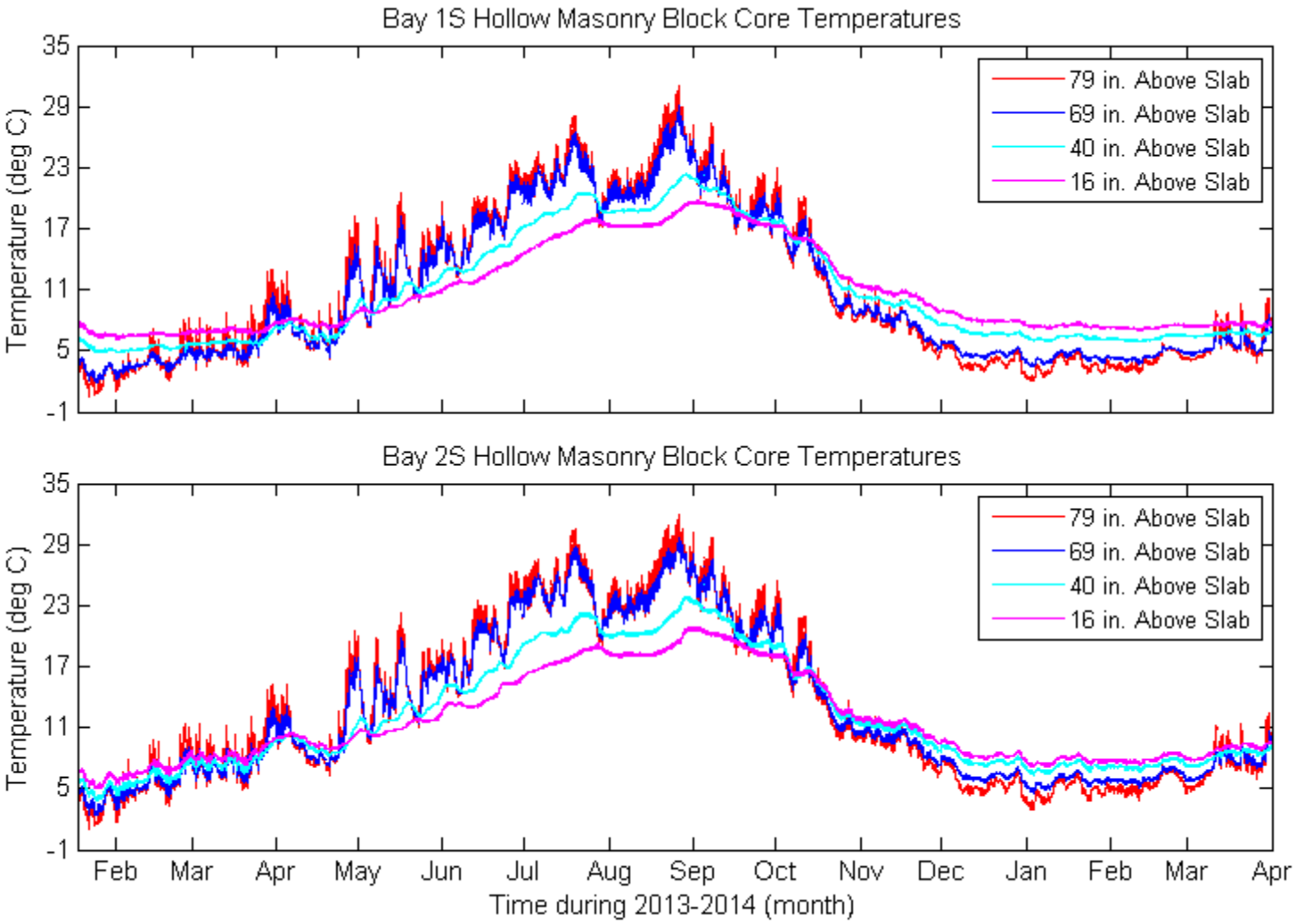

Figure 5-36: Bay 1S and 2S Hollow Masonry Block Core Temperatures

5.4.3 Cavity Flow Dynamics

The Grashof Number provides a means of assessing the potential for buoyant cavity flow. The top-to-bottom and side-to-side temperature differences are the two drivers for this flow. The top-to-bottom Grashof Number and the side-side Grashof Number indicate the likelihood for buoyant cavity flow to exist within a cavity, but they do not indicate the direction or magnitude of heat transfer. The heat transfer is generally from side-to-side (Probert and Dixon 1979), even though the primary driver of the buoyant cavity flow may be the top-to-bottom temperature difference. This is largely because the side-to-side heat transfer takes place over a larger surface area than the top-to-bottom heat transfer. The following analysis evaluates the potential for buoyant cavity flow to exist within a cavity and makes no assessment of the direction or magnitude of the heat transfer. No experimental data was collected that specifically allows for a comparison of the magnitudes of the top-to-bottom and side-to-side heat transfer.

The Grashof Number is a dimensionless term that is a ratio of the buoyant to viscous forces in a fluid and is expressed by the following equation:

$$Gr = \frac{g\beta(T_H - T_L)L^3}{\nu^2}$$ **Equation 5-1**

where g is the acceleration due to gravity, β is the coefficient of thermal expansion, T_H is the warm surface temperature, T_L is the cold surface temperature, L is the characteristic length, and ν is the kinematic viscosity. The characteristic length is the distance between the driving temperature surfaces. In this experiment, L for side-to-side flow was $8^5/_8$ in. and for top-to-bottom flow was $64^1/_8$ in. Since L is cubed, it is the dominant term and hence the potential for buoyant cavity flow is greatest due to a temperature gradient between the top and bottom surfaces. Further exacerbating this effect was the fact that the largest temperature difference ($T_H - T_L$) existed between the top and bottom of the wall since the top of the wall was closely linked to outdoor ambient conditions (Figure 5-44 and Figure 5-45).

To calculate the Grashof Number for top-to-bottom flow, the following assumptions were made:

- T_L was the temperature of the top surface (bond beam) and was an average of the interior and exterior face shell temperature sensors at the highest level (86 in. above the slab);
- T_H was the temperature of the bottom surface (grouted core) and was an average of the interior and exterior face shell temperature sensors at the lowest level (5.5 in. above the slab);
- The relative humidity of the air was an average of the four core humidity sensors; and,
- The terms β and ν were based on the average relative humidity and temperature of the air in the hollow core.

The temperatures, T_H and T_L, used to calculate the Grashof Number were approximations. The temperatures were based on the average of two sensors instead of an exact reading. Further, the interior and exterior face shell temperatures used to calculate the average temperature were approximately 4 in. above the bounding surface at the top of the wall and approximately 6 in. below the bounding surface at the bottom of the wall. The other option was to use the core temperature at 79 in. and 16 in. above the slab. This also would have been an approximation as it was the temperature of the air instead of the bounding surface and the sensors were approximately 4 in. away from the bounding surfaces.

For north exposures, Figure 5-38 compares the average of the interior and exterior face shell temperatures to the core temperature, either of which could have been used for the calculation of the Grashof Number. For Bays 1 and 2 during the heating season, the core temperature was colder than the average temperature of the face shells at the bottom of the wall and warmer than the average temperature of the face shells at the top of the wall. The temperature difference ($T_H - T_L$), and in turn the Grashof Number, was greater using the core temperatures than the average face shell temperatures. The actual temperatures of the bounding surfaces and Grashof Numbers were likely an intermediate value of the two limits. During the heating season, the average temperature of the two face shells was used for the calculation of the Grashof Number and was a more conservative option.

During the cooling season for Bays 1 and 2, the difference between the average of the interior and exterior face shell temperatures and the core temperatures at the top and bottom of the wall was approximately 1 deg. C (Figure 5-38). Unlike during the heating season, the core temperature was warmer than the average temperature of the face shells at the bottom of the wall and colder than the average temperature of the face shells at the top of the wall. Therefore using the average temperature of the two face shells was the less conservative option. However, because of the small temperature difference between the two options and for consistency between the heating and cooling seasons, a different method was not justified for the cooling season and the average temperature of the two face shells was used for the calculation of the Grashof Number.

The difference between the average interior and exterior face shell temperature and the core temperature for south exposures are shown in Figure 5-39. The relationship between the average temperatures of the interior and exterior face shells and the core temperatures was the same for the south exposure as for the north exposure. At the top of the wall, the south exposure had a more prominent diurnal variation than the north exposure. Further, the average face shell temperatures had a greater diurnal variation than the core temperatures. By using the average face shell temperature, the diurnal variation of the concrete block was better captured than if the core temperature was used.

Anytime ($T_H - T_L$) was negative for top-to-bottom flow (Figure 5-45), the Grashof Number was not calculated because the temperature difference for buoyant cavity flow did not exist. In Figure 5-40, if the Grashof Number is graphed, it indicates that the top of the wall was colder than the bottom of the wall. Breaks in the line indicate that the top of the wall was warmer than the bottom of the wall.

To calculate the Grashof Number for side-to-side flow, the following assumptions were made:

- T_L was the temperature of the face shell with the lower temperature and T_H was the temperature of the face shell with the higher temperature;

    - For Bays 1 and 2, an average Grashof Number was calculated where T was an average of the face shell temperatures at approximately 40 in. and 69 in. above the slab;
    - For Bay 4, the Grashof number was calculated separately for the sensors at approximately 40 in. and 69 in. above the slab where T was the temperature of the face shell at the given height;
- The relative humidity of the air was an average of the four core humidity sensors; and,
- The terms β and ν were based the average relative humidity and temperature of the air in the hollow core.

For side-to-side buoyant cavity flow, the direction of the flow loop depended on the temperature of the face shells. If the interior face shell was warmer than the exterior face shell, the cold air dropped down the exterior face and the warm air rose up the interior face (Figure 5-29) and if the interior face shell was colder than the exterior face shell, the cold air dropped down the interior face and the warm air rose up the exterior face (Figure 5-30).

Heat transfer is by conduction for $Gr < 6 \times 10^3$, above this threshold laminar buoyant cavity flow is present. Buoyant cavity flow becomes turbulent at $Gr > 2 \times 10^5$ (Kreith 1967).

The Grashof Numbers for top-to-bottom buoyant cavity flow for Bays 1 and 2 were approximately the same (Figure 5-40). Both north and south exposures had a Grashof Number greater than 10^8 for the majority of the heating season. The maximum Grashof numbers for the north and south exposures were approximately 10^{10}. The north exposure had little diurnal variation whereas the south exposure had diurnal variation as large as approximately 7×10^9.

From January 2013 to April 2013 and December 2013 to April 2014, the Grashof Numbers for side-to-side buoyant cavity flow for Bays 1 and 2 with a south exposure were approximately the same with a value of 2.5×10^6 (Figure 5-42). During the same time period, for the north exposure, the Grashof Number for Bays 1 and 2 was approximately 3×10^6 (Figure 5-41).

The magnitudes of the Grashof Numbers provide insight into the heat transfer mechanism and the nature of the flow. During the heating season, the average Grashof Number for top-to-bottom flow and for side-to-side flow exceeded 2×10^5. This indicates that buoyant cavity flow was an important heat transfer mechanism and the flow was turbulent. The Grashof Number for top-to-bottom buoyant cavity flow was more than 1,000 times greater than the Grashof Number for side-to-side flow. Therefore, during the heating season, the potential for a buoyant cavity flow loop to exist in a wall with interior insulation was dominated by the top-to-bottom temperature gradient.

During the cooling season, the Grashof Number for top-to-bottom buoyant cavity flow for Bays 1 and 2 needs to be analyzed in conjunction with the hollow core temperatures. Periodically during the cooling season, the Grashof Number was large enough to indicate buoyant cavity flow (Figure 5-40). The times when the Grashof Number indicated buoyant cavity flow correlated with the average face shell temperature at 86 in. above the slab dropping below the hollow core temperature at 79 in. above the slab (Figure 5-38 and Figure 5-39). However, the average face shell temperature did not remain colder than the hollow core temperature long enough to cool the air in the hollow core and cause buoyant cavity flow to begin. This is evident because during the cooling season the temperature gradient across the height of the hollow core was not correct for top-to-bottom buoyant cavity flow (the warm less dense air was at the top and the cold dense air was at the bottom) (Figure 5-26 and Figure 5-36).

The difference in temperature between the interior and exterior face shells at 40 in. and 69 in. above the slab was less than or equal to $\pm$ 0.5 deg. C (Figure 5-44). Since the calculation of the Grashof Number takes the width of the cavity to the third power, the Grashof Number can be large despite a small temperature difference. Figure 5-37 shows the effect of the cavity width on the value of the Grashof Number for a 0.5 deg. C temperature difference. As can be seen, conduction is the dominant heat transfer mechanism in a 1 in. cavity. However, in a cavity $4^5/_8$ in. and wider, buoyant cavity flow is significant even for such a small temperature difference.

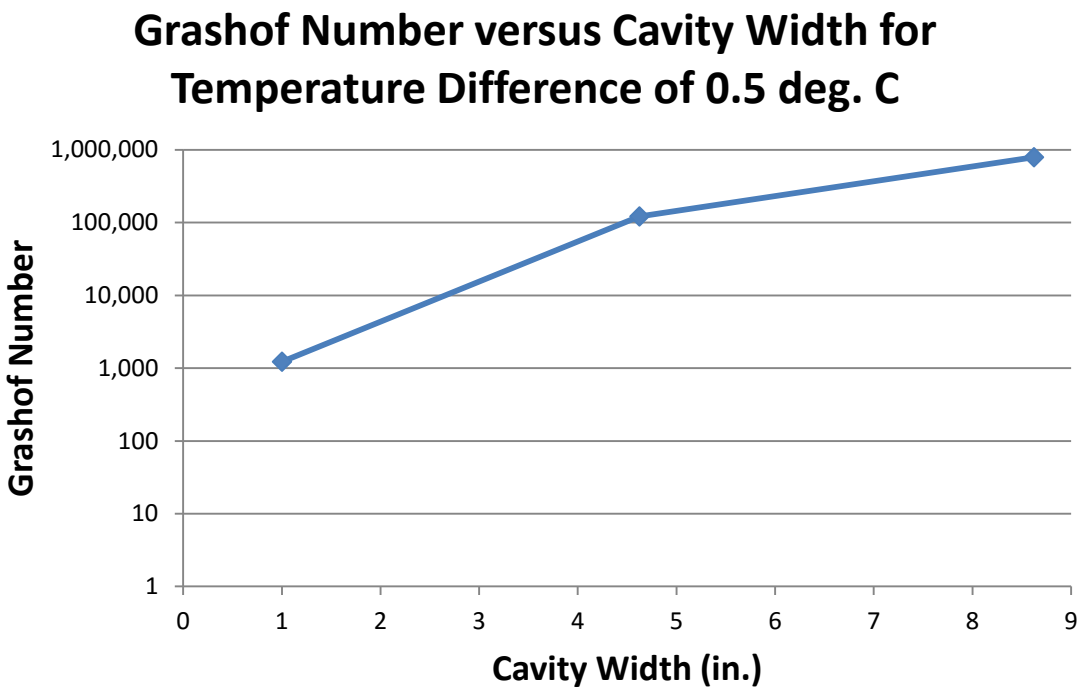

Figure 5-37: Grashof Number for Side-to-Side Buoyant Cavity Flow for Different Cavity Widths[12]

The calculation of the Grashof Number for this experiment was approximate. For Bays 1 and 2, for side-to-side flow, the values for T_H and T_L were an average of the two interior and exterior face-shell sensors respectively (at 40 in. and 69 in. above the slab). In addition, the temperature was taken on the exposed face of the face shell, not the core side of the face shell. Conduction across the $1^1/_2$ in. face shell would cause these two temperatures to be different. Also, the accuracy of the temperature sensors was $\pm$ 0.5 deg. C, meaning a temperature difference of less than 1 deg. C is beyond the accuracy of the sensors. For these reasons, the side-to-side Grashof Numbers from the cooling season are simply an approximation for predicting the presence of buoyant cavity flow.

The side-to-side Grashof Numbers for Bays 1 and 2 from June 2013 to mid-September 2013 for north exposures and from May 2013 to mid-October 2013 for south exposures varied between bays and exposures (Figure 5-41 and Figure 5-42, respectively). Bay 1S had a Grashof Number greater than 7 x 10^4, but it was constantly oscillating

[12] β and ν were calculated based on T=18 deg. C, RH=99%, and P=101,325 Pa

between the interior face shell being the warm surface and the exterior face shell being the warm face. Bay 2S had a Grashof Number greater than 7×10^4 with the exterior face shell consistently the warm surface. Bay 1N had a Grashof Number greater than 7×10^4 with the interior face shell consistently the warm surface. Bay 2N had a Grashof Number greater than 7×10^4 with the exterior face shell consistently the warm surface from mid-June 2013 to August 2013 and the interior face shell consistently the warm surface from August 2013 to September 2013.

The presence of buoyant cavity during the cooling season depended on a side-to-side temperature difference (since a negative top-to-bottom temperature gradient did not exist) and the side-to-side Grashof Number for each bay must be analyzed independently. Bay 1N consistently had a Grashof Number greater than 6×10^3 with the interior face shell consistently the warm surface. For this reason, it is likely that buoyant cavity flow driven by a side-to-side temperature difference existed during the cooling season where the direction of the flow loop was the same as that during the heating season. Bay 2S consistently had a Grashof Number greater than 6×10^3 with the exterior face shell consistently the warm surface. Since the exterior face shell was the warm surface, the direction of the flow loop would have reversed from that during the heating season. Because the exterior surface was consistently the warm surface during the cooling season and the Grashof Number was large enough to indicate buoyant cavity flow, it is probable that the flow loop had sufficient time to reverse from that of the heating season and buoyant cavity flow existed during the cooling season. Bay 1S had a Grashof Number greater than 6×10^3 but the warm surface was constantly oscillating between the interior face shell and the exterior face shell. It is therefore concluded that buoyant cavity flow did not exist because the flow loop would constantly be reversing direction and the period between reversals did not allow for a steady flow in either direction to persist for a significant period. Bay 2N had a Grashof Number greater than 6×10^3 with the exterior face shell consistently the warm surface from mid-June 2013 to August 2013 and the interior face shell consistently the warm surface from August 2013 to September 2013. Early in the cooling season the flow loop would have reversed from that during the heating season, then late in the cooling season it would have reversed again to match that during the heating season. Buoyant cavity flow may have existed during the cooling season in Bay 2N, but it is difficult to be certain because it is unclear how much time is required for the flow loop to reverse. In the bays where buoyant cavity

flow existed during the cooling season, the strength of the flow was significantly weaker than that during the heating season as was evident by the order of magnitude of the Grashof Numbers.

The design of Bay 4 requires it to be analyzed independent of Bays 1 and 2. Bay 4 had exterior half-height insulation on the upper half of the wall instead of full-height interior insulation. The exterior insulation and exterior face shell temperature sensors were installed on June 6, 2013 and hence this analysis only considers the insulated wall since this provides a different condition from that discussed for Bays 1 and 2.

Between November 2013 and April 2014 for Bay 4, the top-to-bottom Grashof Number oscillated between zero and approximately 1×10^9 (Figure 5-40). Mid-October 2013 to November 2013 was the only time when the Grashof Number was steadily greater than zero with a value of approximately 8×10^8. This period coincides with the only time that the hollow core temperature gradient was cold on top and warm on bottom (Figure 5-43).

The top-to-bottom Grashof Number and hollow core temperature gradient provide insight into the buoyant cavity flow in Bay 4. The top-to-bottom Grashof Number was large enough to indicate the potential for buoyant cavity flow (greater than 6×10^3) at various times between October 2013 and April 2014 (Figure 5-40). Between October 2013 and April 2014, the oscillation of the Grashof Number indicates that the temperature difference was not consistent for buoyant cavity flow to begin. This is reinforced by the hollow core temperature gradient that was incorrect for top-to-bottom buoyant cavity flow (warm on the top and cold on the bottom). Mid-October 2013 to November 2013 was the only time that the conditions were consistently correct for buoyant cavity flow. The Grashof Number was consistently greater than 6×10^3 and the hollow core temperature gradient was cold on the top and warm on the bottom.

The Bay 4 side-to-side Grashof Number was calculated separately for the sensors at 40 in. and 69 in. above the slab (Figure 5-41 and Figure 5-42 for the north and south exposures, respectively). The sensors at 69 in. above the slab had insulation on the exterior face and the sensors at 40 in. above the slab were located 3 in. below the bottom of the insulation. Bay 4, at 69 in. above the slab, from mid-November 2013 to April 2014 had a side-to side Grashof Number of approximately 2.7×10^6 for the north

exposure and approximately 2.5 x 10^6 for the south exposure. These values were approximately the same magnitudes as the side-to-side Grashof Number for Bays 1 and 2 (average of sensors at 40 in. and 69 in. above the slab). For the same time period at 40 in. above the slab, the Bay 4 side-to-side Grashof Number was approximately 4.7 x 10^6 for the north exposure and approximately 4.4 x 10^6 for the south exposure.

For both exposures, the side-to-side Grashof Numbers at 40 in. and 69 in. above the slab are greater than 2 x 10^5 during the heating season, indicating turbulent, buoyant cavity flow. For both exposures the Grashof Number was larger at 40 in. above the slab than at 69 in. above the slab, indicating that buoyant cavity flow was stronger below the insulation. However, the magnitude of the Grashof Numbers at 40 in. and 69 in. above the slab, indicate that buoyant cavity flow existed over the insulated and uninsulated parts of the wall.

During the heating season, the potential for buoyant cavity flow in Bay 4 existed primarily due to a side-to-side temperature gradient. This was unlike Bays 1 and 2 where a top-to-bottom temperature gradient was the primary indicator of the potential for buoyant cavity flow. During the heating season, the Grashof Numbers for side-to-side buoyant cavity flow in Bay 4 were approximately 1,000 times smaller than the Grashof Numbers for top-to-bottom buoyant cavity flow in Bays 1 and 2 (Figure 5-40, Figure 5-41, and Figure 5-42). Thus indicating a greater potential for buoyant cavity flow in Bays 1 and 2. However, the magnitude of the side-to-side Grashof Numbers for Bay 4 still classify the buoyant cavity flow as turbulent.

From mid-June 2013 to mid-September 2013, Bay 4N had a side-to-side Grashof Number at 40 in. and 69 in. above the slab greater than 2 x 10^5 with the interior face shell the warm surface (Figure 5-41). During the same time period, Bay 4S had a side-to-side Grashof Number at 69 in. above the slab greater than 2 x 10^5 with the exterior face shell the warm surface (Figure 5-42). At 40 in. above the slab in Bay 4S, the side-to-side Grashof Number was greater than 2 x 10^5, but the warm surface alternated between the interior and exterior face shell. From mid-June 2013 to late July 2013 and during August 2013 the interior face shell was the warm surface and during late July 2013 and from late August 2013 to mid-September 2013 the exterior face shell was the warm surface.

The Bay 4 side-to-side Grashof Numbers provide insight into the buoyant cavity flow during the cooling season. Because the Bay 4N side-to-side Grashof Numbers were consistently large enough to indicate buoyant cavity flow (greater than 6 x 10^3) and the direction of the buoyant cavity flow did not change from the heating season to the cooling season (the interior surface remained the warm surface), it is likely that buoyant cavity flow persisted through the cooling season. However, the strength of the flow would have been reduced from the heating season due to the decreased temperature difference between the interior and exterior face shells (Figure 5-44). In Bay 4S, the magnitude (greater than 6 x 10^3) and consistency of the side-to-side Grashof Number at 69 in. above the slab (exterior face shell was the warm surface) indicate that buoyant cavity flow may have existed in the upper half of the wall behind the insulation in a direction reverse to that of the flow during the heating season. The bottom of the flow loop would have been around 40 in. above the slab as is evident by the interior and exterior face shell alternating between being the warm surface (Figure 5-42). Further, the side-to-side Grashof number at 40 in. above the slab indicates that a buoyant cavity flow loop may have existed in the bottom of the hollow cavity that flowed in a direction opposite to that in the upper portion of the wall and the same direction as the heating season flow loop. In all cases, the heating season Grashof Numbers were approximately 4 times greater than the cooling season Grashof Numbers such that if buoyant cavity flow existed during the cooling season it was significantly weaker than that during the heating season.

5.4.4 Conclusions

For below-grade walls insulated on the interior face, buoyant cavity flow is an important heat transfer mechanism during the heating season. The potential for buoyant cavity flow is primarily driven by the temperature gradient that exists between the top of the wall and the bottom of the wall. However, the potential for buoyant cavity flow due to the temperature gradient between the interior and exterior face shells of the wall is not negligible and increases the magnitude of the resulting flow velocities. Although the top-to-bottom temperature gradient is the primary indicator of buoyant cavity flow, it does not provide any real insight into the direction or magnitude of the wall heat transfer. However, the measured horizontal wall temperature profiles discussed in Chapter 5.4.1

and Chapter 6 allow the inference that the primary measured heat transfer likely was from side-to-side.

The top of a below-grade wall is typically exposed to the exterior ambient conditions (in this experiment the upper 10 in.) which have a significant impact on the buoyant cavity flow. The height of the exposed wall, the solar exposure, and the snow pack all influence the exterior thermal boundary and, in turn, the buoyant cavity flow.

Below-grade walls insulated on the interior face have the potential for buoyant cavity flow during the cooling season and it is driven by a temperature difference between the interior and exterior face shells of the wall. If present, the strength of the buoyant cavity flow during the cooling season is weaker ($Gr \geq 10^5$) than the buoyant cavity flow that exists in the winter ($Gr \geq 10^9$). The direction of buoyant cavity flow during the cooling season does not necessarily match the direction during the heating season. If the exterior face shell is the warm surface in the cooling season, the air flow reverses direction from the heating season.

Below-grade walls that have exterior half-height insulation on the upper half of the wall have buoyant cavity flow, but the potential is primarily indicated by a side-to-side temperature difference and not a top-to-bottom temperature difference. The exterior insulation effectively eliminated the potential for buoyant cavity flow due to a top-to-bottom temperature difference. Since side-to-side buoyant cavity flow is much weaker ($Gr \geq 10^6$) than top-to-bottom buoyant cavity flow ($Gr \geq 10^9$), it can be concluded that buoyant cavity flow in a wall with exterior half-height insulation is much weaker than in a wall with interior full-height insulation. Additionally, side-to-side buoyant cavity flow is greater in a partially insulated wall than a fully insulated wall because the temperature difference between the interior and exterior face shells is greater in the partially insulated wall.

The strength of the buoyant cavity flow below the half-height insulation is approximately 50% stronger than above the insulation because the temperature difference between the interior and exterior face shells increases. However, the buoyant cavity flow still exists across the full height of the hollow cavity.

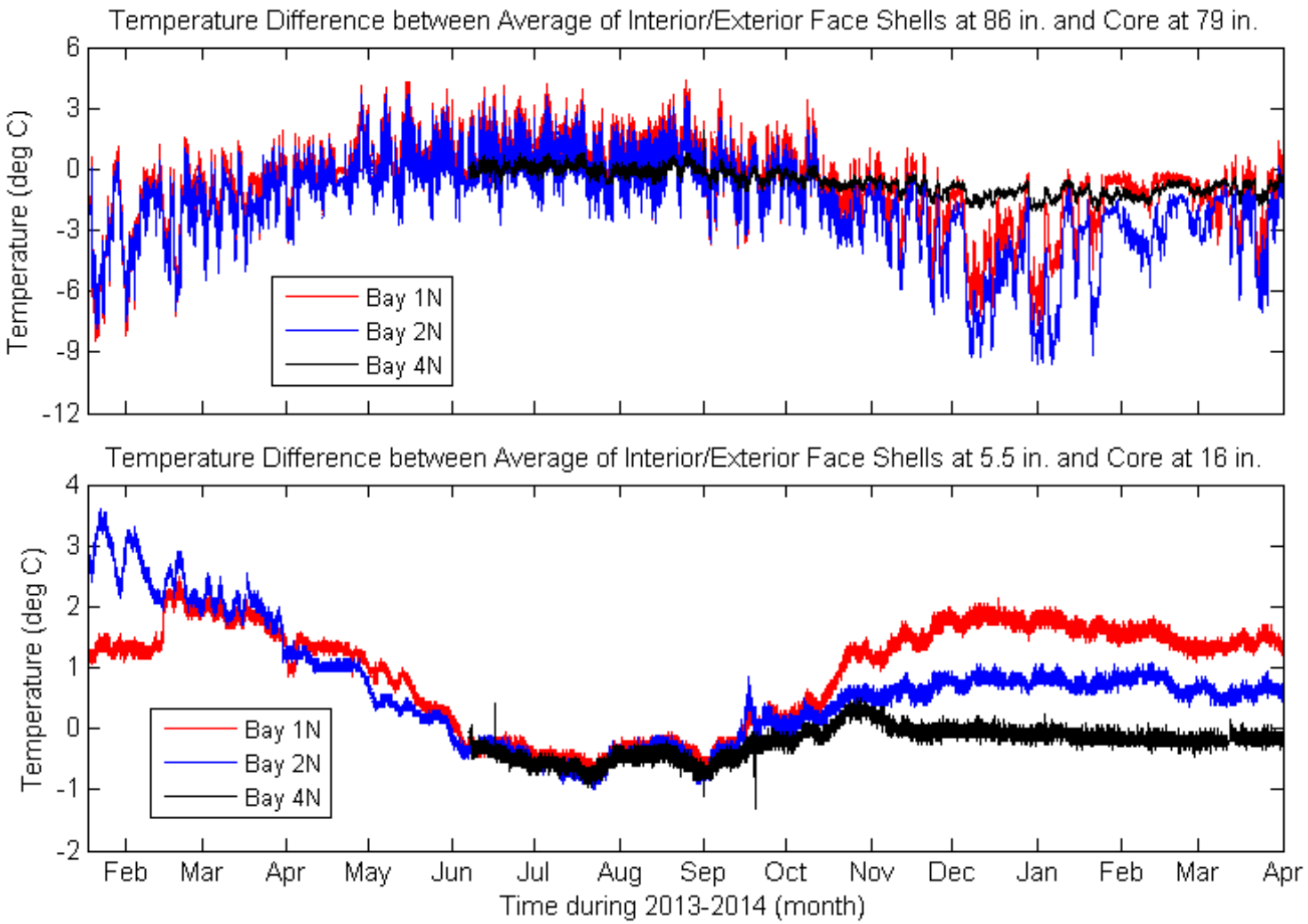

Figure 5-38: Temperature Difference between Average Interior/Exterior Face Shell Temperature and Core for North Exposures

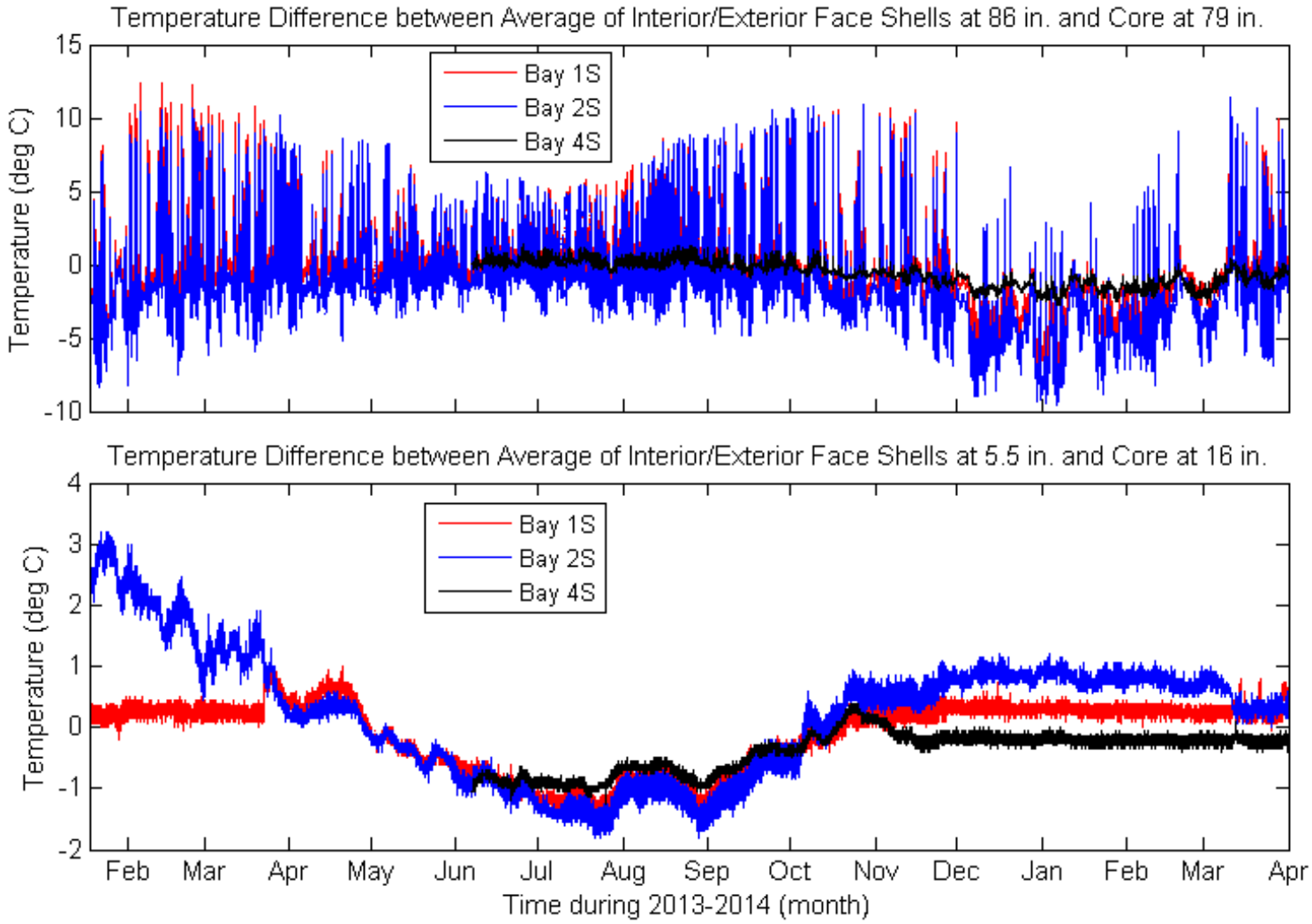

Figure 5-39: Temperature Difference between Average Interior/Exterior Face Shell Temperature and Core for South Exposures

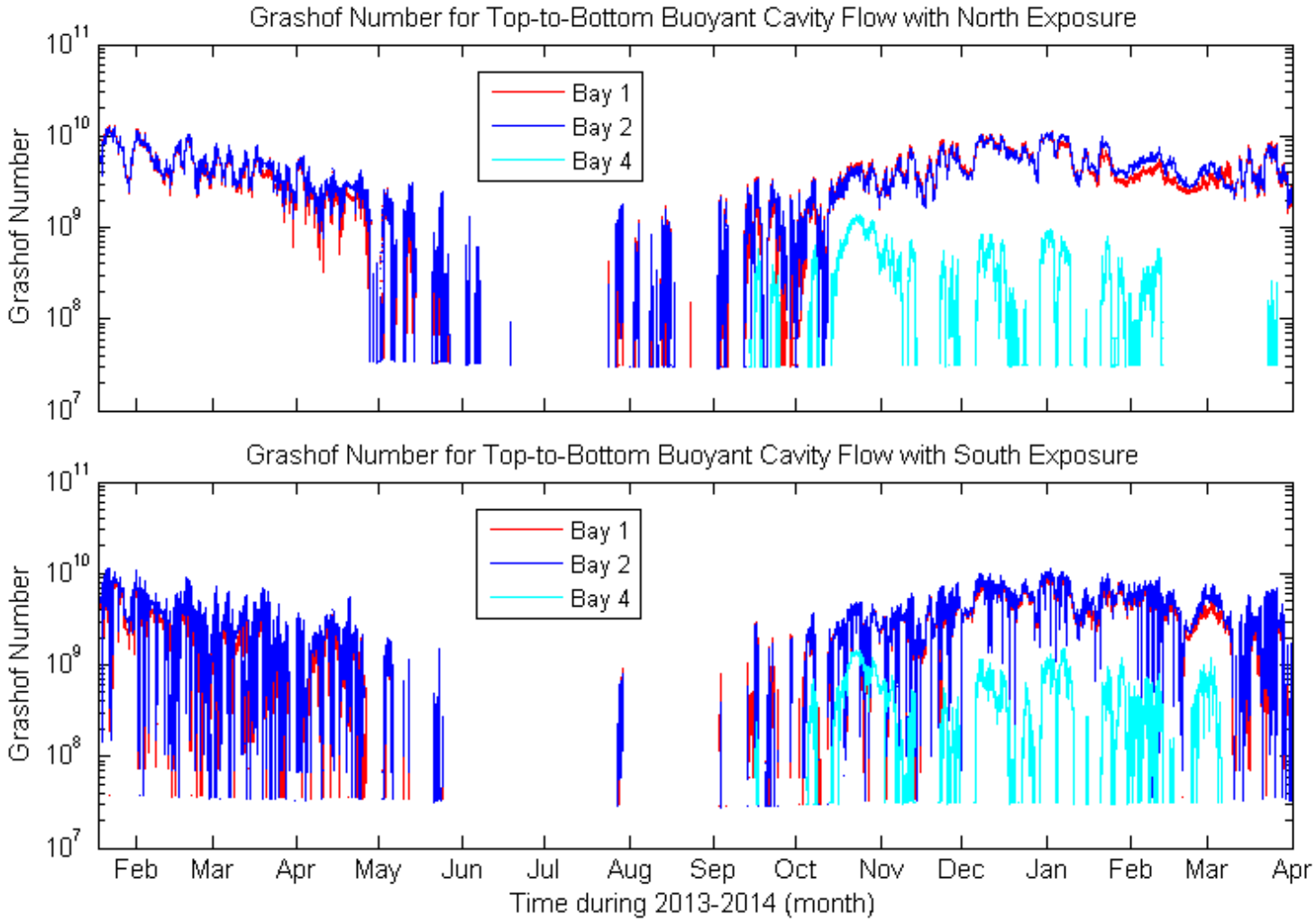

Figure 5-40: Grashof Number for Top to Bottom Buoyant Cavity Flow

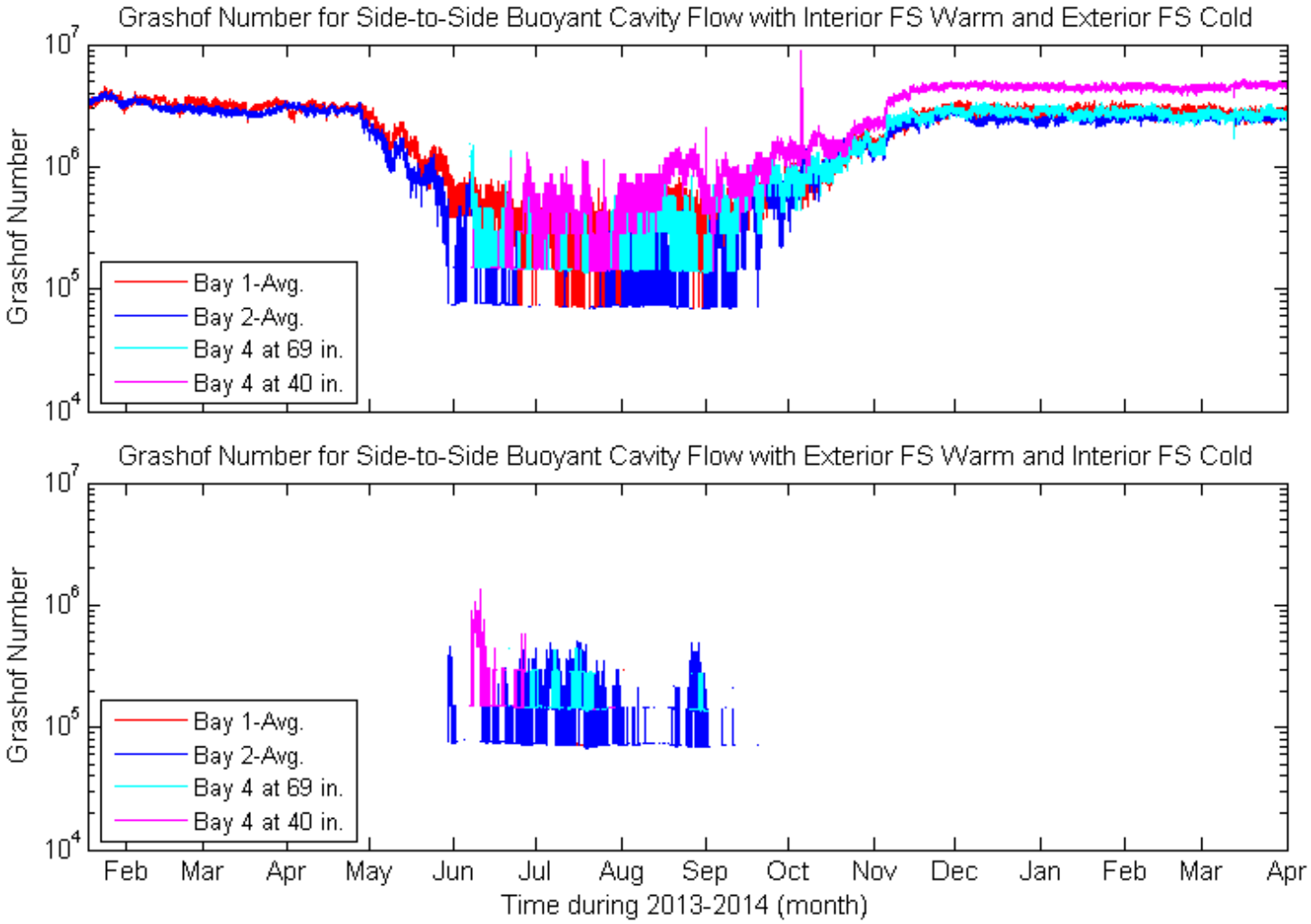

Figure 5-41: Grashof Number for Side-to-Side Buoyant Cavity Flow with North Exposure

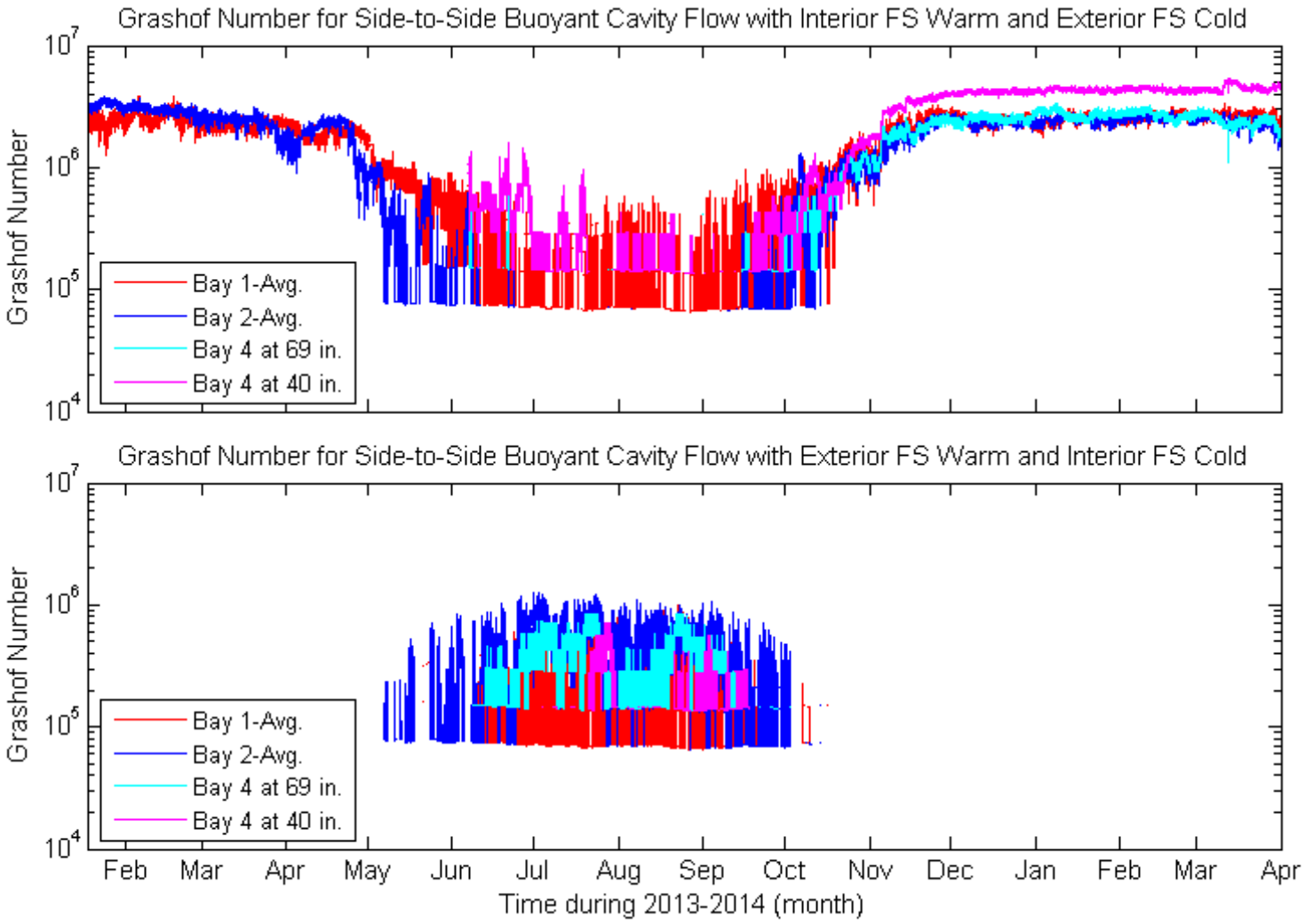

Figure 5-42: Grashof Number for Side-to-Side Buoyant Cavity Flow with South Exposure

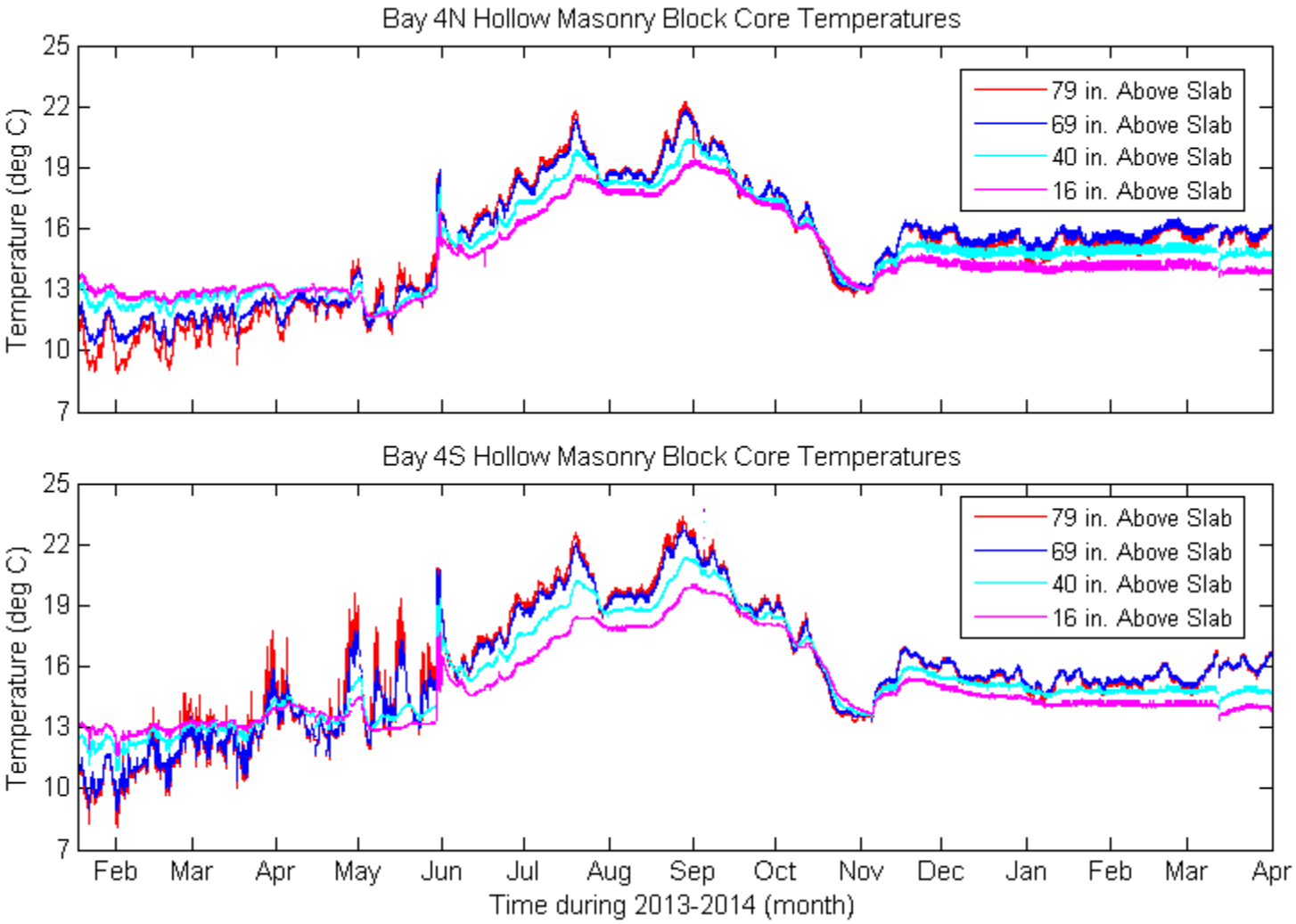

Figure 5-43: Bay 4N and 4S Hollow Masonry Block Core Temperatures

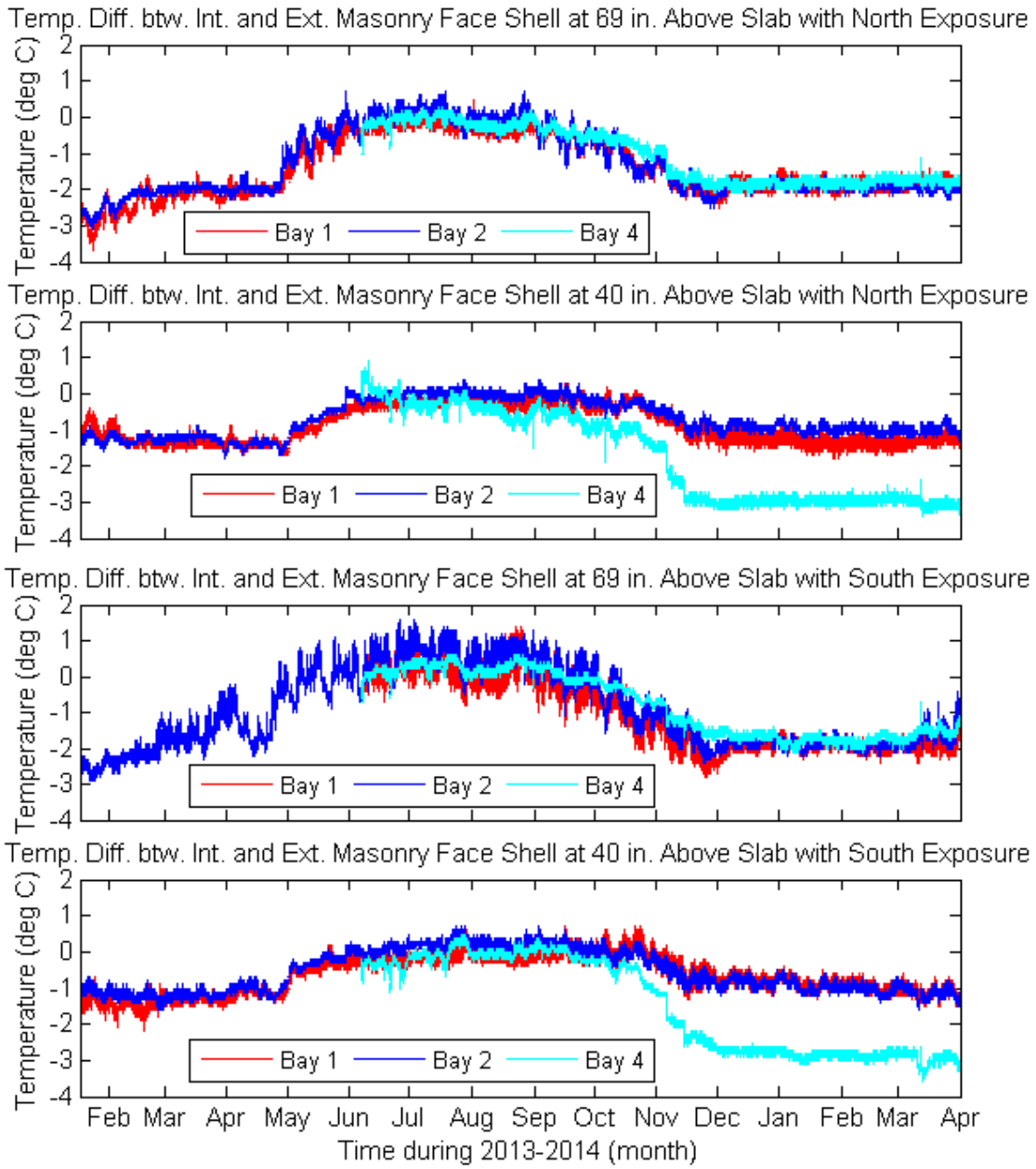

Figure 5-44: Temperature Difference between Interior and Exterior Masonry Face Shells

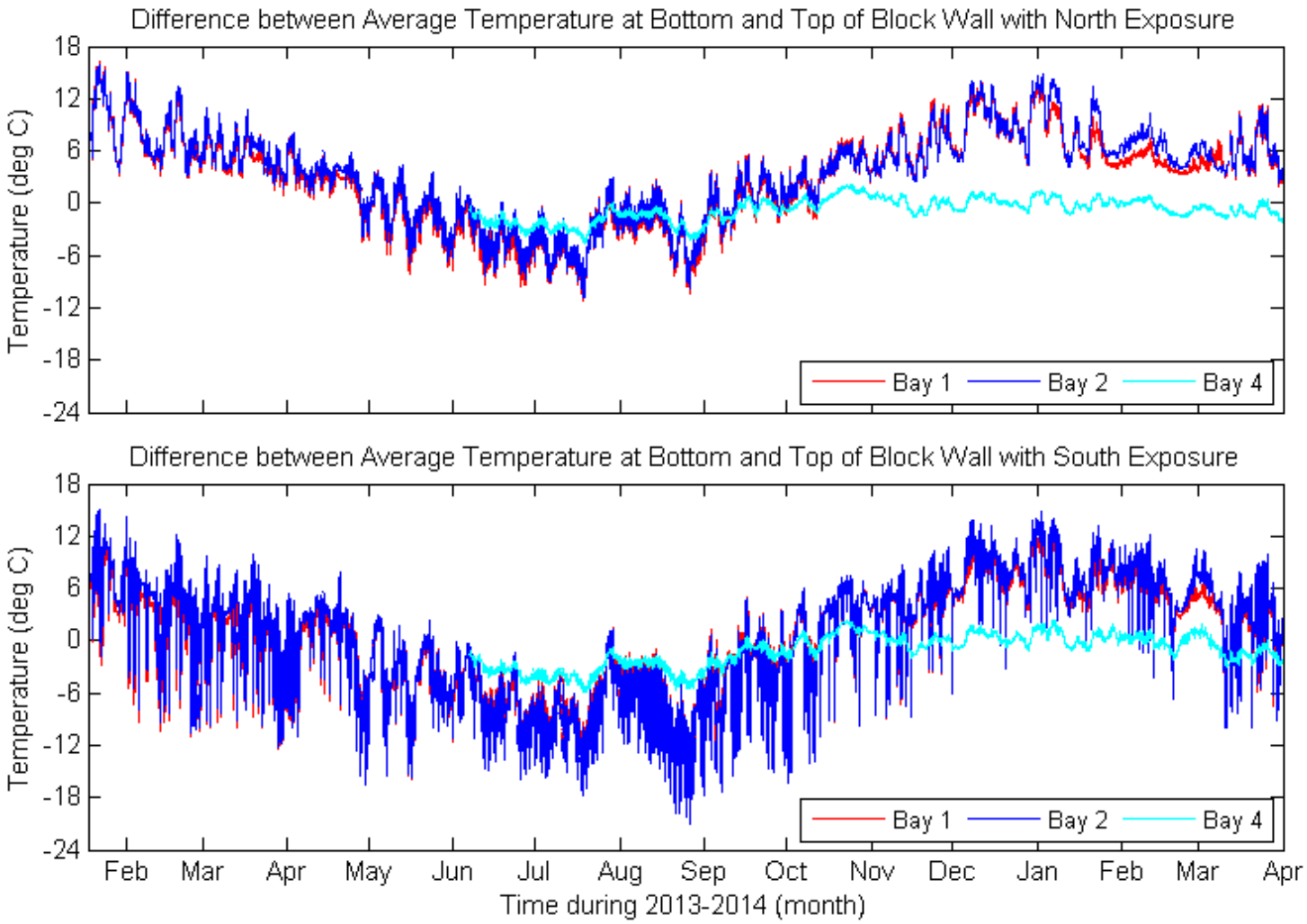

Figure 5-45: Difference between Average Temperature at Bottom and Top of Masonry Block Wall

5.5 Soil and Concrete Masonry Unit Wall Moisture Performance

5.5.1 Soil Moisture Performance

The soil volumetric moisture content 5 in. from the face of the wall and 5.5 in., 40 in., and 69 in. above the slab for Bays 1, 2, and 3 is shown in Figure 5-46 and Figure 5-47 for north and south exposures, respectively. From mid-January 2013 to April 2014, Bays 1N, 1S, and 3N had the highest soil moisture content at 5.5 in. above the slab. During the same time period, for Bays 2N, 2S, and 3S, the soil moisture contents at 5.5 in and 40 in. above the slab were approximately the same but greater than the soil moisture content at 69 in. above the slab. This was typical year round and did not change with the season. The average soil moisture content at 5.5 in. above the slab for Bay 1N was 28%, for Bay 1S was 22%, for Bay 2N and 2S was 5%, for Bay 3N was 17%, and for Bay 3S was 13%.

The flow of water in soil is dependent on the hydraulic potential, not on the moisture content gradient (Hanks and Ashcroft 1980). For like boundary conditions, the hydraulic potential profile is equivalent across soil types whereas the moisture content is not. The total hydraulic potential includes gravitational, matric, and pressure potentials. The matric potential of a soil is dependent on the attraction of soil and water molecules and the attraction between water molecules resulting in surface tension (Jury, Gardner, and Gardner 1991). For a given matric potential a loam has a larger volumetric moisture content than a sand.

Across the height of the soil, the loam soil (Bay 1) had the highest moisture contents, then the sand with silt (Bay 3), and the sand (Bay 2) had the lowest moisture contents. This follows what is expected for different soil types with equivalent hydraulic potential. The capillary rise due to the matric potential was the greatest in the loam soil as was evident by the decrease in soil moisture content from the soil at 5.5 in. to 40 in. above the slab (approx. 8%). The sand with silt soil (Bay 3) showed evidence of capillary rise on the north side with an approximate 3% decrease in soil moisture content from the soil at 5.5 in. to 40 in. above the slab. The sand (Bay 2) did not show any evidence of capillary rise because the soil moisture contents at 5.5 in. and 40 in above the slab were approximately equal.

The moisture content at 5.5 in. above the slab was greater than the moisture content at 69 in. above the slab regardless of season for Bays 1, 2, and 3. Seasonal rain and snow melt never caused the soil at 69 in. above the slab to have the highest moisture content for any prolonged period of time. This reinforced the presence of a high water table because the moisture source was from the deep ground versus the surface.

From June 2013 through April 2014, soil moisture content data was available for all bays. During this time period, the soil moisture contents at 5 in. from the face of the wall at all heights (5.5 in., 40 in., and 69 in. above the slab) varied between approximately 17% and 30% for Bay 1N, 12% and 26% for Bay 1S, 4 % and 8% for Bay 2N, 3% and 7% for Bay 2S, 12% and 20% for Bay 3N, and 10% and 16% for Bay 3S (Figure 5-46 and Figure 5-47). The range in soil moisture content across the height of the wall was approximately 13% for Bay 1, 4% for Bay 2, and 7% for Bay 3. The high moisture contents and large difference in moisture contents across the height in Bay 1 indicate that loam is a poorly drained soil compared to sand (Bays 2 and 3).

Figure 5-48 shows the difference in soil moisture content between the north and south exposures for Bay 1 and Figure 5-49 shows the difference in soil temperature between the north and south exposures for Bay 1. At 69 in., 40 in., and 5.5 in. above the slab the soil moisture content on the north side of Bay 1 was approximately 6%, 2%, and 4% greater than on the south side, respectively. The soil temperatures at 69 in. and 40 in. above the slab on the south side were warmer than on the north side from April 2013 to December 2013. At 5.5 in. above the slab, the south soil temperatures were warmer than the north from mid-July 2013 to December 2013. From December 2013 to mid-March 2013 the soil temperatures on the north side were warmer than the south side at all levels and from mid-January 2013 to mid-March 2013 the soil temperatures on the north and south side were approximately the same at all levels. April 2013 to December 2013 showed a greater variation in the soil moisture content across all heights and at 69 in. above the slab showed a greater diurnal temperature variation than during the remainder of the experimental period. The temperature of the soil at the weather station (open field) 4 in. below the surface was greater than 0 deg. C from May 2013 to December 2013 (Figure 5-49).

From approximately April 2013 to December 2013 when the soil surface was not frozen, there was greater evaporation on the south side than on the north side of the building due to increased solar exposure. Evaporation at the soil surface decreased the surface moisture content, in turn decreasing the moisture content across the depth of the soil. This caused the soil moisture contents on the south side to be lower than on the north side.

During the heating season, the depth of the ground water table appeared to remain relatively constant. This is evident because the soil moisture content at 5.5 in. above the slab, that was influenced to a greater extent by the ground water table due to its proximity, remained fairly level. Typically, it might be expected that the ground water table would drop during the heating season when it is not recharged by liquid precipitation and run-off. However, this did not appear to be the case for the CRRF. Knowing the height and variation in the height of the water table is a critical element for any below-grade thermal or hygrothermal model as is discussed in Chapters 5.3 and 6.2.

During the heating season, the moisture contents across the depth of the soil had little variation. The majority of the precipitation during this season was in the form of snow, thus reducing the infiltration of liquid water. There was likely some snow melt at the ground /snow boundary, however, it was likely insignificant as the soil moisture contents at 69 in. above the slab were relatively steady during the heating season (Figure 5-46 and Figure 5-47). The moisture contents on the south side of the building remained lower than on the north side. During the heating season the soil temperatures on the north side of the building were warmer than on the south side because the higher snow pack on the north side (Figure 5-5) provided more insulation. During this time, no change in the relative soil moisture contents between the north and south could be seen in the data. For this reason it can be deduced that the difference in soil temperatures between the north and south sides of the building had a negligible effect on the difference in soil moisture content. Instead the difference in moisture contents between the north and south during the heating season was primarily impacted by the moisture content of the soil prior to snow accumulation and this difference in moisture content was influenced by evaporation at the soil surface due to solar irradiance.

Bay 2 showed a similar phenomenon but to a lesser extent (Figure C-1 and Figure C-3). The soil moisture contents on the north side were greater than on the south side at 69 in. above the slab and at 40 in. and 5.5 in. above the slab they were approximately the same. This is because sand is a well-drained soil, so surface effects do not influence the full depth of the soil profile the way they do in a loam soil (Bay 1). In Bay 3, the north soil moisture contents were larger than the south soil moisture contents at all heights (Figure C-2) and the north versus south temperature profiles (Figure C-4) were similar to Bay 1.

The soil temperature at 5.5 in., 40 in., and 69 in. above the slab for Bays 1, 2, and 3 for the north and south exposures is graphed in Figure 5-50 and Figure 5-51, respectively. The ground temperature at 69 in. above the slab in Bays 1S and 2S neared 0 deg. C once in mid-January 2013. On the north side of the building, the soil at 69 in. above the slab in Bays 1 and 2 neared or reached 0 deg. C twice, once in mid-January 2013 and once in early February 2013. The freezing temperatures coincide with a sharp drop in the soil moisture content (Bay 2S went all the way down to 0% MC) (Figure 5-46 and Figure 5-47). Also, in mid-January 2013 and once in early February 2013, were the only times that the weather station temperature at 4 in. below grade (far field) dropped below -2 deg. C (Figure 5-49).

These observations can be explained as follows: as the temperatures were clearly below 4 deg. C, the soil entered the anomalous freezing zone in which the water expands prior to freezing solid. Thus the moisture content data were closely coupled to the soil temperature. When the soil water froze and turned to ice, the soil sensors were not calibrated to determine the soil moisture content (ice and water) and the sensor read low, because it was not accounting for the ice as moisture. The soil moisture content sensors are a dielectric permittivity sensor. This type of sensor relies on water having a high permittivity compared to the other soil materials. The dielectric permittivity of the components of soil can be found in Table 5-2. The large difference in dielectric permittivity between water and ice caused the sensor to yield low moisture content readings as temperatures approached 0 deg. C.

	Dielectric Permittivity
Dry Soil [13]	1-5
Pure Water (20 deg. C)[13]	78.54
Air	1
Ice	3.2

Table 5-2: Dielectric Permittivity of Soil Components

The sensors in Bays 1 and 2 were installed 12 in. below grade in August 2012. With settlement they may have been as deep as $21^{7}/_{8}$ in. in Bay 1 and $14^{5}/_{8}$ in. in Bay 2 (Table 3-3). Rain and snow melt helped to compact the soil. Some of the compaction would have occurred in 2012 prior to the ground freezing, but likely much of the settlement occurred in the spring and summer of 2013 during the highest periods of snow melt and rain fall. For this reason, the sensors were likely not fully settled in January/February of 2013. Since the temperature of the soil was near 0 deg. C, the frost line never reached the upper-most soil sensor. The far field temperature at 4 in. below grade only dropped below -2 deg. C twice, supporting the conclusion that the frost line was relatively shallow adjacent to the insulated and heated building.

For the remainder of the experimental period, the ground at the soil sensors was not frozen as is evident by soil temperatures greater than 0 deg. C and no sharp drops in the soil moisture content. Therefore the soil moisture content readings were accurate as there was no ice present with the exception of the brief periods mentioned in January and February 2013, and the frost line was above the upper soil sensor.

Figure 5-52 and Figure 5-53 show the soil volumetric moisture content at 40 in. above the slab and approximately 5 in., 18 in., and 32 in. away from the wall for Bays 1N/2N and 1S/2S. The soil moisture content profiles show high variability. There was no consistent pattern to the magnitude of the moisture contents as a function of distance from the wall.

Because of the inconsistency, no pattern was determined as to how the water infiltrates and percolates through the soil based on soil type or exposure. This prevented a model

[13] Source is Stevens Water Monitoring System, Inc. 2007

from being developed based on the experimental data. A variety of factors affected the water infiltration and percolation and any model would need to account for these factors. The infiltration rate of sand is higher than loam. There was more vegetation on the north side of the building. There was an 18 in. roof overhang that sheet-drained water from the roof to the ground below. The force of the falling water created a trough in the soil below the overhang. The troughs were deeper on the south side of the building .The native sand (Bays 3 and 4) had the deepest troughs and the imported sand (Bay 2) had the shallowest, the loam (Bay 1) fell between the two. The cribs containing the imported soils were constructed of an impermeable material that was located 36 in. from the face of the wall and extended from approximately 4 in. above the grade to the top of the footing elevation, so all the water impinging on the soil surface of the crib drained through the soil contained within it.

In April 2013, Bays 1N and 2N both showed a spike in soil moisture content across all heights of the wall (Figure 5-46) and at all distances from the wall (Figure 5-52). Bay 2S showed the same phenomenon in late-February 2013 (Figure 5-47 and Figure 5-53). In April 2013, Bay 1S had a spike in soil moisture content at 69 in. above the slab (Figure 5-47) and at 40 in. above the slab and 32 in. away from the wall (Figure 5-53). There was no spike at 5.5 in. above the slab or 40 in. above the slab at 5 in. and 18 in. from the wall; instead at these levels there was a gradual increase in moisture content from mid-March 2013 to June 2013.

The spikes in soil moisture content in late-February 2013 and April 2013 roughly coincide with when the ground thawed. The increased moisture content was due to infiltration from snow melt. Bays 1N, 2N, and 2S showed a consistent increase in moisture content across all heights and widths. However, Bay 1S lacked this uniformity. The spike occurred at some locations in the soil but not consistently with depth. This reinforces the unpredictability of moisture infiltration and percolation and the difficulty in creating a standard model.

In conclusion, the frost depth adjacent to a heated building with interior insulation and hollow CMU walls is generally shallow (<22 in. at the CRRF). The water table has a significant impact on the moisture content of the soil adjacent to a basement wall, even when the water table is below the bottom of the basement wall. It is critical to know the

height and variation in height of the water table for thermal and hygrothermal below-grade models. In this experiment it was found that the annual water table depth was fairly constant. Further, it is difficult to predict and model the infiltration and percolation of water through the soil adjacent to a building owing to the randomness of the flow paths inherent in soils as well as the randomness of the surface percolation rates.

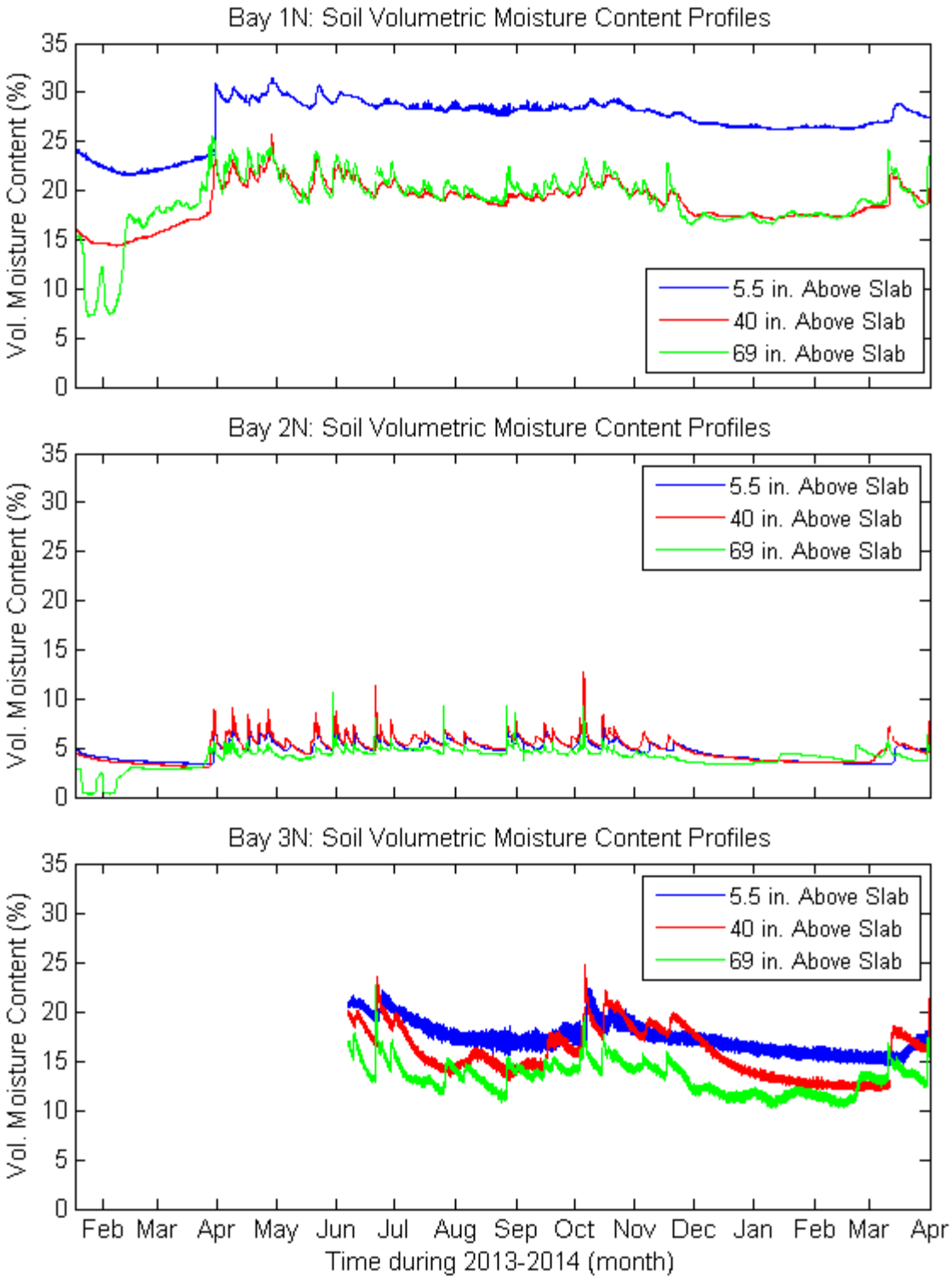

Figure 5-46: Soil Volumetric Moisture Content Profiles across the Height of the Wall at 5 in. from the Face of the Wall for North Exposures

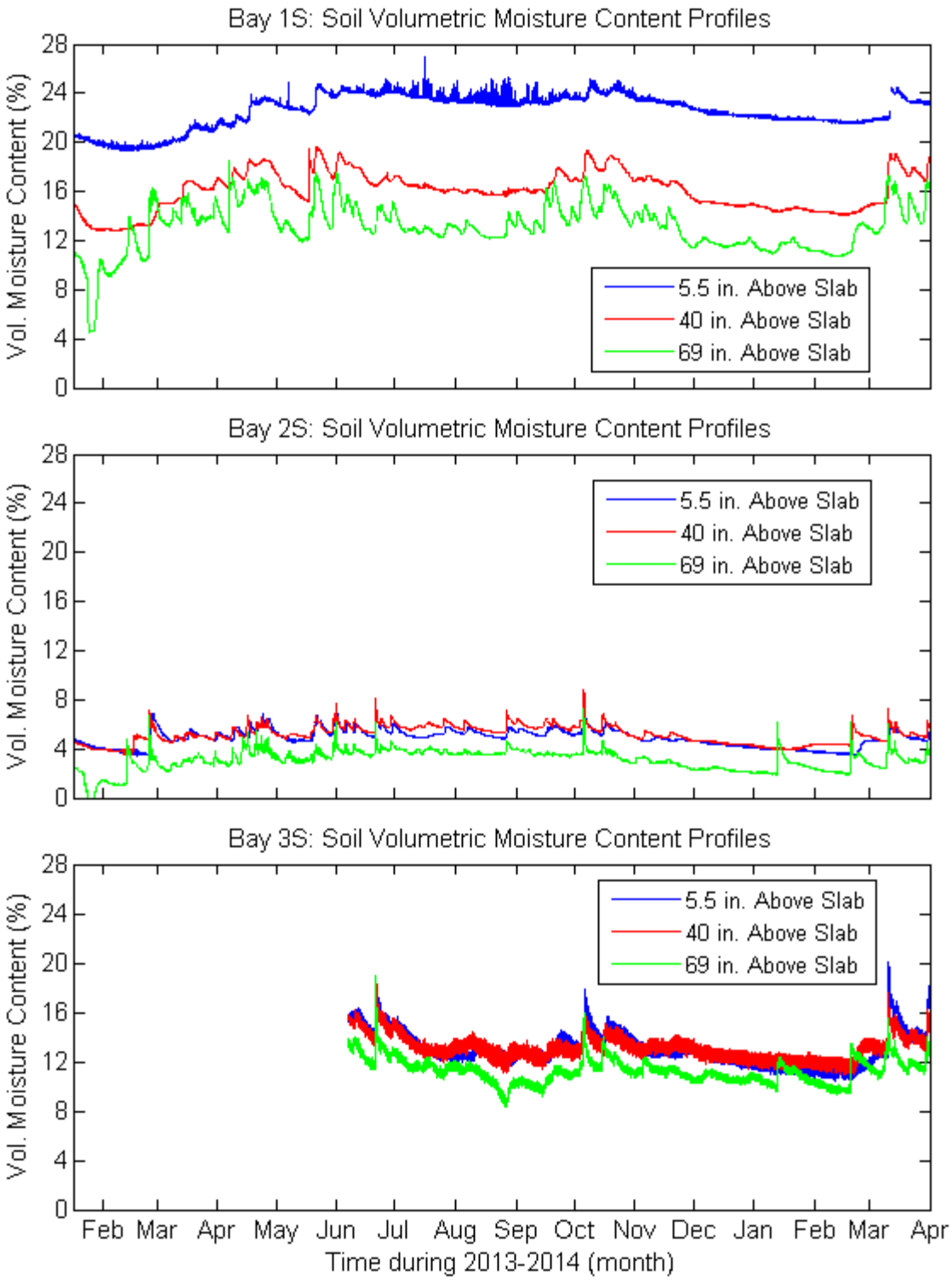

Figure 5-47: Soil Volumetric Moisture Content Profiles across the Height of the Wall at 5 in. from the Face of the Wall for South Exposures

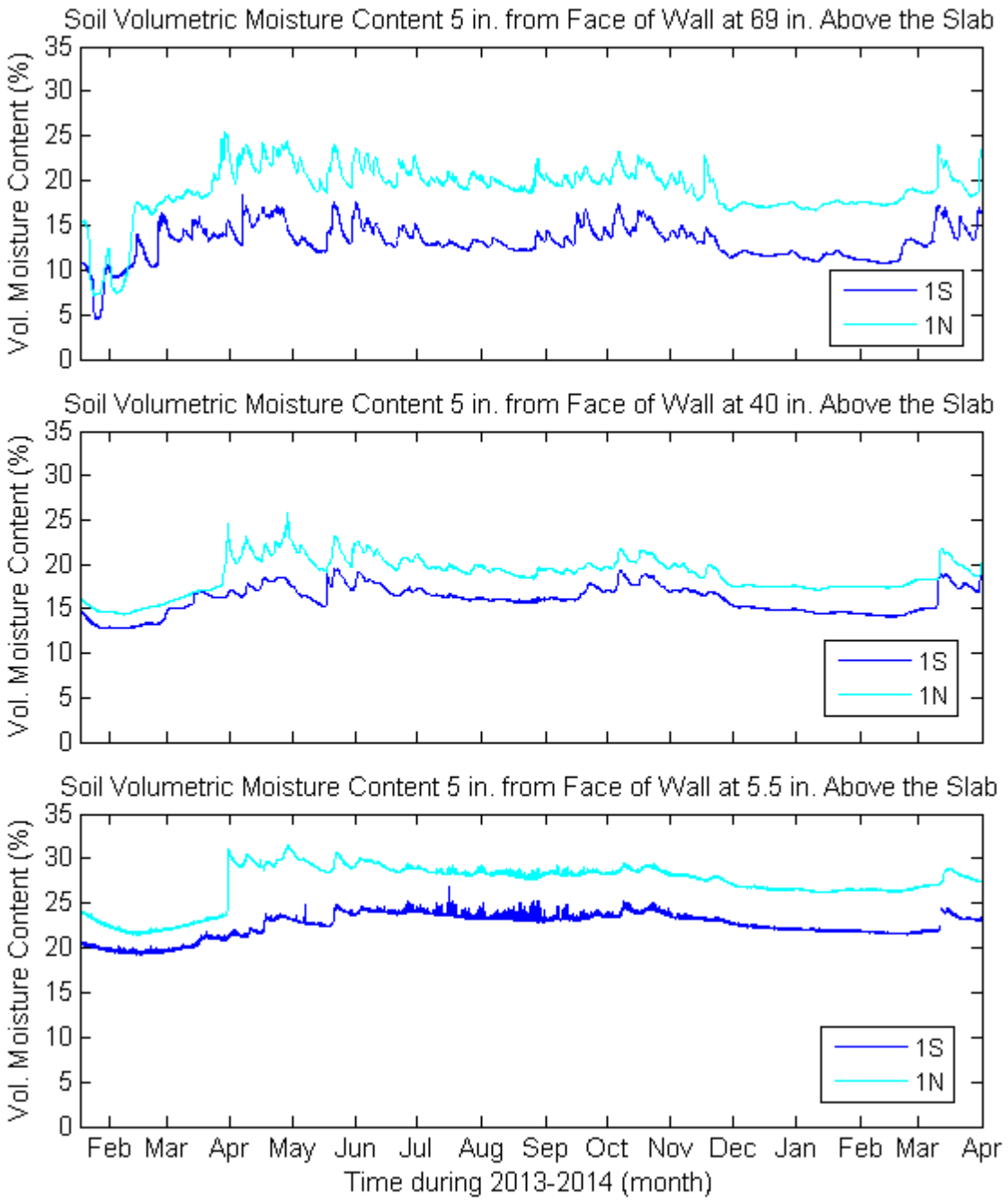

Figure 5-48: Bay 1 Soil Volumetric Moisture Content across the Height of the Wall at 5 in. from the Face of the Wall for North and South Exposures

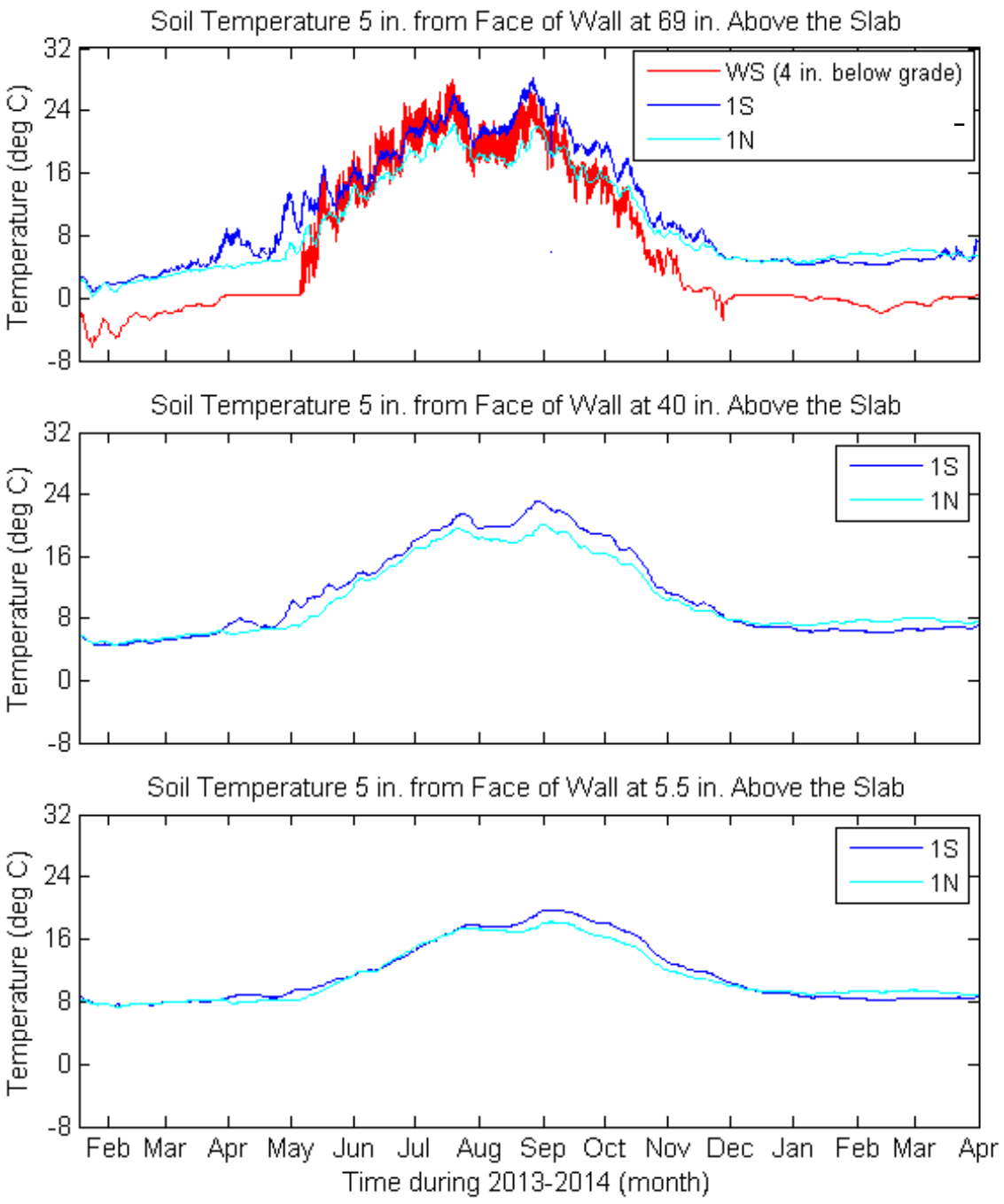

Figure 5-49: Weather Station (WS) and Bay 1 Soil Temperatures across the Height of the Wall at 5 in. from the Face of the Wall for North and South Exposures

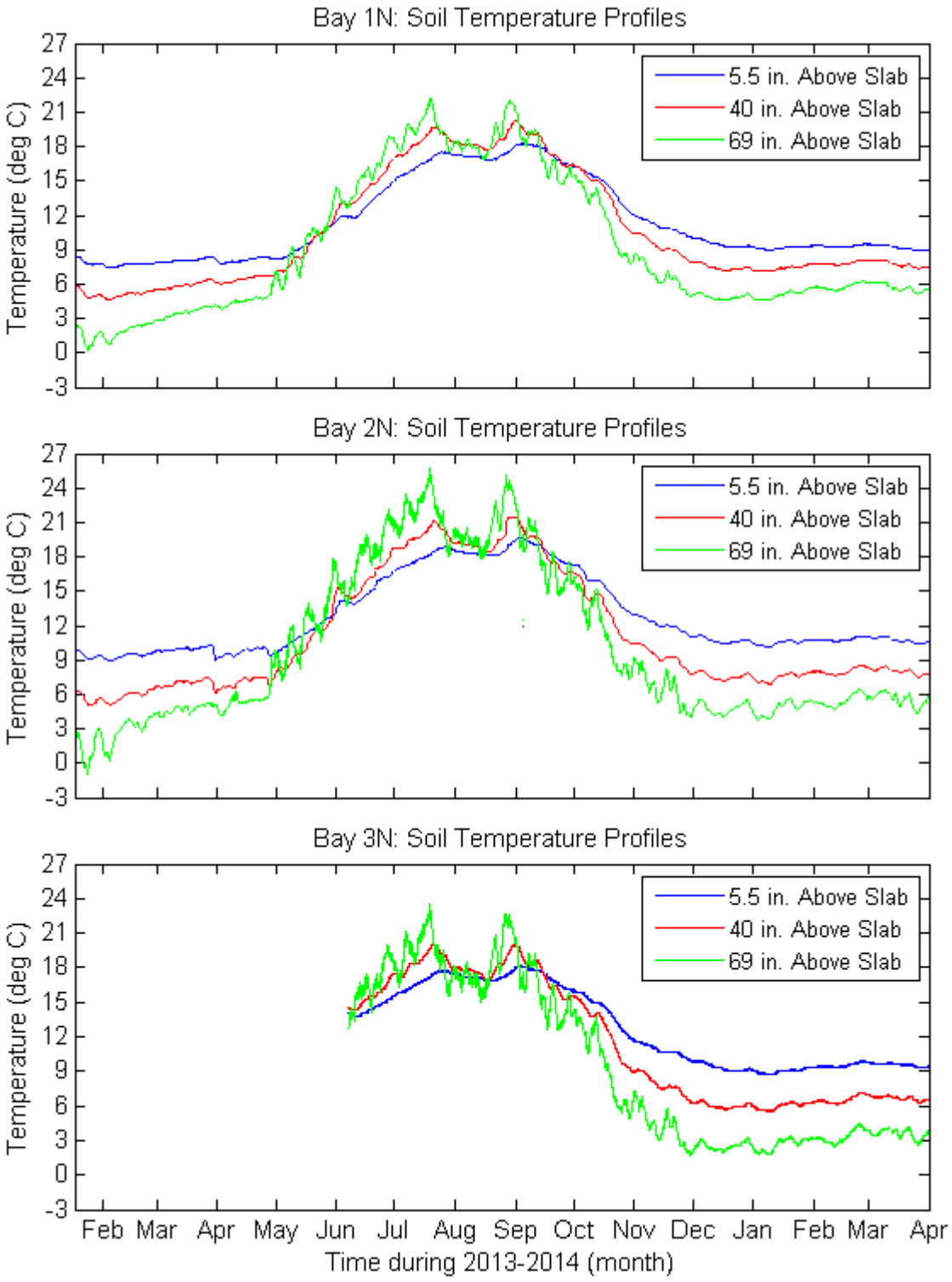

Figure 5-50: Soil Temperature Profiles across the Height of the Wall at 5 in. from the Face of the Wall for North Exposures

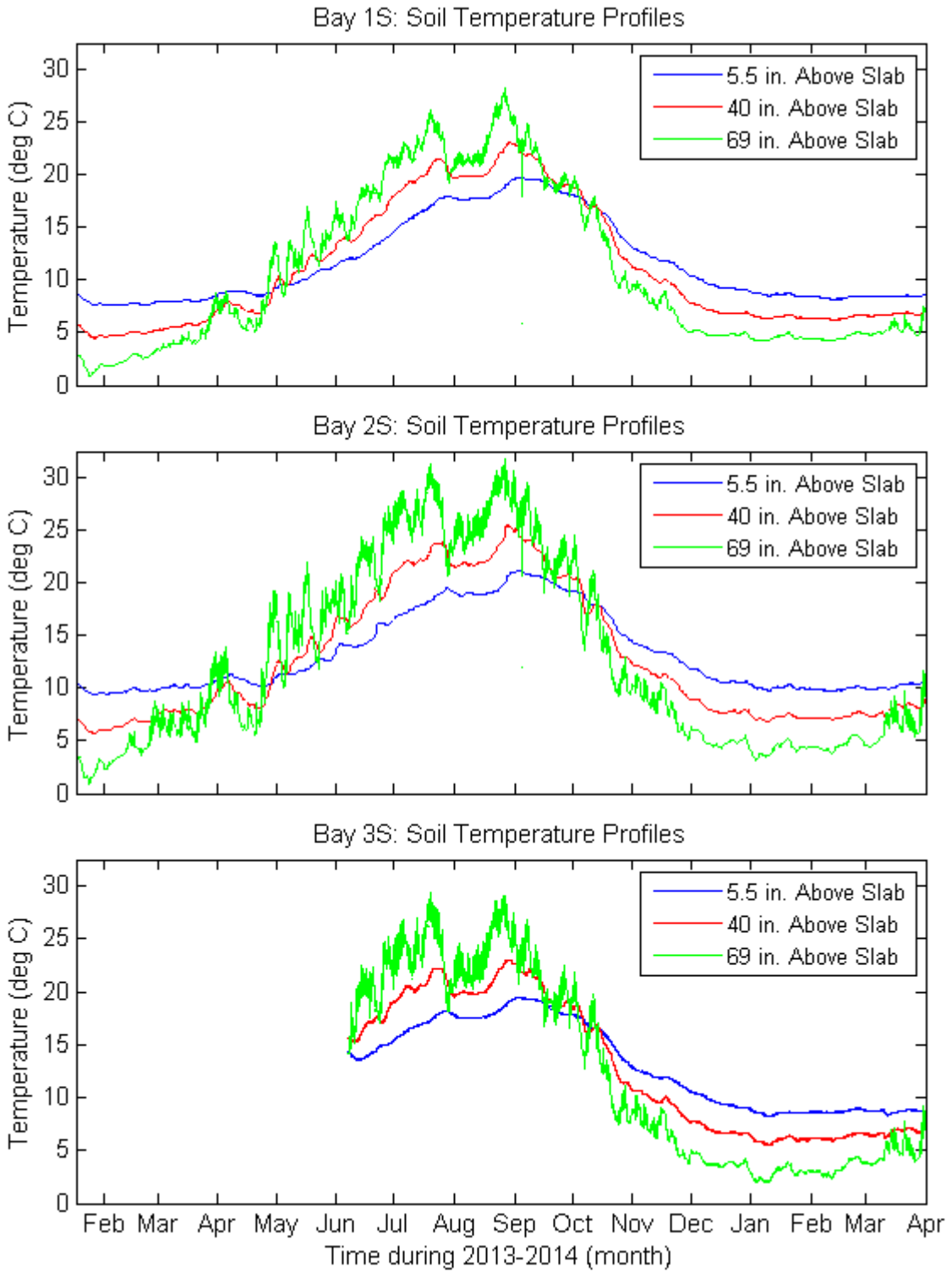

Figure 5-51: Soil Temperature Profiles across the Height of Wall at 5 in. from the Face of the Wall for South Exposures

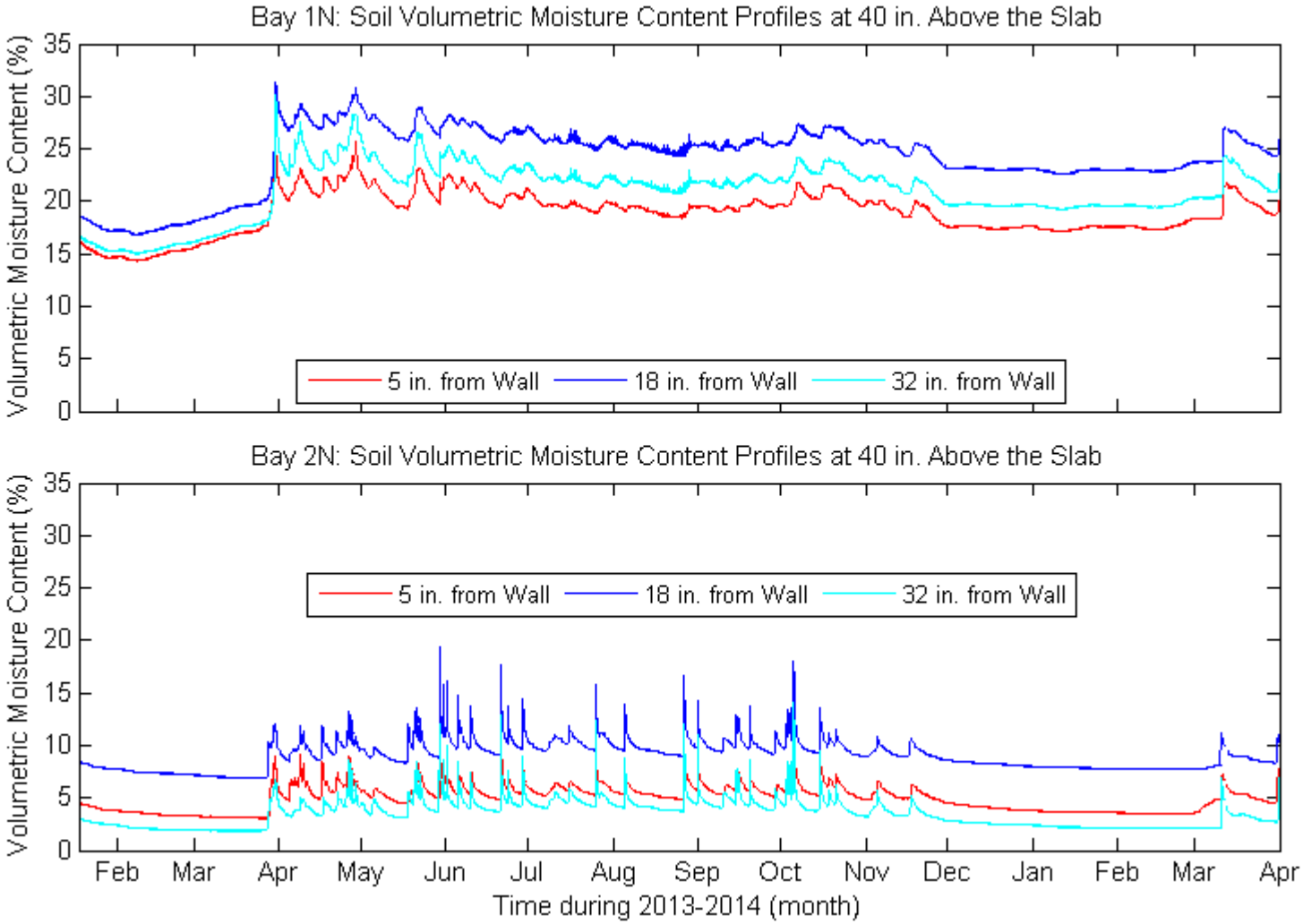

Figure 5-52: Soil Volumetric Moisture Content Profiles at 40 in. Above the Slab for North Exposures

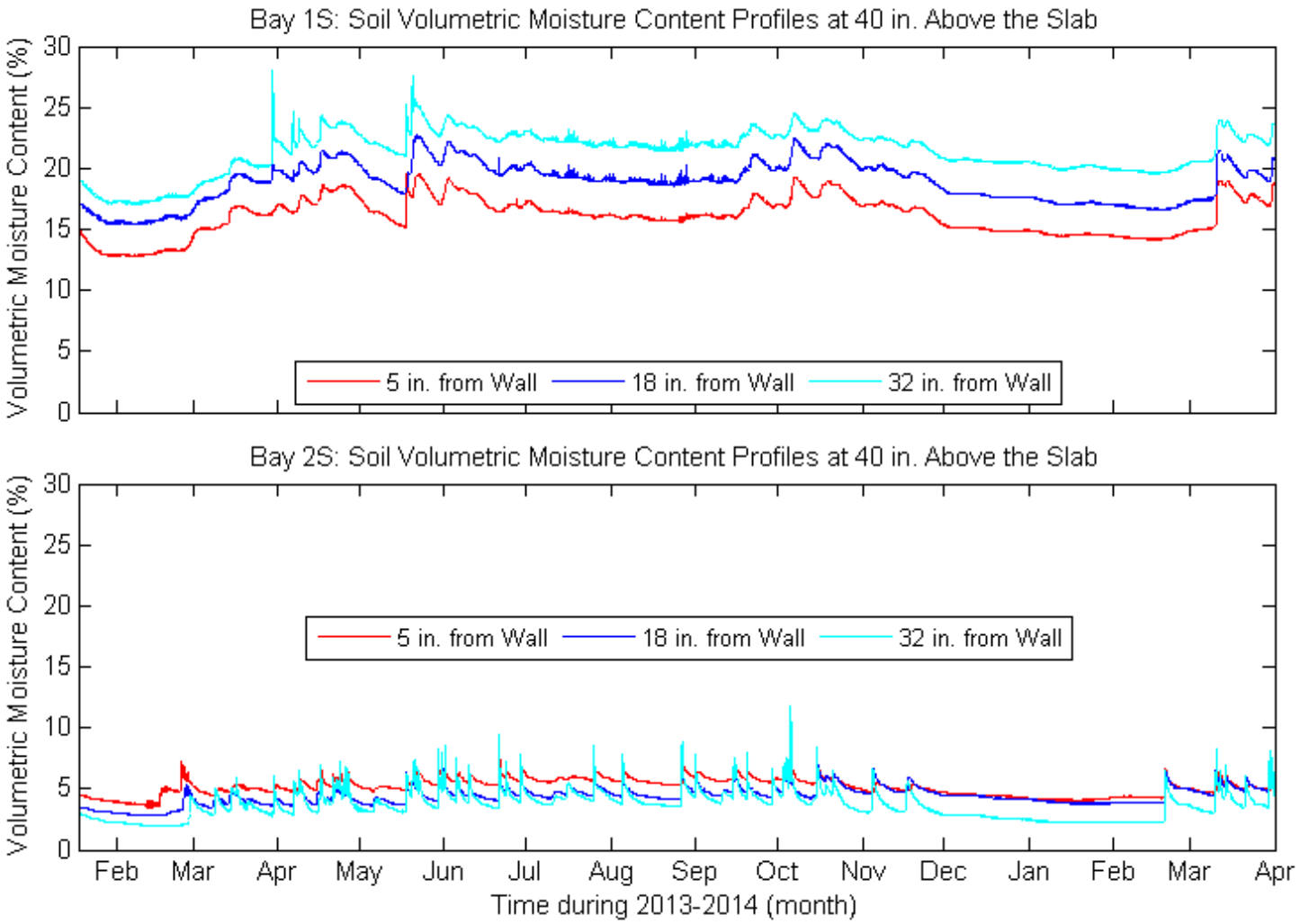

Figure 5-53: Soil Volumetric Moisture Content Profiles at 40 in. Above the Slab for South Exposures

5.5.2 Concrete Masonry Unit Wall Moisture Performance

The moisture content of the concrete masonry unit (CMU) wall was examined in terms of volumetric moisture content. The volumetric moisture content is the ratio of the volume of water to the total volume of the material (solids, water, and air). The experimental wall had a porosity of 11.73%. Therefore a volumetric moisture content of 11.73% was equivalent to 100% saturation across the sensor.

Between September 4, 2013 and October 11, 2013 water was injected between the water separation plane and the CMU wall on Bay 3. A one to two second pulse of water was injected every 1.5 to 2 hours during this period. A one second pulse equated to approximately 14-16 mL of water. The water was injected at approximately 75 in. above the slab.

Figure 5-54 graphs the wall moisture profile including the soil, the exterior face shell, the hollow core, and the interior face shell at 5.5 in., 40 in., and 69 in. above the slab for Bay 2S. The exterior face shell moisture content at 5.5 in., 40 in., and 69 in. above the slab had abrupt drops in moisture content during the experimental period. In late September 2013, the sensor at 69 in. above the slab dropped from approximately 4.5% to approximately 2% moisture content after a series of oscillations between the two values. The moisture content then remained fairly constant. In mid-February 2013 and early April 2013, the moisture content at 40 in. and 5.5 in. above the slab, respectively, had sharp drops in the moisture content from approximately 6% to approximately 2% moisture content. After the drops, both moisture contents remained fairly constant with occasional spikes.

Figure 5-55 shows the interior and exterior CMU face shell moisture contents for Bay 4. Around July 2013 in Bay 4S, the exterior face shell moisture contents at 5.5 in. and 40 in. above the slab had sharp drops in moisture content from approximately 10% to 2%. The moisture contents then remained level at approximately 2%, with the exception of a few spikes at 40 in. above the slab between February 2013 and April 2013. The exterior face shell moisture content sensor at 69 in. above the slab did not have an abrupt change in moisture content. It instead showed smooth variation in moisture content that varied between approximately 3.5% and 7%.

The same abrupt drop in moisture contents followed by a lower, constant moisture content also occurred for the exterior face shell moisture contents at 5.5 in., 40 in. , and 69 in. above the slab in Bays 1N, 1S, 2N, 3N, and 3S (Figure 5-58, Figure C-5, Figure 5-57, Figure 5-56, and Figure C-6). This phenomenon also occurred in Bay 4N for the exterior face shell moisture contents at 5.5 in. and 40 in. above the slab (Figure C-7). Figure 5-56 shows wall moisture profiles at 5.5 in, 40 in., and 69 in. above the slab for Bay 3N. At 40 in. above the slab on the interior face shell, moisture content abruptly dropped from approximately 7% to 3% in late-September 2013. All the abrupt drops occurred at varying times throughout the experimental time period.

The exterior face shell moisture content in Bay 4S at 69 in. above the slab was wetter than the example face shell at 5.5 in. and 69 in. above the slab (Figure 5-55) for the majority of the experimental time period. Intuitively, this does not make sense since the insulation acted as waterproofing and should have reduced the transport of bulk soil water to the wall. The abrupt drops in moisture content only occurred at sensors that were exposed to wet conditions. This included all the sensors exposed to soil and the interior face shell sensor at 40 in. above the slab on 3N during the period of water injection. The Bay 4 exterior face shell moisture content sensors at 69 in. above the slab that had 3 in. of rigid insulation between them and the soil did not have the abrupt drop in moisture content.

The abrupt drop in face shell moisture content to a steady low moisture content and the randomness of when a sensor experienced the sudden drop indicates that the sensor failed. The sensor reading was based on a correlation between electrical conductivity and moisture content. The conductivity of water is large compared to air. The abrupt drops indicate that suddenly there was more air between the electrodes or there was poor contact between the electrodes and the block. This could have occurred from the electrically conducting graphite paste around the graphite rod breaking down. It is speculated that the paste was water-based,[14] hence, prolonged exposure to water would have dissolved the paste thus reducing the contact between the graphite rod and

[14] No specifications listing this level of detail for the graphite paste used could be found. The paste was chosen for its low cost as the non-water based epoxy alternatives used silver (not graphite) as the conducting material and were prohibitively expensive for the amount required to build the experiment.

the CMU. Alternatively, a crack could have formed in or around the graphite rod that was not bridged by water. Prior to failure (first abrupt drop), the moisture content followed a smooth profile that appears to be physically reasonable and thus may be used for analysis.

During the winter months when the exterior face shell moisture content was fairly constant, Bay 2N (Figure 5-57) and Bay 1N (Figure 5-58) each had two sudden drops in moisture content at 69 in. above the slab. One was in mid-January 2013 and the other in early February 2013. These drops in moisture content corresponded with a drop in the soil moisture content. As discussed earlier in this section, the drop in soil moisture content was due to the water in the soil freezing. The drops in the moisture content in the exterior face shell were similarly caused by the water (part or all) in the block freezing. The conductivity of water is greater than that of ice. Since the block moisture content sensor reading was based on a correlation between electrical conductivity and moisture content, a reduced conductivity due to the presence of ice resulted in a drop in the moisture content reading. The reduced moisture content reading accounted for liquid water but not for ice. The sensor was not calibrated to account for ice as moisture, although in the future it would be possible to account for ice as moisture by calibrating the block in freezing conditions. This was the only time this phenomenon occurred in Bays 1-3 for north and south exposures during the experimental time period.

Figure 5-59 and Figure 5-60 show the interior face shell moisture content and the hollow core absolute humidity for Bays 1 and 2 at 40 in. and 69 in. above the slab. At these locations, the face shell moisture content sensor and hollow core sensor are at the same nominal height, unlike the sensors at the top and bottom of the wall (5.5 in. and 86 in. nominal above the slab) where the hollow core sensors were offset due to filled cores. The interior face shell moisture content was approximately 4.5% or less and varied 2% or less throughout the experimental time period for Bays 1 and 2, north and south exposures (Figure 5-59 and Figure 5-60). Although the moisture content variation was small, it increased from June 2013 to August 2013 and decreased from September 2013 to December 2013. The hollow core absolute humidity increased and decreased over the same time frame as the interior face shell moisture content (Figure 5-59 and Figure 5-60).

At 69 in. and 40 in. above the slab the variation of the interior face shell moisture content followed the variation of the hollow core absolute humidity, indicating a direct correlation between the two. The local variations in absolute humidities were also seen in the interior face shell moisture contents with minimal time lag between the two, indicating that there was an almost immediate change in face shell moisture content in response to a change in the hollow core absolute humidity. The relationship between the face shell moisture content and the hollow core absolute humidity was due to capillary condensation and evaporation. The vapor pressure in the hollow core and the vapor pressure in the CMU face shell were in equilibrium and an increase in the mass of water vapor in the hollow core (increased absolute humidity) caused condensation in the pores of the face shell in order to maintain vapor pressure equilibrium. This resulted in an increase in the moisture content of the face shell. For the reverse, a decrease in the mass of water vapor in the hollow core caused evaporation in the pores of the face shell and a decrease in the face shell moisture content.

Bay 3 had a non-adhered WSP that formed a $^{1}/_{4}$ in. gap between the WSP and the face of the CMU wall. Figure 5-56 graphs the absolute humidity in this cavity along with the absolute humidity in the hollow core for Bay 3N at 40 in. and 69 in. above the slab. From January 2013 to mid-June 2013 the absolute humidity in the WSP-wall gap was approximately 1.5% less than in the hollow core and from mid-June 2013 to the end of the experiment, the two were almost identical. The same trend occurred in Bay 3S (Figure C-6). Figure 5-61 shows the Bay 3N relative humidity in the WSP-wall gap and the hollow core. At 40 in. and 69 in. above the slab, the hollow core relative humidity was 100% for almost the entire experiment. The WSP-wall relative humidity at 40 in. above the slab was approximately 80% and at 69 in. above the slab was approximately 90% from January 2013 to mid-June 2013, after which they both were at 100% relative humidity for the remainder of the experiment.

The early difference in absolute humidity was due to initial conditions after construction. The WSP was installed during November of 2013. Initially, the absolute humidity of the air between the WSP and wall would have been the same as the interior basement. Over time, diffusion through the face shell of the CMU brought the hollow core and WSP-wall gap into equilibrium. Once the two reached equilibrium, the absolute humidities of the two tracked each other throughout the remainder of the experiment.

The after-construction relative humidity in the WSP-wall gap was a function of the absolute humidity of the basement air and the temperature in the gap. The relative humidity remained fairly constant from January 2013 to June 2013 after which it increased to 100% relative humidity. The increase in relative humidity corresponded with an increase in the hollow core absolute humidity (Figure 5-56 and Figure 5-61). The drying potential in the WSP-wall cavity was small such that once the air space reached saturated conditions it did not drop below saturated conditions for the remainder of the experiment.

Water was injected in Bay 3 between the WSP and the CMU wall from September 4, 2013 to October 11, 2013. During this time period, the WSP-wall cavity absolute humidity did not increase above the hollow core absolute humidity, instead they maintained the same magnitudes (Figure 5-56). This occurred because the WSP-wall gap was already at 100% relative humidity when water injection began, so the air could not hold any more water vapor (Figure 5-61). Also, the absolute humidities of the hollow core and WSP-wall gap decreased during the water injection time period. Again, since the cavities were already at 100% relative humidity the air could not hold any more water vapor, so instead the trend in absolute humidly was correlated to the temperature. The temperature in the WSP-wall gap and hollow core decreased during this period (Figure B-5), thus decreasing the amount of water vapor the air could hold. This would have caused water vapor to condense out of the air and the absolute humidity to decrease.

By the time Bay 3 water injection began on September 4, 2013, all the exterior face shell moisture content sensors in Bay 3 had failed (Figure 5-56 and Figure C-6). Figure 5-62 shows the interior face shell moisture contents for Bay 3. During the period of water injection, the interior face shell moisture content sensor at 40 in. above the slab in Bay 3N failed and at a later date, after water injection was terminated, the interior moisture content sensors at 40 in. and 69 in. above the slab in Bay 3S also failed (Figure 5-62). The Bay 3N interior face shell moisture content at 5.5 in. and 40 in. above the slab spiked when water injection began, but in Bay 3S, the starting spikes were evident instead at 40 in. and 69 in. above the slab (Figure 5-62). In Bays 3N and 3S there was no change in the interior face shell moisture content at 86 in. above the slab at the start of water injection. The moisture content at 86 in. above the slab was at its

approximate maximum of 2.5% when water injection began and had little variation from this value for the remainder of the experiment (Figure 5-62).

The moisture content sensors at 86 in. above the slab were located above the water injection spray bar (located at approximately 75 in. above the slab), therefore they were not exposed directly to bulk water. This is evident because there was no spike in moisture content when water injection began. The spray bar was located in the $^{1}/_{4}$ in. gap created by the dimples of the WSP. This gap meant there was the potential for the water to drip down the WSP, the CMU wall, or both. The moisture content sensors below the spray bar that had spikes in moisture content were likely exposed directly to bulk water (3N and 3S at 40 in., 3N at 5.5 in., and 3S at 69 in.). Those that did not have large spikes were likely exposed to limited bulk water (3S at 5.5 in. and 3N at 69 in.). This was probably due to the angle of the spray and how the water dripped down the wall/WSP to the water collection trough at the base of the wall. The sensors that were exposed to bulk water showed a decrease in moisture content after the water injection period ended, however they did not return to their pre-water injection moisture content. In general, all sensors whether they were exposed to bulk water or not, stayed at elevated moisture contents for the remainder of the experiment. This indicates that the interior face shell requires a long time period to dry after wetting. The interior WSP prevented drying to the interior, so all drying had to occur to the exterior.

Prior to the failure of the exterior face shell moisture content sensors, the exterior face shell moisture content varied between approximately 6% and 10% for Bay 2N (Figure 5-57), 4% and 6% for Bay 2S (Figure 5-54), and 8% and 11% for Bay 3N (Figure 5-56). Bay 2N at 69 in. above the slab increased in moisture content from approximately May 2013 to July 2013 (Figure 5-57). Bay 2S at 69 in. above the slab increased in moisture content from approximately April 2013 to mid-July 2013 (Figure 5-54). The other exterior moisture content sensors did not have a long enough period of valid data for analysis.

The increase in exterior moisture content at 69 in. above the slab for Bays 2N and 2S occurred simultaneously with a general increase in the hollow core absolute humidity and the soil moisture content (Figure 5-57 and Figure 5-54, respectively). Local variations in the hollow core absolute humidity are mirrored in the exterior face shell

moisture content with a negligible time lag between the two. This phenomenon is the same as that between the hollow core absolute humidity and the interior face shell moisture content and is also attributable to capillary condensation and evaporation. Local variations in the soil moisture content are not mirrored in the exterior face shell moisture content. The exterior of the wall was coated with masonry parging and a bituminous damp-proofing that slowed the diffusion of water into the CMU face shell such that local variations in the soil moisture content did not immediately affect the face shell moisture content. However, the soil moisture content clearly influenced the exterior face shell moisture content. If the exterior face shell moisture content was only dependent on the hollow core absolute humidity, it would be expected that the interior and exterior face shells would have had the same moisture contents, but this was not the case. In all cases the exterior face shell moisture content was always greater than the interior face shell moisture content. Also, the exterior face shell moisture contents on walls with poorly drained soils (i.e. Bay 1 loam) were higher than on walls with well-drained soils (i.e. Bay 2 sand). Additionally, the face shells of the CMU blocks were connected by three webs that allowed for diffusion between the two face shells. Despite this link, the moisture contents varied significantly between the interior and the exterior face shells.

5.5.3 Conclusions

In a below-grade hollow core CMU wall with exterior, below-grade damp-proofing and interior insulation and waterproofing, the CMU interior and exterior face shell moisture contents were strongly correlated to the hollow core absolute humidity. A change in the absolute humidity resulted in an almost immediate change in the interior and exterior face shell moisture contents. The moisture in the soil elevated the moisture content of the exterior face shell. However, the exterior damp-proofing slowed the wetting process, such that the exterior face shell moisture content did not exhibit the same local variations in moisture content as the soil. Walls with poorly drained soils, such as loams, had higher exterior face shell moisture contents than walls with well-drained soils such as sands. In all cases the interior face shell was drier than the exterior face shell. The interior face shell in all bays and exposures stayed relatively dry (vol. MC < 34%) throughout the experiment and did not appear to be significantly impacted by exterior soil moisture conditions. However, if the interior face shell gets wet from bulk

water flow it does not readily dry. Below-grade walls with interior insulation and waterproofing may experience freeze thaw cycles in the exterior face shell just below grade. This potential exists in poorly and well drained soils.

The CMU moisture sensors failed in consistently wet conditions and further development of the sensors is needed. It should be determined if the graphite paste (Anders Products) that coated the graphite rods was water based. If it was water-based, a new electrically conducting paste would be required that would not break down from prolonged exposure to water. It also should be confirmed that the epoxy coating the electrode does not break down at cold temperatures. The electrode installation technique should be refined to ensure that the graphite rod penetrates to the base of the hole and does not crack. If this cannot be improved, other materials besides graphite should be explored. The failure of the exterior face shell moisture content sensors in this experiment limited the analysis of moisture performance in hollow CMU basement walls. A refined moisture content sensor would allow for significant additional information on the moisture content performance of basement walls to be obtained.

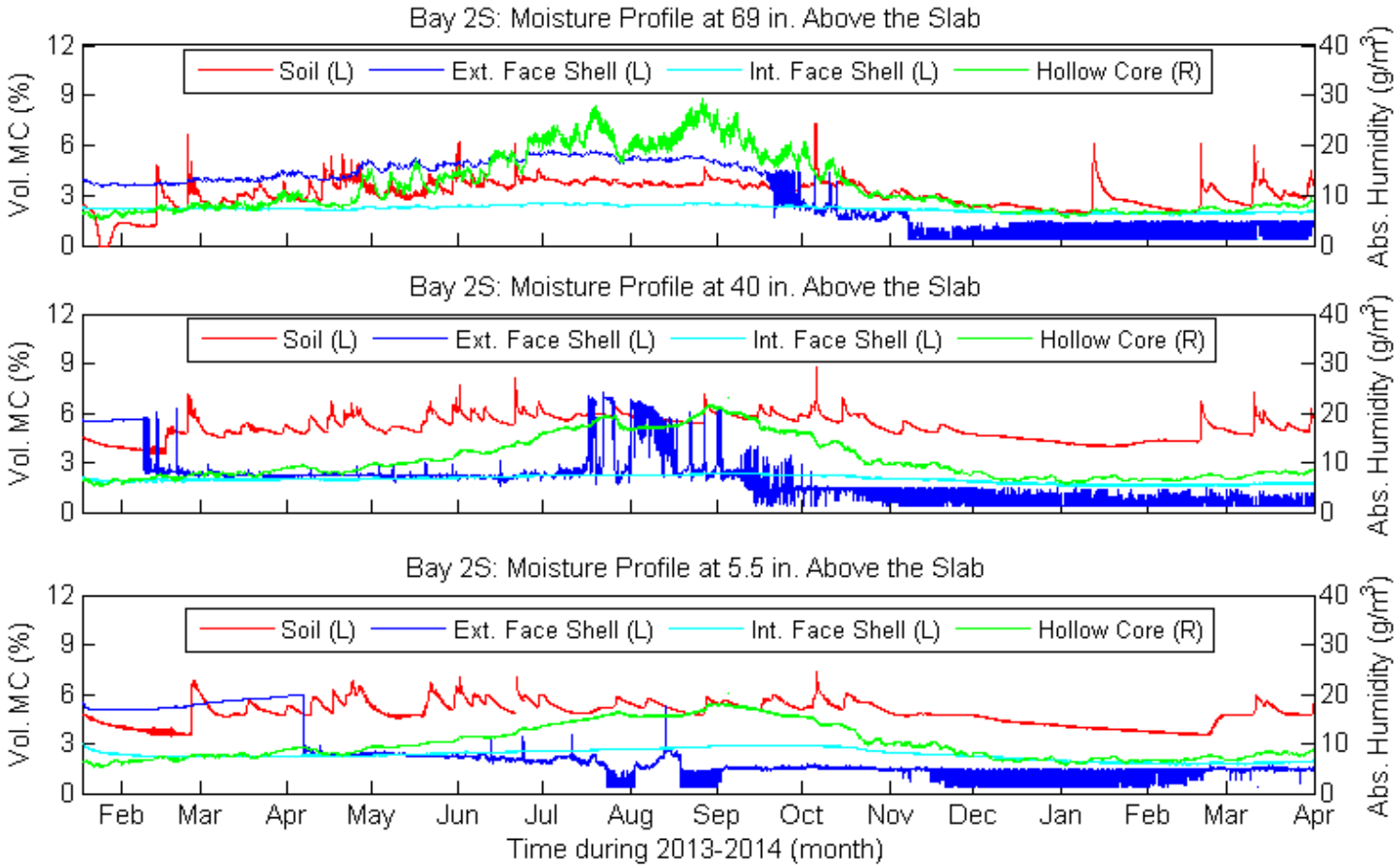

Figure 5-54: Bay 2S Moisture Profile[15]

[15] For the moisture profile 5.5 in. above the slab, the hollow core sensor is actually 16 in. above the slab.

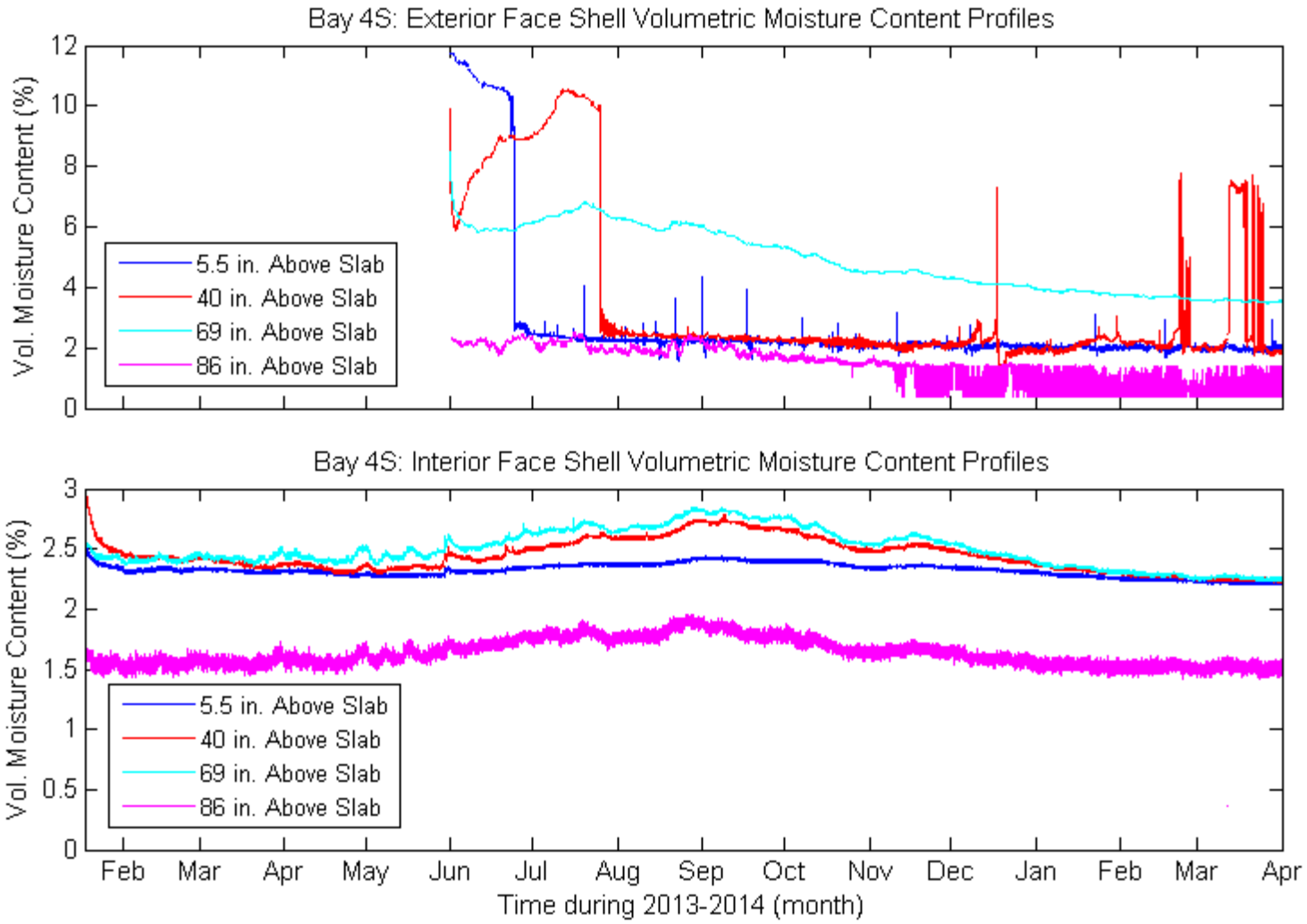

Figure 5-55: Bay 4S Exterior and Interior Face Shell Moisture Content Profiles

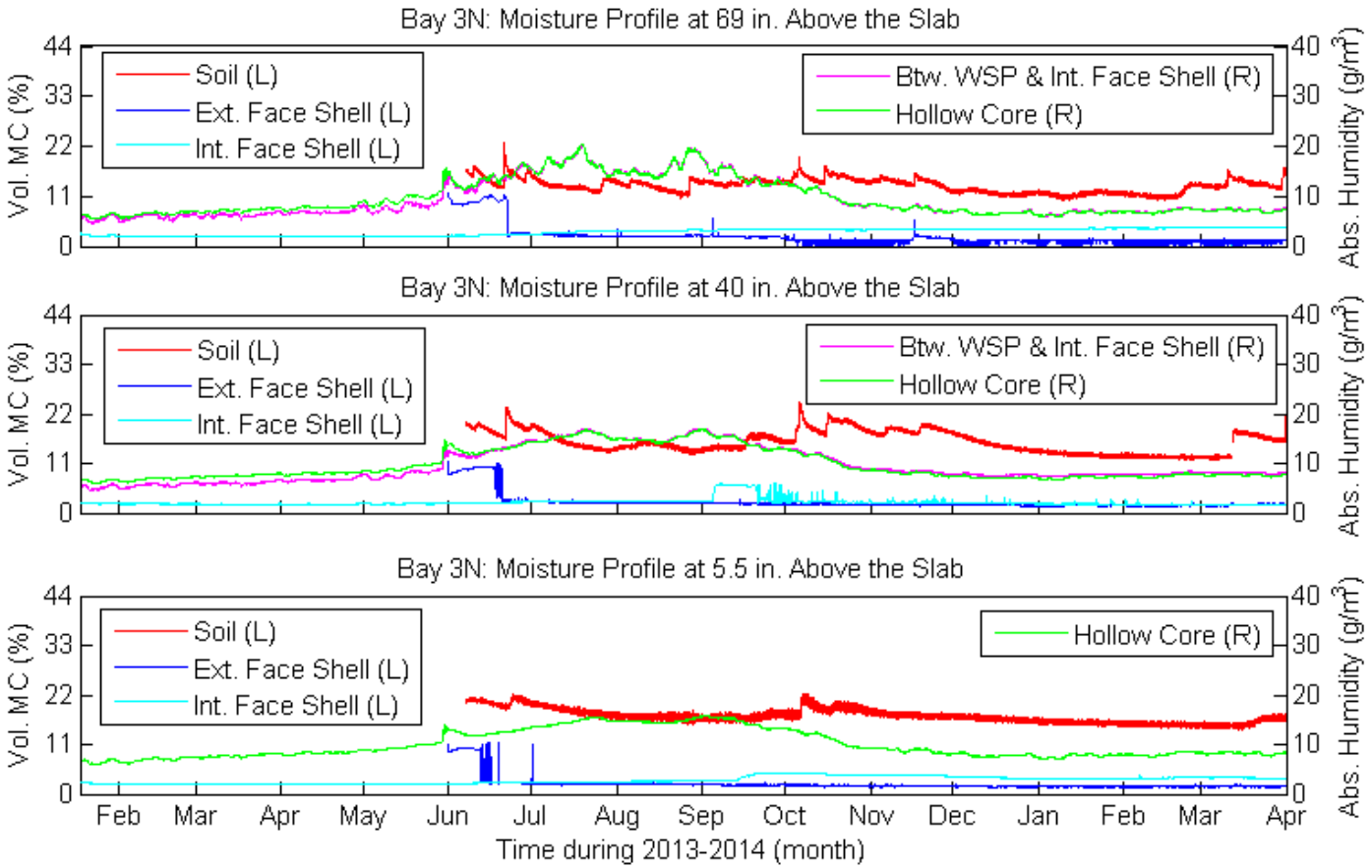

Figure 5-56: Bay 3N Moisture Profile[16] [17]

[16] Water was injected between the CMU and WSP from September 4, 2013 to October 11, 2013.
[17] For the moisture profile 5.5 in. above the slab, the hollow core sensor is actually 16 in. above the slab.

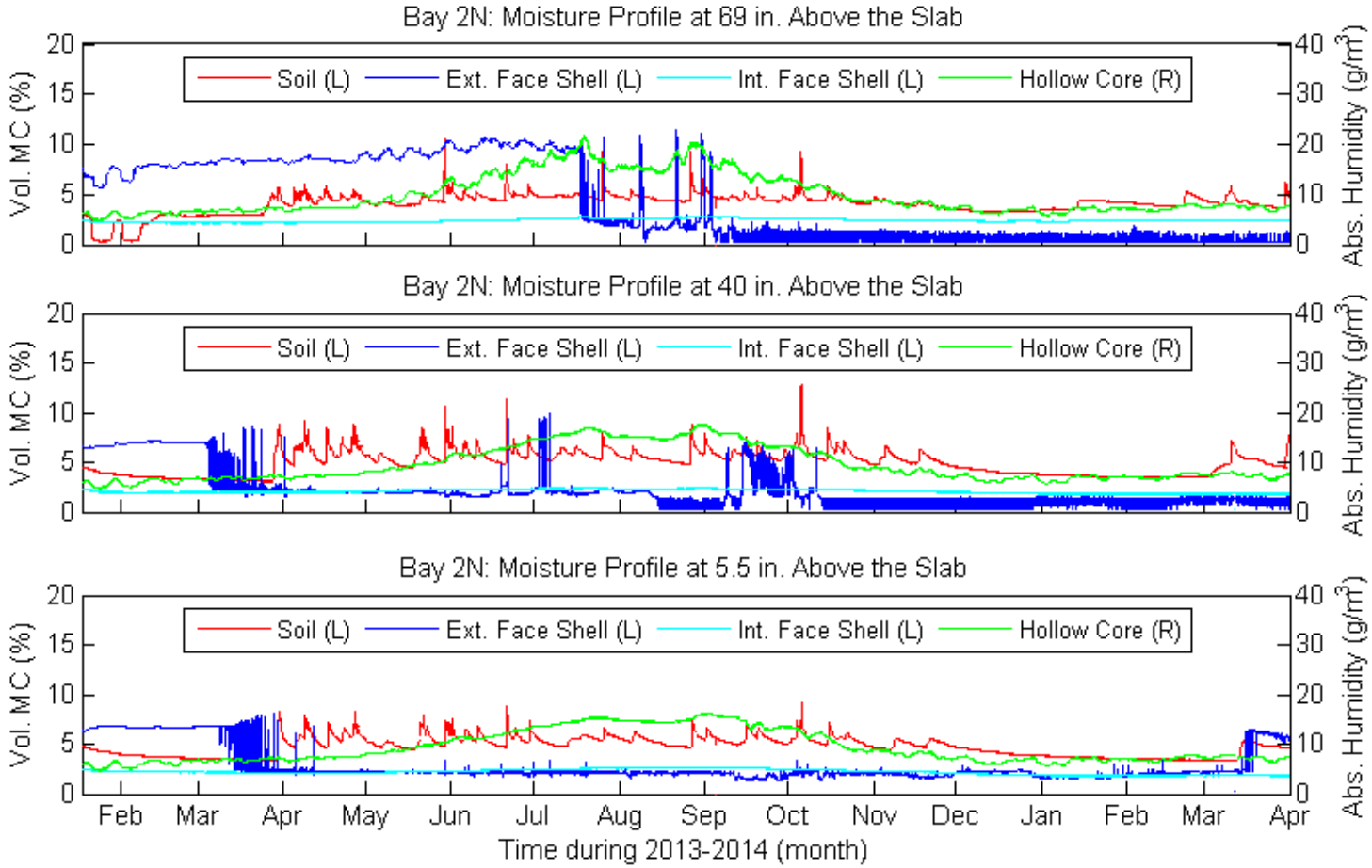

Figure 5-57: Bay 2N Moisture Profile[18]

[18] For the moisture profile 5.5 in. above the slab, the hollow core sensor is actually 16 in. above the slab.

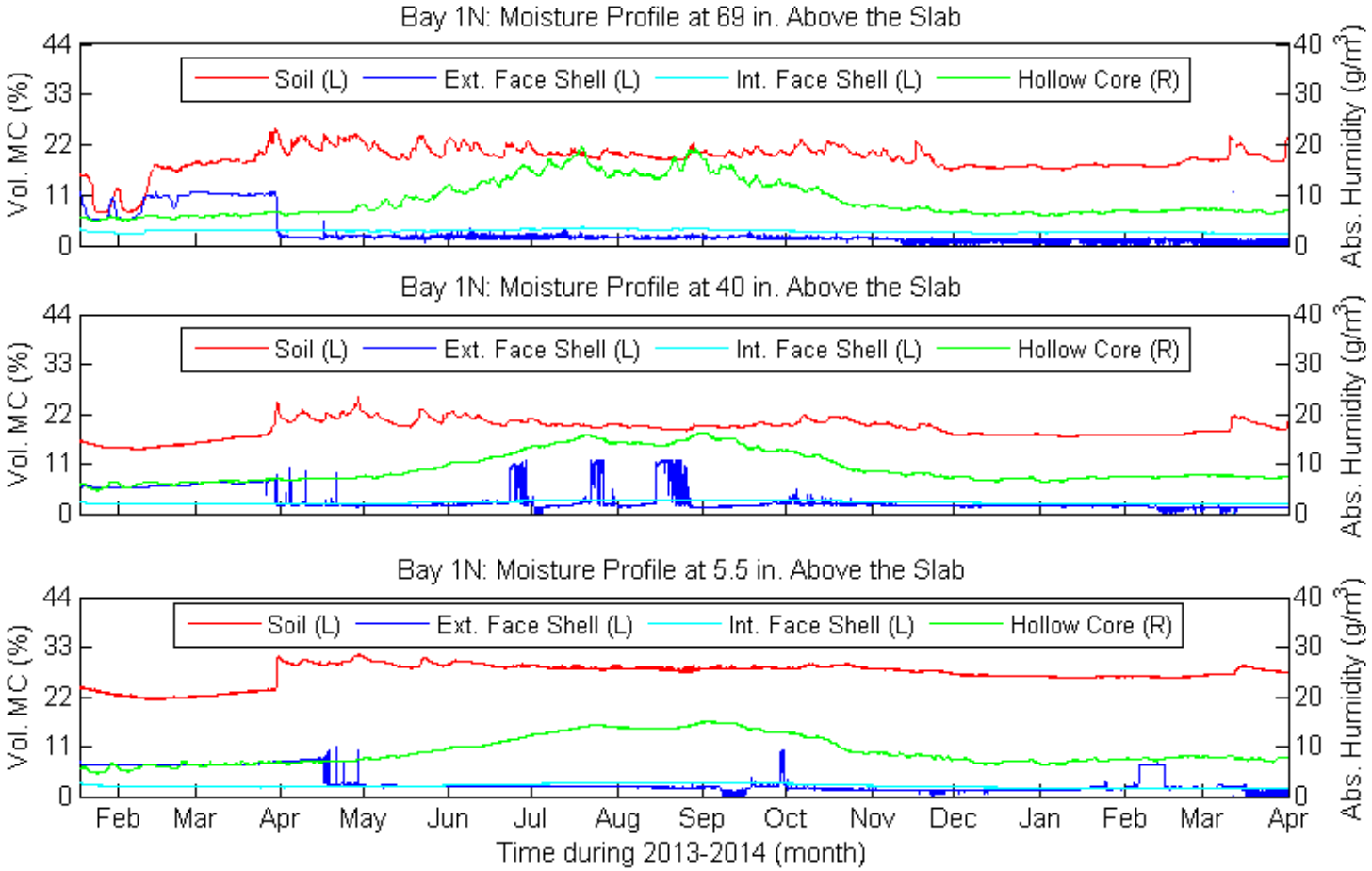

Figure 5-58: Bay 1N Moisture Profile[19]

[19] For the moisture profile 5.5 in. above the slab, the hollow core sensor is actually 16 in. above the slab.

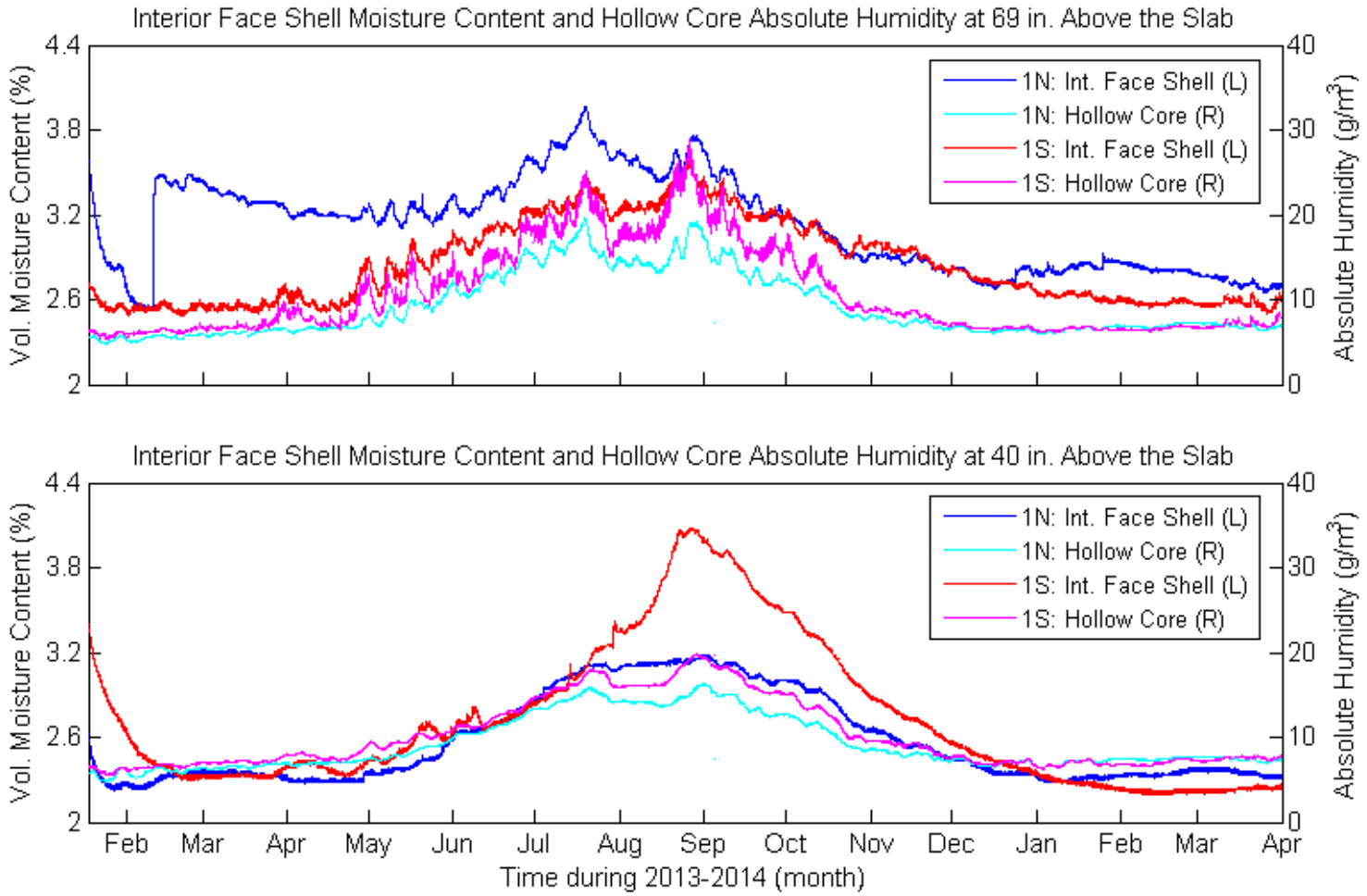

Figure 5-59: Bay 1 Interior Face Shell Moisture Content and Hollow Core Absolute Humidity at 40 in. and 69 in. above the Slab for North and South Exposures

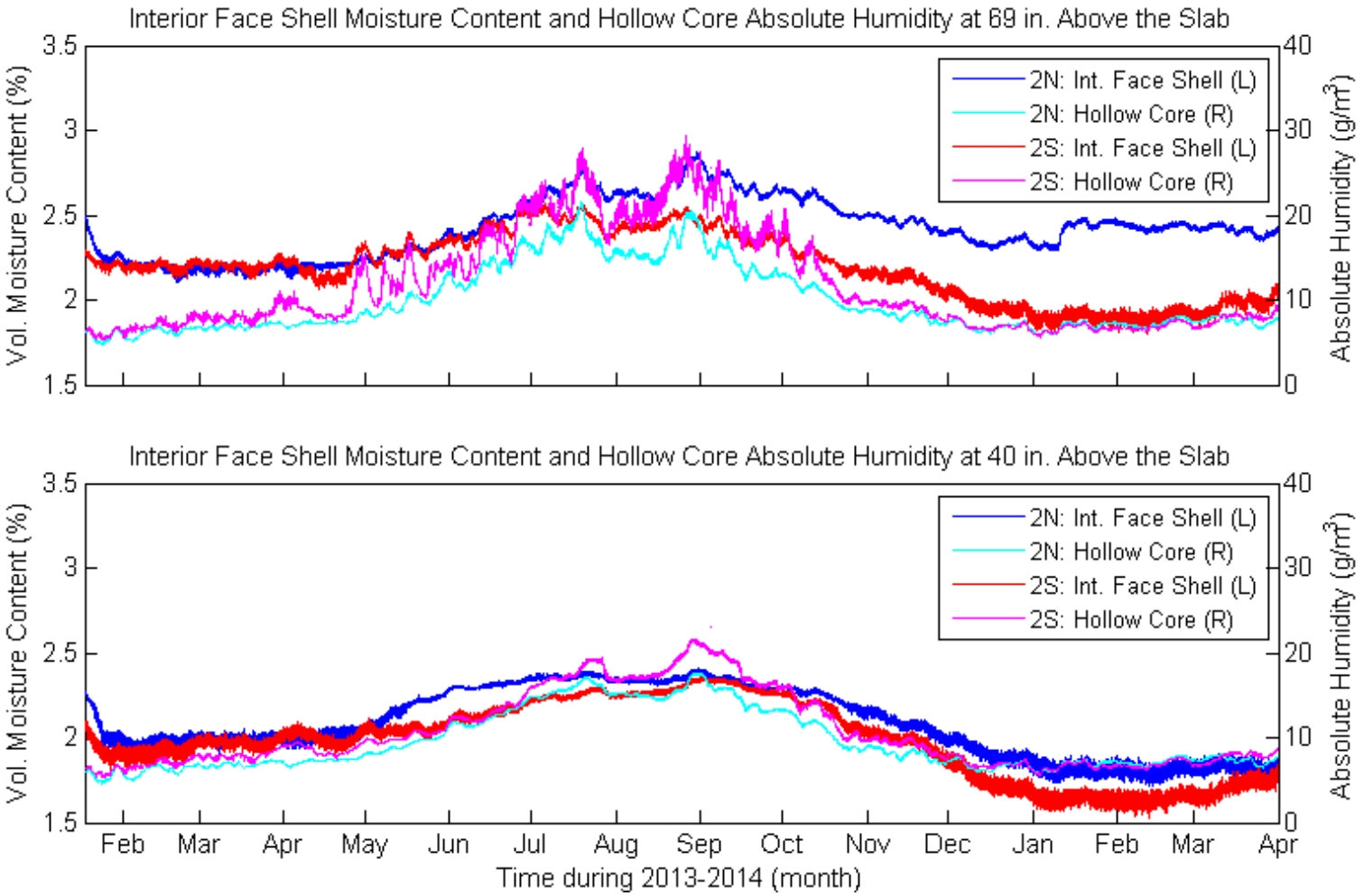

Figure 5-60: Bay 2 Interior Face Shell Moisture Content and Hollow Core Absolute Humidity at 40 in. and 69 in. above the Slab for North and South Exposures

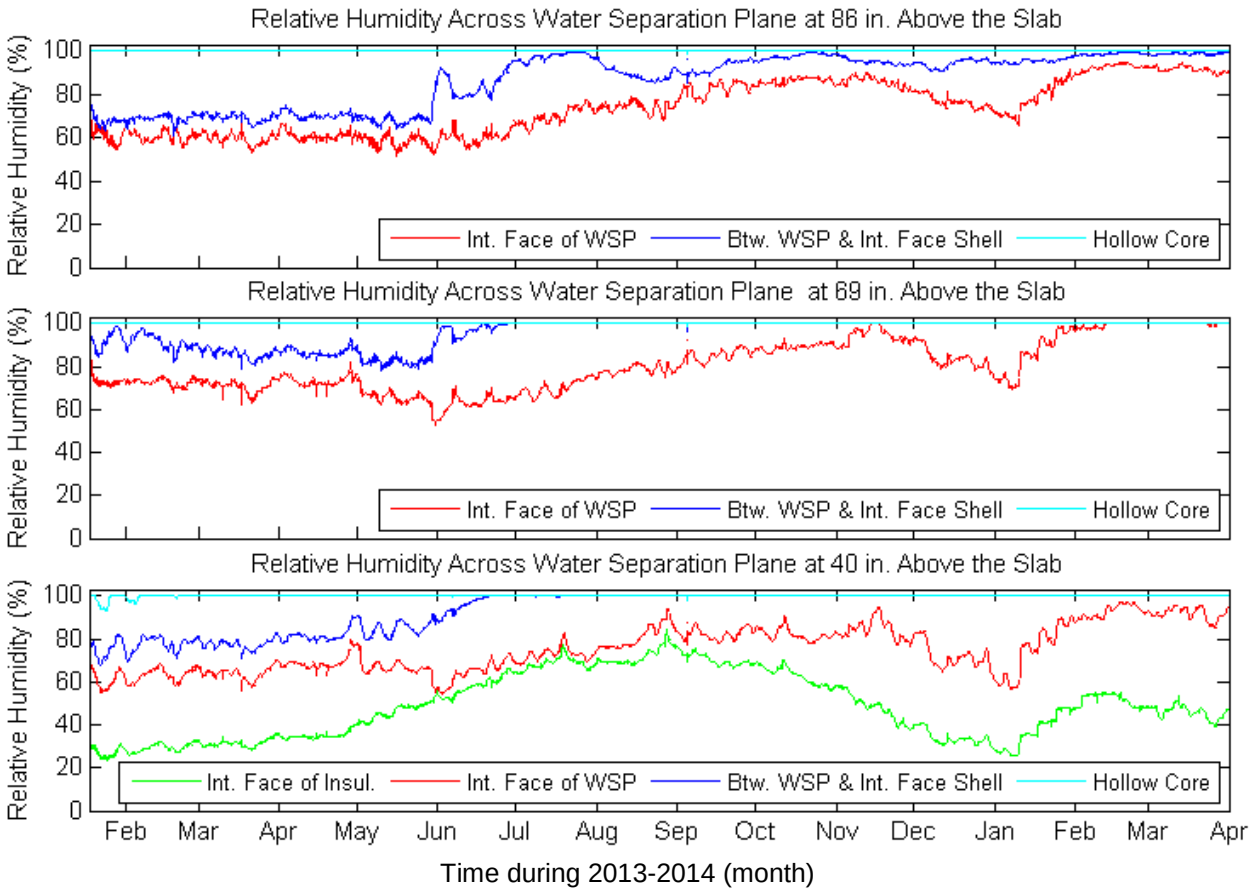

Figure 5-61: Bay 3N Relative Humidity across Water Separation Plane[20] [21]

[20] Water was injected between the CMU and WSP from September 4, 2013 to October 11, 2013.
[21] For the moisture profile 86 in. above the slab, the hollow core sensor is actually 79 in. above the slab.

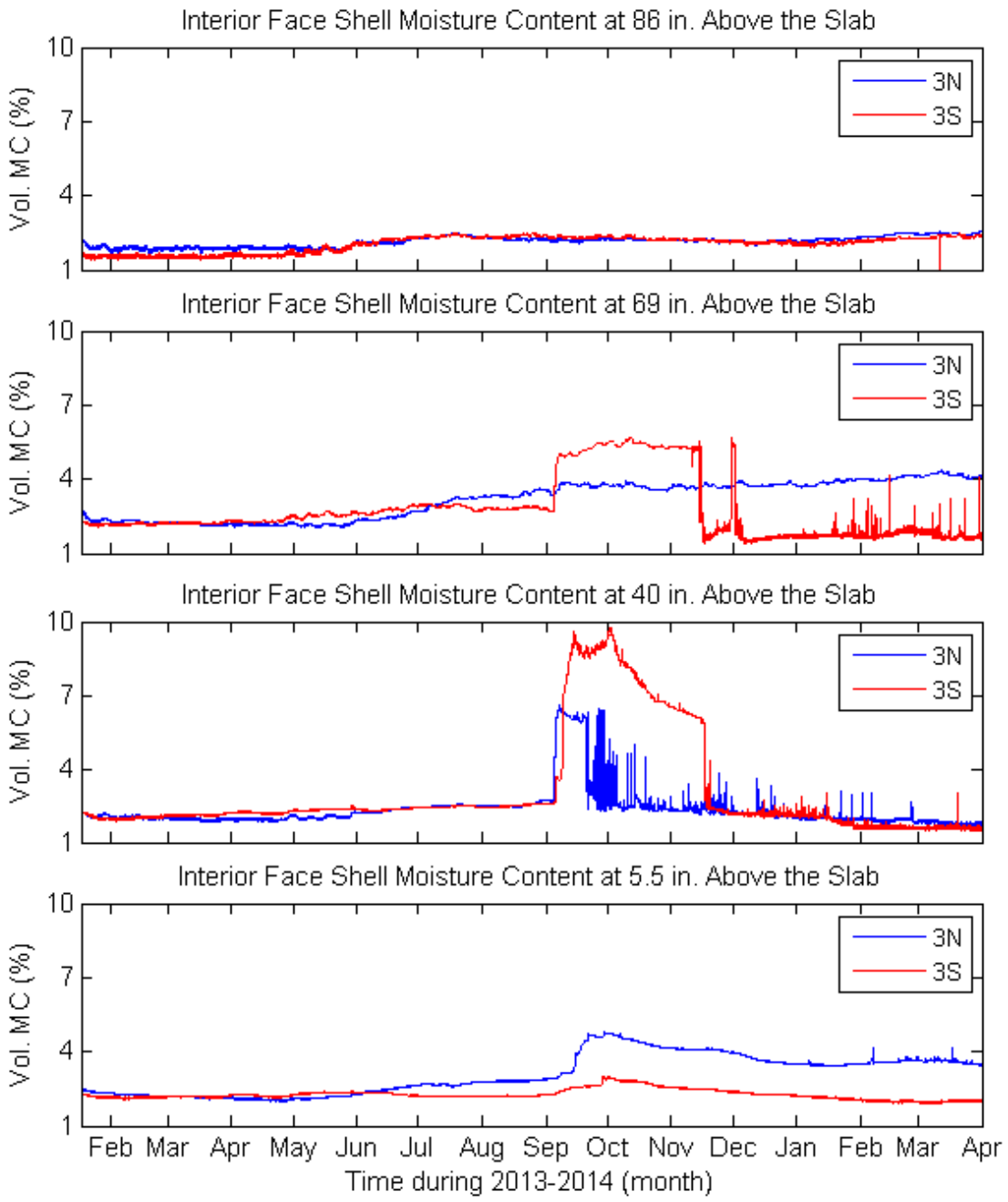

Figure 5-62: Bay 3 Interior Face Shell Moisture Contents at 5.5 in., 40 in., 69 in., and 86 in. above the Slab[22]

[22] Water was injected between the CMU and WSP from September 4, 2013 to October 11, 2013.

Chapter 6: A Comparison of Experimental Data to a Numerical Simulation and Basic Heat Transfer Calculations

6.1 Simulation

Simulations of the CRRF basement walls were conducted for comparison with the experiment. The simulations were conducted by Louise Goldberg,[23] using BUFETS (BUilding Foundation and Energy Transport Simulation, revision C) simulation program (Goldberg and Harmon 2014). BUFETS is proprietary software designed for modeling heat transport through building foundation envelopes. The software has the following features:

- Non-linear material properties as arbitrary functions of temperature and moisture content;
- Three-dimensional geometry;
- Arbitrary, time-dependent boundary conditions;
- Boolean geometry specification and mesh generator;
- Inclusion of fully discontinuous phase change physics with frost-front tracking;
- High speed stable solver that enables multi-year real time simulation of large discrete volume meshes (>100,000 volumes);
- Graphical animation outputs with arbitrary coupling (heat fluxes, temperatures, U-values); and,
- 8760-hours simulated per year with an arbitrary time step size (typically 1 hour to comply with standard Typical Meteorological Year (TMY) weather data).

The software does not account for gaseous advective transport (air, water vapor) such as buoyant cavity flow in hollow CMU construction. It also does not account for moisture transport in the soil domain which influences heat transport. The soil moisture content is entered as an input parameter and held constant throughout the simulation.

Conditioning of the soil domain was a two-step process. First, a one-dimensional far-field simulation was run using a TMY weather file for the upper boundary and the deep ground temperature for the lower boundary. The simulation was run until steady-state

[23] Dr. Goldberg was the project Principal Investigator and my Advisor.

conditions were achieved. The steady-state, one-dimensional temperatures were then used as the initial conditions for the soil domain in the second step. In the second step, the experimental boundary conditions were applied along with the deep ground boundary conditions. The simulation was run from November 20, 2012 through December 31, 2012. This yielded the conditioned domain used as the initial conditions for a simulation beginning on January 1, 2013 and ending on December 31, 2013.

The gravel, sand, silt, and clay fractions in the native and two imported soils were known from ASTM soil tests (refer to the Chapter 3). Using these fractions, the experimental soils were matched to a model soil reported by Kersten (1948). The model soil was used to calculate porosity and skeleton density of the experimental soils for the simulation. The experimental moisture content on November 20, 2012 was used as the constant moisture content throughout the simulation. The dry heat capacities for the model soils were taken from the literature and the thermal conductivities were calculated by Johansen's method (1975) using the skeleton density, porosity, transient temperature, and moisture content (Goldberg and Harmon 2014).

The soil domain extended horizontally 12 ft. from the exterior face of the wall away from the basement and 10 ft. from the exterior face of the wall under the basement slab (to the mid-point of the basement) (Figure 6-1). The soil domain width was 6 ft-6in. (the central section of a test bay) and the depth of the domain relative to grade was different for the two cases modeled (Figure 6-1 and Table 6-1). In Case 1, the ground water table was at the bottom of the soil domain ($50^{1}/_{4}$ in. below the bottom of the footing) with a constant temperature throughout the year of 39 deg. C (U.S. Environmental Protection Agency 2013). For Case 2, the top of the ground water table was at the bottom of the footing and the soil domain extended to 96 in. below the footing. The temperature boundary at the bottom of the soil domain varied. It was held at 45 deg. C during the heating season and 52.5 deg. C during the cooling season. From April 30 to June 1 and from October 1 to November 1 there was a linear gradient between the two temperatures (Table 6-1).

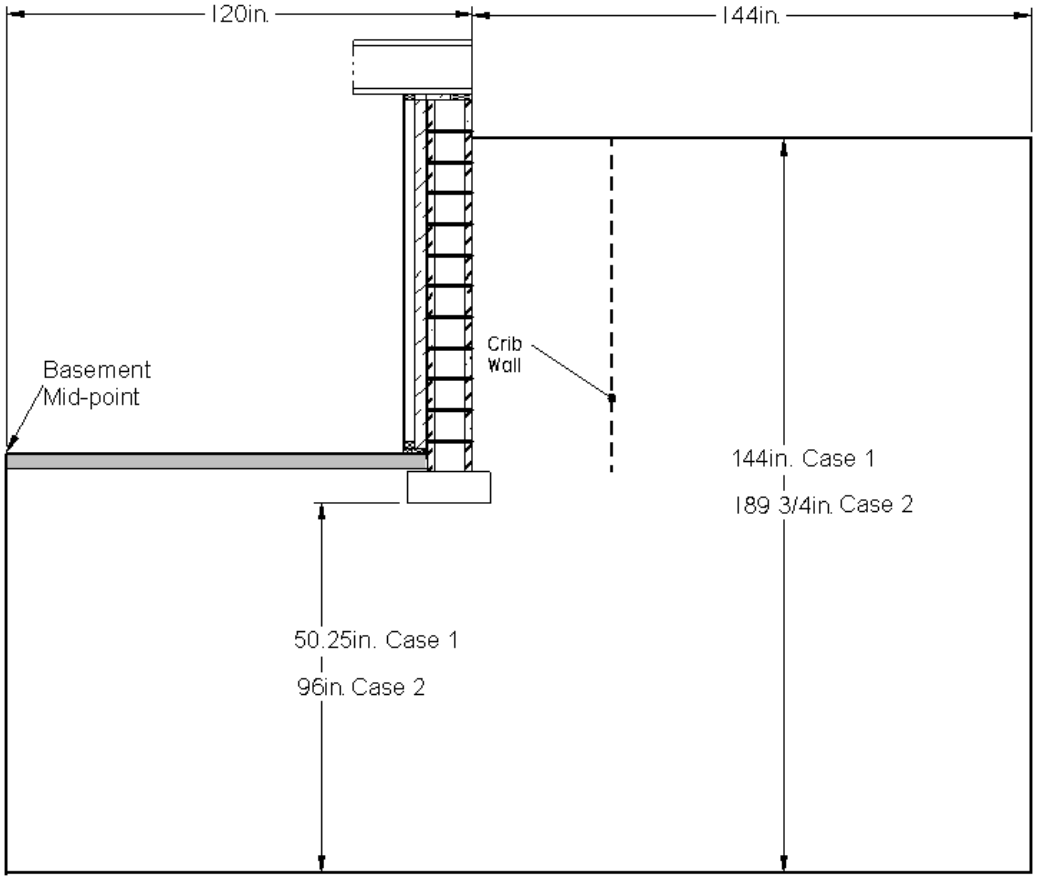

Figure 6-1: Simulation Soil Domain

	Case 1	Case 2
Depth of Soil Domain from Top of Grade (in.)	144	189.75
Depth from Bottom of Footing to Ground Water Table (in.)	50.25	0
Height of Soil Domain below Water Table (in.)	0	96
Heating Season Bottom Boundary Temperature (deg. F/deg. C)	39/3.9	45/7.2
Cooling Season Bottom Boundary Temperature (deg. F/deg. C)	39/3.9	52.5/11.4
Dates of Spring Transition between Bottom Boundary Temperatures	--	April 30 to June 1
Dates of Fall Transition between Bottom Boundary Temperatures	--	October 1 to November 1

Table 6-1: Ground Water Height and Temperatures for Simulation

6.2 Ground Water Table and Soil Moisture Content

Figure 6-2 and Figure 6-3 show the simulated and experimental soil temperatures at 40 in. above the slab and 5 in., $18^{3}/_{4}$ in., and $32^{1}/_{2}$ in. from the face of the wall for Bay 2N for Cases 1 and 2. For Case 1, the experimental soil temperatures were approximately 4 deg. C greater than the simulated temperatures from January 2013 to April 2013 and November 2013 to January 2014. From June 2013 to September 2013, the experimental temperatures were greater by approximately 7 deg. C (Figure 6-2). For Case 2, the experimental soil temperatures were approximately 2 deg. C warmer than the simulated temperatures from January 2013 to April 2013 and December 2013 to January 2014. From June 2013 to September 2013 the experimental temperatures were approximately 5 deg. C warmer than the simulated temperatures (Figure 6-3).

During the heating season, the decreased temperature difference between the experimental and simulated soil temperatures from Case 1 to Case 2 for Bay 2N can be explained by the difference in thermal capacity of the two soil domains. The soil domain below the bottom of the footing was smaller for Case 1 ($50^{1}/_{4}$ in. deep) than for Case 2 (96 in. deep). This means that in the Case 2 simulation there was a greater heat capacity from the soil skeleton alone than in Case 1. Further, for Case 2 the water table was at the bottom of the footing, while for Case 1 it was $50^{1}/_{4}$ in. below the bottom of the footing. The thermal capacity of water (4.2 kJ/kg-K) is greater than air (1.0 kJ/kg-K) and the soil skeleton (0.85 kJ/kg-K), so in Case 2, the soil domain had a substantially larger thermal heat capacity per unit volume than did Case 1. Since the interior basement temperature (approx. 68 deg. C during the heating season) was always greater than the temperature of the soil domain below the slab, heat was always transferred from the basement to the soil domain. Case 2 was able to store a greater amount of heat in the soil below the slab than Case 1. During the heating season, when the soil surface was colder than the soil below the slab, heat was transferred to the soil surface, thus elevating the soil temperatures adjacent to the basement wall. The increased thermal capacity of Case 2 meant more heat was transferred to the soil surface and soil temperatures were higher than those of Case 1.

During the cooling season, the decreased temperature difference between the experimental and simulated soil temperatures from Case 1 to Case 2 can be explained

by the heating season soil temperatures. As discussed above, during the heating season the soil temperatures adjacent to the wall were greater for Case 2 than for Case 1 because of the increased heat transported from the soil below the slab to the soil surface due to the greater heat capacity of the soil domain. This meant at the beginning of the cooling season the Case 2 soil temperatures were elevated compared to the Case 1 soil temperatures and this relationship was carried through the cooling season.

The thermal capacity of the soil domain and the temperature of the bottom soil boundary reinforce the impact of the water table depth and temperature on the soil temperature profiles. Case 2 had a higher and warmer water table than Case 1 and it improved the accuracy of the simulation. This supports the argument that the CRRF site had a high water table (Chapter 5.3).

For Cases 1 and 2, the larger difference between experimental and simulated soil temperatures during the cooling season (7 and 5 deg. C, respectively) versus the heating season (4 and 2 deg. C, respectively) was partially due to the fact that the simulation used a constant moisture content and did not account for bulk water transport. As noted in Chapter 6.1, the moisture content used for the simulation was the experimental moisture content on November 20, 2012. Generally, soil moisture contents at this time of year are lower than during the spring and summer months. The soil thermal conductivity is based on the thermal conductivities of its constituent parts, soil particles, air, and water. The thermal conductivity of water is high compared to that of air, so increased soil moisture in the void spaces increases the thermal conductivity of the soil. An increased soil thermal conductivity means the soil is better able to conduct heat, which results in elevated soil temperatures. If the simulation moisture content and calculated soil thermal conductivities were lower than reality, the simulated temperatures would be lower than the experimental temperatures.

The transfer of sensible heat by bulk water transport was not accounted for in the simulation. During the simulation period, the greatest amount of liquid precipitation occurred between June 2013 and September 2013 (Figure 5-4, note that this graph records rain and snow as liquid precipitation). During this period the outdoor ambient conditions tended to be warmer than the soil (Figure 5-10). Assuming the precipitation during this period was at the same temperature as the air, precipitation transported

sensible heat from the surface to the soil. Since the simulation did not account for this bulk water transport, the experimental temperatures would be greater than the simulation temperatures.

Figure 6-4 and Figure 6-5 graph the experimental and simulated CMU wall and soil temperature profiles at 5.5 in. above the slab for Bay 2N for Case 1 and Case 2, respectively. The simulated wall and soil temperature profiles were closer to the experimental data for Case 2 than for Case 1. The profiles showed a maximum temperature difference between the experimental and simulated at the beginning of September of approximately 8 deg. C for Case 1 and 4 deg. C for Case 2. The simulated results are closer to the experimental results during the heating season than during the cooling season.

Like the soil sensors at 40 in. above the slab, the improved modeling accuracy of Case 2 over Case 1 for the wall and soil temperatures at 5.5 in. above the slab can be attributed to the height and temperature of the water table and the size of the soil domain which affect the thermal capacity of the soil domain below the slab and the thermal gradient of the soil adjacent to the basement wall. The use of a constant moisture content in the simulation and the exclusion of bulk water transport from the simulation as was discussed for the soil sensors at 40 in. above the slab further explains the larger temperature differences between the experimental and simulated data at 5.5 in. above the slab for the cooling season versus the heating season

At 5.5 in. above the slab, the experimental soil temperature was warmer than the experimental interior and exterior face shell temperatures the entire year except for April 2013 (Figure 6-4 and Figure 6-5). At the same height for Cases 1 and 2, the simulated soil temperature was colder than the simulated interior and exterior face shell temperatures throughout the year.

During the cooling season, the fact that the experimental soil temperature was warmer than the interior and exterior face shells and the simulated soil temperature was colder than the interior and exterior face shells can be partially attributed to the use of a constant soil moisture content throughout the simulation and not accounting for the bulk moisture transport. The phenomenon is the same as discussed above for why there was a larger divergence between experimental and simulated soil temperatures

between the cooling and heating seasons at 40 in. above the slab. The simulated soil temperatures did not account for the sensible heat transported from the soil surface to the deep ground by advection or the increased soil thermal conductivities due to the elevated soil moisture contents. These two factors contributed to experimental soil and face shell temperatures at 5.5 in. above the slab that resulted in heat flowing from the soil to the wall during the cooling season.

During the heating season, the elevated soil temperatures relative to the face shell temperatures may be explained by the direction and magnitude of heat loss from the basement and soil below the slab. The soil temperature at 5.5 in. above the slab is influenced by the heat lost from the basement horizontally through the slab and wall and the heat lost from the soil domain below the slab to the soil surface above. If the heat loss from the soil domain below the slab is substantially greater than that lost horizontally through the slab and wall, it has the potential to elevate the soil temperature above the wall face shell temperatures. If this is the case, the simulation is over-estimating the heat lost horizontally through the slab and wall or under-estimating the heat lost from the soil below the slab to the soil surface. This is reinforced by the fact that when insulation was placed on the floor of Bay 3, it had no effect on the wall and soil temperatures (Chapter 5.3 and Figure 5-15). This experiment shows that the heat loss from the soil below the slab is substantially greater than that horizontally through the slab and wall. The other potential reason for the elevated soil temperatures relative to the face shell is buoyant cavity flow (discussed in Chapter 6.3).

From January 2013 to April 2013 and mid-November 2013 to January 2014 at 40 in. above the slab, the simulated soil temperature for Case 1 was approximately 0.3 deg. C colder than the exterior face shell (Figure 6-7). During the same time frame, the Case 2 simulated soil temperature at 40 in. above the slab was approximately the same temperature as the exterior face shell (Figure 6-9).

The decreased temperature difference between the soil and the exterior face shell from Case 1 to Case 2 was due to the heat capacity of the soil below the slab. For Case 2, the soil below the slab had a larger heat capacity because it had a higher water table and a larger soil domain. The increased heat capacity of the soil below the slab resulted in greater heat loss through the soil crib. This caused the Case 2 soil temperatures to

increase and decrease the temperature difference between the soil and the exterior face shell.

From January 2013 to April 2013 at 69 in. above the slab for the Case 2 simulated data, the soil, exterior face shell, and hollow core temperatures were approximately the same and slightly colder than the interior face shell (Figure 6-8). During December 2013 at 69 in. above the slab for the Case 2 simulated data, the soil temperature was warmer than the interior and exterior face shell and the hollow core.

The Case 2 simulated soil temperature elevated above the interior face shell temperature at 69 in. above the slab can be attributed to the initialization of the soil domain and the large heat capacity below the slab. The simulated soil domain was initialized using a far field data set followed by approximately six weeks of experimental basement boundary conditions (Chapter 6.1). This initialization period was short for a building that had been in service for more than 15 years (but it was not heated from 2005 to 2012) and the soil below the slab had likely achieved approximate thermal equilibrium. The short initialization period with a temperature-controlled boundary and the large heat capacity in the soil below the slab, meant that when the simulation began, there was a large potential for heat storage below the slab. During the first heating and cooling seasons, large amounts of heat were transferred from the basement and stored in the soil below the slab.[24] This meant at the beginning of the second heating season there was more heat stored in the soil below the slab than at the beginning of the first heating season. This caused the second heating season to have a greater heat loss through the soil crib to the soil surface than the first heating season. The increased heat loss through the crib elevated the crib soil temperatures. This is why during the second heating season, but not the first heating season, the simulated soil temperature exceeded the interior face shell temperature. To better simulate the experimental data, a larger initialization period that matches the experimental conditions over several prior years would be required. The soil temperature exceeding the interior face shell temperature also shows that the heat loss through the soil crib was much larger than the heat loss horizontally through the wall.

[24] The CRRF had been dormant with the basement unheated from 2005 – 2012.

To a lesser extent this phenomenon can be seen in the Case 1 simulated data. During the first heating season, the soil temperature was colder than the interior face shell temperature (Figure 6-6). In December 2013, the soil temperature was approximately the same temperature as the interior face shell. Case 1 had a smaller soil domain below the slab and a lower water table such that its total heat capacity was much smaller than Case 2. Therefore it is expected that the difference in crib heat loss between the heating seasons would be smaller for Case 1 than for Case 2. This is why the change in soil temperature in relation to the interior face shell temperature from the first heating season to the second heating season is less dramatic for Case 1.

Further, this phenomenon can be seen in the experimental data. During the first heating season the soil temperature at 69 in. above the slab was approximately 1.5 deg. C colder than the interior face shell temperature (Figure 6-8). During December 2013 at 69 in. above the slab, the experimental soil temperature was less than 1 deg. C colder than the interior face shell temperature.

In the experimental data, the decreased difference between the soil temperature and the interior face shell temperature from the first heating season to the second heating season shows that more heat was being added to the soil crib during the second heating season. This makes sense as the system was not at steady-state when the experiment began because the basement had not been heated for several years previously. Therefore it would be expected that the first and second heating seasons show non-steady-state conditions. However, the difference would not be as dramatic as with the simulation, since the soil domain had been conditioned to some extent during the previous cooling seasons.

Overall, comparing the experimental data to the simulated data indicates that the water table acts like a heat sink absorbing heat from the basement throughout the year and in so doing substantially elevates the temperature of the soil beneath the slab. During the heating season, this heat is transferred from the soil below the slab to the soil surface above and elevates the temperatures of the soil adjacent to the insulated basement wall. During the cooling season, heat is transported from the soil surface to the water table, further elevating the temperature of the soil below the slab. The temperature of

the water table affects the soil temperatures adjacent to the basement wall throughout the year.

The experiment did not collect data on the height and temperature of the ground water table for input into the simulation. The simulation/experimental data comparison demonstrates that this information is critical for modeling below-grade heat transfer. The BUFETS simulation data aligned with the findings of Deru and Kirkpatrick (2002b) that a constant soil thermal conductivity in a thermal-only numerical model does not accurately predict the seasonal heat loss (Chapter 2.2.2). For an accurate estimate of temperatures and heat loss, temperature and height data for the water table should be provided. Additionally, foundation simulation software should ideally include moisture transport in the soil domain. Bulk water transport and soil thermal conductivities significantly impact the temperature profiles and heat loss. If moisture transport in the soil domain is not accounted for, a time-varying soil moisture content should be used to account for the seasonal variation.

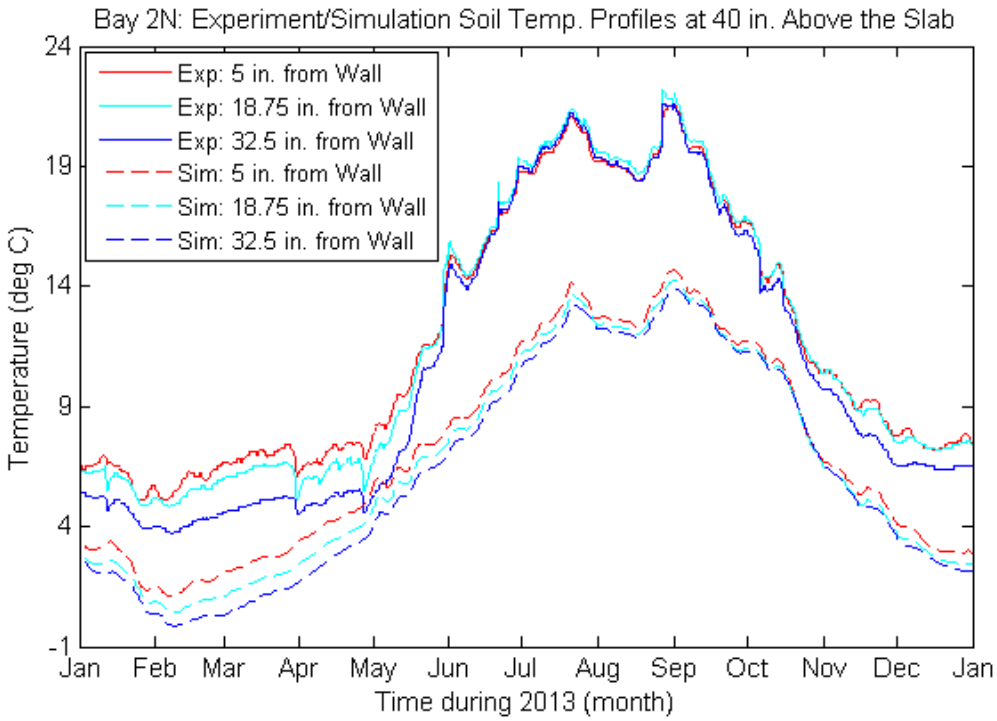

Figure 6-2: Comparison of Experimental and Simulation Soil Temperatures at 40 in. Above the Slab in Bay 2N for Case 1 (Water Table 50-1/4 in. below Bottom of Footing)

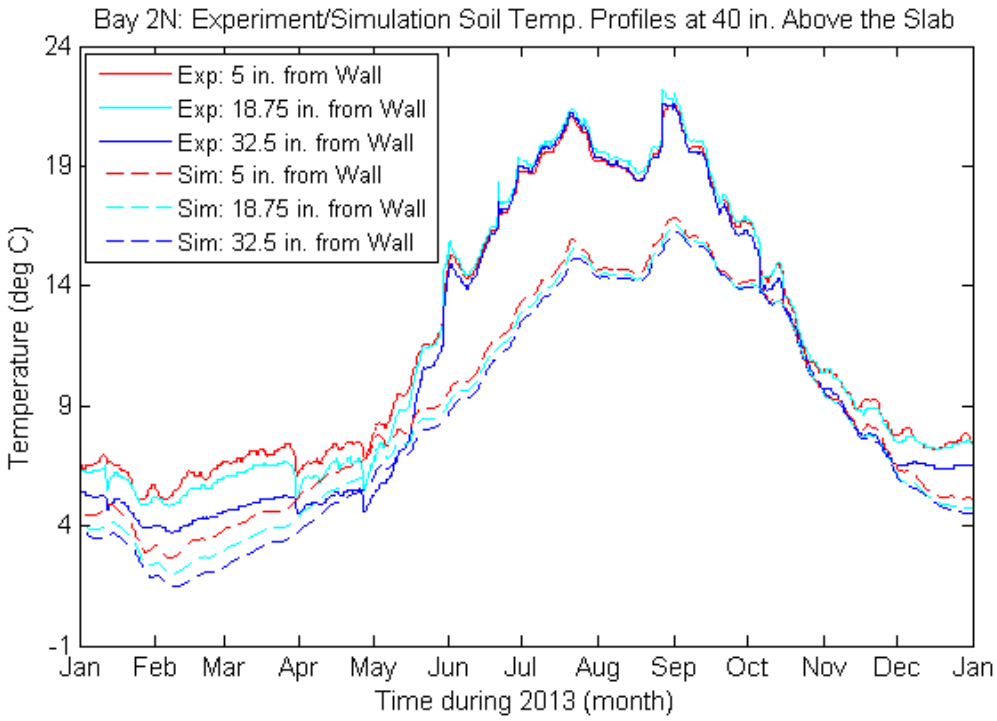

Figure 6-3: Comparison of Experimental and Simulation Soil Temperatures at 40 in. Above the Slab in Bay 2N for Case 1 (Water Table at Bottom of Footing)

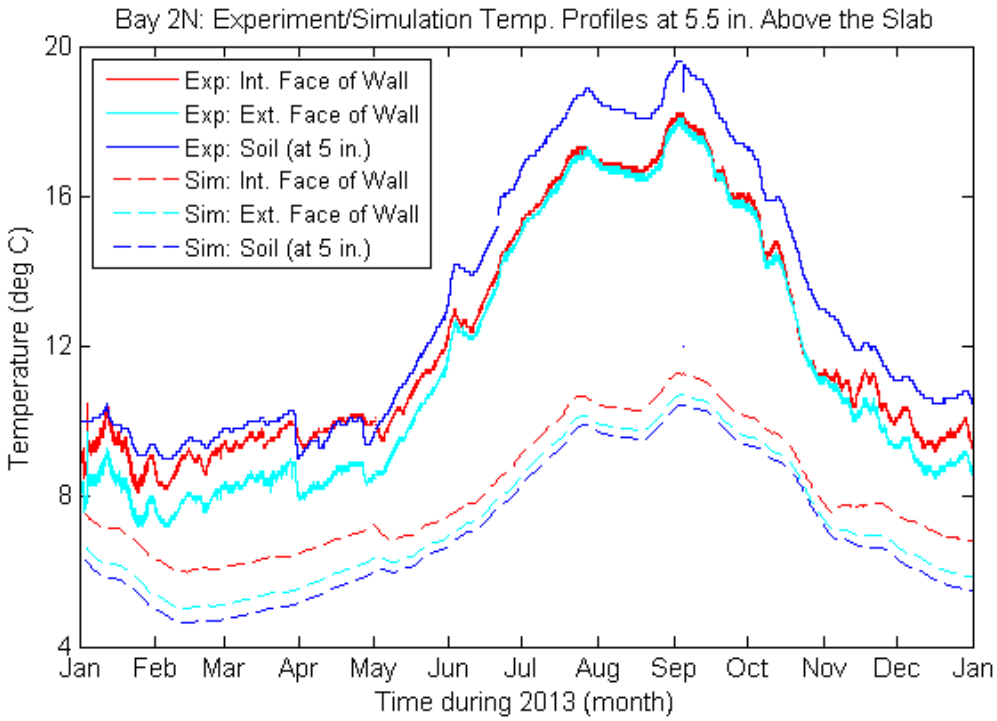

Figure 6-4: Comparison of Experimental and Simulation Wall and Soil Temperatures at 5.5 in. Above the Slab in Bay 2N for Case 1 (Water Table 50-1/4 in. below Bottom of Footing)

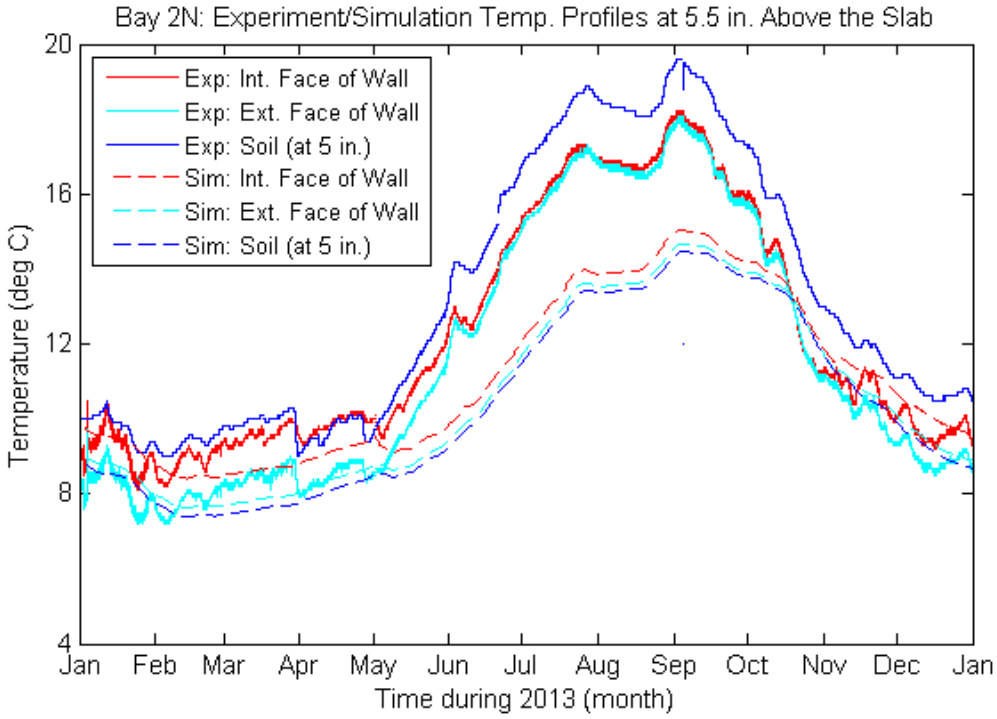

Figure 6-5: Comparison of Experimental and Simulation Wall and Soil Temperatures at 5.5 in. Above the Slab in Bay 2N for Case 2 (Water Table at Bottom of Footing)

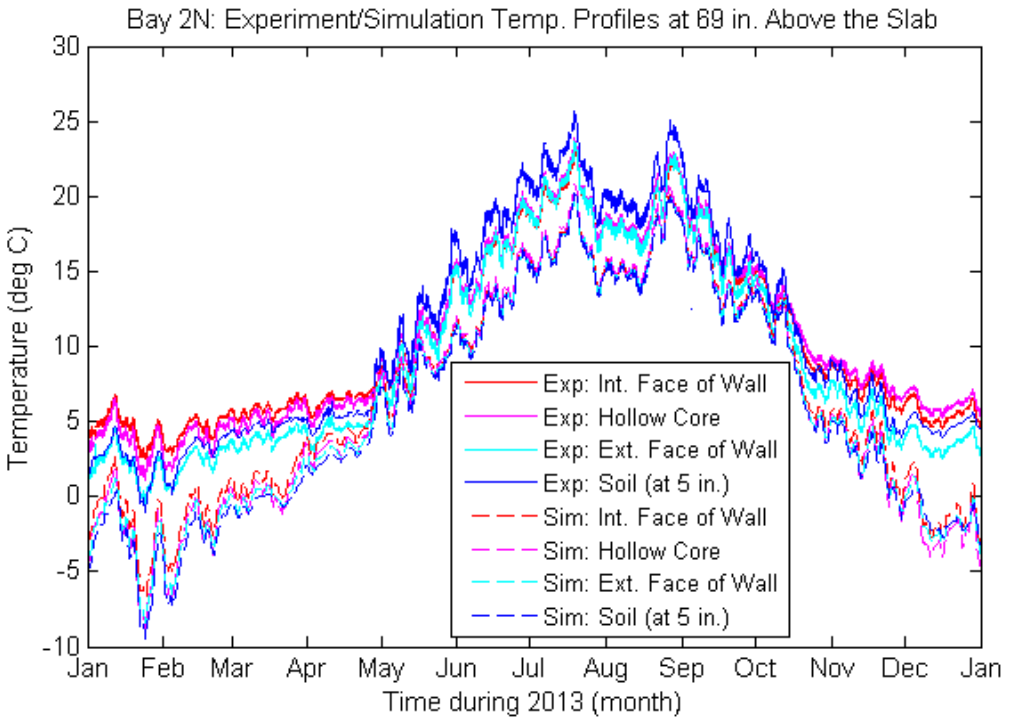

Figure 6-6: Comparison of Experimental and Simulation Wall and Soil Temperatures at 69 in. Above the Slab in Bay 2N for Case 1 (Water Table 50-1/4 in. below Bottom of Footing)

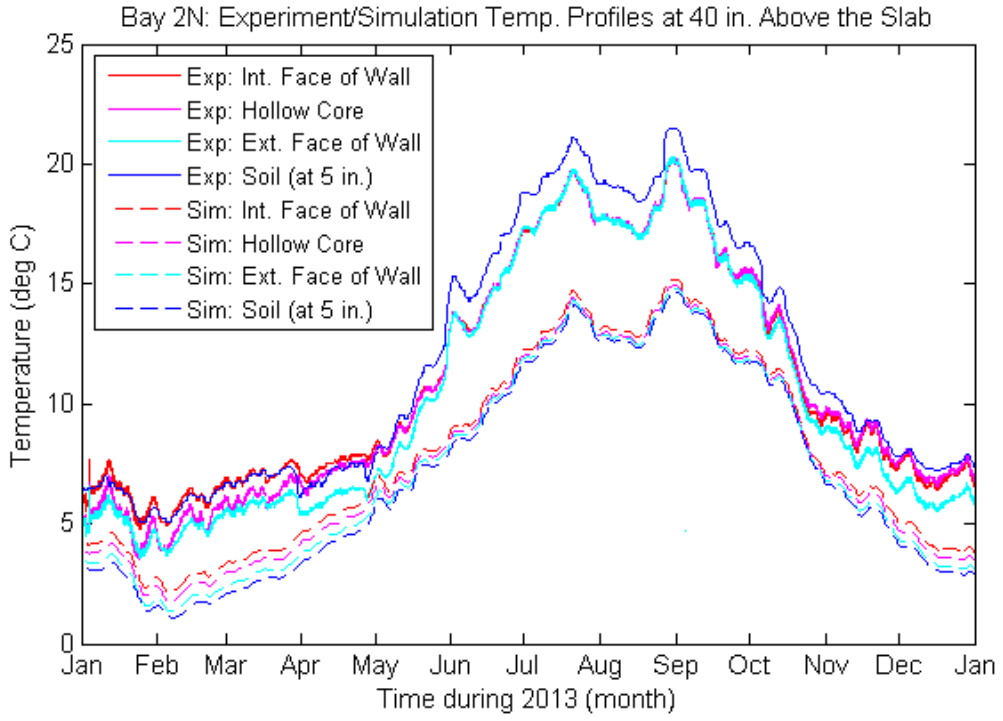

Figure 6-7: Comparison of Experimental and Simulation Wall and Soil Temperatures at 40 in. Above the Slab in Bay 2N for Case 1 (Water Table 50-1/4 in. below Bottom of Footing)

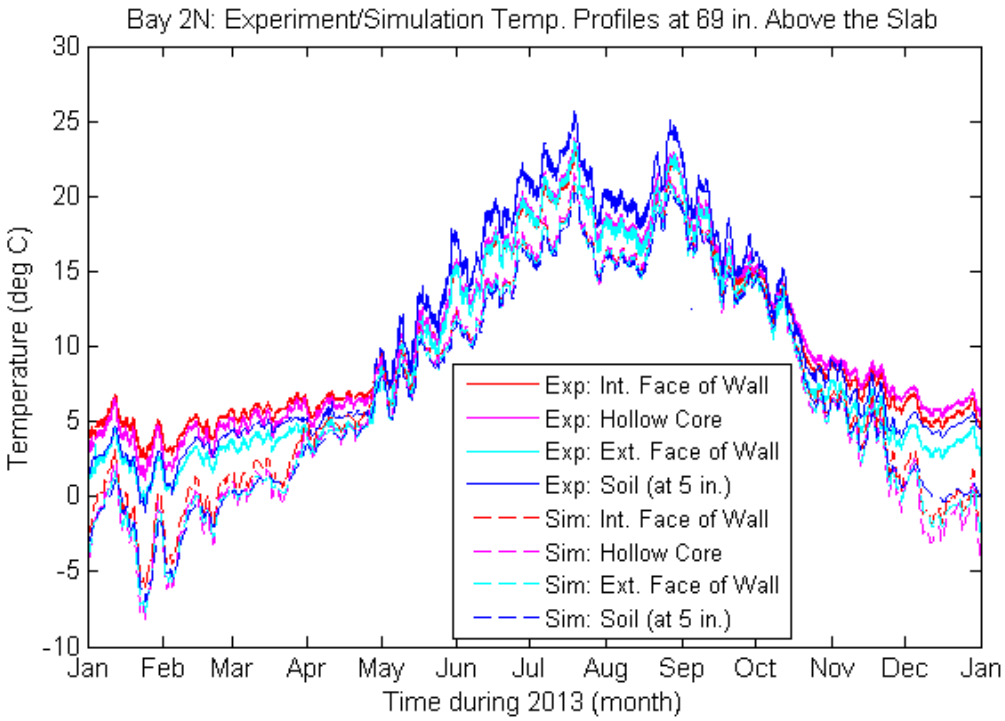

Figure 6-8: Comparison of Experimental and Simulation Wall and Soil Temperatures at 69 in. Above the Slab in Bay 2N for Case 2 (Water Table at Bottom of Footing)

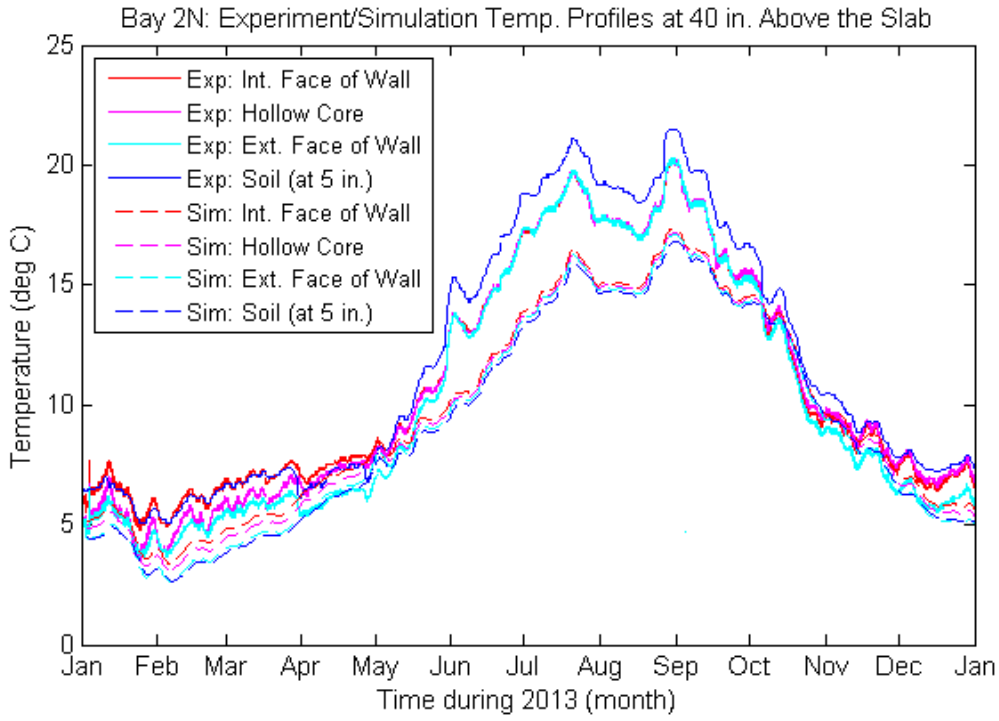

Figure 6-9: Comparison of Experimental and Simulation Wall and Soil Temperatures at 40 in. Above the Slab in Bay 2N for Case 2 (Water Table at Bottom of Footing)

6.3 Buoyant Cavity Flow

Figure 6-7 and Figure 6-9 show the temperature profiles at 40 in. above the slab for Cases 1 and 2, respectively. From January 2013 to April 2013, the experimental data show that the temperatures of the hollow core and exterior face shell were approximately the same and colder than the interior face shell. From mid-November 2013 to January 2014, the experimental data show the interior face shell and hollow core approximately at the same temperature and warmer than the exterior face shell. For the simulated data, from January 2013 to April 2013 and mid-November 2013 to January 2014, the interior face shell was approximately 0.4 deg. C warmer than the hollow core and the hollow core was approximately 0.4 deg. C warmer than the exterior face shell.

The experimental and simulated data show different relationships between the interior face shell, hollow core, and exterior face shell temperatures which were due to different primary heat transfer mechanisms. The simulated data show a temperature profile produced by pure conduction. The thermal gradient from warm to cold was from the interior to the exterior and the temperature differences between the interior face shell/hollow core and the hollow core/exterior face shell were approximately equal due to the nearly equivalent thermal resistances. This was expected since the simulation software did not model buoyant cavity flow. However, it reinforced the presence of buoyant cavity flow in the experimental data because the experimental data did not follow this pattern. As discussed in Chapter 5.4, buoyant cavity flow can cause the hollow core temperature (mid-width of the cavity) to be close to that of one of the face shells when the upward and downward flowing air plumes are not equal in width. This causes the hollow core temperature to be closer to the temperature of the wider air plume which is approximated by the face shell temperature. This is why the experimental data show the hollow core temperature approximately equal to one of the face shells.

The temperature profiles at 69 in. above the slab for Cases 1 and 2 are shown in Figure 6-6 and Figure 6-8, respectively. For Cases 1 and 2, from January 2013 to April 2013, the simulated temperature of the hollow core, exterior face shell, and soil were very similar. For the same period, the experimental data showed that the hollow core was

warmer than the exterior face shell and soil and the soil was warmer than the exterior face shell.

At 69 in. above the slab, the different relationships between the wall and soil temperatures of the simulated and experimental data were again due to the different primary heat transfer mechanism in force in each case. Conduction was the primary heat transfer mechanism for the simulated data. At 69 in. above the slab (approximately 12 in. below the soil surface) the wall and soil temperatures were closely linked to the exterior ambient conditions. Further, the heat flow was nearly vertical adjacent to the wall exterior and this is why there was a very limited gradient between the wall and soil temperatures. However with the experimental data, buoyant cavity flow caused the soil to be warmer than the exterior face shell. As discussed in Chapter 5.4, buoyant cavity flow caused the exterior face shell temperature to be depressed, yielding an exterior face shell temperature colder than the adjacent soil temperature. As discussed in Chapter 6.2 for the simulated data at 40 in. above the slab, an elevated water table results in greater heat loss through the soil crib, elevated soil temperatures, and a decreased temperature difference between the exterior face shell and the soil. The combination of a high water table and buoyant cavity flow exacerbate the temperature difference between the exterior face shell and the soil.

The experimental soil temperature was warmer than the experimental interior and exterior face shell temperatures at 5.5 in. above the slab the entire year except for April 2013 (Figure 6-4 and Figure 6-5). For Cases 1 and 2 at the same height, the simulated soil temperature was colder than the simulated interior and exterior face shell temperatures throughout the year.

At 5.5 in. above the slab, the elevated experimental soil temperature may have been due partially to buoyant cavity flow. At 5.5 in. above the slab, the wall was probably not hollow because mortar droppings likely filled the core such that the primary heat transfer mechanism would have been conduction. Because of this it would be expected that there would be a decreasing or increasing thermal gradient from the interior face shell to the soil. The simulation, which did not include buoyant cavity flow, shows this with the interior face shell warmer than the exterior face shell and the exterior face shell warmer than the soil. However, with the experimental data this is not the case during

the heating season with the soil the warmest, then the interior face shell, and the exterior face shell the coldest (Figure 6-4 and Figure 6-5). Although buoyant cavity flow likely does not occur in this part of the wall, the phenomenon may be the result of the buoyant cavity flow above. Buoyant cavity flow in the hollow CMU cores caused cold air to drop down the exterior face of the cores and resulted in a cold air mass at the bottom, exterior side of the cores. Heat was transferred by conduction from the exterior face shell and the mortar filled core to the air mass. This inward and upward flow of heat to the hollow core from the exterior face shell and the filled core may explain why the exterior face shell is colder than the soil adjacent to the wall at 5.5 in. above the slab. It can be further explained by a high water table and heat loss through the soil crib that elevate the soil temperatures relative to the wall exterior temperature (Chapter 6.2).

Buoyant cavity flow has a significant effect on the thermal profile of a below-grade wall. Much of the heat loss through a hollow CMU wall to the above-grade ambient air may be by buoyant cavity flow with a small portion, by comparison, through the adjacent soil. It is essential to include buoyant cavity flow in a simulation if an accurate temperature profile and heat loss estimate is desired. Buoyant cavity flow can reduce the exterior face shell temperatures below those of the adjacent soil. This effect can be further exacerbated by a high water table (Chapter 6.3) that can raise the soil temperatures above that of the adjacent wall.

6.4 Heat Transfer Calculations

To further understand the experimental and BUFETS simulated data, and to independently validate the hypothesized impact of the thermal storage beneath the slab, calculations were performed to estimate the quantity of heat transferred between:

- The basement and the soil below the slab;
- The outdoor ambient environment and the soil below the crib; and,
- The basement and the soil adjacent to the wall.

The calculations were done for Bay 2N with the imported sand. The intent of the calculations was to provide insight into the effect of the water table on the thermal performance of the soil below the slab and adjacent to the wall. The calculations included three cases, A, B, and C, for differing soil conditions that are discussed below

(Figure 6-11, Figure 6-12, and Figure 6-13, respectively). The calculations were performed using three different methods, 1, 2, and 3, which are discussed below.

6.4.1 Soil Domain and Properties

In all cases, the soil crib moisture content was based on the 2013 averaged measured soil volumetric moisture content for sensors at 5.5 in., 40 in., and 69 in. above the slab. The volumetric moisture content at the soil surface was assumed the same as the averaged soil volumetric moisture content at 69 in. above the slab (approximately 12 in. below the soil surface). A linear gradient was used for the volumetric moisture content between sensor heights.

The basement is 20 ft. wide from outside face of wall to outside face of wall. Half the width of the basement was used for the calculations, that is, the heat flow was assumed to be symmetric about the east-west basement centerline axis. All calculations were two-dimensional and based on a north-south plane with a 1 ft. width. The width of the slab through which heat was transferred extended from the centerline of the basement to the interior face of the insulation (Figure 6-14, Figure 6-15, and Figure 6-16). This resulted in A_{base} of 8.781 ft^2 (0.8158 m^2). The installed crib was 3 ft. from the exterior face of the wall. However, for the heat transfer calculations, an additional 1 ft. of soil adjacent to the soil crib was included giving a total soil width of 4 ft. A_{crib} was 4 ft^2 (0.3716 m^2). The soil in the crib was a sand and the soil outside the crib was a silty sand per the Unified Soil Classification System (Chapter 3.2.1). However, both fell in the ‘sand’ section of the USDA Soil Classification Triangle and for this reason, in the calculations, the same material properties were used for both.

For all three cases, the soil domain extended 96 in. below the bottom of the footing (same as in BUFETS Case 2). Case B had the top of the water table located at the bottom of the footing (same as in BUFETS Case 2) (Figure 6-12). Cases A and C had the top of the water table located 96 in. below the bottom of the footing at the bottom of the soil domain. Case A had a linear soil volumetric moisture content gradient from the averaged soil volumetric moisture content at 5.5 in. above the slab down to the water table (Figure 6-11). Case C assumed the averaged soil volumetric moisture content at 5.5 in. above the slab was constant down to 24 in. above the water table and from there down to the water table a linear gradient was used (Figure 6-13).

The soil thermal conductivity, k, was based on values provided by Oak Ridge National Laboratory that related the soil moisture content, θ_s, to the thermal conductivity for a sand with a porosity, ξ, of 0.404 and a dry density of 1579 kg/m^3 (Table 6-2) (Kehrer et al. 2012). The data provided extended up to a soil moisture content of 375 kg/m^3, which is less than the maximum soil moisture content of 403.88 kg/m^3. The thermal conductivity above a soil moisture content of 375 kg/m^3 was assumed constant (Table 6-2). Using the value for the soil moisture content, the volumetric moisture content, θ_v, was calculated by:

$$\theta_v = \frac{\theta_s}{\rho_{water\ at\ 10\ deg.C}} \qquad \textbf{Equation 6-1}$$

The degree of saturation, S, was then calculated using the following equation:

$$S = \frac{\theta_v}{\xi} \qquad \textbf{Equation 6-2}$$

Soil Moisture Content, θ_s	Volumetric Moisture Content, θ_v	Degree of Saturation, S	Thermal Conductivity, k
kg/m^3	--	--	W/(m-K)
0	0.000	0.000	0.505
53	0.053	0.131	0.505
85	0.085	0.210	0.824
117	0.117	0.290	1.315
150	0.150	0.371	1.611
182	0.182	0.451	1.781
214	0.214	0.530	1.897
246	0.246	0.609	1.986
278	0.278	0.688	2.057
311	0.311	0.770	2.116
343	0.343	0.849	2.167
375	0.375	0.928	2.212
403.88	0.404	1.000	2.212

Table 6-2: Soil Properties for Sand

The relationship between volumetric moisture content and thermal conductivity is not linear. For this reason, the thermal conductivity was calculated at 1/4 in. increments through the domain based on the volumetric moisture content. The thermal resistance, R_i, was calculated as follows:

$$R_i = 2L \sum_{j=1}^{N} \frac{1}{k_j + k_{j+1}} \qquad \textbf{Equation 6-3}$$

where L is the height of the trapezoid segments. For these calculations L of 1/4 in. (6.35 mm) was used. Table 6-3 provides the thermal resistances used in the calculations with the soil domains shown in Figure 6-15 and the thermal resistance from the interior surface of the slab to a point horizontally 24 in. from the exterior face of the wall on the D-A soil domain boundary (labeled 'Horizontal').

Thermal Resistance for Heat Flow into Soil Domain, R_i (m²K/W)			
Domain	**Case A**	**Case B**	**Case C**
B	0.207	0.207	0.207
P	0.321	0.178	0.428
A	0.728	0.551	2.414
C	0.571	0.551	1.613
D	4.438	4.114	4.715
E	0.859	0.669	2.924
Horizontal	--	0.778	1.637

Table 6-3: Thermal Resistances Used in Calculations

For all methods and cases the interior temperature sensor 10 in. from the face of the Bay 2N wall and 5.5 in. above the top of the slab was used for the interior boundary condition. The temperature at the weather station was used for the exterior boundary condition. The temperature sensor above the crib was not used because it was not installed until October 11, 2013. For the experimental time period when the crib temperature and weather station were both available, Figure 6-10 shows the difference in temperature between the weather station and the crib for Bay 2, north and south exposures. The weather station was a close approximation for Bay 2N, with the crib temperature averaging approximately 1 deg. C warmer than the weather station. The

time step for the calculations was based on the frequency of data collection of the interior and exterior boundary sensors which was between 10 and 12 minutes.

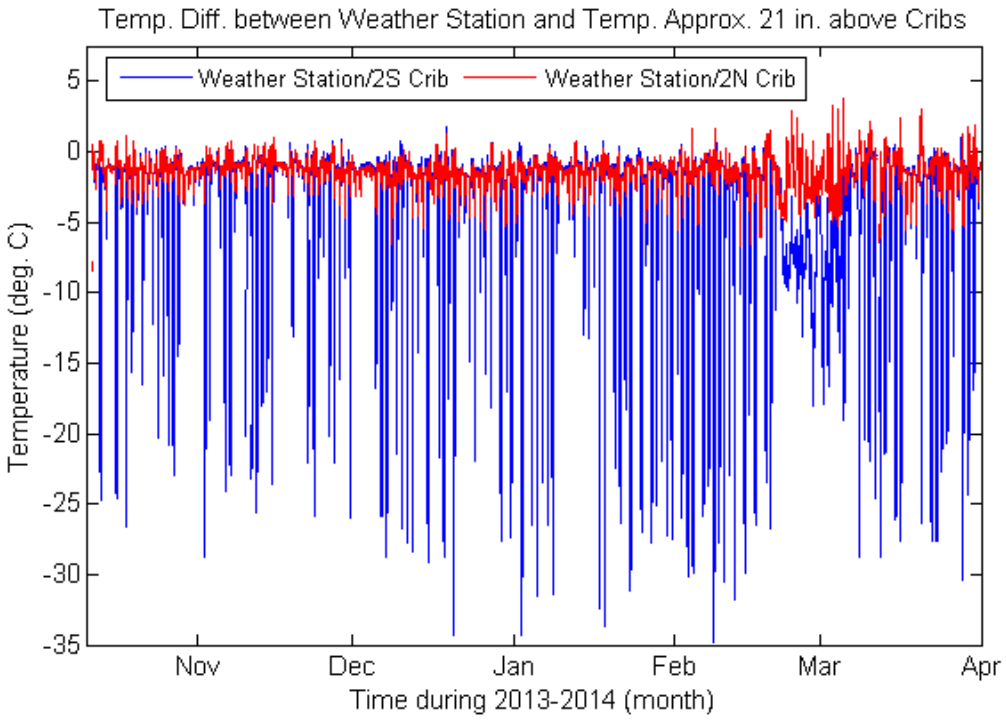

Figure 6-10: Difference between Weather Station and Bay 2 Crib Temperatures

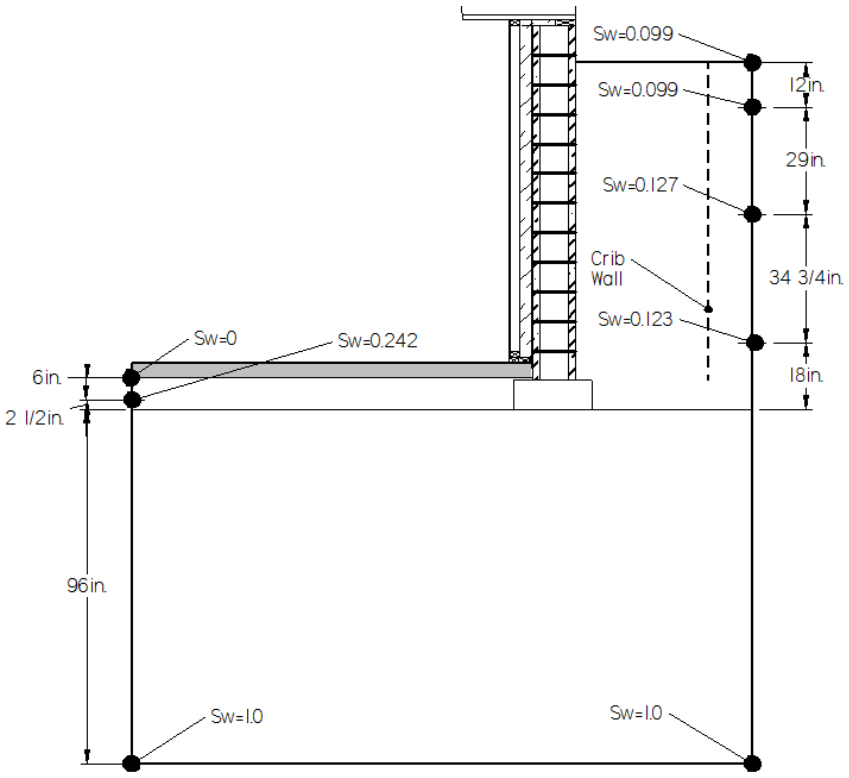

Figure 6-11: Case A for Heat Transfer Calculations

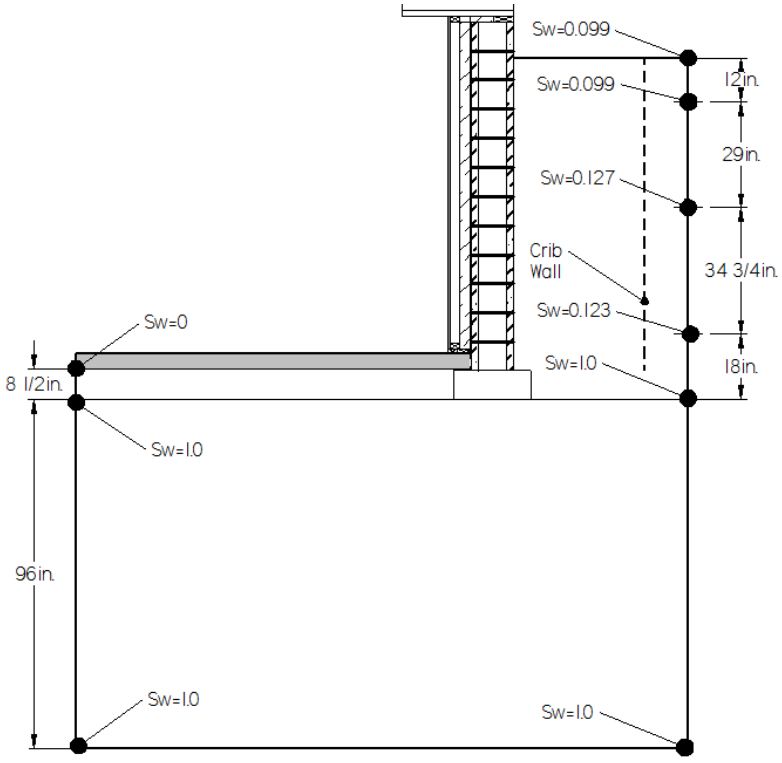

Figure 6-12: Case B for Heat Transfer Calculations

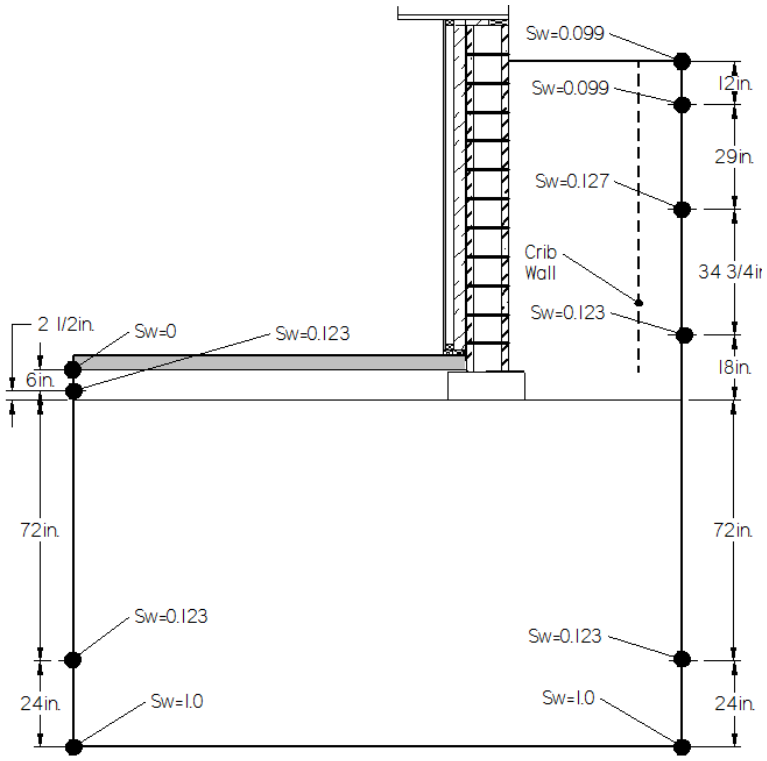

Figure 6-13: Case C for Heat Transfer Calculations

6.4.2 Method 1

Figure 6-14 is a diagram of the soil domain and heat flow for Method 1. The annual heat transfer was calculated based on a constant deep ground temperature, T_{dg}, of 7.22 deg. C, specified at the bottom of the domain. The annual heat transfer between the basement and the deep ground, Q_{base}, and the crib and the deep ground, Q_{crib}, were calculated separately using the following equation:

Equation 6-4

$$Q_i = \frac{A_i}{R_i}\sum_{j=1}^{N}\left[\frac{1}{2}\left(T_{i,j} + T_{i,j+1}\right) - T_{dg}\right]\left(t_{j+1} - t_j\right)$$

Where i, represents the element under consideration (basement or crib), A_i, is the area, $T_{i,j}$ is the basement or soil surface boundary temperature at time step j and t_j is the time at time step j.

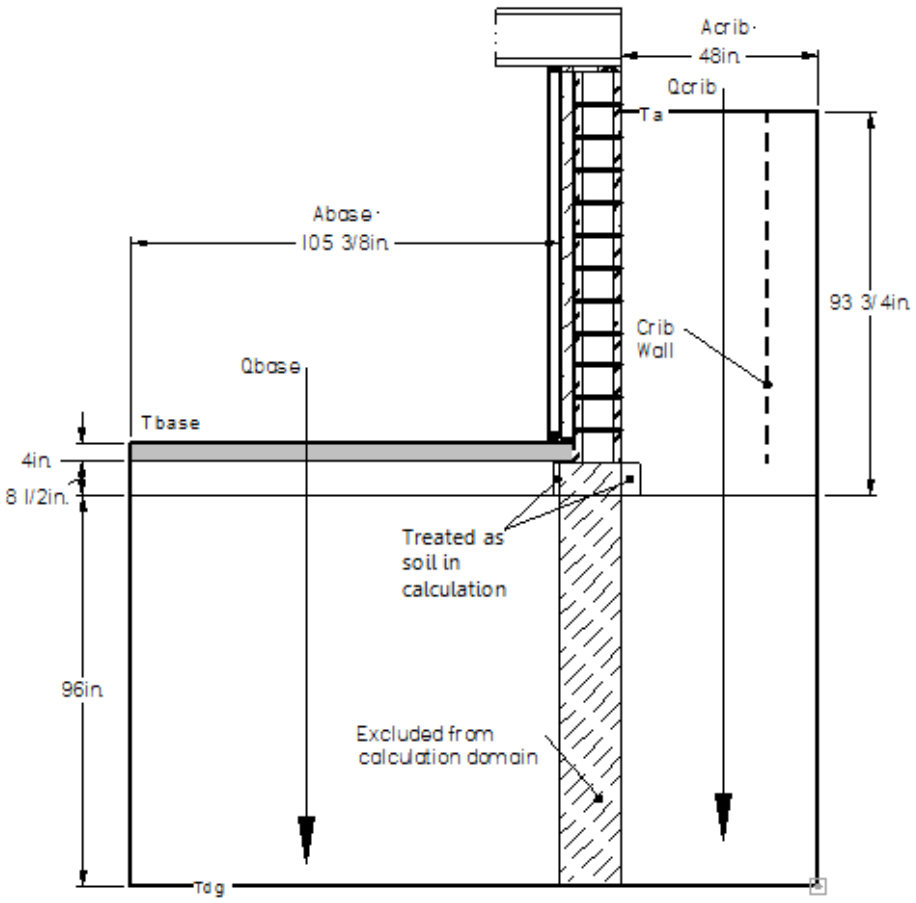

Figure 6-14: Diagram of Method 1 Heat Transfer

6.4.3 Method 2

The soil domain and heat flows for Method 2 are shown in Figure 6-15. A time-varying soil temperature, T_m, was specified at 48 in. below the bottom of the footing (mid-point of the soil control volume below the footing). At the bottom of the soil control volume, the deep ground temperature, T_{dg}, was held constant at 7.22 deg. C. This method assumed all heat transferred between the basement/domain A and the soil surface/domain A was stored in or lost from domain A. This assumption was justified by the test where 3 in. XPS insulation was placed on the floor in Bay 3 (Chapter 5.3). During this test there were no changes to the soil temperatures at 5.5 in., 40 in., or 69 in. above the slab. This indicated that the heat lost from the basement was primarily to the deep ground and not to the soil adjacent to the wall (Chapter 5.3).

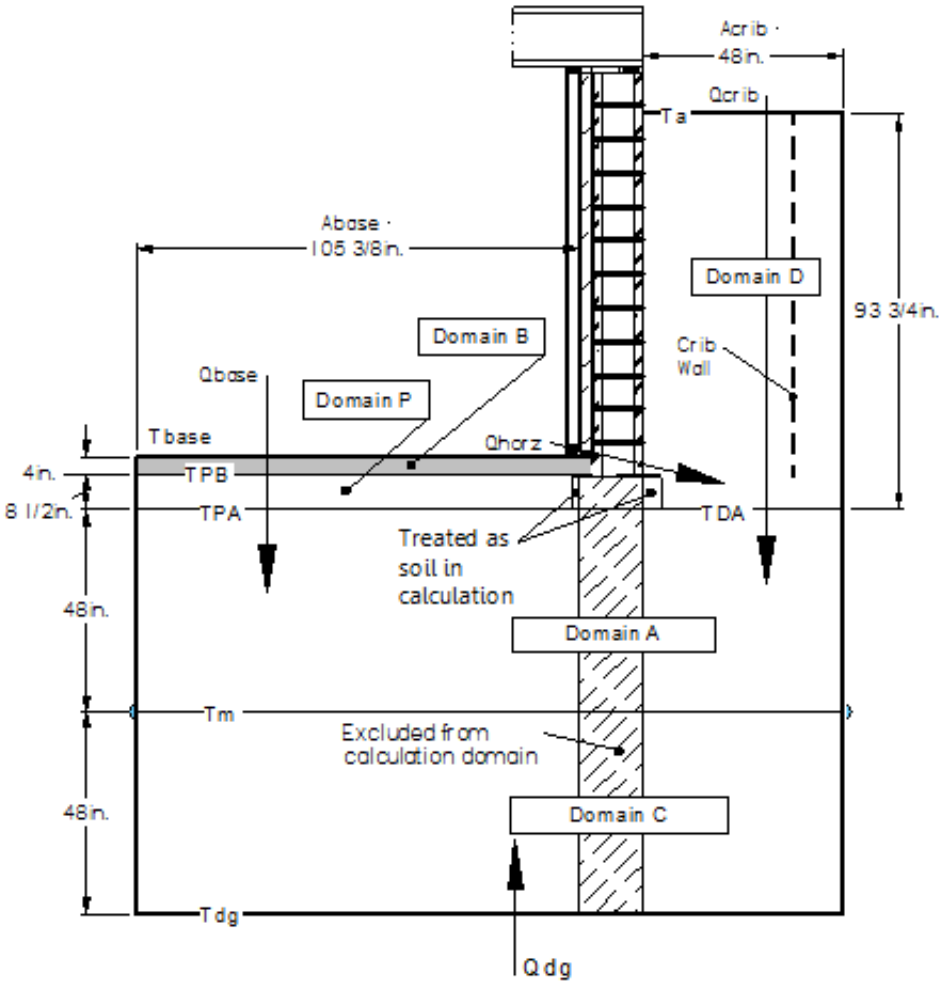

Figure 6-15: Diagram of Method 2 Heat Transfer

The annual basement heat transfer, Q_{base}, was calculated by:

$$Q_{base} = \frac{A_{base}}{R_{base-m}} \sum_{j=1}^{N} \left[\frac{1}{2} \left(T_{base,j} + T_{base,j+1} \right) - T_m \right] \left(t_{j+1} - t_j \right) \quad \textbf{Equation 6-5}$$

The annual crib heat transfer, Q_{crib}, was calculated by:

$$Q_{crib} = \frac{A_{crib}}{R_{crib-m}} \sum_{j=1}^{N} \left[\frac{1}{2} \left(T_{crib,j} + T_{crib,j+1} \right) - T_m \right] \left(t_{j+1} - t_j \right) \quad \textbf{Equation 6-6}$$

The annual deep ground heat transfer, Q_{dg}, was calculated by:

$$Q_{dg} = \frac{A_{crib} + A_{base}}{R_{dg-m}} \sum_{j=1}^{N} [T_{dg} - T_m](t_{j+1} - t_j)$$ **Equation 6-7**

The net heat flow, Q_{net}, was defined as:

$$Q_{net} = Q_{base} + Q_{crib} + Q_{dg}$$ **Equation 6-8**

where all heat flows were defined as positive into the soil domain.

The heat transfers across the domain boundaries basement-B, B-P, and P-A were assumed to be equal so that all the heat from the basement was transported to domain A. $\bar{T}$, the average temperature at a time step, was used to equate the heat flows:

$$\frac{\overline{T_{base}} - \overline{T_{BP}}}{R_B} = \frac{\overline{T_{BP}} - \overline{T_{PA}}}{R_P} = \frac{\overline{T_{PA}} - T_m}{R_A}$$ **Equation 6-9**

Solving Equation 6-9 for $\overline{T_{PA}}$ resulted in:

$$\overline{T_{PA}} = \left[\overline{T_{base}} + T_m\left(\frac{R_B + R_P}{R_A}\right)\right]\left(\frac{1}{1 + \frac{R_B + R_P}{R_A}}\right)$$ **Equation 6-10**

which allows the heat flowing from the basement into the domain to be expressed in terms of the unknown T_m only.

Similarly, the heat transfers across the domain boundaries soil surface-D and D-A were assumed to be equal so that heat from/to the soil surface was all transported to/from domain A. The heat flows were equated by the following equations:

$$\frac{\overline{T_a} - \overline{T_{DA}}}{R_D} = \frac{\overline{T_{DA}} - T_m}{R_A}$$ **Equation 6-11**

Solving Equation 6-11 for $\overline{T_{DA}}$ resulted in:

$$\overline{T_{DA}} = \frac{\overline{T_a}R_A + T_m R_D}{R_A + R_D}$$ **Equation 6-12**

A weighted average temperature, $\overline{T_{avg}}$, was calculated for the top boundary of domain A based on $\overline{T_{PA}}$and $\overline{T_{DA}}$ as follows:

$$\overline{T_{avg}} = \frac{\overline{T_{PA}}A_{base} + \overline{T_{DA}}A_{crib}}{A_{base} + A_{crib}}$$ **Equation 6-13**

Using a linear temperature gradient between $\overline{T_{avg}}$, T_m, and T_{dg}(with T in Kelvin) and the height, h, of the soil domain A and C (48 in.), the change in temperature due to the net heat flow, Q_{net}, between time steps, j, was written as:

$$\left(\overline{T_{avg,j+1}} + T_{m,j+1}\right)\frac{h}{2} - \left(\overline{T_{avg,j}} + T_{m,j}\right)\frac{h}{2} + \left(T_{m,j+1} + T_{dg}\right)\frac{h}{2} - \left(T_{m,j} + T_{dg}\right)\frac{h}{2} = \frac{Q_{net}}{(c\rho)_{mat}(A_{base} + A_{crib})} \quad \textbf{Equation 6-14}$$

where $(c\rho)_{mat}$ was of the soil matrix (water and soil particles). Equation 6-14 was then solved for $T_{m,j+1}$:

$$T_{m,j+1} = \frac{Q_{net}}{(c\rho)_{mat}(A_{base} + A_{crib})h} + \frac{\overline{T_{avg,j}}}{2} + T_{m,j} - \frac{\overline{T_{avg,j+1}}}{2} \quad \textbf{Equation 6-15}$$

The following three variables were defined:

$$X = \left(\frac{R_B + R_P}{R_A}\right) \quad \textbf{Equation 6-16}$$

$$W = \left(\frac{1}{1 + \frac{R_B + R_P}{R_A}}\right) \quad \textbf{Equation 6-17}$$

$$Z = \left(\frac{1}{R_A + R_D}\right) \quad \textbf{Equation 6-18}$$

Combining Equation 6-10, Equation 6-12, and Equation 6-13 using variables *X, W,* and Z, $\overline{T_{avg,j+1}}$ was written as:

$$\overline{T_{avg,j+1}} = \left(\frac{1}{A_{base} + A_{crib}}\right)\left[A_{base}W_{j+1}\left(\overline{T_{base,j+1}} + T_{m,j+1}X_{j+1}\right) + A_{crib}Z_{j+1}\left(\overline{T_{a,j+1}}R_A + T_{m,j+1}R_{D,j+1}\right)\right] \quad \textbf{Equation 6-19}$$

where the variables *X, W, Z,* and R were time step dependent due to the direction of heat flow and the varying surface film coefficient.

Combining Equation 6-15 and Equation 6-19 and solving for $T_{m,j+1}$:

$$T_{m,j+1} = \left(\frac{1}{1 + \frac{A_{base} W_{j+1} X_{j+1} + A_{crib} Z_{j+1} R_{D,j+1}}{2(A_{base} + A_{crib})}} \right) \left[\frac{Q_{net}}{(c\rho)_{mat}(A_{base} + A_{crib})h} + \frac{\overline{T_{avg,j}}}{2} \right.$$

$$\left. + T_{m,j} - \frac{A_{base} W_{j+1} \overline{T_{base,j+1}} + A_{crib} Z_{j+1} R_A \overline{T_{a,j+1}}}{2(A_{base} + A_{crib})} \right] \quad \textbf{Equation 6-20}$$

Equation 6-20 is an equation for the time-varying temperature, T_m, based on the net heat flow into the control volume below the slab and crib (domain A and C). The variable T_m was used to calculate the basement, crib, and deep-ground heat transfer at each time step, unlike in Method 1 where a constant deep-ground temperature was used for the calculation of the basement and crib heat flows.

The heat transferred from the basement horizontally through the slab and wall to the soil adjacent to the wall, Q_{horz}, was calculated as a comparison to the heat lost to the soil below the slab, Q_{base}. The temperature driver for the heat transfer, Q_{horz}, was the interior basement temperature, T_{base}, and $\overline{T_{DA}}$. The area used for the calculation was based on the 4 in. depth of the concrete slab and a 1 ft. wide strip, yielding A_{horz}=0.333 ft^2 (0.0310 m^2). The thermal resistance from the interior surface of the slab to a point horizontally 24 in. from the exterior face of the wall on the D-A soil domain boundary, R_{horz}, is provided in Table 6-3. The equation used for the horizontal heat transfer was:

$$Q_{horz} = \frac{A_{horz}}{R_{horz}} \sum_{j=1}^{N} \left[\frac{1}{2} \left(T_{base,j} + T_{base,j+1} \right) - \overline{T_{DA,j}} \right] \left(t_{j+1} - t_j \right) \quad \textbf{Equation 6-21}$$

6.4.4 Method 3

Figure 6-16 is a schematic of the soil domain and heat flows for Method 3. Method 3 was similar to Method 2 in that both included the heat transferred from the deep ground and the time-varying variable T_m at 48 in. below the bottom of the footing. For Method 3, domains A and C were only below the slab as opposed to Method 2 where they extended below the slab and the crib. Domain E was introduced below the crib between the bottom of the footing and the elevation of T_m (48 in. below the bottom of the footing). In Method 3, the heat transferred through the crib was based on a radial path through domain E.

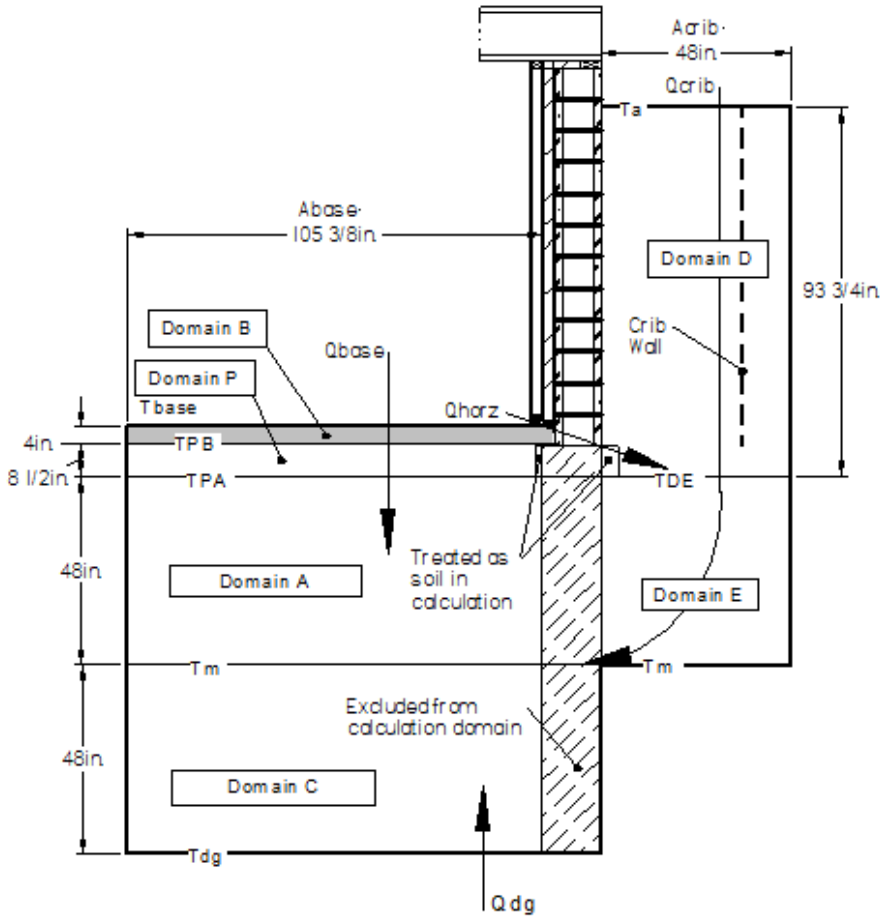

Figure 6-16: Diagram of Method 3 Heat Transfer

The annual basement heat transfer, Q_{base}, was calculated using Equation 6-5. The annual deep ground heat transfer, Q_{dg}, was calculated by:

$$Q_{dg} = \frac{A_{base}}{R_{dg-m}} \sum_{j=1}^{N} [T_{dg} - T_m](t_{j+1} - t_j) \qquad \textbf{Equation 6-22}$$

The annual crib heat transfer, Q_{crib}, was calculated by:

$$Q_{crib} = \frac{A_{crib}}{R_{crib-m^*}} \sum_{j=1}^{N} \left[\frac{1}{2}(T_{crib,j} + T_{crib,j+1}) - T_m\right](t_{j+1} - t_j) \qquad \textbf{Equation 6-23}$$

where R_{crib-m^*} is the thermal resistance between the soil surface and the plane between domain A and C based on a radial path through domain E.

The net heat flow, Q_{net}, was defined as:

$$Q_{net} = Q_{base} + Q_{dg} + Q_{crib}$$ **Equation 6-24**

The heat transferred across the domain boundaries basement-B, B-P, and P-A was set equal such that the heat from the basement was all transferred to domain A. The heat transferred across the domain boundaries soil surface-D and D-E was set equal such that heat from/to the soil surface was all transported to/from domain E. The temperature, $\overline{T_{PA}}$, was defined by Equation 6-10. The heat flows through the crib were equated by the following equations:

$$\frac{\overline{T_a} - \overline{T_{DE}}}{R_E} = \frac{\overline{T_{DE}} - T_m}{R_A}$$ **Equation 6-25**

Solving Equation 6-25 for $\overline{T_{DE}}$ resulted in:

$$\overline{T_{DE}} = \frac{\overline{T_a} R_E + T_m R_D}{R_E + R_D}$$ **Equation 6-26**

The equation for $T_{m,j+1}$ was the same as Equation 6-15 except $\overline{T_{avg,}}$ was replaced by $\overline{T_{PA}}$ and the area only included A_{base} so that:

$$T_{m,j+1} = \frac{Q_{net}}{(c\rho)_{mat}(A_{base})h} + \frac{\overline{T_{PA,j}}}{2} + T_{m,j} - \frac{\overline{T_{PA,\,j+1}}}{2}$$ **Equation 6-27**

Using variables X and W defined in Equation 6-16 and Equation 6-17, respectively, and combining Equation 6-27 and Equation 6-10 and solving for $T_{m,j+1}$:

$$T_{m,j+1} = \left(\frac{1}{1 + \frac{W_{j+1}X_{j+1}}{2}}\right)\left[\frac{Q_{net}}{(c\rho)_{mat}(A_{base})h} + \frac{\overline{T_{PA,j}}}{2} + T_{m,j} - \frac{W_{j+1}\overline{T_{base,j+1}}}{2}\right]$$ **Equation 6-28**

Equation 6-28 was used to calculate the time-varying temperature below the slab based on the heat flow from the basement, deep ground, and soil surface.

As with Method 2, the heat transferred from the basement horizontally through slab and wall to the soil adjacent to the wall, Q_{horz}, was calculated as a comparison to the heat lost to the soil below the slab, Q_{base}. Equation 6-21 was used for the calculation of Q_{horz} where R_{horz} is provided in Table 6-3.

6.4.5 **Calculation Results**

Figure 6-17 shows the results of the calculations. Q_{base} is the heat gain to the soil below the slab from the basement, Q_{crib} is the heat gain to the soil below the slab and crib (Method 2) or below the slab (Method 3) from the outdoor ambient, Q_{dg} is the heat gain to the soil domain below the slab and crib (Method 2) or below the slab (Method 3) from the deep ground, and Q_{horz} is the heat gain to the soil adjacent to the wall and footing from the basement due to horizontal heat transfer through the slab. Positive heat flows indicate that heat was added to the soil domain and negative values indicate that heat was lost from the soil domain. If there was heat gain and loss over the course of the year, the break down is provided in parenthesis in Figure 6-17. BUFETS Case 2 (Chapter 6.1) was similar to Case B. Case 2 and Case B were the same except the Case 2 deep ground soil temperature was elevated from 7.2 deg. C to 11.4 deg. C during the cooling season whereas the Case B deep ground temperature was held at 7.2 deg. C during the cooling season. Also, the Case 2 soil moisture contents were the values on November 20, 2012 whereas the Case B soil moisture contents were the averages of the 2013 experimental data. Both of these factors would have caused the Case B heat losses to be greater than the Case 2 heat losses. Despite the differences, the Case 2 simulation heat loss Q_{base} of 154 MJ/ft/yr confirms the order of magnitude of the calculations that for Case B had a Q_{base} of 188-210 MJ/ft/yr.

Method 1: Q_{base} and Q_{crib} independent and driven by T_{dg} **Case A:** Linear MC gradient from crib to H_2O table 96 in. below btm. of ftg.

Method 2: T_m drives Q_{base} and Q_{crib}, domain A below slab and crib **Case B:** H_2O table at bottom of footing

Method 3: T_m drives Q_{base} and Q_{crib}, domain A below slab **Case C:** H_2O table 96 in. below btm. of ftg., constant MC to 24 in. above H_2O table

Note: Positive values indicate heat gain to the soil domain. Heat gain and loss provided in parenthesis when applicable.

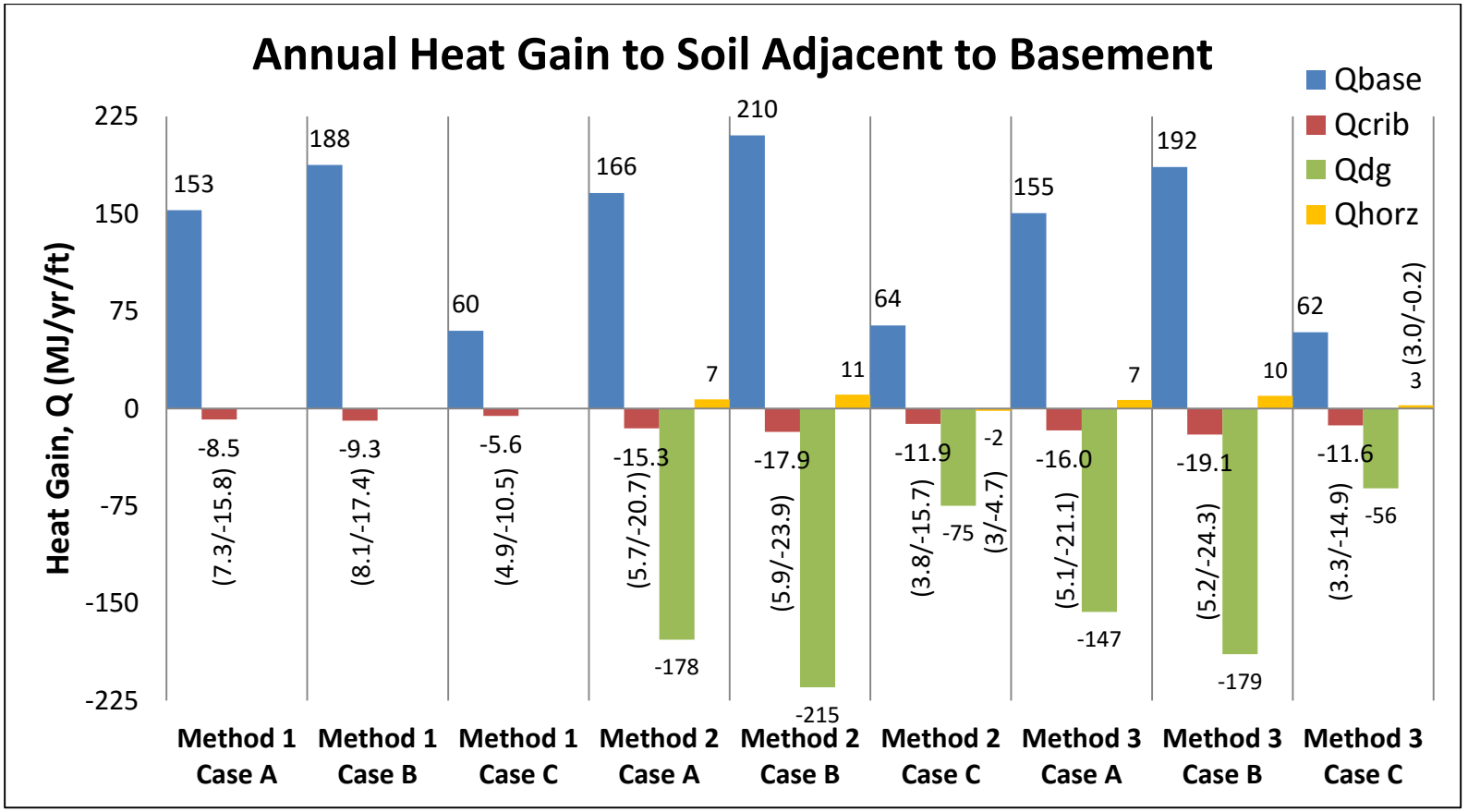

Figure 6-17: Calculation Results – Annual Heat Gain to Soil Adjacent to Basement

Method 1 calculated Q_{base} and Q_{crib} independent of one another. Q_{crib} was effectively a far field heat loss calculation because it did not account for heat loss from the basement. It would be expected that the actual value of Q_{crib} and Q_{base} would be greater than the values calculated in Method 1 if Q_{base} and Q_{crib} were dependent on one another. In this calculation, the driving deep ground temperature for the calculation of Q_{base} did not change as heat was added to the soil domain. This change in the deep ground temperature would have resulted in a decrease in the actual Q_{base}. The Case B annual basement heat loss was 188 MJ/ft/yr and the annual crib heat loss was 9.3 MJ/ft/yr (Figure 6-17).

In Method 2, it was assumed that Q_{base} and Q_{crib} were evenly distributed under the basement and crib. In reality, the heat from the basement would have a greater impact on the soil directly below the slab and a reduced effect on the soil below the crib. Q_{base} and Q_{crib} were interrelated as they were both used to calculate an intermediate, time-varying soil domain temperature T_m. The initialized value of T_m (12.74 deg. C) was based on a linear gradient between T_{base} and T_{dg}. The Case B annual basement heat loss was 210 MJ/ft/yr and the annual crib heat loss was 17.9 MJ/ft/yr (Figure 6-17).

With Method 3, Q_{base} was concentrated below the basement slab and Q_{crib} was concentrated below the soil crib. Both Q_{base} and Q_{crib} were used to calculate an intermediate, time-varying soil domain temperature T_m. The initialized value of T_m (12.74 deg. C) was the same as with Method 2. This method approximated the case where all of the basement heat was lost to the soil below the slab and there was a radial heat loss from the soil below the slab to the soil surface through the crib. The Case B annual basement heat loss was 192 MJ/ft/yr and the annual crib heat loss was 19.1 MJ/ft/yr (Figure 6-17).

Methods 2 and 3 were more accurate than Method 1 where Q_{base} and Q_{crib} had no impact on one another. For Methods 2 and 3, if the heat loss from the basement, Q_{base}, increased, so did the heat loss through the soil crib to the soil surface, Q_{crib}. In other words, the more heat that was stored in the soil below the slab, the more heat there was to be lost through the crib to the soil surface during the heating season. More heat lost through the crib caused a greater increase in the crib soil temperatures.

A comparison of Q_{crib} and Q_{horz} provides insight into the primary source of heat influencing the soil temperatures adjacent to the basement wall. For all methods and cases, during a portion of the year (primarily the cooling season) the value of Q_{crib} was positive indicating heat gain to the soil domain below the crib and during the remainder of the year (primarily the heating season) the value was negative, indicating heat loss from the soil domain below the crib to the soil surface. For all methods and cases, the annual Q_{crib} was negative. For Methods 2 and 3, Cases A and B, Q_{horz} was always positive indicating that heat loss was from the basement horizontally through the slab to the soil adjacent to the wall year-round. For Methods 2 and 3, Case C, during part of the year, the basement gained heat horizontally through the slab from the soil. For Cases A and B, the soil adjacent to the footing and below the footing had more moisture than for Case C. The additional moisture reduced the rise in soil temperature during the cooling season because of the higher heat capacity, such that the horizontal heat flow, Q_{horz}, was always from the interior to the exterior for Cases A and B. However for Case C, the exterior temperature increased such that Q_{horz} was from the exterior to the interior.

For Cases A and B, the annual heat transfer from below the crib to the soil surface (Q_{crib}) was approximately 2.3 and 1.8 times greater than the annual heat transfer from the basement to the crib (Q_{horz}) (Table 6-4). For Case C, Method 3, the annual heat transfer from below the crib to the soil surface (Q_{crib}) was approximately 4.1 times greater than the annual heat transfer from the basement to the crib (Q_{horz}). For Case C, Method 2, the annual horizontal heat transfer, Q_{horz}, was into the basement. For the heating season only, the average ratio of the heat transfer from below the crib to the soil surface (Q_{crib}) to the heat transfer from the basement to the crib (Q_{horz}) was 4.0 and 3.1 for Cases A and B, respectively (Table 6-5). For Case C, Method 3, the ratio was 5.1 and for Case C, Method 2, the heat transfer from the basement to the crib was approximately zero. These values are not conservative because the thermal resistance, R, used to calculate Q_{crib} did not include the thermal resistance of the snow. This increased thermal resistance would have decreased the magnitude of the heat loss, Q_{crib}, during the heating season when snow was present. Regardless, it can be concluded that the elevated soil temperatures adjacent to the basement wall were primarily due to the heat stored in the soil domain below the basement slab and lost to the soil surface during the heating season.

	Case A	Case B	Case C
Method 2	2.2	1.7	--[25]
Method 3	2.4	1.9	4.1

Table 6-4: Annual Q_{crib}/Q_{horz}

	Case A	Case B	Case C
Method 2	4.0	3.0	--[26]
Method 3	4.1	3.1	5.1

Table 6-5: Heating Season Q_{crib}/Q_{horz}

The calculation results of a high ratio of Q_{crib} to Q_{horz} are reinforced by the experiment where insulation was placed on the floor of Bay 3. The insulation had no effect on the temperature of the wall and soil, indicating that the primary heat source was not the heat lost horizontally through the slab (Chapter 5.3).

In the experimental data there was an increase in the soil temperature between January 1, 2013 and December 31, 2014 at 5.5 in. above the slab (approx. 0.75 deg. C) and 40 in. above the slab (approx. 1.5 deg. C) (Figure 6-2 and Figure 6-4). Prior to the commencement of this experiment, the basement had not been conditioned during the heating season for approximately seven years. During the first experimental heating season (November 2012 to June 2013), there would have been an increased heat loss from the basement to the soil domain below the slab. This additional heat would have been stored in the soil domain and resulted in an increased heat loss to the soil surface during the second heating season over the first heating season. The additional heat loss during the second heating season would have caused soil temperatures adjacent to the wall to increase between heating seasons as the system approached a new steady state. This explanation reinforces that heat was being added to the crib as the calculation results show. It is also possible that the elevated soil temperatures were due to the early and high snow pack of the second heating season as compared to the first heating season (Figure 5-5). The early and high snow pack would reduce the heat loss

[25] Heat flow, Q_{horz}, was into the basement.
[26] Heat flow, Q_{horz}, was approximately zero.

from the soil and prevent the soil temperatures from dropping as low as the first heating season.

For all methods, the heat loss from the basement to the soil below the slab, the heat loss from the soil below the crib to the soil surface, and the heat loss from the basement horizontally through the slab to the soil was the greatest for Case B and the least for Case C. This was due to the amount of water in the soil below the basement slab. Case B had the water table at the bottom of the footing which was the closest approximation to the water table height prevailing during the experiment (Chapter 5.3). Cases A and C had the water table at the bottom of the domain (96 in. below the bottom of the footing). In Case C, the soil domain below the footing was kept relatively dry to within 24 in. of the water table. The more water there was in the soil, the greater the heat capacity of the soil. This increased the heat loss from the basement and increased the heat loss to the soil surface through the crib. This reinforces the effect the water table height has on the basement heat loss and soil temperatures. Additionally, the type of soil not only adjacent to the basement wall, but below the basement slab and above the water table affects the basement heat loss and soil temperatures. This is because well-drained soils such as sands, hold less water than poorly drained soils such as loams, thus effecting the heat capacity of the soil.

The high water table used for Case B (at the bottom of the footing) most closely models the experimental conditions. Of the methods, Method 3 best represents the actual heat transfer mechanisms because Q_{base} and Q_{crib} are related and the heat transfer path between the two is radial. In conclusion, the simplified calculations validate the experimental observations. The elevated crib soil temperatures are explained by the heat loss from the soil domain below the slab that acts as a large heat sink. The Method 3, Case B calculations confirm this because the heat loss from the domain below the slab to the soil surface is 3.1 times greater than the horizontal heat loss through the slab to the crib during the heating season and 1.9 times greater on an annual basis. This shows that for a basement wall with R-15 insulation, the primary heat loss is through the basement slab. The heat capacity of the soil domain below the slab is increased significantly by the high water table. The calculations reinforce the impact of the high water table on basement heat loss where for Method 3, the basement heat loss for Case B was three times greater than for Case C (relatively dry soil domain).

Chapter 7: Conclusions and Future Work

7.1 Conclusions

A summary of the research findings with reference to the objectives given in Chapter 1.3 is as follows:

Generate Experimental Data / Obtain Reliable CMU Moisture Content Data

A primary objective of this research was to generate a reliable hygrothermal dataset for in-situ below-grade walls. Reliable data collection began on November 10, 2012 for Bays 1 and 2 and on January 18, 2013 for Bays 3 and 4. Data collection continued until November 24, 2014 when it was shut down. During that time, data was collected at maximum intervals of 12 minutes and had a data availability of 98% based on the recorded data (this does not account for sensor failures). Data were collected from temperature, humidity, heat flux, and concrete masonry unit (CMU) moisture content sensors located throughout the wall system and temperature and moisture content sensors located in the soil. Additionally, a range of interior boundary conditions and climate data were collected. CMU moisture content sensors that were exposed to wet conditions (exterior face of CMU and interior face of CMU where bulk water was introduced) failed, thus limiting the moisture content data available. All the data from this experiment is in the public domain.

Expand Understanding of the Effects of Buoyant Cavity Flow

During the heating season, buoyant cavity flow is an important heat transfer mechanism in below-grade CMU walls with full-height insulation on the interior face. The top-to-bottom temperature difference is the primary indicator of this flow. However, the side-to-side temperature difference is not insignificant and increases the magnitude of the flow velocity. Exterior half-height insulation on the upper half of the wall essentially eliminates the top-to-bottom temperature difference so that the primary driver of buoyant cavity flow is the side-to-side temperature difference.

Study the Relationship between Soil Moisture and Wall Moisture

It is difficult to predict and model the infiltration and percolation of water through the soil adjacent to a building due to the randomness of the flow paths. Instead a simplified relationship between soil moisture content and the CMU moisture content was identified. It was found that walls with poorly drained soils have higher exterior face

shell moisture contents than walls with well-drained soils. For below-grade hollow core CMU walls with exterior, below-grade damp-proofing and interior insulation and waterproofing, the interior face shell stayed relatively dry (< 34% vol. MC), was drier than the exterior face shell, and did not appear to be affected by soil moisture. Both the interior and exterior CMU face shell moisture contents were strongly correlated with the hollow core absolute humidity.

Simplified Thermal Calculations / Evaluate Accuracy of a Below-Grade Computer Model

Independent simplified thermal calculations were performed to determine the primary heat loss mechanism in below grade spaces with well-insulated walls. It was found that the heat loss through the slab is substantial, greatly impacted by the moisture content of the soil below the slab, and, more specifically, the height of the water table. In the case of below-grade CMU walls insulated with R-15 full-height interior insulation, during the heating season, the temperature of the soil adjacent to the wall is primarily driven by the heat stored in the soil domain below the slab and lost to the soil surface. During the heating season, the heat lost from the soil below the slab to the soil surface is at least three times larger than the heat lost from the basement through the uninsulated base of the wall. The soil below the slab effectively acts as a heat sink and a high water table increases its thermal capacity.

A comparison of the experimental and simulated data reinforces this finding. At 40 in. above the slab during the heating season, the experimental soil temperatures were 2 to 4 deg. C warmer than the simulated soil temperatures. The discrepancy between the experimental and simulated temperatures was reduced when the height of the water table and the size of the soil domain below the slab were increased in the model. This finding explains a major part of the experiment/simulation discrepancies found.

Software that accurately models below-grade walls is needed for developing new wall systems and understanding the thermal and moisture performance of these walls. Hygrothermal ground-coupled models have the capacity of being more accurate than thermal ground-coupled models because they account for the transport of heat by moisture, the thermal properties of the materials based on their moisture content, and the latent heat. Additionally, they have the potential to identify durability problems

related to moisture. However, there are few hygrothermal models that can model below-grade walls with the fuzzy boundary conditions and material properties which are a reality in practice. This research provides a valuable experimental data set that can be used for the development and validation of such models. Further, to improve these models' capabilities and accuracy, the research shows the importance of including the following:

- The water table height and associated time-varying temperature profile;
- Buoyant cavity flow in hollow CMU walls; and,
- Inclusion of soil and CMU wall moisture transport in the simulation, or time-varying moisture content in the soil and wall domains, for use in simulations that model thermal transport only.

7.2 Future Work

A primary objective of this research was to generate a reliable experimental data set for below-grade walls. The experiment ran from November 10, 2012 to November 24, 2014. Ideally, the experiment should run for longer than this two-year period, at least until a pseudo steady-state condition is reached. This would allow the steady-state condition to be analyzed and allow long-term trends to be distilled out of the data. For example, a longer data set would allow trends such as moisture accumulation to be studied. Additionally, during the first winter the excavated soils had not been consolidated by snow melt and rain. A longer data set would allow for the examination of the differences in heat and moisture transport in unconsolidated and consolidated soils. Further, it would provide a data set that more closely reflects the long-term pseudo-steady state operational performance of the wall for the validation of computer models. If this experiment were to continue running, it would be valuable to bore a well to continuously monitor the water table depth and temperature. If this is cost prohibitive, a reasonable alternative would be a set of test borings during multiple seasons that record the water table depth and temperature.

Nonetheless, the available experimental data still allows for the validation of the heat and moisture transport processes used in simulation models. Hence full advantage should be taken of the data, whether using the existing data set or an extended data

set, to develop, refine and/or validate thermal and hygrothermal models of below-grade walls.

After the experiment has been completed, the walls should be carefully dismantled and inspected. During the dismantling, the walls should be checked for any signs of moisture damage such as mold, mildew, or rot. The adhered water separation plane (WSP) should be checked for delamination from the wall. The joints of the adhered and non-adhered WSP's should be inspected to determine if they are still intact.

Additional experimental work is needed to better understand buoyant cavity flow in below grade walls. Temperature and velocity sensors located in the hollow core adjacent to the interior and exterior face shells and at the mid-point of the core would provide an understanding of the magnitude of the flow. The sensors should be located, at a minimum, at the one-third points of the height of the hollow core. Heat flux plates on the interior and exterior face shells and aligned with the hollow core sensors would provide insight into the portion of the heat transfer that was by conduction and the portion that was by buoyant cavity flow. The difference in heat flux between an interior and exterior heat flux plate at a given height would indicate the portion of heat transfer that was by buoyant cavity flow at that height. Additionally, a set of interior/exterior heat flux plates should be located just below the termination of the insulation on the base of the wall or on the slab adjacent to the wall. This set of heat flux plates would provide understanding as to the amount of heat lost through this joint to the soil and hollow cavity. These data would improve the understanding of the impact of buoyant cavity flow on the thermal performance of below-grade walls. Additionally, they would allow thermal and hygrothermal models to include this heat transfer mechanism. Additional heat flux plates should be located on the slab to measure the amount of heat lost from the basement to the soil domain below the slab. A minimum of two heat flux plates should be used, one near the perimeter and one at the one-third point of the basement. These heat flux plates would provide understanding on the impact of the water table height on basement heat loss.

Further work is required to develop the CMU moisture content sensors that were used in this research for wet conditions. To improve the sensors, the installation process and materials need to be evaluated. If the graphite paste (Anders Products) that coated the

graphite rods is water-based, a new electrically conducing paste is needed that does not break down when exposed to water for extended periods. Additionally, it should be determined whether the epoxy covering the top of the electrodes breaks down at cold temperatures. The installation technique needs to be improved to ensure that the graphite rods penetrate to the base of the hole and do not crack. If these changes are not possible, other non-corroding materials should be explored for developing the moisture content measurement electrodes.

More research is needed to understand the soil and CMU moisture content. This research had a limited number of soil sensors and was unable to identify a pattern for the infiltration and percolation of water through the soil. However, if more sensors are deployed, a pattern may be recognized that can be used for modeling purposes. Since in this experiment the CMU moisture content sensors on the below-grade exterior face of the walls failed, additional research with improved sensors is needed to reevaluate the relationship between the soil and CMU moisture contents.

Bibliography

Anders Products. "Wire Glue." Accessed July 12, 2014. http://www.wireglue.us/.

ASTM International. 2007. "Standard Test Methods for Direct Moisture Content Measurement of Wood and Wood- Base Materials." Chap. D4442, In *Annual Book of American Society for Testing and Materials*. Vol. 04.10.

ASTM International. 2012. "Standard Test Methods for Sampling and Testing Concrete Masonry Units and Related Units." Chap. C140, In *Annual Book of American Society for Testing and Materials*. Vol. 04.05.

Campbell Scientific Inc. 2011. "Instruction Manual: SR50A Sonic Ranging Sensor." http://s.campbellsci.com/documents/us/manuals/sr50a.pdf.

Carlisle Coatings & Waterproofing. 2013. *"*Section 071326, Self-Adhering Sheet Waterproofing, CCW MiraDRI 860/861." In *Manufacturer's Guide Specifications*.

CertainTeed. "Form-A-Drain." Accessed October 7, 2014. http://www.certainteed.com/resources/40-95-27.pdf.

Claesson, Johan and Carl-Eric Hagentoft. 1991. "Heat Loss to the Ground from a building—I. General Theory." *Building and Environment* 26 (2): 195-208. doi:10.1016/0360-1323(91)90027-9.

Delmhorst Instrument Co. "Moisture Meters for Flooring and Wood Products." Accessed November 6, 2014. http://www.delmhorst.com/Moisture-Meters/Flooring-Wood-Products.

Deru, M. 2003*. A Model for Ground-Coupled Heat and Moisture Transfer from Buildings.* National Renewable Energy Laboratory.

Deru, Michael and Allan Kirkpatrick. 2002a. "Ground-Coupled Heat and Moisture Transfer from Buildings Part 1–Analysis and Modeling." *Journal of Solar Energy Engineering* 124 (1): 10. doi:10.1115/1.1435652.

Deru, Michael and Allan Kirkpatrick. 2002b. "Ground-Coupled Heat and Moisture Transfer from Buildings Part 2–Application." *Journal of Solar Energy Engineering* 124 (1): 17. doi:10.1115/1.1435651.

Dow. "Styrofoam Brand Square Edge Insulation Product Information." Accessed May 19, 2013. http://building.dow.com/na/en/products/insulation/squareedge.htm.

Fraunhofer IBP. "WUFI Pro, 2D, Plus." Accessed October 24, 2014, http://www.wufi.de/index_e.html.

Goldberg, L. and B. Steigauf. 2013*. Cold Climate Foundation Retrofit Energy Savings: The Simulated Energy and Experimental Hygrothermal Performance of Cold Climate Foundation Wall Insulation Retrofit Measures -- Phase I, Energy Simulation.* USDOE Office of Energy Efficiency and Renewable Energy Building Technologies Program.

Goldberg, L. and M. Stender. 2013. "The Experimental Hygrothermal Performance of a Robust Cold-Climate Retrofit Interior Foundation Wall Insulation System." In *Thermal Performance of the Exterior Envelopes of Whole Buildings XII International Conferen*ce, Clearwater Beach, Florida, December 1-5, 2013.

Goldberg, L. F. and A. C. Harmon. 2014*. Cold Climate Foundation Retrofit Experimental Hygrothermal Performance: CRRF Laboratory Results*. Building America Research Report (in review), Building Technologies Program, EERE Office, U.S. Dept. of Energy.

Hanks, R. J. and G. L. Ashcroft. 1980. *Applied Soil Physics: Soil Water and Temperature Application*s. New York: Springer-Verlag.

Huelman, P., L. Goldberg, and R. Jacobson. 2013*. Innovative Retrofit Insulation Strategies for Concrete Masonry Foundations.* U.S. Department of Energy.

Janssen, H. 2002. "The Influence of Soil Moisture Transfer on Building Heat Loss Via the Ground." PhD diss., Catholic University of Leuven.

Janssen, Hans, Jan Carmeliet, and Hugo Hens. 2004. "The Influence of Soil Moisture Transfer on Building Heat Loss Via the Ground." *Building and Environment* 39 (7): 825-836. doi:10.1016/j.buildenv.2004.01.004.

Johansen, O. 1975. "Thermal Conductivity of Soils." Ph.D. diss., Trondheim, Norway. (CRREL Draft Translation 637, 1977). ADA 044002.

Jury, W. A., W. R. Gardner, and W. H. Gardner. 1991. *Soil Physics*. 5th ed. New York: John Wiley & Sons, Inc.

Kehrer, M., S. Pallin, L. Goldberg, and A. Harmon. 2012*. Hygrothermal Simulation of Foundations: Part 1 Soil Material Properties.* Oak Ridge National Laboratory.

Kersten, M. S. 1948. "The Thermal Conductivity of Soils." *Proc. Highway Research Board* vol. 29: 391-409.

Kovler, Konstantin and Nicolas Roussel. 2011. "Properties of Fresh and Hardened Concrete." *Cement and Concrete Research* 41 (7): 775-792. doi:http://dx.doi.org/10.1016/j.cemconres.2011.03.009.

Krarti, M., D. Claridge, and J. Kreider. 1988a. "ITPE Technique Applications to Time-Varying Two-Dimensional Ground-Coupling Problems." *International Journal of Heat and Mass Transfer* 31 (9): 1899-1911. doi:10.1016/0017-9310(88)90203-7.

Krarti, M., D. Claridge, and J. Kreider. 1988b. "The ITPE Technique Applied to Steady-State Ground-Coupling Problems." *International Journal of Heat and Mass Transfer* 31 (9): 1885-1898. doi:10.1016/0017-9310(88)90202-5.

Kreith, F. 1967. *Principles of Heat Transfer*. 2nd ed. Scranton, Pennsylvania: International Textbook Company.

Latta, J. and G. Boileau. 1969. "Heat Losses from House Basements." *Canadian Builders* 19 (10).

Master Masonry. Accessed June 30, 2014. http://www.mastermasonry.com/history2.htm.

McBride, M. 2013. "Natural Convection in Below Grade Open Cell Concrete Block Walls." In T*hermal Performance of the Exterior Envelopes of Whole Buildings XII International Conference, Clearwater Beach, Florida, December 1-5, 2013.*

Mitalas, G. 1983. "Calculation of Basement Heat Loss." *ASHRAE Transactions* 89 (1): 420-428.

National Climatic Data Center. "Climate Data Online Search." Accessed November 11, 2014. http://www.ncdc.noaa.gov/cdo-web/search?datasetid=GHCNDMS.

National Climatic Data Center. "NOAA's 1981-2010 Climate Normals." Accessed October 4, 2014. http://www.ncdc.noaa.gov/oa/climate/normals/newnormals.html.

Probert, S.D., and M. Dixon. 1979. "Free convection within a vertical, rectangular cavity subjected to large temperature differences." *Applied Energy* 5 (3): 233-241.

Santos, G. and N. Mendes. 2006. "Simultaneous Heat and Moisture Transfer in Soils Combined with Building Simulation." *Energy and Buildings* 38 (4): 303-314.

Shen, Lester S. and James W. Ramsey. 1988. "An Investigation of Transient, Two-Dimensional Coupled Heat and Moisture Flow in the Soil Surrounding a Basement Wall." *International Journal of Heat and Mass Transfer* 31 (7): 1517-1527. doi:http://dx.doi.org/10.1016/0017-9310(88)90259-1.

Shipp, P. H. 1983. "Natural Convection within Masonry Block Basement Walls." *ASHRAE Transactions* 89 (1).

Shipp, P. H. 1979. "The Thermal Characteristics of Large Earth-Sheltered Structures." PhD, University of Minnesota.

State of Minnesota. *Residential Energy Code,* (2009). N1102.2.6-12.

Straube, J. and E. Burnett. 2005. "Moisture Storage and Transport in Porous Media." In *Building Science for Building Enclosures.* Westford, MA: Building Science Press.

Thomas, H.R. and S.W. Rees. 1998. "The Thermal Performance of Ground Floor Slabs—a Full Scale in-Situ Experiment." *Building and Environment* 34 (2): 139-164.

U.S. Department of Energy. "Building Energy Software Tools Directory." Accessed October 26, 2014. http://apps1.eere.energy.gov/buildings/tools_directory/subjects.cfm/pagename=subjects/pagename_menu=materials_components/pagename_submenu=envelope_systems.

U.S. Environmental Protection Agency. "Average Temperature of Shallow Ground Water." Accessed July 14, 2014. http://www.epa.gov/athens/learn2model/part-two/onsite/ex/jne_henrys_map.html.

U.S. Geological Survey. 1954. *Iverson, MN (46092F5)* [map]. 1:24,000.

U.S. Department of Agriculture. "Soil Texture Calculator." Accessed October 6, 2014. http://www.nrcs.usda.gov/wps/portal/nrcs/detail/soils/survey/?cid=nrcs142p2_054167.

Wang, F. S. 1979. "Mathematical Modeling and Computer Simulation of Insulation Systems in Below Grade Applications." http://web.ornl.gov/sci/buildings/2012/1979%20B1%20papers/033.pdf.

Western Regional Climate Center. "NCDC 1981-2010 Monthly Normals." Accessed August 15, 2013. http://www.wrcc.dri.edu/cgi-bin/cliMAIN.pl?mn1630.

Western Regional Climate Center. "Period of Record General Climate Summary-Heating Degree Days." Last modified October 31, 2012. http://www.wrcc.dri.edu/cgi-bin/cliMAIN.pl?mn1630.

Zoras, Stamatis. 2009. "A Review of Building Earth-Contact Heat Transfer." *Advances in Building Energy Research* 3: 289-314. doi:10.3763/aber.2009.0312.

Appendix A: Interior Water Separation Plane and Partial Exterior Insulation

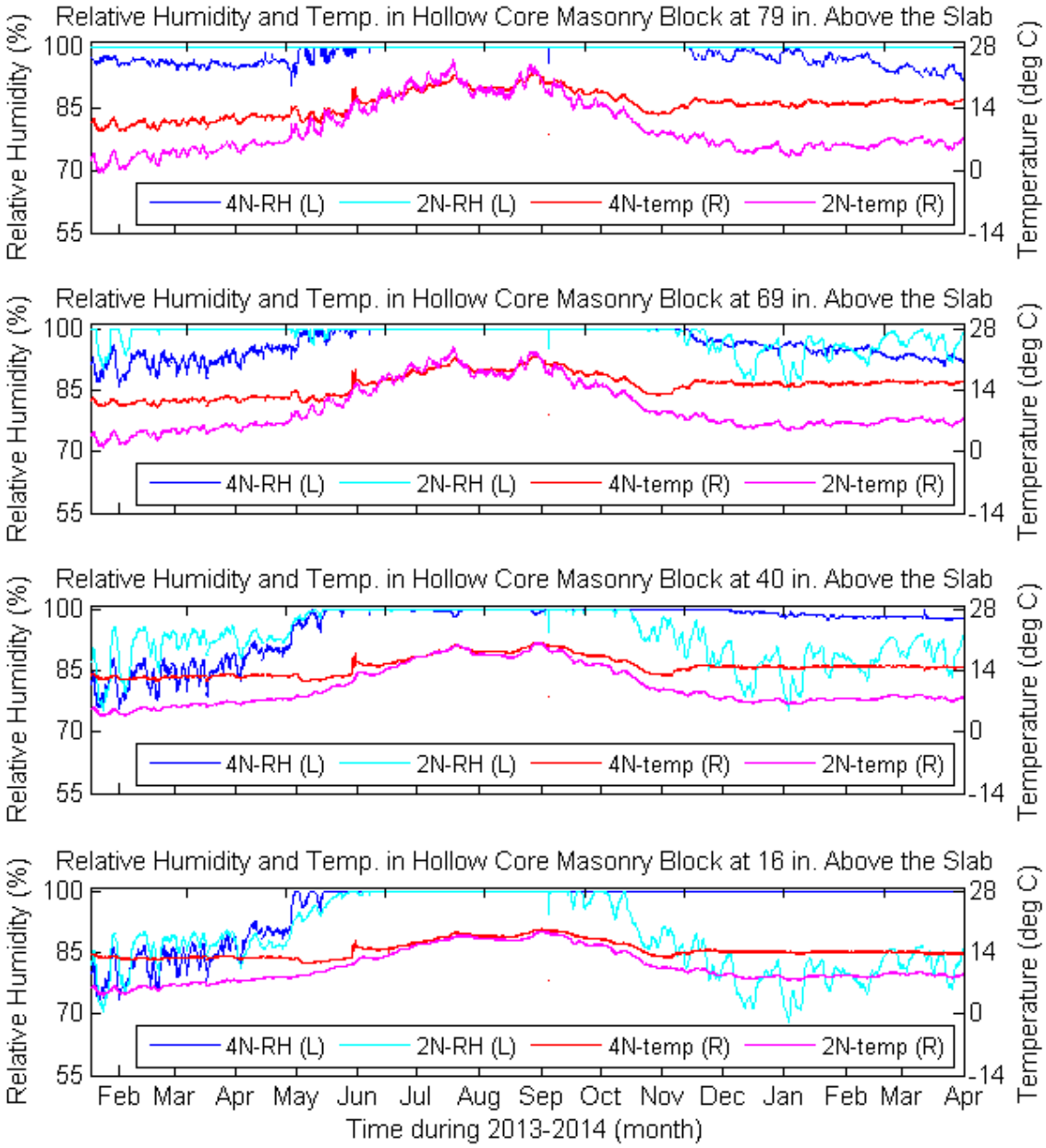

Figure A-1: Comparison of Hollow Core Masonry Block Relative Humidities and Temperatures in Bay 2 (Full-Height Interior Insulation) and Bay 4 (Half-Height Exterior Insulation) with North Exposure

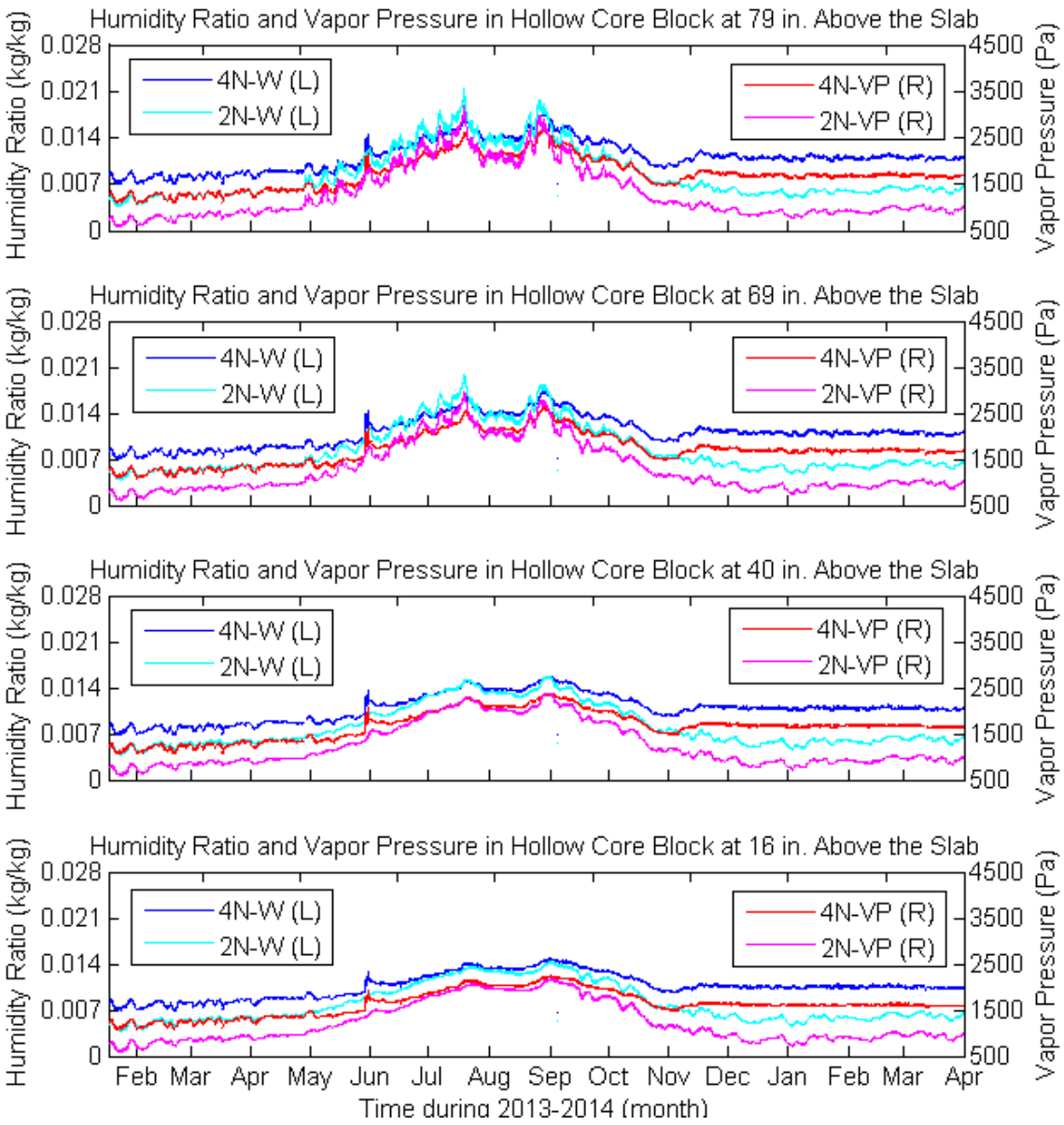

Figure A-2: Comparison of Hollow Core Masonry Block Humidity Ratios and Vapor Pressures in Bay 2 (Full-Height Interior Insulation) and Bay 4 (Half-Height Exterior Insulation) with North Exposure

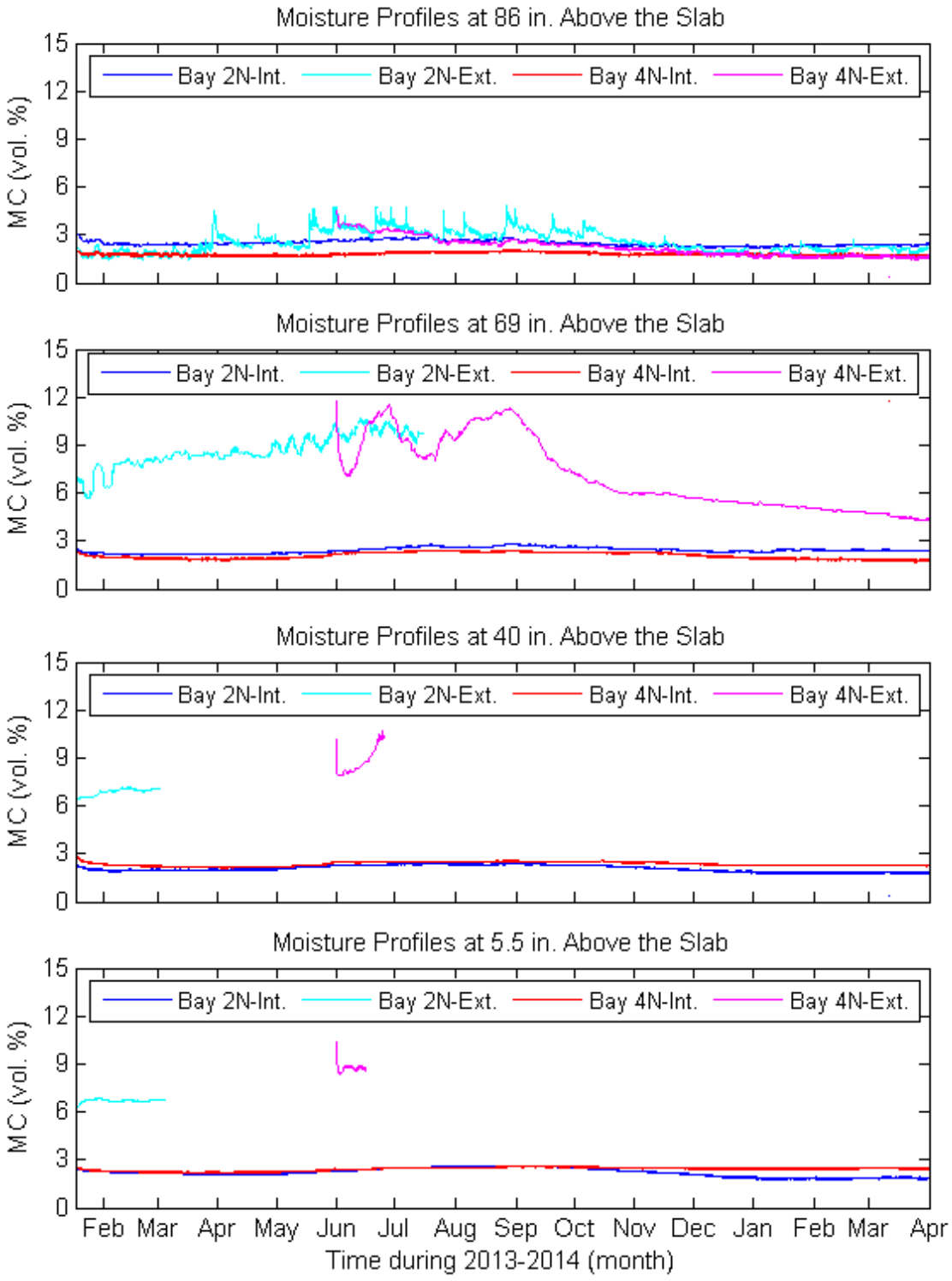

Figure A-3: Comparison of Interior and Exterior Block Moisture Content in Bay 2 (Full-Height Interior Insulation) and Bay 4 (Half-Height Exterior Insulation) with North Exposure

Appendix B: Temperature Data

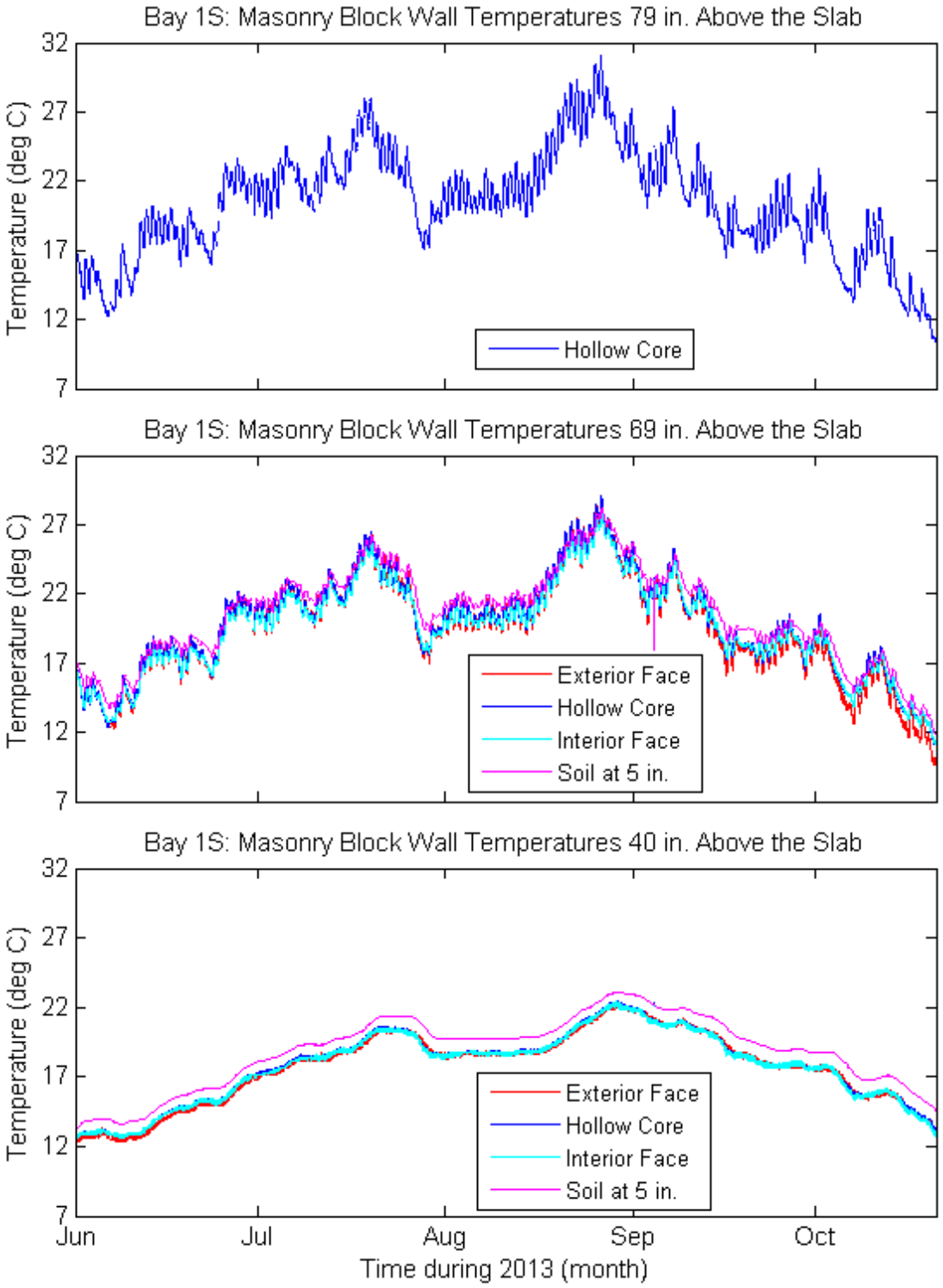

Figure B-1: Bay 1S Masonry Block Wall and Soil Temperatures during Cooling Season at Upper Heights of Wall

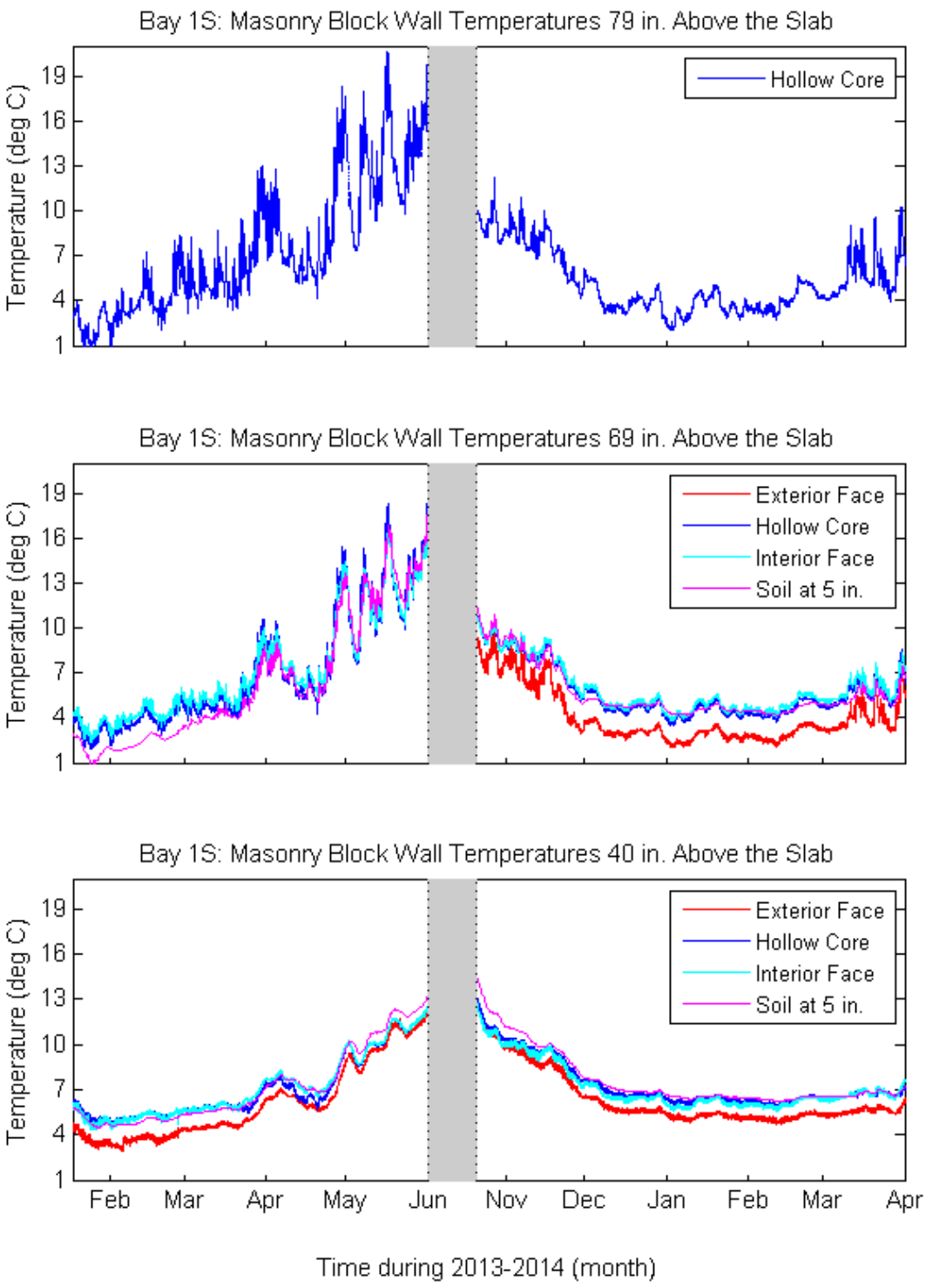

Figure B-2: Bay 1S Masonry Block Wall and Soil Temperatures during Heating Season at Upper Heights of Wall

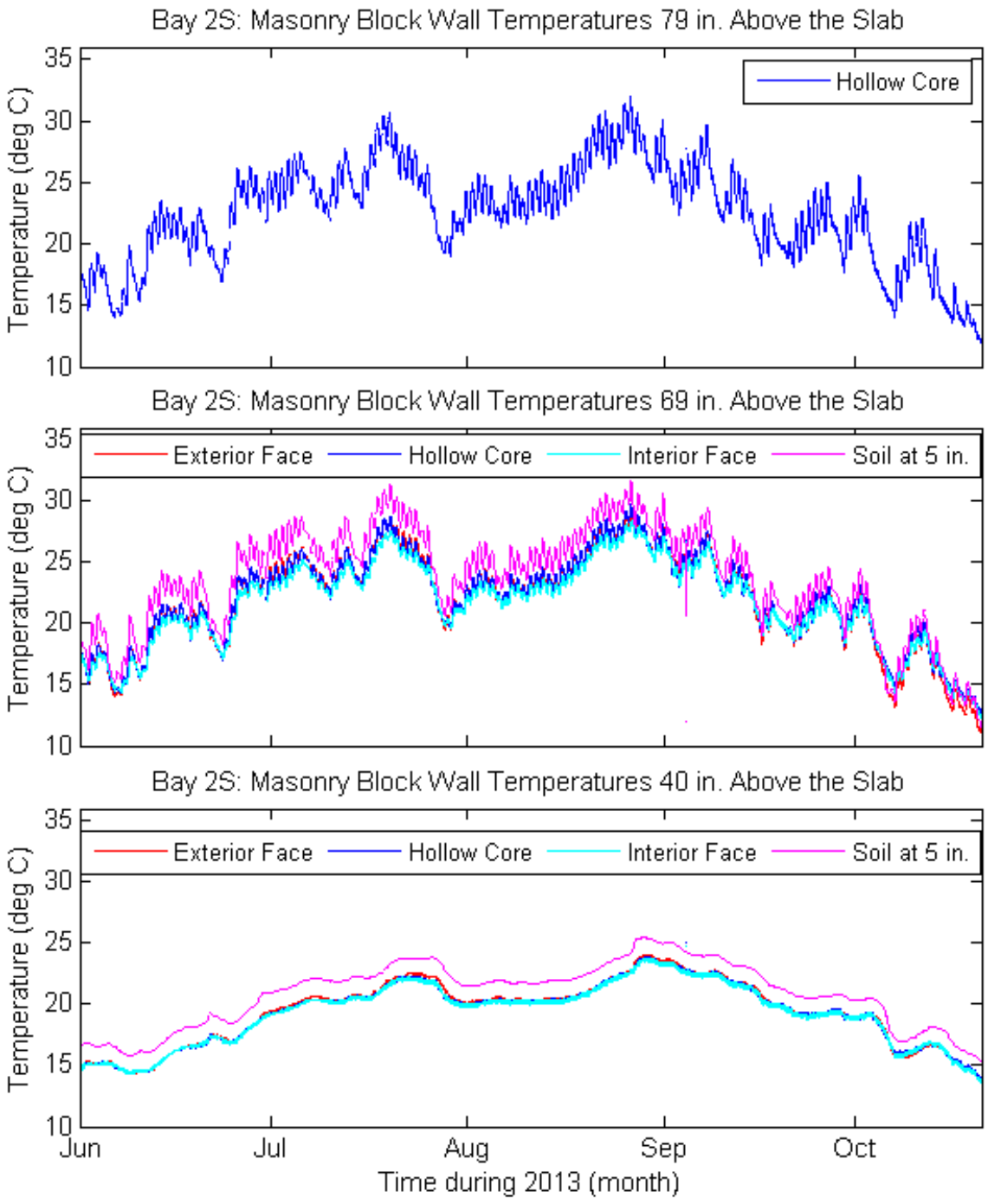

Figure B-3: Bay 2S Masonry Block Wall and Soil Temperatures during Cooling Season at Upper Heights of Wall

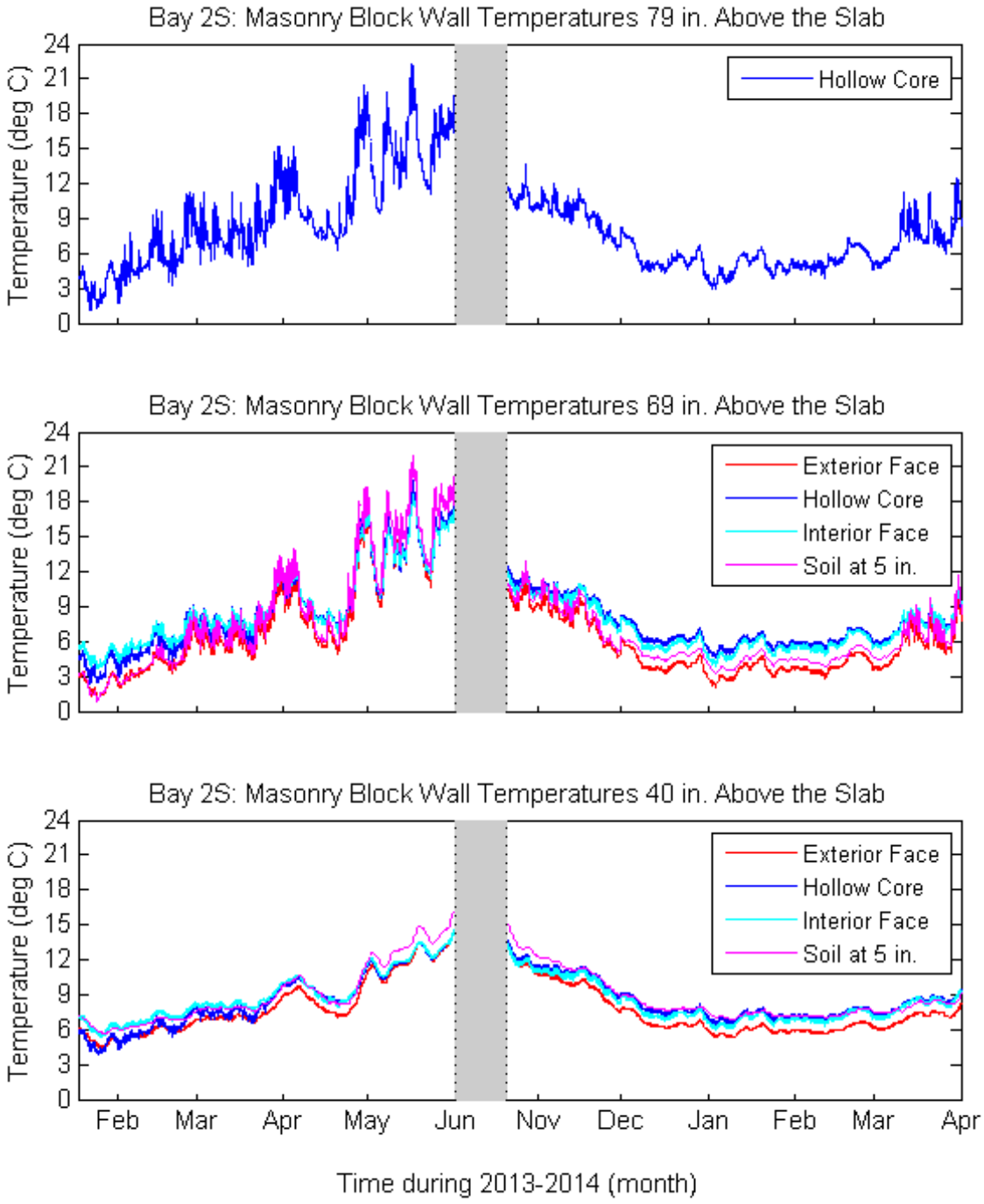

Figure B-4: Bay 2S Masonry Block Wall and Soil Temperatures during Heating Season at Upper Heights of Wall

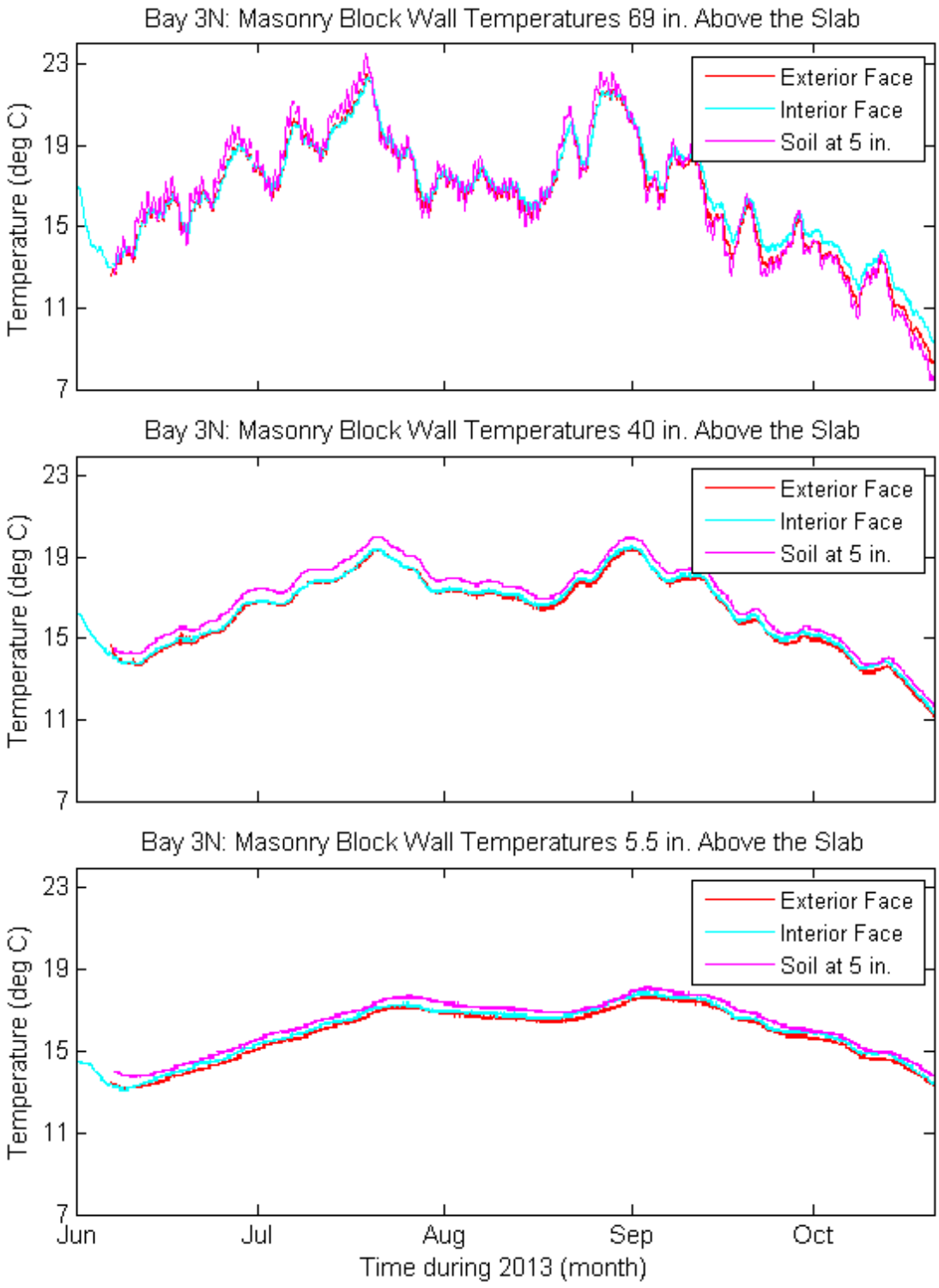

Figure B-5: Bay 3N Masonry Block Wall and Soil Temperatures during Cooling Season

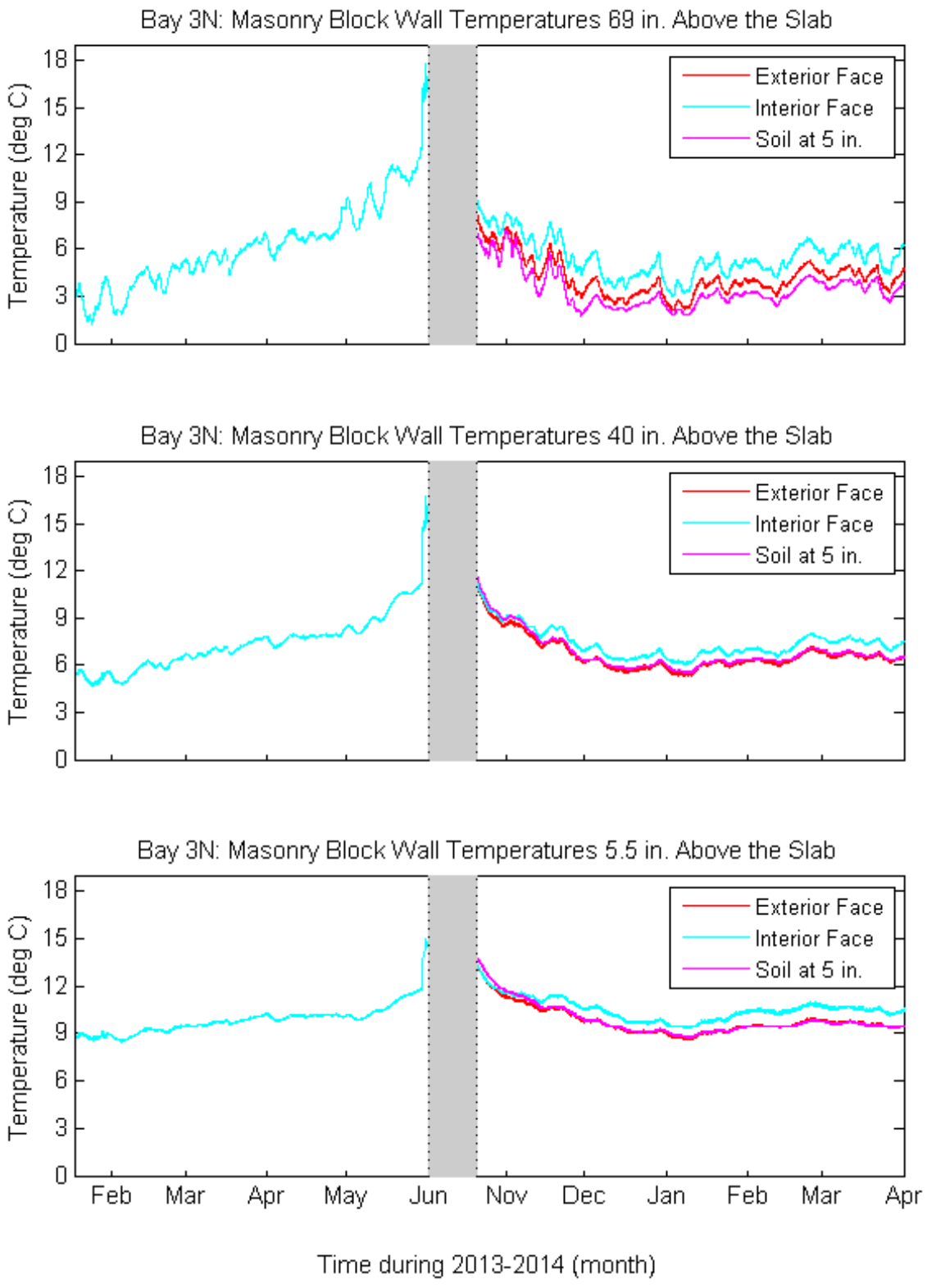

Figure B-6: Bay 3N Masonry Block Wall and Soil Temperatures during Heating Season

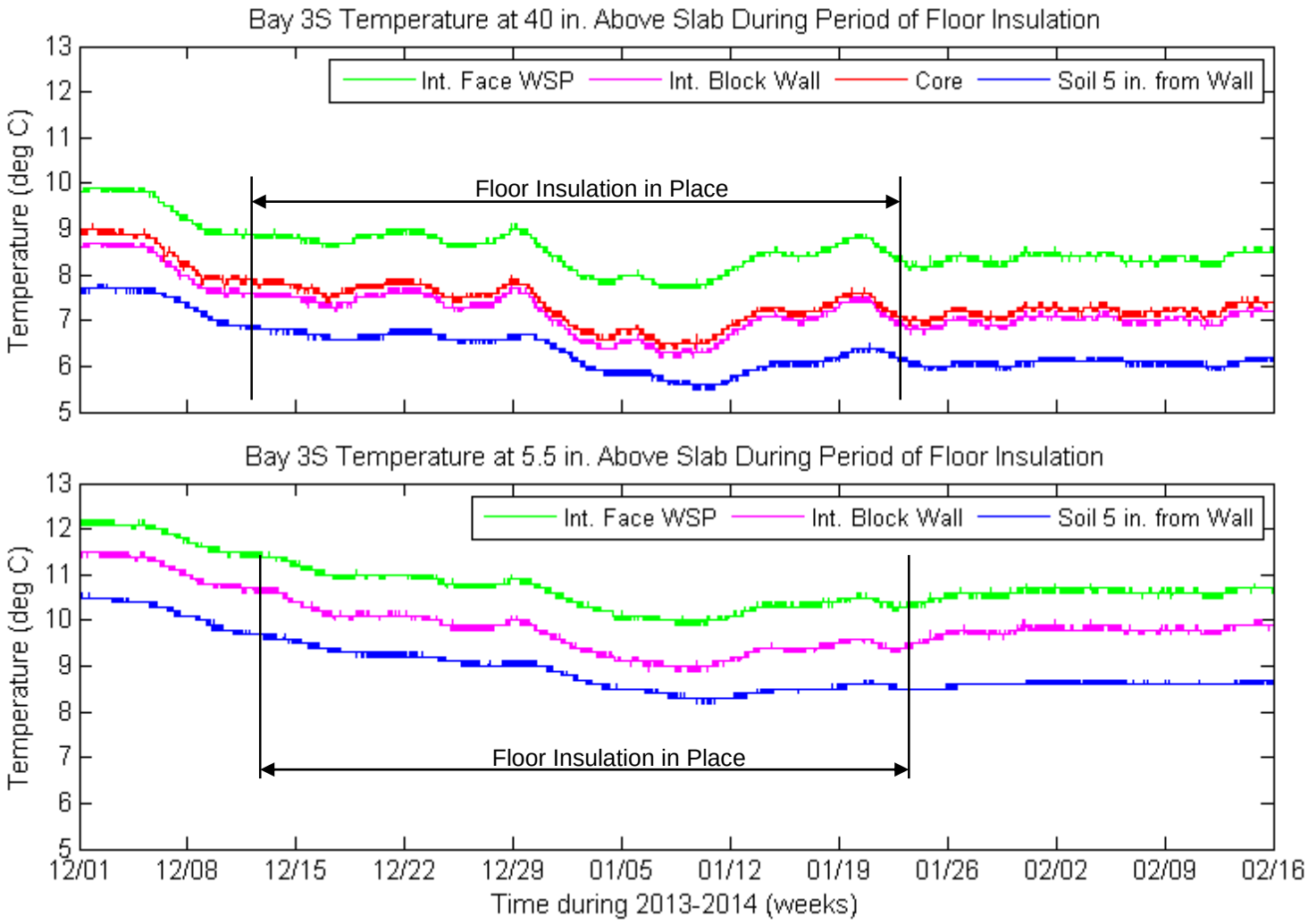

Figure B-7: Bay 3S with Floor Insulation Dec. 13, 2013 through Jan. 22, 2014

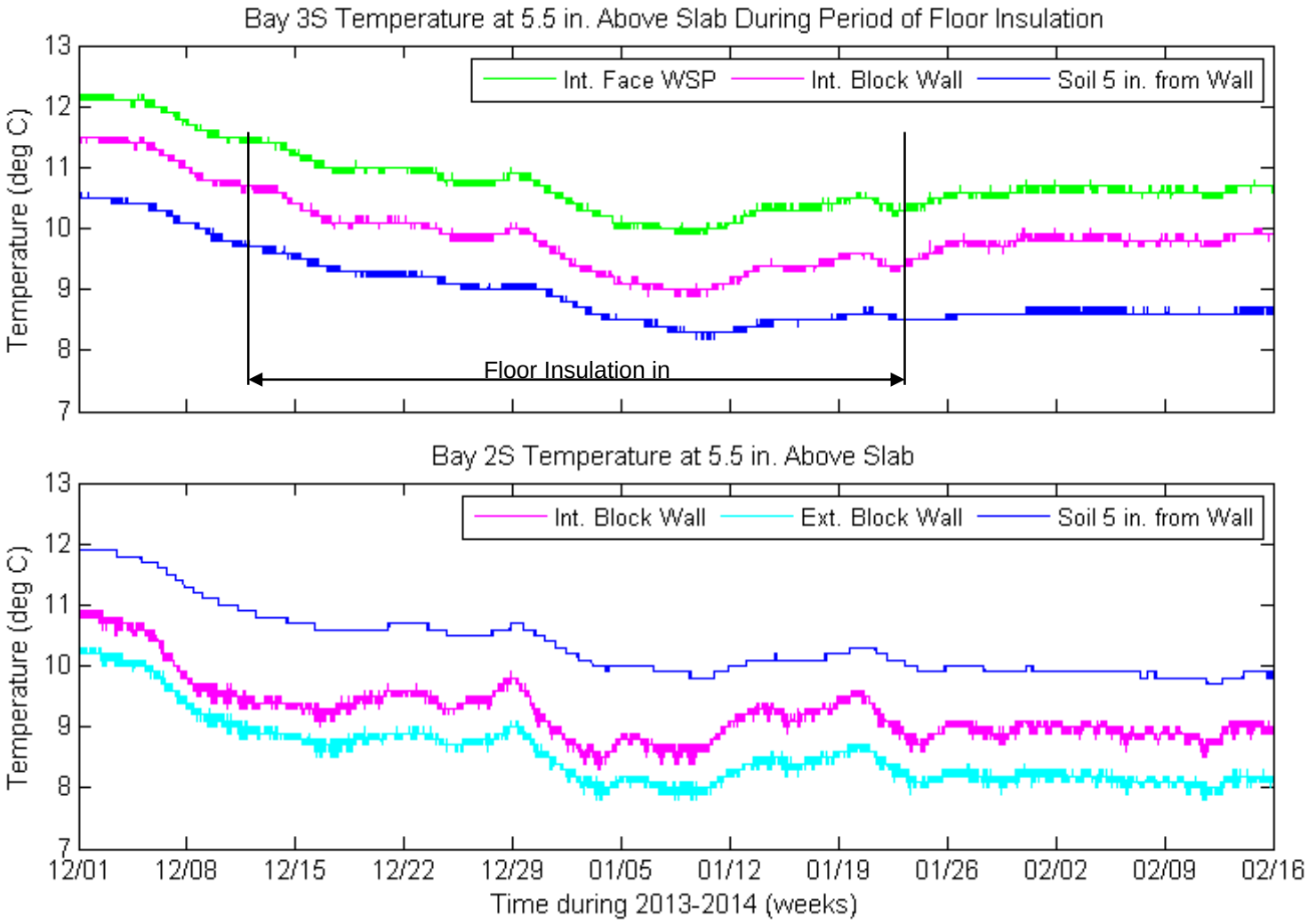

Figure B-8: Comparison of Bay 3S with Floor Insulation and Bay 2S without Floor Insulation

Appendix C: Moisture Content Data

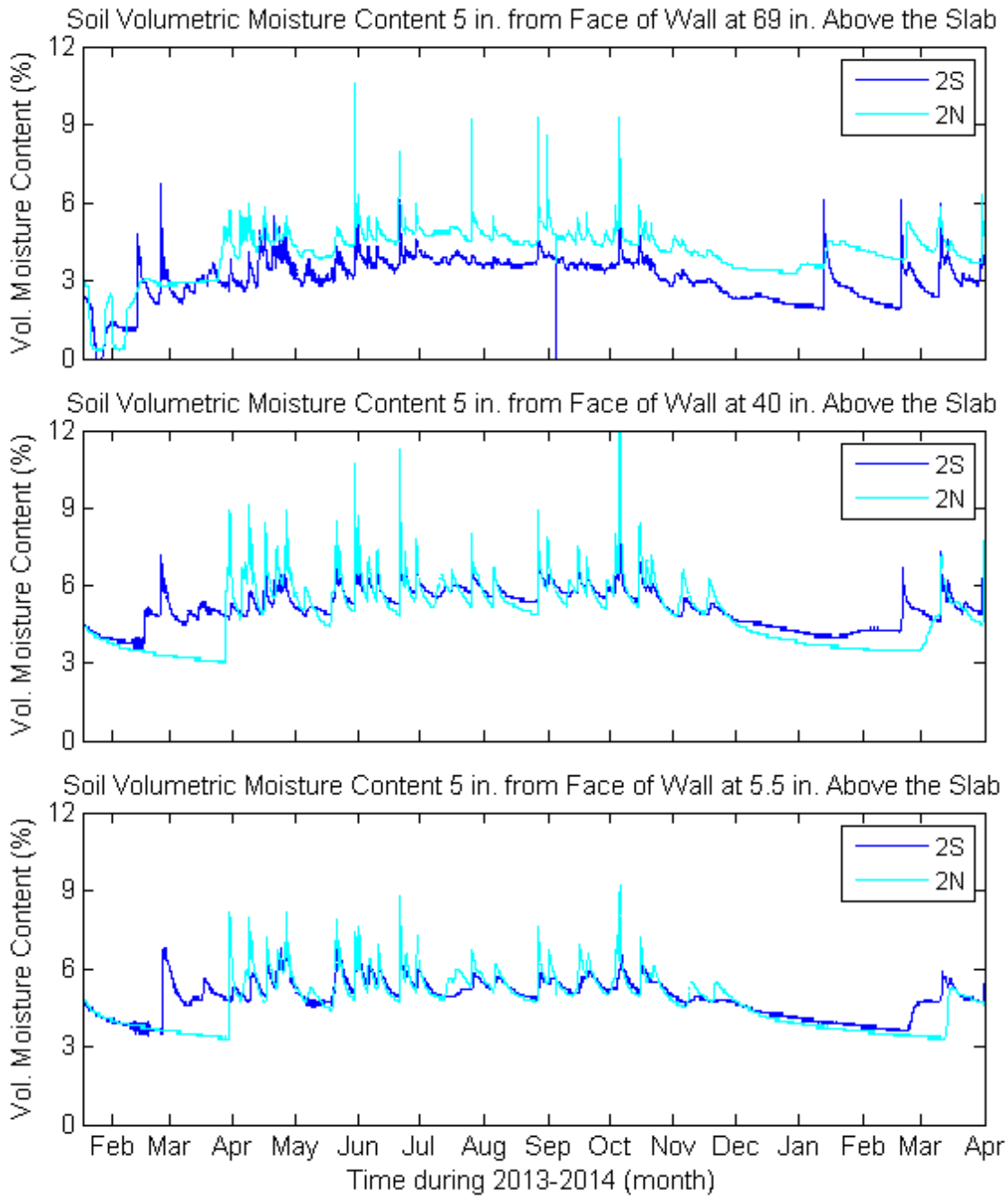

Figure C-1: Bay 2 Soil Volumetric Moisture Content across the Height of the Wall at 5 in. from the Face of the Wall for North and South Exposures

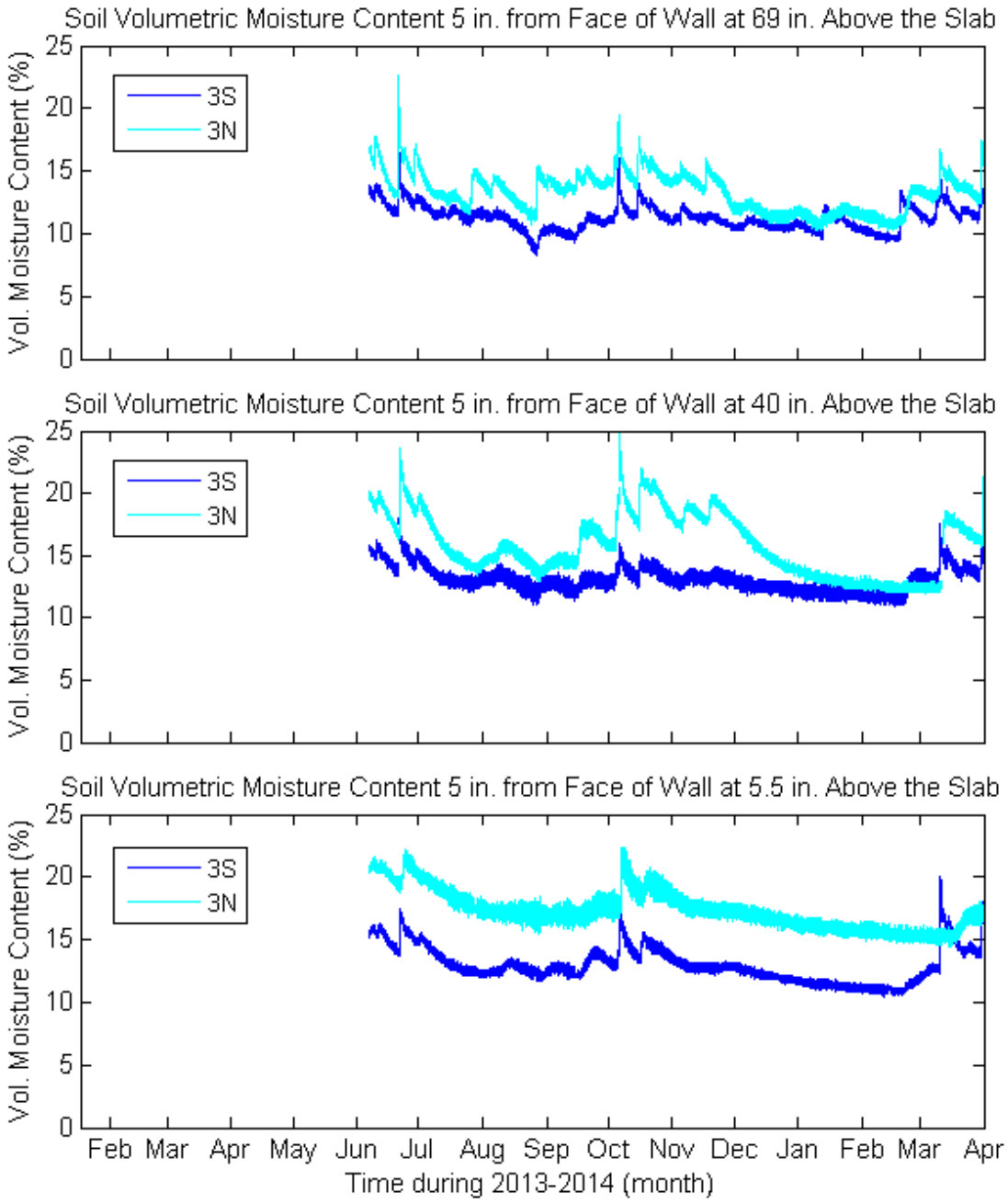

Figure C-2: Bay 3 Soil Volumetric Moisture Content across the Height of the Wall at 5 in. from the Face of the Wall for North and South Exposures

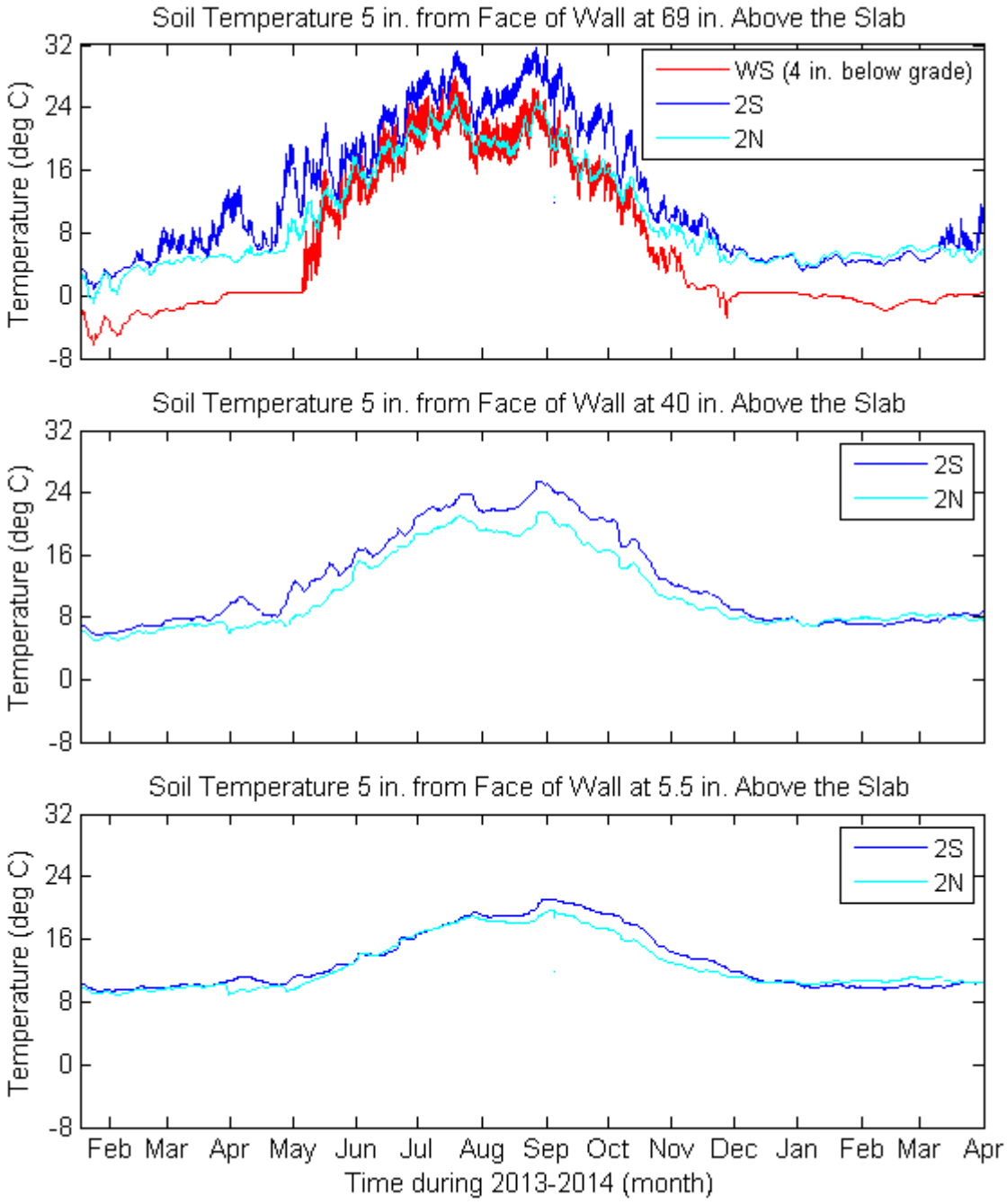

Figure C-3: Weather Station (WS) and Bay 2 Soil Temperatures across the Height of the Wall at 5 in. from the Face of the Wall for North and South Exposures

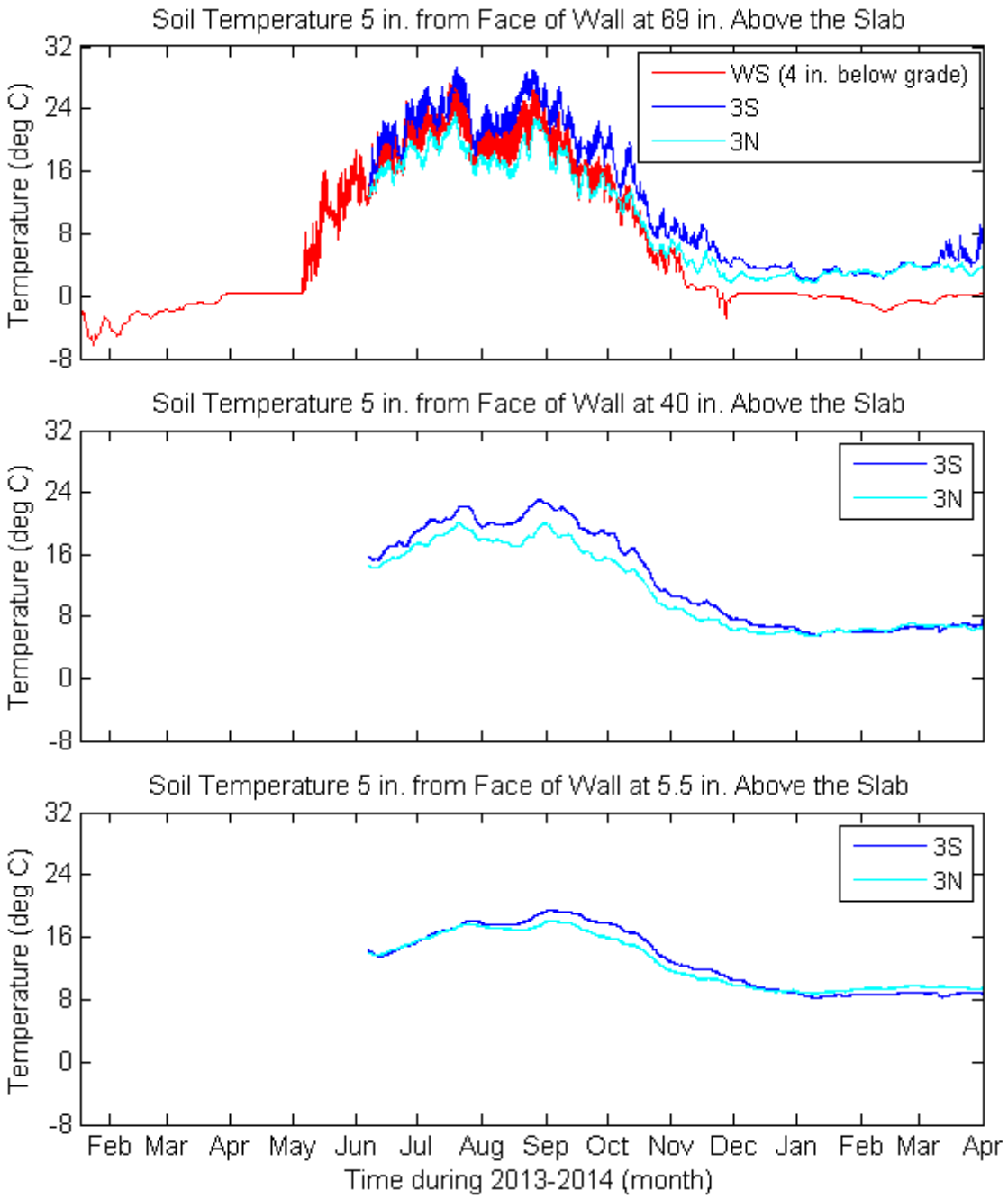

Figure C-4: Weather Station (WS) and Bay 3 Soil Temperatures across the Height of the Wall at 5 in. from the Face of the Wall for North and South Exposures

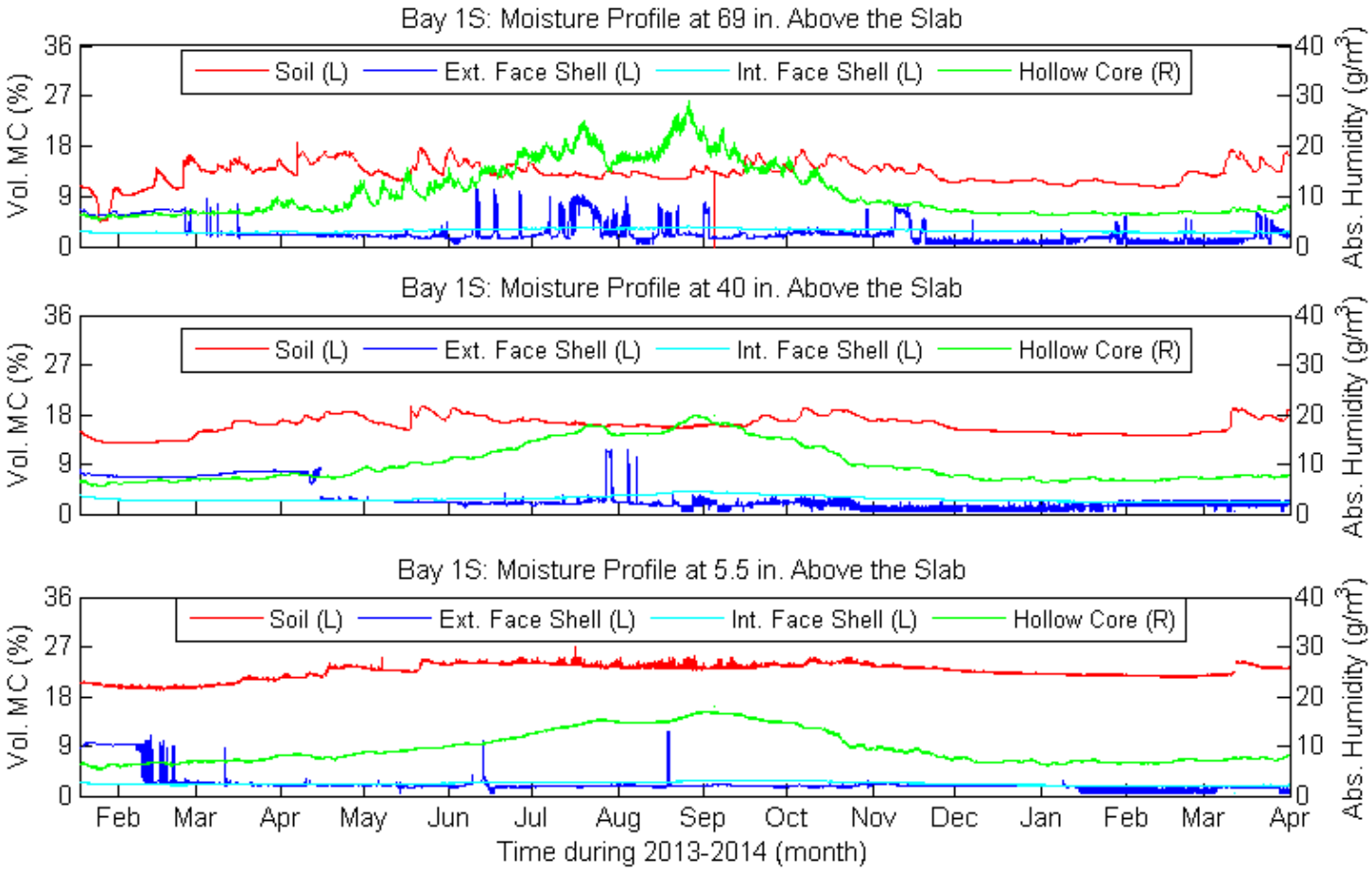

Figure C-5: Bay 1S Moisture Profile[27]

[27] For the moisture profile 5.5 in. above the slab, the hollow core sensor is actually 16 in. above the slab.

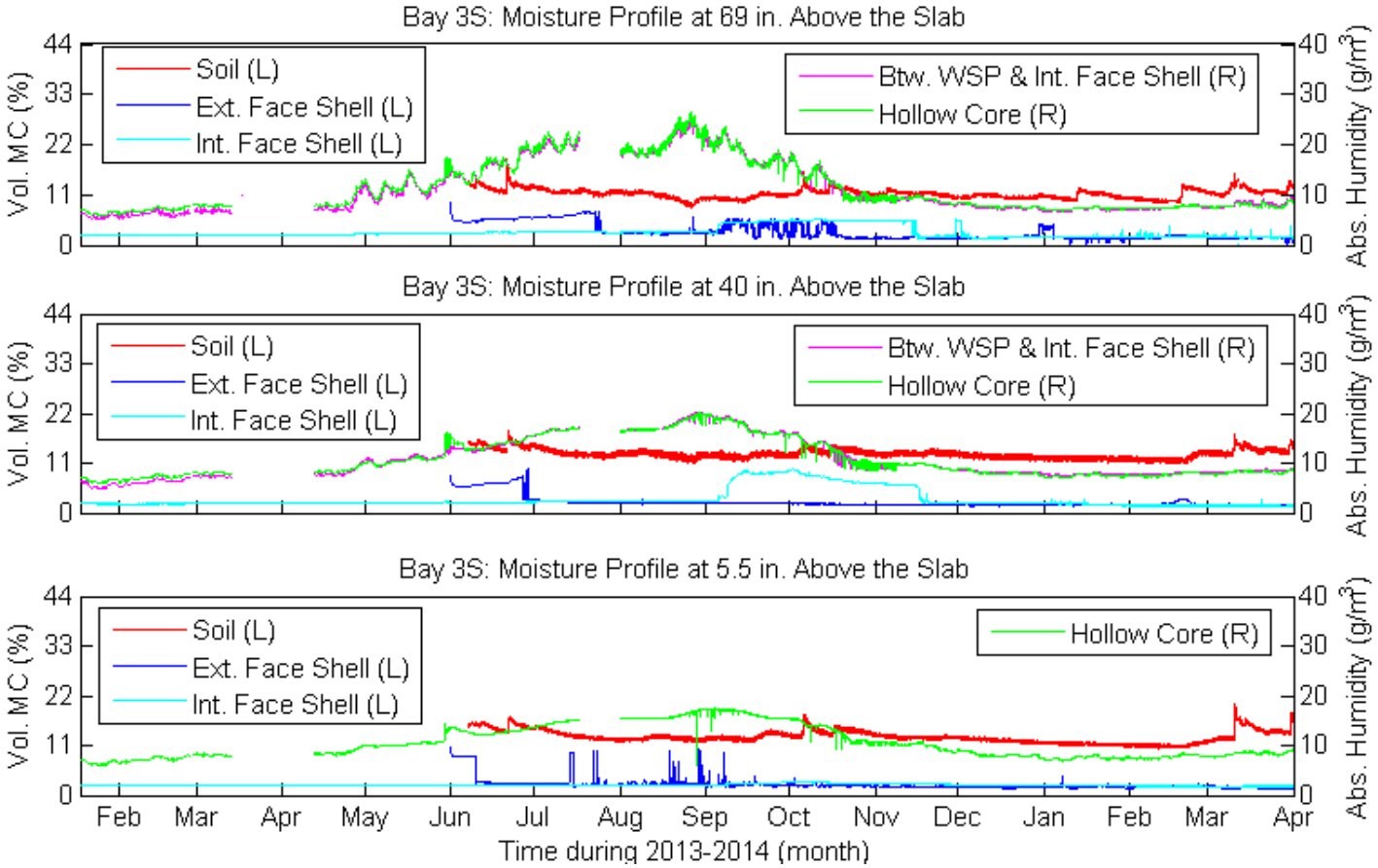

Figure C-6: Bay 3S Moisture Profile[28] [29]

[28] Water was injected between the CMU and WSP from September 4, 2013 to October 11, 2013.

[29] For the moisture profile 5.5 in. above the slab, the hollow core sensor is actually 16 in. above the slab.

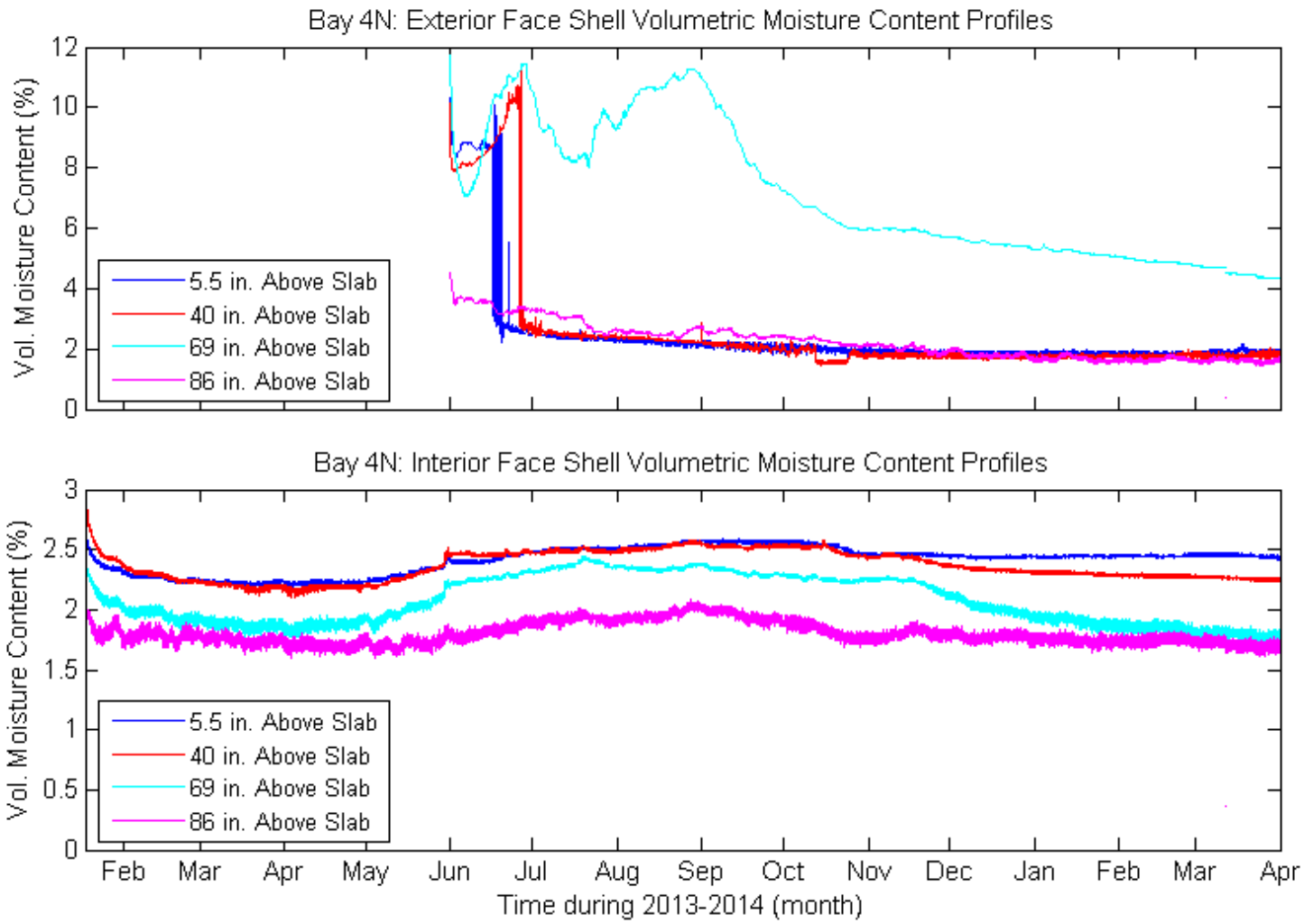

Figure C-7: Bay 4N Exterior and Interior Face Shell Moisture Content Profiles

Appendix D: Soils Report (August, 2000)

DRAFT

DESIGN REPORT
ONSITE WASTEWATER TREATMENT AND DISPERSAL SYSTEM

UNIVERSITY OF MINNESOTA
SCHOOL OF NATURAL RESOURCES
CLOQUET FORESTRY CENTER
175 University Road
Cloquet, Minnesota

AYRES ASSOCIATES
2445 DARWIN ROAD
MADISON, WISCONSIN

AUGUST, 2000

MATRIX Soils & Systems

August 15, 2000

Mr. Rick Apfel
Ayres Associates
2445 Darwin Road
Madison, WI 53704-3186

Re: Onsite Wastewater Treatment and Dispersal Capability Evaluation

Dear Rick,

You recently retained MATRIX Soils & Systems to evaluate treatment and dispersal capability of a site proposed for installation of an onsite wastewater system to serve the Cloquet Forestry Center. This letter presents results and conclusions regarding evaluation of site soil conditions.

The site is on an approximately 1.1-acre portion of forestry center property in part of the northwest ¼ of the northwest ¼ of Section 29, Township 49 North, Range 17 West, City of Cloquet, Carlton County, Minnesota. The site is an open, relatively level area bordered on the south by a research building and surrounded on the other sides by woods. Because the center is rural, water supply and wastewater systems are provided on site. The existing wastewater system, a package plant that discharges to subsurface infiltration trenches, needs to be upgraded. Installation of standard subsurface infiltration trenches for treatment and dispersal of septic tank effluent is being considered for the site.

Evaluation of site and soil conditions for wastewater treatment and dispersal purposes occurred during a site visit on August 14, 2000. Soil test pits were excavated to collect information for determining treatment and dispersal capability. Five test pits were excavated by backhoe. Observed soil profiles were described using U.S. Department of Agriculture nomenclature. In addition, saturated hydraulic conductivity was measured within two soil horizons using a compact constant head permeameter. Test pits and hydraulic conductivity measurement points were subsequently horizontally and vertically located and are shown on the attached site plan.

Soil of the area formed in glacial outwash materials. Morphology throughout the site is relatively uniform. The surface horizon typically consists of 6 inches of weakly structured fine loamy sand fill above 14 inches of weakly to unstructured fine loamy sand to fine sand subsoil. Underlying substrate soils are unstructured sands and coarse sands. Mottled soil, an indication of periodic saturation, was observed as shallow as 20 inches below ground surface (bgs). Mottling in the upper horizons is considered to be relict, i.e. not indicative of current periodically saturated conditions. The shallowest depth of mottling that represents current periodically saturated conditions is 76 inches bgs as observed in test pit TP3. Ground water was observed at 109 inches bgs in test pit TP1. Detailed soil profile descriptions are attached.

RAAl02

MATRIX Soils & Systems, Inc.
3990 Fairview Road, Duluth, MN 55803-2708
(218)728-3961, FAX (218)724-8381
e-mail: matrixss@uswest.net

As expected measured hydraulic conductivities are quite high ranging from 500 inches per day (in./day) to 970 in./day, which is equal to 310 gallons per day per square foot (gpd/ft²) to 610 gpd/ft², and approximately equivalent to a percolation rate range of 2 minutes per inch (mpi) to 3 mpi. A copy of the field data sheets are attached.

Soil conditions of the site are suitable for treatment and dispersal of residential strength septic tank effluent. Soil water movement within the site will be primarily vertical. Site loading rates will be dependent on soil conditions and type of wastewater discharged to the soil. For the soil conditions observed, an infiltrative surface loading rate of 0.8 gpd/ft² is recommended for residential strength septic tank effluent discharged to subsurface infiltration trenches installed 30 inches to 40 inches bgs.

This letter should provide the information needed to proceed with system planning. If you or City of Cloquet Zoning Department representatives have any questions regarding this letter, I may be reached at (218)728-3961.

Sincerely,

MATRIX Soils & Systems, Inc.

Robert W. Whitmyer, CPSS, MnPSS, Designer I
President

Attachments

MATRIX Soils & Systems, Inc.
3990 Fairview Road, Duluth, MN 55803-2708
(218)728-3961, FAX (218)724-8381
e-mail: matrixss@uswest.net

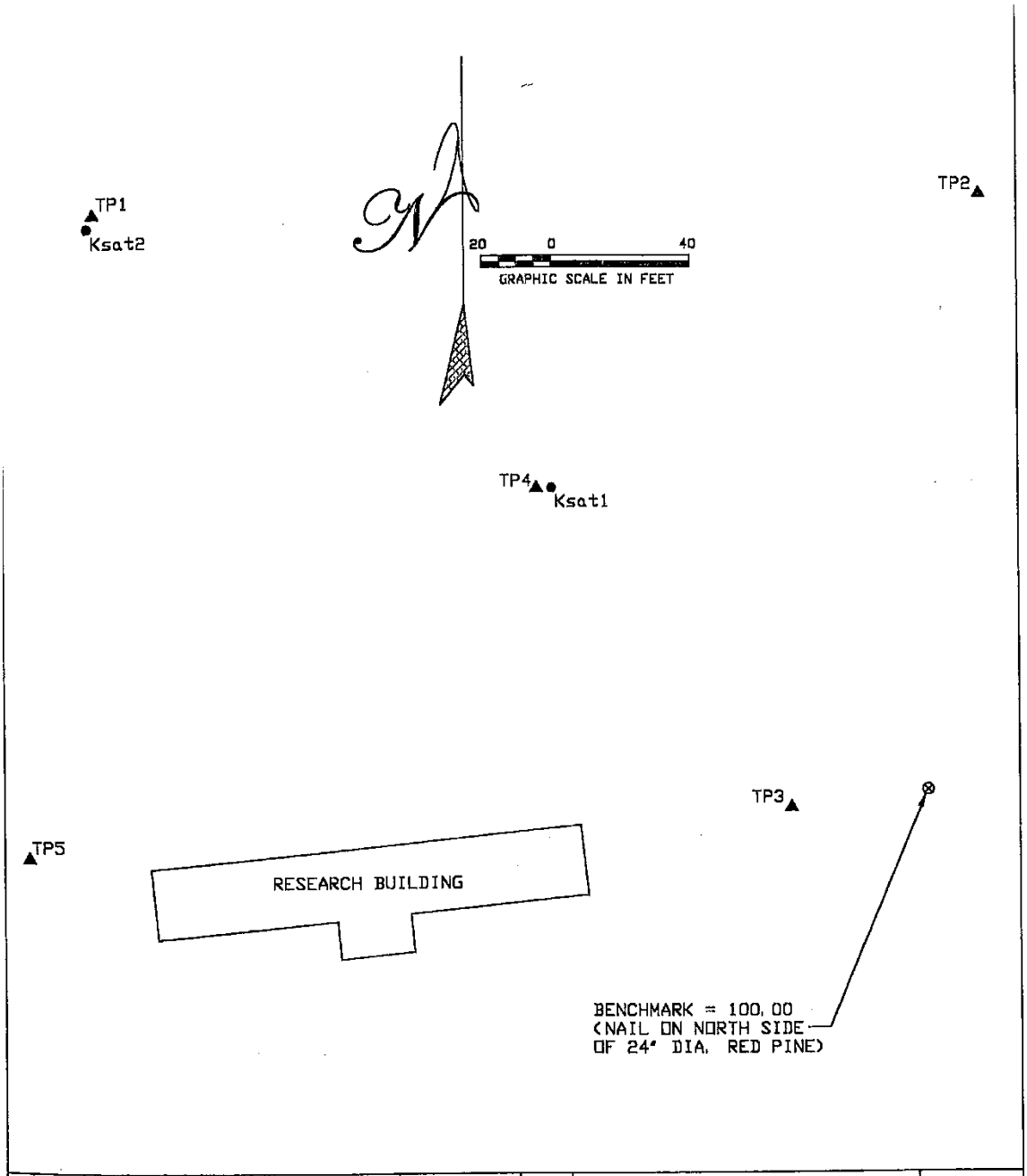

DRAWN		AS SHOWN	0	SOIL TEST LOCATIONS	08/14/00
RWW	SITE PLAN	SCALE	REV.	DESCRIPTION	DATE
	MATRIX Soils & Systems, Inc.	CLOQUET FORESTRY CENTER PT NW 1/4 NW 1/4 SEC. 29 T49N, R17W CLOQUET, MINNESOTA			FIGURE 1

SOIL PROFILE DESCRIPTION

PROJECT Cloquet Forestry Center
TEST PIT TP1
DESCRIPTION BY R.W. Whitmyer, CPSS, MnPSS, Designer I

SCOPE Site Evaluation
ELEVATION 98.06 ft
DATE 8/14/00

DEPTH (in.)	MATRIX COLOR	TEXTURE	STRUCTURE-CONSISTENCE	MOTTLES	OTHER	STE LOADING RATE (gpd/ft²)*
0 - 7	7.5YR 4/3	loamy sand to fine sand (fill)	moderate to weak, medium subangular blocky; soft, dry to moist		many very fine and fine, and common medium roots; abrupt smooth boundary	0.6
7 - 22	7.5YR 4/6	fine sand to sand	single grain; soft, dry to moist		few fine and medium roots; diffuse wavy boundary	0.6
22 - 40	7.5YR 4/4	sand; <5% gravel	single grain; loose to soft, dry to moist	common, medium, faint, 7.5YR 4/6 (relict)	abrupt smooth boundary	0.8
40 - 42	7.5YR 4/4	sand	single grain; loose to soft, dry to moist	many, fine, lamella, 7.5YR 2.5/1 (relict)	abrupt smooth boundary	0.8
42 - 90	7.5YR 5/4	sand; <5% gravel	single grain; loose, moist to dry	few, coarse, faint, 7.5YR 4/4 (relict)	abrupt wavy boundary	0.8
90 - 102	7.5YR 4/3	coarse sand; 5-10% gravel	single grain; loose, moist to dry	few, medium, distinct, 5YR 4/6	abrupt smooth boundary	NP†
102 - 109	7.5YR 4/3	coarse sand; 5-10% gravel	single grain; loose, very moist			NR‡
109					GROUNDWATER	

* STE (septic tank effluent), gpd/ft² (gallons per day per square foot).

† Not permitted.

‡ Not recommended.

MATRIX Soils & Systems, Inc.
3990 Fairview Road, Duluth, MN 55803-2708
(218) 728-3961, FAX (218) 724-8381, e-mail: matrixss@uswest.net

SOIL PROFILE DESCRIPTION

PROJECT Cloquet Forestry Center
TEST PIT TP2
DESCRIPTION BY R.W. Whitmyer, CPSS, MnPSS, Designer I

SCOPE Site Evaluation
ELEVATION 97.74 ft
DATE 8/14/00

DEPTH (in.)	MATRIX COLOR	TEXTURE	STRUCTURE-CONSISTENCE	MOTTLES	OTHER	STE LOADING RATE (gpd/ft²)*
0 - 4	7.5YR 4/3	fine loamy sand to loamy sand (fill)	weak to moderate, medium subangular blocky; very friable, moist to dry		many very fine, and few fine and medium roots; abrupt smooth boundary	0.6
4 - 12	7.5YR 4/6	fine sand to sand; <5% gravel	single grain; soft to loose, dry to moist		few very fine roots; diffuse wavy boundary	0.6
12 - 39	7.5YR 4/4	coarse sand; 5-10% gravel	single grain; loose, dry to moist		abrupt wavy boundary	1.0
39 - 93	7.5YR 5/4	sand; <5% gravel	single grain; loose, dry to moist	few, coarse, faint, 7.5YR 4/4 (relict)	abrupt smooth boundary	0.8
93 - 10	7.5YR 4/3	sand to coarse sand; <5% gravel	single grain; loose, moist	few, medium, distinct, 5YR 4/6		NP†
100					END OF EXCAVATION	

* STE (septic tank effluent), gpd/ft² (gallons per day per square foot).

† Not permitted.

MATRIX Soils & Systems, Inc.
3990 Fairview Road, Duluth, MN 55803-2708
(218) 728-3961, FAX (218) 724-8381, e-mail: matrixss@uswest.net

SOIL PROFILE DESCRIPTION

PROJECT Cloquet Forestry Center
TEST PIT TP3
DESCRIPTION BY R.W. Whitmyer, CPSS, MnPSS, Designer I

SCOPE Site Evaluation
ELEVATION 97.71 ft
DATE 8/14/00

DEPTH (in.)	MATRIX COLOR	TEXTURE	STRUCTURE-CONSISTENCE	MOTTLES	OTHER	STE LOADING RATE (gpd/ft²)*
0 - 5	7.5YR 4/4	loamy sand to sand (fill)	weak, coarse platy; soft, dry to moist		many very fine, common fine, and few medium roots; clear smooth boundary	0.8
5 - 20	7.5YR 4/4	sand to fine sand; <5% gravel and cobbles	single grain; soft, dry to moist		few very fine and fine roots; abrupt smooth boundary	0.8
20 - 23	7.5YR 3/2	fine sand	single grain; loose to soft, dry to moist		few very fine and fine roots; abrupt smooth boundary	0.6
23 - 27	7.5YR 4/4	sand; <5% gravel	single grain; friable to very friable, moist to dry		diffuse irregular boundary	0.8
27 - 76	7.5YR 5/4	sand to coarse sand; <5% gravel	single grain; loose, dry to moist	few, coarse, faint, 7.5YR 4/4 (relict)	diffuse wavy boundary	0.8
76 - 90	7.5YR 4/3	sand to fine sand	single grain; loose to very friable, moist	many, medium, distinct, 5YR 4/6	abrupt smooth boundary	NP†
90 - 96	7.5YR 4/3	sand	single grain; loose, very moist			NR‡
96					END OF EXCAVATION	

* STE (septic tank effluent), gpd/ft² (gallons per day per square foot).

† Not permitted.

‡ Not recommended.

MATRIX Soils & Systems, Inc.
3990 Fairview Road, Duluth, MN 55803-2708
(218) 728-3961, FAX (218) 724-8381, e-mail: matrixss@uswest.net

SOIL PROFILE DESCRIPTION

PROJECT Cloquet Forestry Center
TEST PIT TP4
DESCRIPTION BY R.W. Whitmyer, CPSS, MnPSS, Designer I

SCOPE Site Evaluation
ELEVATION 98.02 ft
DATE 8/14/00

DEPTH (in.)	MATRIX COLOR	TEXTURE	STRUCTURE-CONSISTENCE	MOTTLES	OTHER	STE LOADING RATE (gpd/ft²)*
0 – 5	7.5YR 4/3	fine sand (fill)	weak, coarse angular blocky; soft to slightly hard, dry to moist		many very fine and common fine roots; clear wavy boundary	0.6
5 – 10	7.5YR 4/3	fine loamy sand; <5% gravel	weak to moderate, coarse platy; slightly hard to soft, dry to moist		few very fine roots; abrupt smooth boundary	0.6
10 – 20	7.5YR 4/6	fine sand; 5-10% gravel	single grain; loose to soft, dry to moist		diffuse wavy boundary	0.6
20 – 92	7.5YR 5/4	sand to coarse sand; <5% gravel and cobbles	single grain; loose, dry to moist	few, coarse, faint, 7.5YR 4/4 (relict)	abrupt smooth boundary	0.8
92 – 104	7.5YR 4/3	sand to fine sand	single grain; very friable, very moist			NR†
104					END OF EXCAVATION	

* STE (septic tank effluent), gpd/ft² (gallons per day per square foot).

† Not recommended.

MATRIX Soils & Systems, Inc.
3990 Fairview Road, Duluth, MN 55803-2708
(218) 728-3961, FAX (218) 724-8381, e-mail: matrixss@uswest.net